

UNIVERSIDADE DE SÃO PAULO
INSTITUTO DE QUÍMICA
Programa de Pós-Graduação em Química

IAN POMPERMAYER MACHADO

**Versatilidade ótica e de tamanho em materiais
fotônicos de oxissulfetos de terras raras**

Versão corrigida da Tese conforme Resolução CoPGr 5890
O original se encontra disponível na Secretaria de Pós-Graduação do IQ-USP

São Paulo

Data do Depósito na SPG:
26/04/2021

IAN POMPERMAYER MACHADO

**Versatilidade ótica e de tamanho em materiais
fotônicos de oxissulfetos de terras raras**

*Tese apresentada ao Instituto de Química da
Universidade de São Paulo para obtenção do
Título de Doutor em Ciências (Química)*


*Orientador: Prof. Dr. Hermi Felinto de Brito
Coorientador: Prof. Dr. Lucas Carvalho Veloso Rodrigues*

São Paulo
2021

Ficha Catalográfica elaborada eletronicamente pelo autor, utilizando o programa desenvolvido pela Seção Técnica de Informática do ICMC/USP e adaptado para a Divisão de Biblioteca e Documentação do Conjunto das Químicas da USP

Bibliotecária responsável pela orientação de catalogação da publicação:
Marlene Aparecida Vieira - CRB - 8/5562

M149v	Machado, Ian Pompermayer Versatilidade ótica e de tamanho em materiais fotônicos de oxissulfetos de terras raras / Ian Pompermayer Machado. - São Paulo, 2021. 161 p.
	Tese (doutorado) - Instituto de Química da Universidade de São Paulo. Departamento de Química Fundamental. Orientador: Brito, Hermi Felinto Coorientador: Rodrigues, Lucas Carvalho Veloso
	1. Materiais luminescentes. 2. Nanomateriais. 3. Espectroscopia. 4. Terras raras. I. T. II. Brito, Hermi Felinto, orientador. III. Rodrigues, Lucas Carvalho Veloso, coorientador.

ATA. Julgamento da Tese de Doutorado em Química de **IAN POMPERMAYER MACHADO**. Aos vinte e sete dias do mês de maio do ano de dois mil e vinte e um, às treze horas e trinta minutos, por videoconferência, instalou-se a Comissão Julgadora da Tese de Doutorado intitulada "**Versatilidade ótica e de tamanho em materiais fotônicos de oxissulfetos de terras raras**", para a obtenção do título de Doutor em Ciências - no Programa de Química, apresentada por **IAN POMPERMAYER MACHADO**, cujos estudos pós-graduados visando o doutorado iniciaram-se em abril de dois mil e dezesseis, neste Instituto de Química. A Comissão Julgadora indicada nos termos do artigo 102 do Regimento Geral da Universidade de São Paulo constituiu dos Professores Doutores: Henrique Eisi Toma (Instituto de Química - USP), Rogéria Rocha Gonçalves (Faculdade de Filosofia, Ciências e Letras de Ribeirão Preto - USP) e Paulo Cesar de Sousa Filho (Instituto de Química - UNICAMP). Verificado o cumprimento das exigências regulamentares, a Comissão Julgadora passou a arguir o(a) candidato(a) na seguinte ordem: Professores Doutores: Paulo Cesar de Sousa Filho, Rogéria Rocha Gonçalves e Henrique Eisi Toma. Concluídas as arguições, a Comissão Julgadora atribuiu, em sessão secreta, os seguintes conceitos: Professores Doutores: Paulo Cesar de Sousa Filho (Aprovado), Rogéria Rocha Gonçalves (Aprovado) e Henrique Eisi Toma (Aprovado). Em conclusão, o(a) candidato(a) foi considerado(a) **APROVADO**. Em seguida, a Comissão Julgadora elaborou relatório a ser encaminhado à Comissão de Pós-Graduação. Reaberta a sessão, o(a) Senhor(a) **Hermi Felinto de Brito (Orientador e Presidente)**, anunciou os resultados e deu por encerrados os trabalhos. E para constar eu, Milton Cesar Santos Oliveira  Chefe do Serviço de Pós-Graduação, lavrei a presente Ata, que vai datada e assinada pelos membros examinadores. São Paulo, 27 de maio de 2021.



Prof. Dr. Paulo Cesar de Sousa Filho



Profa. Dra. Rogéria Rocha Gonçalves



Prof. Dr. Henrique Eisi Toma



Prof. Dr. Hermi Felinto de Brito (Orientador e Presidente)

AGRADECIMENTOS

Aos meus pais, Marco e Solinéia, e ao meu irmão Levi. Vocês são as melhores pessoas que tive a sorte de conhecer nessa vida, e mais sorte ainda de sermos da mesma família. Obrigado por todo o suporte, todos os puxões de orelha, e ao amor incondicional. Essa tese é dedicada a vocês.

À minha companheira Aryane, há 7 anos me ensinando coisas que teses não podem discutir nem compreender. Muito obrigado pelo seu amor, pela sua amizade, e por permanecer me apoiando sob todas as circunstâncias. “*Ficou com a gente o maior poder*”.

Um agradecimento especial aos meus amigos Leonnam e Dayan. A amizade e o suporte de vocês tornaram esta tese possível. Saibam que levo a amizade de vocês pelo resto da vida.

Ao professor Hermi Felinto de Brito, por ter introduzido ao campo da espectroscopia e por ter me acolhido como seu orientando tanto no mestrado quanto no doutorado. Você transmitiu valiosos ensinamentos sobre química e sobre a vida, que levarei comigo para sempre.

Ao professor Lucas Carvalho Veloso Rodrigues, cujo título de coorientador é uma pura formalidade. Seu conhecimento e sua supervisão fortaleceram o meu amor pela ciência durante essa caminhada. Obrigado pelos ensinamentos e pela amizade.

Ao professor Andries Meijerink, pelo acolhimento, orientação e suporte extraordinários durante toda a minha estadia na Holanda. Você redefiniu vários conceitos de como ser um grande professor, pesquisador e ser humano, e a isso expresse minha total gratidão.

Aos professores Henrique Eisi Toma, Vera Regina Leopoldo Constantino e Rômulo Augusto Ando, pela discussão e por todas as contribuições no exame de qualificação.

À professora Maria Cláudia França da Cunha Felinto, pelas risadas, almoços maravilhosos, discussões sobre espectroscopia, e pelas quase inúmeras análises de difração de raios X realizadas no Centro de Química e Meio Ambiente (CQMA-IPEN).

À minha vó Alzira (*in memoriam*), por toda a amizade e companhia durante minha estadia em São Paulo. Me aguarde, pois um dia estaremos juntos jogando dominó e tomando umas cervejinhas.

Aos amigos do DS: Leonnam, Cássio, Andreza, Bruno, Everton, Helliomar e Juan, por transformarem o nosso laboratório (e o Instituto de Química - IQ, até um certo ponto) num lugar muito mais divertido e agradável para se trabalhar.

Aos amigos do Laboratório dos elementos do bloco f (LEB- f) e nossos amigos agregados: Leonnam, Andreza, Cássio, Cesar, Cezar, Israel, Docinho, Everton, Francine, Helliomar, Lucca, Ivan, Latif, Zahid, Liana, Leo, Danilo, Pedro, Raphael, Bruno, Broto, Gizele, Ronaldo, Simei, Tiago, Zé e Guilherme. O LEB- f é um lugar maravilhoso e diferenciado no IQ, e assim deve permanecer.

Um agradecimento especial ao Cezar Guizzo, pois um bom laboratório só existe quando há um bom técnico. Muito obrigado por todo suporte e pela amizade. Além disso, agradeço a todo o corpo técnico e funcionários do IQ–USP, graças a vocês teses como essa podem ser concluídas.

Aos amigos do Laboratório de Materiais Fotônicos (LMF): Danilo, Luidgi, Miguel, Douglas, Victor, Marcelo, por toda amizade e cooperação (e loucura, no bom sentido).

Aos amigos que fiz no *Condensed Matter and Interfaces* (CMI) da Universidade de Utrecht – Holanda: Naud, Jur, Markus, Beppe, Jintao, Christiaan, Jesper, Claudia, Lyudmila, Maaike, Tim, Saoirse, Serena, Konstantina, Atul, Bo, Rian, Katerina, Bas, Jelmer, Huyguen, Jos, DeChao, e muitos mais. Eu não poderia ter pedido um grupo de pesquisa melhor, tanto para se trabalhar quanto para atividades não relacionadas à trabalho. Um dia nos veremos de novo.

Um agradecimento especial aos amigos Naud, Jur e Beppe, por tornarem minha experiência na Europa muito mais leve, e por me ajudarem a chamar a Holanda de “casa” durante meu doutorado sanduíche. Além disso, gostaria de agradecer aos meus amigos Jintao e Markus, pela colaboração, pela paciência para me explicar as teorias e experimentos, e pela amizade.

Aos amigos do Kung Fu da USP: Aline, Sérgio, Márcio, Paty, Marco, Gian, Lucas, Débora, Rafael, Letícia, Leo e muitos outros. Muito obrigado pelos treinos, pelo companheirismo e pelas risadas. Vocês ajudaram (e muito!) a treinar meu corpo e meu espírito para a paz.

Aos amigos razoavelmente problemáticos da ilustríssima república 83b: Batata, Seu Lunga, Cariri, Pejô, Hânso, Melete, Maneco, Tropeço, Pipoca Man, Tinky Winky e, por último, Rubens Barrichello. O 83b foi mais que uma casa nestes 7 anos morando em São Paulo. Muito obrigado pelos momentos de descontração e pela amizade.

Aos meus amigos da graduação em química da Universidade Federal do Espírito Santo: Leonnam, Bruno, Fernando, Zeca, Dedél, Rohne e mais uma dezena, por todas as alegrias, memórias, e pelo apoio neste tempo. Alguns dessa lista estão devendo finalizar o doutorado!

Aos meus amigos do Templo da Luz Azul (TLA): Lu Paz, Lu Guerra, Ro, Ícaro, Cris, Landa e Si. Um agradecimento especial ao Pai Cláudio e, obviamente, ao Seu Tranca.

Aos meus amigos da minha cidade natal, Vitória: Dayan, Cayo, Henrique, Fábio, Kevin, Celésio, Matheus, Breno e Vitão, pela amizade independentemente da distância. Saudades de vocês, nós iremos tomar umas cervejas quando essa situação de pandemia melhorar.

Ao Laboratório Nacional de Luz Síncrotron (LNLS–CNPEM) e à toda sua equipe: Verônica, Douglas, Flávio, Cristiane, Simone e Natália, pelas extensas análises realizadas, longas madrugadas acordadas e às frutíferas colaborações resultantes.

Um agradecimento especial à Dr. Verônica Teixeira (LNLS), pela amizade, colaboração, e pela enorme contribuição nesta tese. Ah, e pelos puxões de orelha com o sotaque mais gostoso de todos.

À professora Daniele Ribeiro de Araujo e ao laboratório SISLIBIO pela amizade e colaboração, que me proporcionou novos pontos de vista diferentes sobre diferentes assuntos da ciência de materiais, me tornando um profissional mais completo.

À professora Rogéria Rocha Gonçalves e à mestranda Fernanda Hediger, pela contribuição com as análises espectroscópicas dos materiais de upconversion e pelas excelentes discussões.

Ao Laboratório Nacional de Nanotecnologia (LNNano–CNPEM) pelas análises de microscopia eletrônica de varredura dos materiais cintiladores.

À Central Analítica do IQ–USP, pelas análises de espectroscopia de infravermelho (FTIR) e de espectroscopia de absorção atômica (ICP-OES).

Ao Conselho Nacional de Desenvolvimento Científico e Tecnológico (CNPq) pela bolsa de doutorado (#141446/2016-1), pela bolsa de doutorado sanduíche (SWE #204825/2018-0) e pelo suporte financeiro (Universal #427733/2016-2).

À CAPES e à FAPESP pelo suporte financeiro ao laboratório.

À Universidade de São Paulo (USP) e à Universidade de Utrecht (UU), pelas maravilhosas oportunidades e experiências. O ambiente universitário é precioso e deve ser preservado, no Brasil e em todo o mundo.

ACKNOWLEDGEMENTS

To my parents, Marco and Solinéia, and to my brother Levi. You are the greatest people I have been fortunate to meet in this life. Thanks for all the support, for chiding me when necessary, and for the unconditional love. This thesis is dedicated to you.

To my partner Aryane, who has been teaching me, for the last 7 years, things that doctorate theses cannot discuss nor understand. Thank you very much for your love and friendship, and for being always supportive under all circumstances. *“Life is a pendulous fall. But may be worth the pain”*.

Special thanks to my friends Leonnam and Dayan. Your companionship and support made this thesis possible. Please know that I will carry your friendship for the rest of my life.

To professor Hermi Felinto de Brito, for introducing me in the spectroscopy field and supervising me in both my master's and my doctorate. You have taught me valuable knowledges about chemistry and life itself, which I will take with me forever.

To professor Lucas Carvalho Veloso Rodrigues. Please know that title of co-supervisor is a pure formality. Your knowledge and supervision reinforced my love for science during this journey. Thank you for the teachings and for your friendship.

To professor Andries Meijerink, for the extraordinary supervision and support throughout my stay in The Netherlands. You have redefined several concepts of how to be a great teacher, researcher, and a great human being, and I fully express my gratitude to that.

To professors Henrique Eisi Toma, Vera Regina Leopoldo Constantino and Rômulo Augusto Ando, for the fruitful discussion and for all their contributions in the Ph.D. qualifying exam.

To professor Maria Claudia França da Cunha Felinto, for the laughs, wonderful lunches, discussions about spectroscopy, and for the almost countless X-ray diffraction analyzes performed at the *Centro de Química e Meio Ambiente* (CQMA – IPEN).

To my grandmother Alzira (*in memoriam*), for her friendship and support during my stay in São Paulo. One day we will be together again, playing dominoes and having some beers.

To the DS friends: Leonnam, Cássio, Andreza, Bruno, Everton, Helliomar and Juan, for making our laboratory – and the Institute of Chemistry (IQ) up to some extent – a much funnier and enjoyable place to work.

To the friends from the Laboratory of the elements of the *f*block (LEB-*f*) and external IQ members: Leonnam, Andreza, Cássio, Cesar, Cezar, Israel, Sweetie, Everton, Francine, Helliomar, Lucca, Ivan, Latif, Zahid, Liana, Leo, Danilo, Pedro, Raphael, Bruno, Broto, Gizele, Ronaldo, Simei, Tiago, Zé and Guilherme. LEB-*f* is a wonderful place at the IQ, and it must remain so.

Special thanks to Cezar Guizzo. A great laboratory can only exist if there is a great technician behind it. Thank you very much for your support and friendship. In addition, I would like to thank all the technical staff and employees of the IQ–USP for supporting the development of this thesis.

To my friends from the Laboratory of Photonic Materials (LMF): Danilo, Luidgi, Miguel, Douglas, Victor, Marcelo, for all your friendship and cooperation (and madness, in a good sense).

To the friends I made at the Condensed Matter and Interfaces (CMI) at Utrecht University - Netherlands: Naud, Jur, Markus, Beppe, Jintao, Christiaan, Jesper, Claudia, Lyudmila, Maaïke, Tim, Saoirse, Serena, Konstantina, Atul, Bo, Rian, Katerina, Bas, Jelmer, Huyguen, Jos, DeChao, and many more. I could not have asked for a better research group, both to work-related and non-work-related activities. We will see each other again.

A special thanks to my friends Naud, Jur and Beppe, for making my experience in Europe much lighter, and for helping me calling The Netherlands "home" during my internship. In addition, I would like to thank my friends Markus and Jintao, for their collaboration to the developed work, their patience to teach me both theory and practice, and for their friendship.

To my friends from Kung Fu at the University of São Paulo (USP): Aline, Sérgio, Márcio, Paty, Marco, Gian, Lucas, Débora, Rafael, Letícia, Leo, and many more. Thank you so much for the practice lessons, the friendship, and the funny moments. You helped me (a lot!) to train my body and spirit for peace.

To the reasonably problematic friends from the 83b, the best student's house: Batata, Seu Lunga, Cariri, Pejô, Hânso, Melete, Maneco, Tropeço, Popcorn Man, Tinky Winky and, lastly, Rubens Barrichello. The 83b was more than home in these 7 years living in São Paulo. Thank you very much for the funny and relaxing moments, and for your friendship.

To my Chemistry graduation friends from the Federal University of Espírito Santo: Leonnam, Bruno, Fernando, Zeca, Dedél, Rohne and a dozen more, for all the joy, memories, and support during this period. Some of you still have to finish the doctorate, hurry up!

To my friends from the *Templo da Luz Azul* (TLA): Lu Paz, Lu Guerra, Ro, Ícaro, Cris, Landa and Si. A special thanks to Pai Cláudio and, obviously, to Seu Tranca.

To my friends from my hometown, Vitória: Dayan, Cayo, Henrique, Fábio, Kevin, Celésio, Matheus, Breno and Vitão, for your friendship regardless of the distance. I miss you; we should have a few beers after this pandemic situation gets better.

To the Brazilian Synchrotron Light Laboratory (LNLS–CNPEM) and to its team: Verônica, Douglas, Flávio, Cristiane, Simone and Natália, for the extensive analyzes performed, long working hours during the night shift, and the resulting fruitful collaborations.

A special thanks to Dr. Verônica Teixeira (LNLS), for her friendship, collaboration, and for her huge contribution to this thesis. Oh, and for ear tugging me with her lovely accent.

To professor Daniele Ribeiro de Araujo and the SISLIBIO laboratory for the friendship and collaboration, which gave me new insights on different subjects in materials science, turning me into a more complete professional.

To professor Rogéria Rocha Gonçalves and Msc. Fernanda Hediger, for their contribution to the spectroscopic analysis of the upconversion materials and for the excellent discussion.

To the Brazilian Nanotechnology Laboratory (LNNano–CNPEM) for the of scanning electron microscopy analyses of scintillating materials.

To the *Central Analítica* of IQ–USP, for the infrared spectroscopy (FTIR) experiments and atomic absorption spectroscopy (ICP-OES) analyses.

To the National Council for Scientific and Technological Development (CNPq) for the doctorate scholarship (#141446/2016-1), the internship doctorate scholarship (SWE #204825/2018-0), and for the financial support (#427733/2016-2).

To CAPES and FAPESP for the financial support to the laboratory.

To the University of São Paulo (USP) and the University of Utrecht (UU), for the wonderful opportunities and experiences. The university environment is precious and must be preserved, in Brazil and worldwide.

*“This body holding me
Reminds me of my own mortality
Embrace this moment, remember
We are eternal, all this pain is an illusion”*

TOOL – Parabola

RESUMO

Machado, I.P. **Versatilidade ótica e de tamanho em materiais fotônicos de oxissulfetos de terras raras**. 2021. 161p. Tese de Doutorado - Programa de Pós-Graduação em Química. Instituto de Química, Universidade de São Paulo, São Paulo, Brasil.

Materiais luminescentes baseados em oxissulfetos de terras raras RE_2O_2S (RE: Sc, Y, La–Lu) vem sendo extensivamente pesquisados devido à sua elevada estabilidade química/térmica, além da suas estruturas cristalina e eletrônica singulares, que permitem a fácil incorporação de íons lantanídeos para gerar materiais com alta eficiência luminescente. Contudo, a preparação destes materiais é longe de ser simples. O método de síntese de estado sólido convencional, largamente utilizado pela indústria, emprega altas temperaturas (>1000 °C) por longos períodos (>6 h), acarretando um alto gasto energético e, conseqüentemente, um alto custo de produção destes materiais. Além disso, nanomateriais luminescentes de RE_2O_2S são de grande interesse para aplicações na área médica, como em bioimageamento, mas não podem ser obtidos por métodos convencionais. Neste contexto, o objetivo deste projeto de doutorado foi sintetizar materiais fotônicos de oxissulfeto de terras raras investigando duas metodologias distintas: *i*) a síntese no estado sólido assistida por micro-ondas (MASS), buscando materiais óticamente versáteis em escala micrométrica, e *ii*) a síntese coloidal em meio orgânico, buscando nanocristais com alta estabilidade coloidal e elevada eficiência quântica de emissão. Inicialmente, os parâmetros de síntese MASS foram investigados e otimizados para a partir de uma extensa caracterização *ex-situ* de matrizes RE_2O_2S , empregando técnicas como difração de raios X e espectroscopia de absorção de raios X utilizando radiação síncrotron. A condição ótima de síntese destes materiais provou-se ser: dois tratamentos térmicos de 25 min cada, empregando carbono ativado como suscepter de micro-ondas. Dessa forma, vários materiais micrométricos foram preparados por esta metodologia, delineados para exibir propriedades fotônicas diversas: cintilação de raios X – $Gd_2O_2S:Tb$, upconversion (UC) – $Gd_2O_2S:Er(Yb)$, e luminescência persistente (PersL)

– $\text{Y}_2\text{O}_2\text{S}:(\text{Eu},\text{Yb}),\text{Ti},\text{Mg}$. Os materiais cintiladores $\text{Gd}_2\text{O}_2\text{S}:\text{Tb}^{3+}$ exibiram alta eficiência de emissão (546 nm, $^5\text{D}_4 \rightarrow ^7\text{F}_5$) sob uma ampla faixa de energias de excitação, desde o UV (4 eV) até os raios X (8000 eV). Para o fenômeno de UC, foi demonstrado que a substituição dos óxidos Ln_2O_3 precursores por hidroxicarbonatos $\text{Ln}(\text{OH})\text{CO}_3$ (Ln: Gd, Er e Yb) levou a um aumento de quase uma ordem de magnitude na intensidade de emissão UC, tornando os materiais preparados pelo método MASS comparáveis em eficiência a produtos disponíveis comercialmente. Ademais, vários materiais com PersL foram preparados, visando seu potencial para diferentes aplicações. Por exemplo, fabricou-se um novo dispositivo LED recobrimo um chip LED UV com materiais $\text{RE}_2\text{O}_2\text{S}:\text{Ti},\text{Mg}$; este dispositivo emite luz branca quando ligado, e uma emissão laranja autossustentada quando desligado, útil para iluminação de segurança em casos de queda de energia. Também foram investigados materiais $\text{RE}_2\text{O}_2\text{S}:\text{Yb},\text{Ti},\text{Mg}$, que apresentam PersL na região do infravermelho próximo (983 nm), importantes para aplicações em bioimageamento. O mecanismo de PersL foi investigado a partir de ensaios de termoluminescência em materiais $\text{Y}_2\text{O}_2\text{S}:\text{Eu}$ e $\text{Y}_2\text{O}_2\text{S}:\text{Eu},\text{Ti},\text{Mg}$, demonstrando que um efeito sinérgico entre os três íons dopantes e a matriz é responsável pela supremacia deste material como emissor de PersL de cor vermelha. A preparação dos materiais $\text{RE}_2\text{O}_2\text{S}$ pelo método MASS consistiu em uma redução de $\geq 85\%$ em tempo de síntese e de $\geq 95\%$ em consumo de energia comparado a métodos de síntese convencionais. Por fim, o método de síntese coloidal em solvente orgânico foi desenvolvido e mostrou-se reprodutível para a preparação de nanomateriais $\text{Gd}_2\text{O}_2\text{S}:\text{Eu}^{3+}$ e $\text{Y}_2\text{O}_2\text{S}:\text{Eu}^{3+}$. Os nanocristais apresentam tamanho na faixa 20–30 nm, com alta eficiência de emissão na região do vermelho (626 nm, $^5\text{D}_0 \rightarrow ^7\text{F}_2$). Além disso, demonstrou-se que tanto a oleilamina quanto o ácido oleico atuam na nucleação e no crescimento dos cristais. Os próximos desafios consistem em desenvolver nanomateriais tipo *core-shell* com absorção/emissão no infravermelho, promissoras para aplicações em monitoramento/imageamento de processos biológicos.

Palavras-chave: Materiais luminescentes, Oxissulfetos de terras raras, Síntese em micro-ondas, Síntese coloidal, Cintilação, Upconversion, Luminescência persistente.

ABSTRACT

Machado, I.P. **Size and optical versatility in rare earth oxysulfide photonic materials**. 2021. 161p. Doctorate Thesis - Graduate Program in Chemistry. Instituto de Química, Universidade de São Paulo, São Paulo, Brazil.

Luminescent materials based on rare earth oxysulfides RE_2O_2S (RE: Sc, Y, La – Lu) have been extensively researched due to their high chemical/thermal stability, additionally to their unique crystalline and electronic structures, which allow easy incorporation of lanthanide ions to generate highly luminescent materials. However, synthesizing these materials is a task far from trivial. The conventional solid state synthesis method, widely used by industry, employs high temperatures (>1000 °C) for long periods (>6 h), resulting in a high energy consumption, therefore increasing the costs of production. In addition, RE_2O_2S -based luminescent nanomaterials are of great interest for applications in the medical field, such as bioimaging, but they cannot be obtained by conventional methods. In this context, the objective of this doctorate was to synthesize photonic materials based on rare earth oxysulfides by exploring two distinct methodologies: *i*) the microwave-assisted solid-state (MASS) synthesis, aiming at optically versatile bulk materials, and *ii*) the colloidal synthesis in organic solvents, aiming at nanocrystals with high colloidal stability and high quantum efficiency. Initially, the MASS synthesis parameters were investigated and optimized for from an extensive *ex-situ* characterization of RE_2O_2S matrices, using techniques such as X-ray diffraction and synchrotron radiation X-ray absorption spectroscopy. The optimal synthesis condition was shown to be two heat treatments of 25 minutes each, using activated carbon as a microwave susceptor. Thus, several bulk (~ 1 μ m) materials were prepared by this methodology, designed to exhibit versatile photonic properties: scintillation – $Gd_2O_2S:Tb$, upconversion (UC) – $Gd_2O_2S:Er(Yb)$, and persistent luminescence (PersL) – $Y_2O_2S:(Eu,Yb),Ti,Mg$. Scintillating $Gd_2O_2S:Tb^{3+}$ materials exhibited high emission efficiency (546 nm, $^5D_4 \rightarrow ^7F_5$) over a wide range of excitation energies, from UV (4 eV) to

X-rays (8000 eV). For UC phenomenon, it was demonstrated that substituting the oxide Ln_2O_3 precursors by hydroxycarbonates $\text{Ln}(\text{OH})\text{CO}_3$ (Ln: Gd, Er, and Yb) led to an increase of the UC emission intensity in almost one order of magnitude, making MASS-synthesized materials comparable in efficiency to commercially available products. Furthermore, several PersL materials were prepared aiming at their potential for different applications. For instance, a new LED device was fabricated covering an UV LED chip with $\text{RE}_2\text{O}_2\text{S}:\text{Ti},\text{Mg}$ materials; this device yields warm-white light when turned on and a self-sustaining orange emission when turned off, being useful for safety lighting in cases of power outage. The $\text{RE}_2\text{O}_2\text{S}:\text{Yb},\text{Ti},\text{Mg}$ materials were also synthesized, which display near-infrared (NIR - 983 nm) PersL, which are important for bioimaging applications. The PersL mechanism of such systems was investigated through a series thermoluminescence experiments on $\text{Y}_2\text{O}_2\text{S}:\text{Eu}$ and $\text{Y}_2\text{O}_2\text{S}:\text{Eu},\text{Ti},\text{Mg}$ materials, demonstrating that a synergetic effect among the three doping ions and the matrix is responsible for the supremacy of this red-emitting PersL material. The preparation of $\text{RE}_2\text{O}_2\text{S}$ photonic materials by the MASS method consisted in a reduction of $\geq 85\%$ in processing time and $\geq 95\%$ in energy consumption compared to conventional solid-state synthesis methods. Finally, the colloidal synthesis method in organic solvents was developed and proved to be reproducible for the preparation of monodisperse $\text{Gd}_2\text{O}_2\text{S}:\text{Eu}^{3+}$ and $\text{Y}_2\text{O}_2\text{S}:\text{Eu}^{3+}$ nanomaterials. These nanocrystals were synthesized in the 20–30 nm size range, both exhibiting high luminescence efficiency in the red spectral region (626 nm, $^5\text{D}_0 \rightarrow ^7\text{F}_2$) in colloidal form. In addition, it has been shown that both oleylamine and oleic acid act as nucleation and crystal growth agents. Perspectives include the development of core-shell nanomaterials showing NIR absorption/emission, which are promising for monitoring/imaging biological processes.

Keywords: Luminescent materials, Rare earth oxysulfides, Microwave synthesis, Colloidal synthesis, Scintillation, Upconversion, Persistent luminescence.

LIST OF ABBREVIATIONS

MASS	Microwave-assisted solid-state (synthesis method)
UC	Upconversion
PersL	Persistent luminescence
λ	Wavelength
Å	Angstrom
θ	Bragg angle
°	Degree
'	Relative negative charge
×	Relative neutral charge
•	Relative positive charge
CB	Conduction Band
VB	Valence Band
CIE	Commission Internationale de l'Eclairage
e^-	electron
eV	electron-Volt (1 eV = 8065 cm^{-1})
E_g	Energy gap
h^+	Hole
FTIR	Fourier Transform Infrared Spectroscopy
LED	Light Emitting Diode
LMCT	Ligand to metal charge transfer
SEM	Scanning Electron Microscopy
TEM	Transmission Electron Microscopy
CN	Coordination number
<i>NIR</i>	Near Infrared
RE	Rare Earth
TL	Thermoluminescence
UV	Ultraviolet
VUV	Vacuum ultraviolet
XRD	X-ray Diffraction
XANES	X-ray Absorption Near Edge Structure
SR	Synchrotron Radiation

CONTENTS

Agradecimientos	v
Acknowledgements	viii
Resumo	xii
Abstract	xiv
List of abbreviations	xvi
1. INTRODUCTION	1
1.1. Lanthanoid spectroscopy	
1.1.1. Principles of lanthanoid spectroscopy in solid-state materials	4
1.1.2. Scintillation	10
1.1.3. Upconversion	12
1.1.4. Persistent luminescence	15
1.2. Luminescent materials based on rare earth oxysulfides	
1.2.1. Structure and optical properties	21
1.2.2. Challenging preparation and the MASS synthesis	23
1.2.3. Going from bulk to nanoscale	27
1.3. Objectives	30
2. EXPERIMENTAL PART	31
2.1. Preparation of RE₂O₂S-based luminescent materials by the microwave-assisted solid-state (MASS) synthesis	
2.1.1. Optimization of the MASS method	32
2.1.2. Synthesis of Gd ₂ O ₂ S:Tb scintillators	36
2.1.3. Synthesis of Gd ₂ O ₂ S:Er(,Yb) upconversion materials	37
2.1.4. Synthesis of RE ₂ O ₂ S:(Eu, Yb),Ti,Mg persistent luminescence materials ...	40
2.2. Preparation of RE₂O₂S-based luminescent nanoparticles via colloidal synthesis in organic medium	
2.2.1. Colloidal synthesis and washing procedures	42
2.2.2. Influence of oleic acid (OA) addition	47
2.3. Structural and morphological characterization techniques	
2.3.1. X-ray powder diffraction (XRD)	48
2.3.2. Synchrotron radiation X-ray powder diffraction (SR-XRD)	48
2.3.3. Fourier transform infrared spectroscopy (FTIR)	49
2.3.4. Synchrotron radiation X-ray absorption near edge structure (XANES)	49
2.3.5. Scanning electron microscopy (SEM)	50
2.3.6. Transmission electron microscopy (TEM)	50

2.4. Study of luminescence properties	
2.4.1. Photoluminescence (PL) spectroscopy	51
2.4.2. Synchrotron radiation VUV spectroscopy	52
2.4.3. Synchrotron radiation X-ray excited optical luminescence (XEOL)	52
2.4.4. Persistent luminescence (PersL) decay curves and emission spectra	52
2.4.5. Thermoluminescence (TL)	54
3. RESULTS AND DISCUSSION	56
3.1. Microwave-assisted solid-state (MASS) synthesis:	
RE₂O₂S formation versus synthesis time	
3.1.1. Oxysulfide crystal phase formation and morphology	59
3.1.2. Sulfur K-edge X-ray absorption spectroscopy	64
3.1.3. RE ₂ O ₂ S particle formation mechanism	68
3.2. Gd₂O₂S:Tb scintillators	
3.2.1. Materials' structure and morphology	70
3.2.2. Valence of terbium dopant	72
3.2.3. Photoluminescence spectroscopy	74
3.3. Gd₂O₂S:Er and Gd₂O₂S:Er,Yb upconversion (UC) materials	
3.3.1. Crystal structure of Gd ₂ O ₂ S -based UC materials	79
3.3.2. Photoluminescence spectroscopy: UC emission	81
3.4. RE₂O₂S:(Eu,Yb),Ti,Mg persistent luminescence (PersL) materials	
3.4.1. RE ₂ O ₂ S:Ti,Mg self-sustained LEDs	85
3.4.2. RE ₂ O ₂ S:Yb and RE ₂ O ₂ S:Yb,Ti,Mg near-infrared PersL	88
3.4.3. Y ₂ O ₂ S:Eu and Y ₂ O ₂ S:Eu,Ti,Mg: Peering into the PersL mechanism	95
3.5. RE₂O₂S-based luminescent colloidal nanocrystals (NCs)	
3.5.1. Eu ³⁺ as a spectroscopic probe for nano-RE ₂ O ₂ S	111
3.5.2. Attempting UC and PersL RE ₂ O ₂ S NCs	116
4. CONCLUSION AND PERSPECTIVES	122
4.1. Conclusion	123
4.2. Perspectives	126
References	127
Appendix I – Publications	139
Appendix II – Curriculum Vitae	140

Chapter 1

Introduction

1.1 Lanthanoid spectroscopy

- 1.1.1 Principles of lanthanoid spectroscopy in solid-state materials
- 1.1.2 Scintillation
- 1.1.3 Upconversion
- 1.1.4 Persistent luminescence

1.2 Luminescent materials based on rare earth oxysulfides

- 1.2.1 Structure and optical properties
- 1.2.2 Challenging preparation and the microwave-assisted solid-state (MASS) synthesis
- 1.2.3 Going from bulk to nanoscale

1.3 Objectives

1. INTRODUCTION

The discovery of rare earth elements dates to the end of the XVIII century, when distinct black rocks were retrieved at a mine in Ytterby, Sweden. It was later found to be consisted of an iron-based mineral containing elements now called lanthanum, cerium, and yttrium. Since such elements had not been reported anywhere else, they were assumed to be scarce, hence the name “rare earths”. Currently, the lanthanoid (Ln) series refers to the 15 elements in the periodic table going from lanthanum ($_{57}\text{La}$) to lutetium ($_{71}\text{Lu}$). By adding scandium ($_{21}\text{Sc}$) and yttrium ($_{39}\text{Y}$), this whole group of 17 elements is then designated as the rare earths (REs). After two centuries of research, it was shown that RE elements were not actually rare, and their exceptional electronic and magnetic properties could boost the development of novel technologies. As a result, modern society is surrounded by RE materials applied in the most diverse sectors of technology, *e.g.*, Nd-based magnets for wind power, computer hard drives, and electric vehicles, Er-doped optic fibers for global communication networks, and Ce-, Eu- and Tb-activated luminescent materials for solid state lighting and light emitting diode (LED) screens [1,2].

The rich electronic energy level structure of Ln ions is responsible for their unique optical properties among other luminescent centers. It is, therefore, possible to achieve highly efficient luminescent materials by adequately selecting the inorganic absorber host matrix, the lanthanoid dopant, and its concentration. For example, the Ce^{3+} -activated $\text{Y}_3\text{Al}_5\text{O}_{12}$ (YAG:Ce), discovered in 1967 by Blasse *et al.* [3], is an efficient yellow-emitting phosphor via blue light excitation. This material was integrated to the later found GaN-based blue-emitting LEDs to yield bright white light for energy-saving illumination, which resulted in the Nobel prize in Physics of 2014 [4,5]. It is also possible to modulate the photonic properties of lanthanoid-based luminescent materials by engineering the energy levels of one or more Ln ions together with the host electronic structure, producing remarkable optical phenomena, such as: scintillation [6], when high-energy irradiation (*e.g.*, X- and γ -rays) trigger visible luminescence; upconversion [7,8], where two or more excitation

photons are combined to yield a higher-energy emission photon; and persistent luminescence [9–11], where the excitation energy is stored in the material, giving rise to a long-lasting emission (~24 h). The nature of lanthanoid spectroscopy and these special phenomena will be covered in section 1.1.

Among rare earth-based optical materials, rare earth oxysulfides $\text{RE}_2\text{O}_2\text{S}$ (RE^{3+} : La, Gd, Y and Lu) are suitable host lattices for luminescent materials due to their high thermal and chemical stability, low toxicity, and good sensitization of trivalent lanthanoid ions (Ln^{3+}), yielding high luminescence efficiency. The latter characteristic allows $\text{RE}_2\text{O}_2\text{S}$ be versatile optical hosts, meaning that diverse luminescence phenomena can be obtained by tuning the host and dopant composition [12–15]. However, there are still some challenges and open questions regarding these materials. First, synthesizing $\text{RE}_2\text{O}_2\text{S}$ materials is not a trivial task since the formation of RE–S chemical bonds is not favored according to the Pearson theory of hard and soft acids and bases [16]. Usually, the conventional solid-state synthesis (ceramic method) is used to prepare these materials, which requires long periods of thermal treatment (from 4 to 24 h) at high temperatures (>1000 °C) [17–19]. This preparation method leads to disadvantages such as long processing time, high energy consumption, and the possibility of producing inhomogeneous materials due to the high temperature gradients in conventional furnaces. The search for environmental-friendly and cost-effective preparation methods for $\text{RE}_2\text{O}_2\text{S}$ materials is then required.

In addition, going from bulk to nanoscale is particularly challenging for these materials. Some works reports the synthesis of luminescent $\text{RE}_2\text{O}_2\text{S}$ nanoparticles, but not in colloidal form [20–22]. This means that an annealing step was employed to improve crystallinity and optical properties, but under the disadvantage of sintering the particles, therefore losing the potential for applications such as nanoprobe for bioimaging. Works regarding colloidal $\text{RE}_2\text{O}_2\text{S}$ nanoparticles are scarce, and their investigation requires attention due to their potential for technological applications.

In the presented context, this work aims to develop alternative synthetic methods to prepare bulk and nano $\text{RE}_2\text{O}_2\text{S}$ -based luminescent materials and optimize these methods to manufacture

materials exhibiting distinct optical properties. Bulk ($\sim 1 \mu\text{m}$) $\text{RE}_2\text{O}_2\text{S}$ materials (RE^{3+} : La, Gd and Y) were prepared by the microwave-assisted solid-state (MASS) synthesis and designed to exhibit the following optical phenomena: *scintillation* – $\text{Gd}_2\text{O}_2\text{S}:\text{Tb}^{3+}$, *upconversion* – $\text{Gd}_2\text{O}_2\text{S}:\text{Er}^{3+},\text{Yb}^{3+}$, and *persistent luminescence* – $\text{RE}_2\text{O}_2\text{S}:(\text{Eu},\text{Yb})^{3+},\text{Ti}^{4+},\text{Mg}^{2+}$. Finally, a colloidal synthetic approach in organic medium was employed to synthesize $\text{RE}_2\text{O}_2\text{S}:\text{Eu}^{3+}$ (RE^{3+} : Gd and Y) nanocrystals (20–50 nm) exhibiting high emission intensity and colloidal stability. Section 1.1 covers the main aspects of lanthanoid spectroscopy in the solid-state, focusing on the scintillation, upconversion, and persistent luminescence phenomena. Section 1.2 presents a thorough picture of $\text{RE}_2\text{O}_2\text{S}$ -based luminescent materials and their properties, preparation methods for micro- and nanoscale, and challenges to be overcome.

1.1 Lanthanoid Spectroscopy

1.1.1 Principles of lanthanoid spectroscopy in solid-state materials

The main spectroscopic feature that differentiates lanthanoids from the transition metals is that the 4f subshell is shielded from the external chemical environment by the outer filled 5s5p subshells (Figure 1.1). As a result, electronic transitions within the 4f states suffer little influence by the ligand field, resulting in sharp absorption and emission bands, similar to the atomic spectra [23]. Intraconfigurational 4f transitions are parity forbidden (Laporte's rule, $\Delta l = \pm 1$) which leads to low oscillator strengths and relatively long lifetimes (milliseconds) [24]. However, this selection rule can be relaxed when introducing the Ln ion in non-centrosymmetric chemical sites. In this case, a mixture of configurations with different parity $4f^n$ and $4f^{n-1}5d$ occur, allowing intraconfigurational 4f transitions by the forced electric dipole (FED) mechanism [23,25].

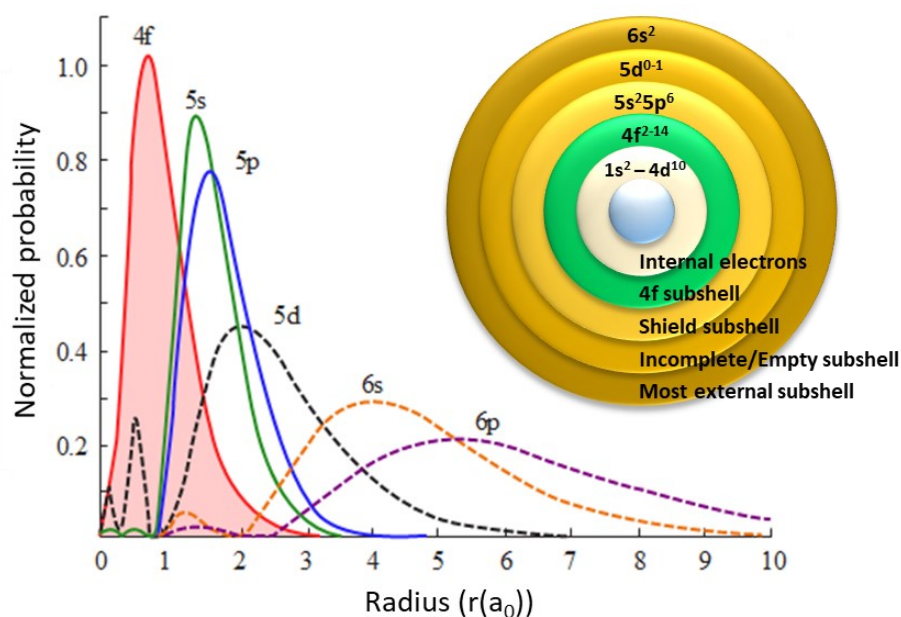


Figure 1.1 Radial probability distribution of hydrogenoid wavefunctions for the 4f, 5s, 5p, 4d, 6s and 6p subshells. The scheme on the right shows the 4f subshell shielded from the external chemical environment by the outer subshells. Adapted from [2].

The energy level structure of the Ln^{3+} ions was solved after an extensive work developed during the 1950 and 1960s, resulting in the Dieke diagram (Figure 1.2) [26,27]. Unlike the Tanabe-Sugano diagrams, which shows how the energy levels of d metals vary with the crystal field strength, the Dieke diagram displays the energy levels of the Ln ions as horizontal bars, since the whole energy structure is mostly independent of the local environment. Moreover, the very small changes on Ln^{3+} energy levels splitting consist in a sensible response from the chemical environment, meaning that these ions can be used as local spectroscopic probes. Based on the Dieke diagram, it is possible to analyze the probable transitions for each lanthanoid and the possible interactions between different Ln ions, therefore designing materials to exhibit unique luminescent properties.

The surprisingly high emission intensities of Ln^{3+} ions, considering that 4f–4f transitions are parity forbidden, were understood by two independent works developed by Judd [28] and Ofelt [29], which would be later called the Judd-Ofelt theory [30]. Considering the $^{2S+1}L_J$ Russel-Saunders notation for spectroscopic term symbols based on the LSJ quantum numbers, it is worth noting that LSJ

selection rules are just as important as symmetry rules in the determination of 4f–4f emission probabilities and intensities [31].

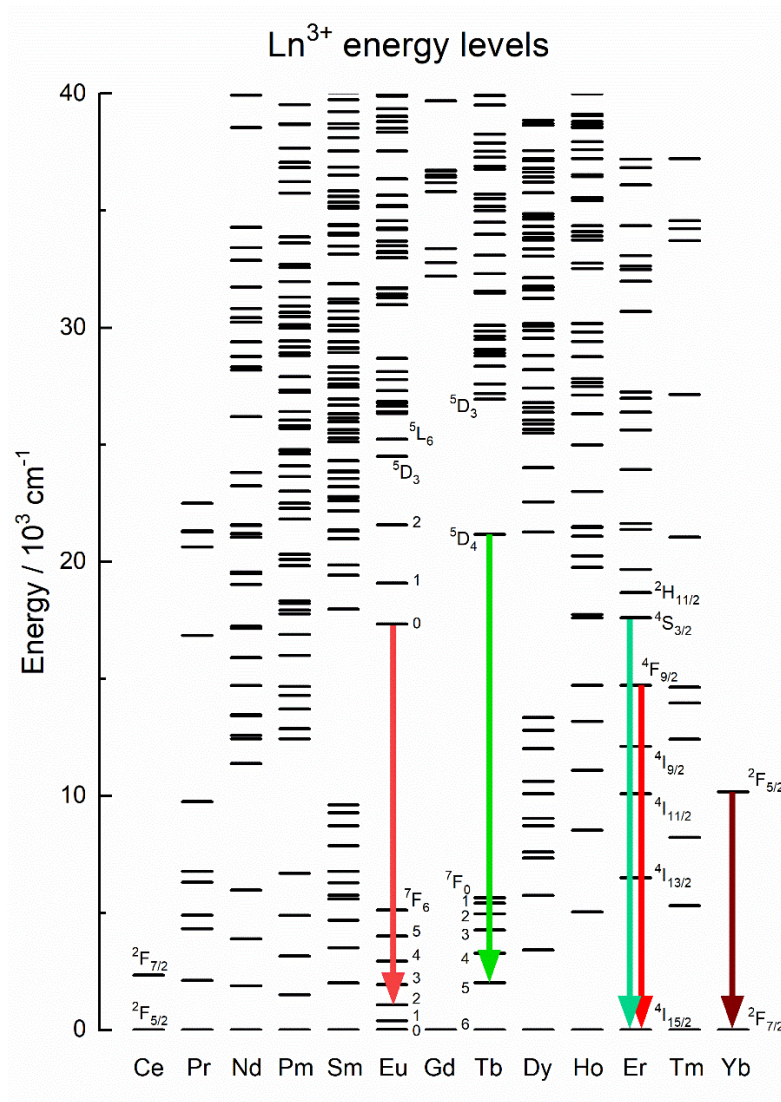


Figure 1.2 Dieke diagram: lower energy levels of the 4fⁿ configuration for Ln³⁺ ions [26,27,32]. La³⁺ and Lu³⁺ were excluded due to their electronic configuration of empty (4f⁰) and full (4f¹⁴) subshell, leading to ¹S₀ configuration. Color arrows highlight the electronic transitions that lead to the main emission bands for the lanthanoids studied in this work.

In general, Ln-doped luminescent materials consist of an inorganic host matrix, *i.e.*, semiconductor or insulator crystals or glasses, in which the Ln ions are incorporated (Figure 1.3). The host matrix may absorb the excitation energy and transfer it to a lanthanoid ion yielding light

emission. In this case, the lanthanoid ion is called activator (Figure 1.3a). It is also possible that a sensitizer ion is added (Figure 1.3b), so this entity will be responsible for absorbing the excitation energy and further transferring it to the activator ion [23]. Sensitizers are particularly important in upconversion materials. For example, Yb^{3+} ion can be used as an efficient absorber of near-infrared light due to its higher absorption cross-section among the Ln series, transferring the absorbed energy to different activator ions, such as Er^{3+} and Tm^{3+} [7].

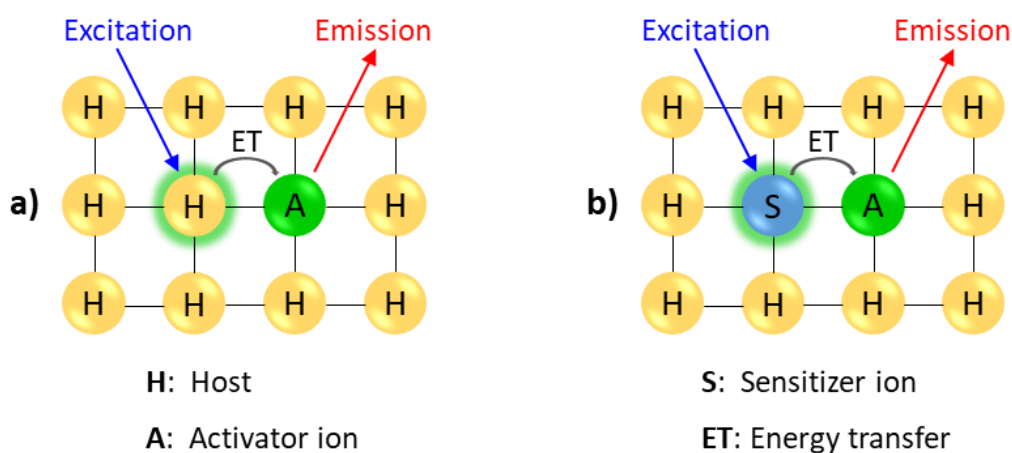


Figure 1.3 Luminescent materials: **a)** The host (H) absorbing the excitation energy and transferring to the activator ion (A), and **b)** a sensitizer (S) ion absorbing the excitation energy and transferring to the activator.

The Dieke diagram (Figure 1.2) shows all energy levels of Ln^{3+} ions up to 40000 cm^{-1} , with the ground states normalized at energy zero. However, when introducing Ln ions in inorganic hosts, each Ln ground state responds differently to the host electronic structure due to their individual and intrinsic spectroscopic characteristics, *e.g.*, ionization energy and effective nuclear charge [33]. Thus, the whole energy diagram for each lanthanoid shifts up or down in energy relative to the valence and conduction bands (VB and CB) of the host matrix, creating the so-called *zig-zag pattern* (Figure 1.4). Notably, this pattern is similar to the $\text{RE}^{2+} \rightarrow \text{RE}^{3+}$ and $\text{RE}^{3+} \rightarrow \text{RE}^{4+}$ ionization energies [34]. The diagram of Figure 1.4 is the basis of the Host Referred Binding Energy (HRBE) model developed by Dorenbos [33,35,36] – “host referred” since the top of the VB is set to zero. If the vacuum energy

above the CB is set to zero, then energy is expressed as increasing negative values from vacuum to the VB, giving a Vacuum Referred Binding Energy (VRBE) diagram.

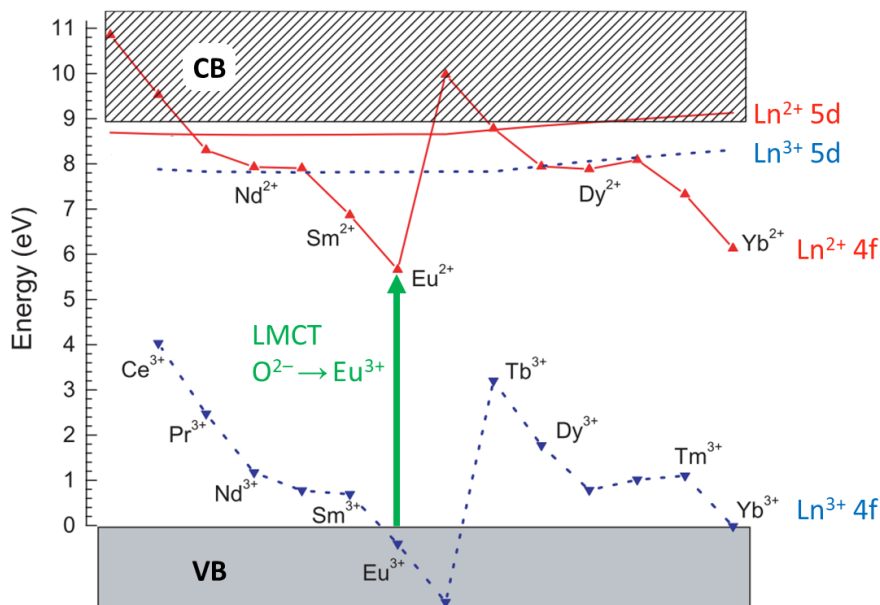


Figure 1.4 Host referred binding energy (HRBE) diagram: energy level structure of lanthanoid ions doped into YPO₄ host, with Ln²⁺ (red) and Ln³⁺ (dashed blue) ground state levels (zig-zag pattern) and lowest 5d levels (VB and CB: valence and conduction bands). In this model, the Ln³⁺ ligand-to-metal charge transfer (LMCT) is considered an electronic transition from the top of VB to the ground state of the respective Ln²⁺ (e.g., Eu³⁺ LMCT in green). Adapted from [37] with permission from Elsevier.

From the HRBE diagram (Figure 1.4), the ground state levels of Ln³⁺ ions have lower energy than the ones of the Ln²⁺. This is due to the differences in coulombic repulsions to minimize the energy, since Ln²⁺ ions are effectively surrounded by a 2– net charge, while Ln³⁺ are surrounded by 3– net charge. In this way, the energy difference between ground states of Ln²⁺ and Ln³⁺ ions, *i.e.*, the distance between the 4f-Ln²⁺ and 4f-Ln³⁺ zig-zag curves varies for the same element by changing host matrix [38,39]. Although the energy difference between the two zig-zag curves is host dependent, the energy difference of ground states between one lanthanoid and the next is practically constant due to the inner character of the 4f subshell, which maintains the Ln^{2+/3+} 4fⁿ double zig-zag pattern for all inorganic matrices.

On the other hand, the spectroscopic behavior of the 5d subshell energy levels is entirely different once this subshell is external and therefore strongly influenced by changes in the crystal field. Hence, the energy values of the 5d levels remain practically constant throughout the lanthanoid series [33]. For instance, by experimentally finding the energy levels of the $\text{Ln}^{2+/3+}$ ground states for a given Ln ion, it is possible to construct a complete diagram of Ln^{2+} and Ln^{3+} ground state energies for all lanthanoid ions. Table 1.1 shows the energy difference between the ground states of Ln^{2+} and Ln^{3+} ions relative to the Eu^{2+} and Gd^{3+} ground states, respectively. As one can observe in the diagram of Figure 1.4, the Eu^{2+} ground state is the lowest energy value in the 4f- Ln^{2+} curve (red zig-zag), as well as the Gd^{3+} ground state is the lowest among the 4f- Ln^{3+} (blue dashed zig-zag). Thus, all energy values in Table 1.1 must be positive.

Table 1.1 Energy difference ΔE between the ground states (GS) of Ln^{2+} and the $\text{Eu}^{2+} {}^8\text{S}_{7/2}$ GS (red) and ΔE between the GS of Ln^{3+} and the $\text{Gd}^{3+} {}^8\text{S}_{7/2}$ GS (blue) [33]. Energy values in eV.

	La	Ce	Pr	Nd	Pm	Sm	Eu	Gd	Tb	Dy	Ho	Er	Tm	Yb	Lu
RE²⁺ GS	² F _{5/2}	³ H ₄	⁴ I _{9/2}	⁵ I ₄	⁶ H _{5/2}	⁷ F ₀	⁸ S _{7/2}	⁷ F ₆	⁶ H _{15/2}	⁵ I ₈	⁴ I _{15/2}	³ H ₆	² F _{7/2}	¹ S ₀	¹ S ₀
$\Delta E_{\text{Eu}^{2+}}$	5.19	3.87	2.65	2.27	2.24	1.21	0	4.32	3.12	2.28	2.23	2.43	1.67	0.47	-
RE³⁺ GS	¹ S ₀	² F _{5/2}	³ H ₄	⁴ I _{9/2}	⁵ I ₄	⁶ H _{5/2}	⁷ F ₀	⁸ S _{7/2}	⁷ F ₆	⁶ H _{15/2}	⁵ I ₈	⁴ I _{15/2}	³ H ₆	² F _{7/2}	¹ S ₀
$\Delta E_{\text{Gd}^{3+}}$	-	6.57	4.73	3,23	2,80	2,60	1,33	0	4,91	3,48	2,39	2,45	4,62	1,57	0,32

Knowledge of HRBE and VRBE diagrams is essential to understand the spectroscopic properties of the lanthanoid-doped luminescent materials. In addition, by combining the $\text{Ln}^{2+/3+}$ energy levels with those of lattice defects, *e.g.*, vacancies and/or interstitial atoms, these diagrams are helpful to design of new materials with a variety of photonic properties. In this work, rare-earth oxysulfide $\text{RE}_2\text{O}_2\text{S}$ (RE^{3+} : La, Gd, and Y) luminescent materials were prepared and optimized to exhibit distinct optical phenomena: scintillation, upconversion, and persistent luminescence, which will be covered in detail in the following sections.

1.1.2 Scintillation

A scintillator is a material that emits light when it is excited by ionizing radiation. RE-activated scintillators have been intensely investigated in recent years [6] in the search for more efficient optical materials for medical imaging using X-rays and gamma rays, luggage imaging for airports, high-energy (*e.g.*, synchrotron radiation) spectroscopy, and diverse industrial applications. Several luminescent materials, such as oxyfluorides, tungstates, silicates, and oxysulfides doped with lanthanoid ions can be incorporated into glasses and polymer matrices to fabricate scintillator panel devices, improving their imaging resolution and application potential [40–43].

The scintillation mechanism is a complex process, which can be simplified into three stages: *i)* absorption/multiplication, *ii)* energy carrier migration, and *iii)* relaxation/emission (Figure 1.5) [44]. In the first stage, the scintillator material is irradiated with high energy photons or particles, creating holes in the inner shells and high energy electrons. The multiplication of electrons (e^-) and holes (h^+) occurs by several processes, such as radiative decay (secondary X-rays) and non-radiative decay (Auger processes).

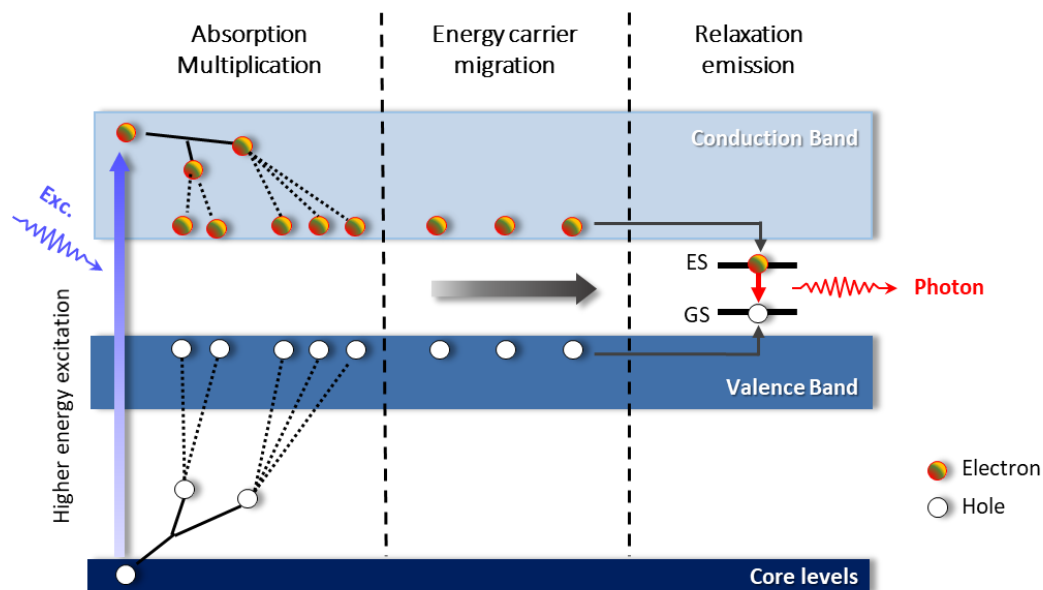


Figure 1.5 Scintillation mechanism scheme, divided into three stages: *i)* absorption/multiplication, *ii)* energy carrier migration, and *iii)* relaxation/emission (GS and ES: ground and excited states of the Ln dopant ion).

Once the electron energy decreases to values lower than the ionization threshold, e^- and h^+ thermalize to the bottom of the conduction band and the top of the valence band, respectively. Here begins the second stage, where the e^- and h^+ charge carriers are free to move within the crystal lattice, until they find a recombination center. The third stage, recombination/emission, happens when the e^-/h^+ pair recombine in the energy levels of the dopant Ln ion to yield visible-range luminescence.

Thanks to an intensive effort between theoreticians and experimentalists, current scintillator performances are reaching intrinsic limits imposed by the crystals. To maximize the emission quantum yield, ground state and the emitting excited states of the Ln^{n+} recombination center should lie above the VB and below the CB in energy, respectively. Moreover, the excited states should not be too close to the CB to avoid non-radiative losses by auto-ionization [42,44]. In this context, knowledge of the HRBE/VRBE model provides powerful tools to improve scintillators' quantum yield by finely tuning the energy levels of the host and activator ion to increase both high-energy radiation absorption and luminescence efficiency [37,45].

Regarding practical applications, additional features are desired for scintillator devices, *e.g.*, fast response (short decay times), high chemical and radiation stability, device versatility, and high energy resolution, *i.e.*, the ability to discriminate between different radiation energies [46]. The intrinsic resolution of a scintillator is defined by the materials' inherent characteristics. However, imperfections such as inhomogeneities and defects in the crystal lattice may result in local variations in light output, affecting the energy resolution. Therefore, understanding defects and associated charge traps acting in scintillation mechanisms and their relation to manufacturing technology are critical in advanced scintillator science [6,47].

1.1.3 Upconversion

Upconversion (UC) is a non-linear optical phenomenon, in which one or more low energy photons (*e.g.*, near-infrared, NIR) are absorbed and converted into a higher energy photon (*e.g.*, visible light). In 1966, Auzel was the first to observe this phenomenon for the $\text{Er}^{3+}, \text{Yb}^{3+}$ pair (Figure 1.6a,b) in borate glasses. Later, the UC process was also found for the $\text{Tm}^{3+}, \text{Yb}^{3+}$ pair, simultaneous and independently by Auzel and Ovsyankin/Feofilov [48], yielding blue-light emission (Figure 1.6c,d). This phenomenon became popular within the next decades due to laser technology advances, which allowed easy excitation of sensitizer ions, overcoming the low intrinsic probabilities of UC energy transfer processes [49]. The well-defined ladder-like structure of the Ln energy levels, combined with low-phonon energy hosts, *e.g.*, NaREF_4 (Figure 1.6) and $\text{RE}_2\text{O}_2\text{S}$, avoids non-radiative energy losses, resulting in highly emissive Ln-doped UC materials [50].

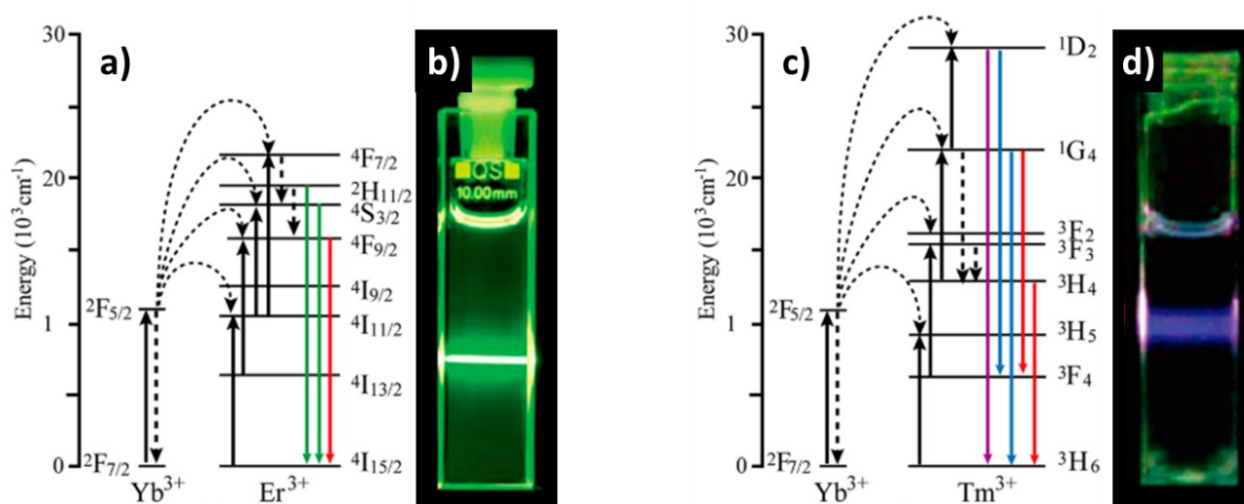


Figure 1.6 a) Upconversion (UC) energy transfer mechanisms in the $\text{Er}^{3+}, \text{Yb}^{3+}$ pair; b) UC emission of $\text{NaGdF}_4:\text{Yb}^{3+}, \text{Er}^{3+}$ nanocrystals in suspension; c) UC mechanisms in the $\text{Tm}^{3+}, \text{Yb}^{3+}$ pair; d) UC emission of $\text{NaYF}_4:\text{Yb}^{3+}, \text{Tm}^{3+}$ nanocrystals (λ_{ex} : 980 nm). Adapted from [7] with permission from the American Chemical Society.

The Ln upconversion mechanisms can be divided into three main classes: excited-state absorption (ESA), energy-transfer upconversion (ETU), and photon avalanche (PA) [7]. ESA process

is an appropriate pumping mechanism for singly doped UC materials (Figure 1.7a). Under an excitation that is resonant with the transition from the ground state (GS) to the intermediate excited level (ES1), this long-lived metastable state can successively absorb another photon and then populate a higher excited state (ES2). Upconversion emission occurs with a radiative decay from the higher-energy excited state to the ground state (ES2→GS). Low Ln dopant concentrations are necessary in this case to avoid transfer losses through cross-relaxation between luminescent centers [51].

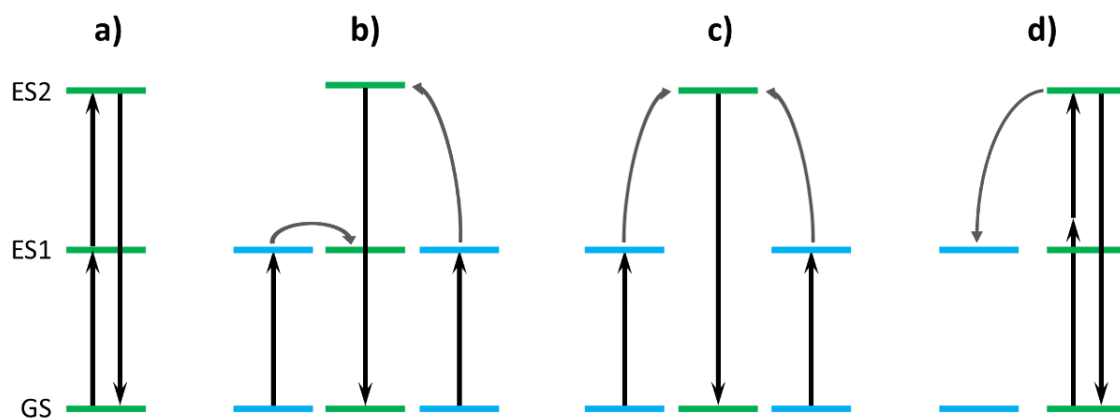


Figure 1.7 Distinct upconversion (UC) mechanisms: **a)** excited-state absorption (ESA); **(b,c)** general mechanisms related to energy-transfer upconversion (ETU): **b)** energy-transfer followed by excited-state absorption; **c)** cooperative sensitization; and **d)** photon avalanche (PA). GS: ground state, ES1: first, or intermediate excited state, ES2: second, or final excited state. [49]

Energy-transfer upconversion (ETU), which involves at least two Ln ions, is by far the most efficient upconversion mechanism, *i.e.*, most lanthanoid-doped UC materials achieve efficient upconversion emissions through these processes (Figure 1.7b and 1.7c) [7,52]. In the first ETU mechanism, energy-transfer followed by excited-state absorption (Figure 1.7b), two sensitizer ions absorb the excitation energy (ground state absorption, GSA) and transfer to a real intermediate ES1 acceptor’s level. After two consecutive non-radiative energy transfers, the higher excited ES2 state is populated, leading to UC emission. Cooperative sensitization (Figure 1.7c) happens when there is no excited intermediate level in the acceptor that is resonant with the donor’s energy level structure.

The main advantage of ETU over ESA is that ETU mechanisms do not suffer from concentration quenching. In fact, the concentration of Ln ions in UC materials that operate via ETU mechanisms should be sufficiently high to increase ion–ion interactions and improve energy transfer. The last case, photon avalanche (Figure 1.7d) is a special UC case [53]. Under a series of conditions, an abrupt increase in the number of optically active ions is observed after excitation above a given pump threshold. A high number of intermediate metastable energy levels will be populated, triggering the photon avalanche. Up to 2020, this phenomenon was only found in bulk materials, until Lee *et al.* observed giant photon-avalanching responses from upconversion nanoparticles [54], which can drastically improve UC intensity outcome and imaging resolution for biological systems.

In the context of applications, UC materials are promising as solar cell sensitizers (Figure 1.8a). The efficiency of solar cells is limited by, among other factors, the mismatch between the solar spectrum and the solar cell absorption. For instance, the infrared (>1100 nm) portion of the solar spectra is lost in solar cells such as c-Si and CdTe. Er³⁺-doped materials can upconvert part of the infrared spectra (~1520 nm) due to the ⁴I_{15/2}→⁴I_{13/2} absorption transition into the 980 (⁴I_{11/2}→⁴I_{15/2}) and 833 nm (⁴I_{9/2}→⁴I_{15/2}) wavelengths, which are more efficiently absorbed by c-Si cells [52,55,56].

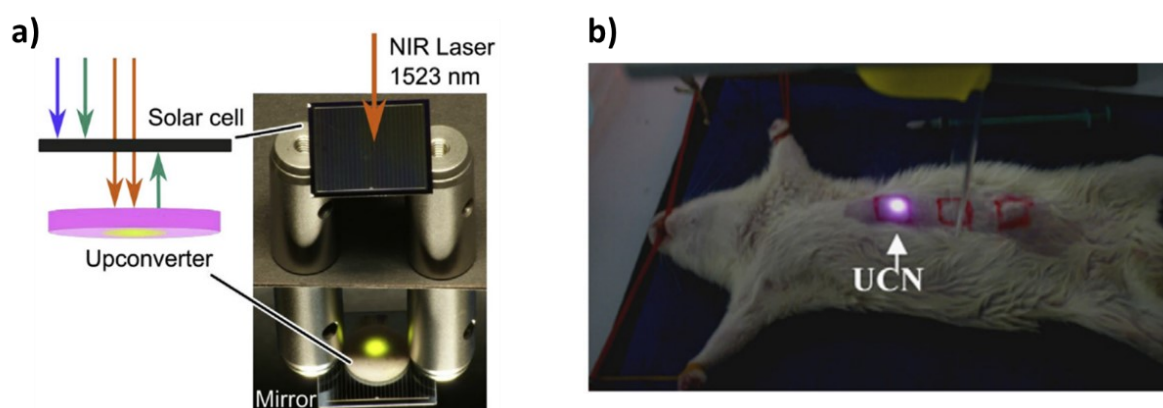


Figure 1.8 a) Bifacial silicon photovoltaic cell (2x2 cm²) containing an UC material at the bottom, taking advantage of sub band-gap photons not absorbed by the solar cell [56]. b) Detection of UC luminescence from NaYF₄:Er³⁺,Yb³⁺ nanocrystals (λ_{ex} : 980 nm) injected under the abdominal skin of a mouse [60]. Reproduced with permission from Elsevier.

Concerning applications as optical bioprobes (Figure 1.8b), UC materials are interesting since they can be excited by NIR light, which is less absorbed/scattered in biological media, considerably reducing the autofluorescence of tissues [57]. One of the main challenges is that UC emission quantum yields reduce exponentially with reducing the particle size, due to the luminescence quenching from the vibrational states of organic molecules attached to the surface of the particles [58]. Core-shell nanoparticles consist of an effective alternative to overcome this limitation [58,59], but their preparation needs to be optimized for each system individually.

1.1.4 Persistent luminescence

Persistent luminescence (PersL) is a unique optical phenomenon. A PersL material can absorb the excitation energy (*e.g.*, visible–UV light, X, γ -rays) and store it as trapped charge carriers in the lattice structure, leading to an emission that can last for several hours after ceasing the excitation [9,61]. This long-lasting emission should not be confused with phosphorescence, which is specific for organic molecules and has different mechanism. The long emission time in phosphorescence arises from a spin-forbidden electronic transition ($\Delta S \neq 0$), orders of magnitude longer (μs – s) than the spin-allowed ($\Delta S = 0$) fluorescence (ns – μs) [62]. Various names were given to refer to PersL phenomenon (afterglow, long phosphorescence) but the correct term is now defined as “persistent luminescence” [63,64]. In modern society, PersL materials surround our daily lives with diverse glow-in-the-dark applications, from decorative objects to security lighting in cases of a power outage.

The first reported persistent luminescence dates from more than 1000 years ago, in China, where a cow painting was described to remain visible during the night [62]. However, the most famous report – the Bologna Stone, dates from 1603 [65], when the Italian shoemaker and alchemist Vincenzo Cascariolo synthesized the Stone by calcining barite (BaSO_4) minerals found at Monte Paderno, near Bologna (Italy). The synthesized Stone exhibited an orange-reddish glow-in-the-dark

if it was previously irradiated by sunlight or flames. More than 400 years later, Lastusaari *et al.* [66] proved that the afterglow (λ_{em} : 610 nm) emitted from the Stone originates from the $3d^94s^1 \rightarrow 3d^{10}$ transition of Cu^+ impurities in the reduced product of the barite mineral, BaS.

The first commercial PersL material was $ZnS:Cu^+,Co^{2+}$ (λ_{em} : 530 nm), available from 1900s onwards due to the efforts of Sidot [62] and Lenard [67]. However, it suffered from short persistent emission time and moisture sensitivity. The great revolution in the field came in 1996, when Matsuzawa *et al.* reported the $SrAl_2O_4:Eu^{2+},Dy^{3+}$ material (λ_{em} : 520 nm), that exhibit 24 hours of persistent luminescence [68]. Several works were then published focusing on Eu^{2+} -activated PersL materials [10]. By changing the host matrix (aluminates, silicates, borates) it was possible to tune the $Eu^{2+} 4f^65d^1 \rightarrow 4f^7$ emission wavelength from violet to green (400–535 nm), preserving the long emission time. However, red and NIR PersL are difficult to achieve with Eu^{2+} , since it requires exceptionally strong crystal field splitting of $Eu^{2+} 5d$ energy levels, together with covalency effects, to redshift its $4f^65d^1 \rightarrow 4f^7$ emission towards longer wavelengths. This issue will be addressed later.

The PersL mechanism for is still a subject of debate among scientists, mainly because each system has its own mechanistic particularities. Nonetheless, an agreement was asserted after Aitasalo *et al.* [69] regarding the mechanism for Eu^{2+} -activated PersL materials. In this mechanism, intrinsic lattice defects (oxygen vacancies) and intentional extrinsic defects (Nd^{3+}/Dy^{3+} co-dopants) are considered as trap centers responsible for the energy storage and persistent emission. In this sense, PersL is a type of thermally stimulated luminescence [70,71]. A general PersL mechanism model is presented on Figure 1.9, where 1.9a shows the case of a high energy excitation, leading to an electron transfer from the valence band (VB) to the conduction band (CB), and 1.9b shows the case of a lower energy excitation, directly pumping the luminescent center, *e.g.*, an Eu^{2+} ion. Despite this variation, these two mechanisms operate through the same processes, which were labeled 1–4 (Figure 1.9 and Table 1.2): 1 - excitation, 2 - trapping, 3 - detrapping, and 4 - recombination/luminescence.

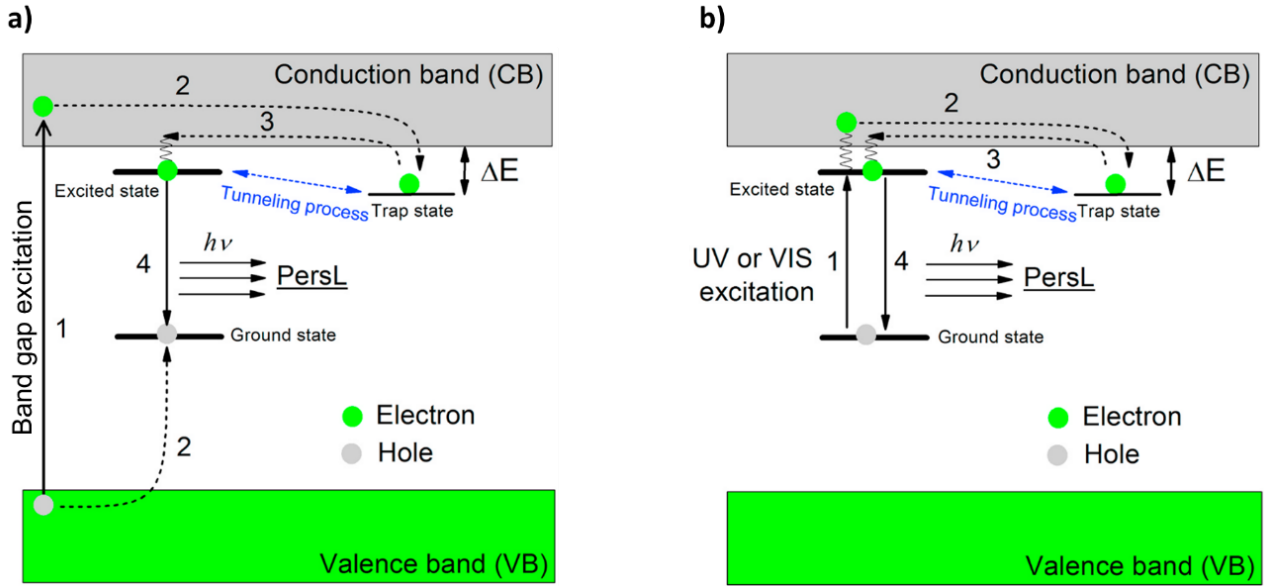


Figure 1.9 Persistent luminescence (PersL) mechanism: schematic illustrations of the *electron* trapping-detrapping model in the case of **a)** higher energy band gap excitation, and **b)** low energy UV–visible light excitation (pumping only the emitter ions). Adapted from [62] with permission from Elsevier.

Table 1.2 Sequential processes involved in the *electron* trapping-detrapping model of PersL mechanism (e^- : electron, h^+ : hole, VB: valence band, CB: conduction band, GS: ground state, ES: excited state).

e^- mechanism	Band gap excitation (Figure 1.9a)	Activator ion excitation (Figure 1.9b)
1. Excitation	Excitation of an e^- from VB to CB; Creation of a free e^- in CB and a free h^+ in VB	Excitation of an e^- from the activator ion GS to its ES, close in energy to the CB; Creation a free e^- in CB and a h^+ in the ion's GS
2. Trapping	e^- in CB finds a trap (e.g., anion vacancy or co-dopant energy level); h^+ in VB finds the GS of activator ion	e^- in CB finds a trap (e.g., anion vacancy or co-dopant energy level)
3. Detrapping	e^- is released from the trap to CB as a function of kT (k : Boltzmann constant)	Identical as 1.9a
4. Recombination	Radiative e^- - h^+ recombination at the activator ion, yielding PersL	Identical as 1.9a

The PersL mechanism model shown in Figure 1.9 and explained in Table 1.2 is a general model for PersL materials that operate by electron trapping-detrapping mechanism via CB, for example, Eu^{2+} -activated PersL materials. This means the electron is the main charge carrier responsible for energy storage. However, some PersL materials can operate via a hole trapping-

detrapping mechanism (Figure 1.10), in which the hole is the main charge carrier. It is captured by traps close in energy to the VB instead of electron traps close to CB. Table 1.3 explains the processes involved in the hole trapping-detrapping model, labeled from 1 to 4 in the same way as for the electron trapping-detrapping model. It is worth noting that the excitation process 1 in Figure 1.10b might also be referred to a Ln^{3+} LMCT excitation ($e^-_{\text{VB}} \rightarrow \text{Ln}^{2+}$) due to the inner character of the Ln^{3+} 4f subshell.

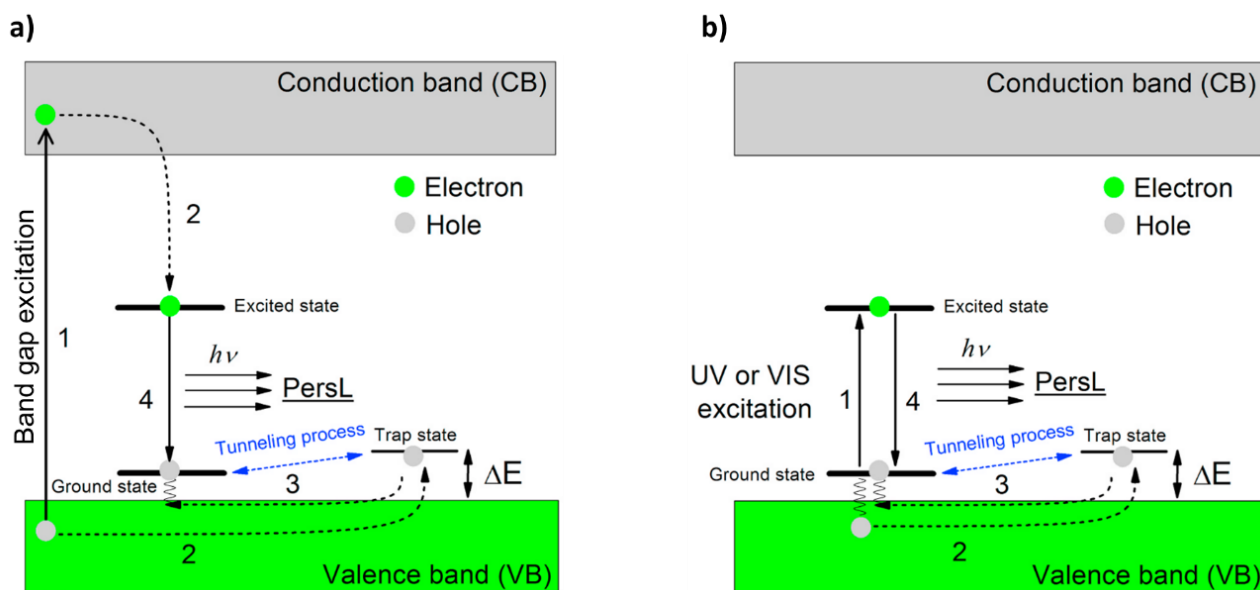


Figure 1.10 Persistent luminescence (PersL) mechanism: schematic illustrations of the *hole* trapping-detrapping model in the case of **a)** high energy band gap excitation, and **b)** low energy excitation at the activator ion or at the LMCT transition. Adapted from [62] with permission from Elsevier.

Table 1.3 Sequential processes involved in the *hole* trapping-detrapping model of PersL mechanism (e^- : electron, h^+ : hole, VB: valence band, CB: conduction band, GS: ground state, ES: excited state).

h^+ mechanism	Band gap excitation (Figure 1.10a)	Activator ion excitation (Figure 1.10b)
1. Excitation	Excitation of an e^- from VB to CB; Creation of free h^+ in VB and free e^- in CB	Excitation of an e^- from the activator ion GS to its ES (or LMCT excitation) h^+ can migrate to the VB
2. Trapping	h^+ in VB finds a trap (e.g., cation vacancy or interstitial anions); e^- in CB finds the ES of activator ion	h^+ in VB finds a trap (e.g., cation vacancy or interstitial anions)
3. Detrapping	h^+ is released from its trap to VB as a function of kT (k : Boltzmann constant)	Identical as 1.10a
4. Recombination	Radiative e^- - h^+ recombination at the activator ion yielding PersL	Identical as 1.10a

One could affirm that a hole is just the lack of an electron where it is supposed to be in a non-excited system; therefore, it does not make sense to attribute distinct mechanism models for the electron and the hole. While the first statement is correct, assuming the hole as an entity is quite common in electronics and can simplify the visualization of some processes in PersL mechanisms [72]. In addition, it is worth mentioning that tunneling mechanisms can also play an important role in PersL. It allows the charge carriers to move back and forth from activator ions to traps, without passing through the valence or conduction bands. Since tunneling has a strong distance dependence, investigation of tunneling effects can be conducted by modulating Ln dopant concentrations [73].

It is clear from Figures 1.9 and 1.10 that the HRBE/VRBE diagrams are powerful tools to modulate the properties of PersL, as well as design new materials [74,75]. This is especially important to design red/NIR PersL systems that evade Eu^{2+} as the activator ion [11]. The main examples are the $\text{Y}_2\text{O}_2\text{S}:\text{Eu}^{3+},\text{Ti}^{4+},\text{Mg}^{2+}$ oxysulfides (λ_{em} : 626 nm) [17,76], and the Cr^{3+} - and Yb^{3+} -doped gallate/germanates (λ_{em} : 716 and 980 nm) [77–80]. These materials are compelling candidates for *in vivo* optical imaging (Figure 1.11a), once they can be charged prior the injection in the biological system, reducing the autofluorescence of tissues to zero [81–83].

An extra possibility is to interplay with the trapping-detrapping processes between filled traps with different energies [84]. In this way, it is possible to refresh the PersL material already inside the biological media of study, *e.g.*, cell culture and mice (Figure 1.11b). For such purposes, the main challenge consists in obtaining efficient NIR PersL materials that maintain their long emission time at the colloidal nanocrystal form [85].

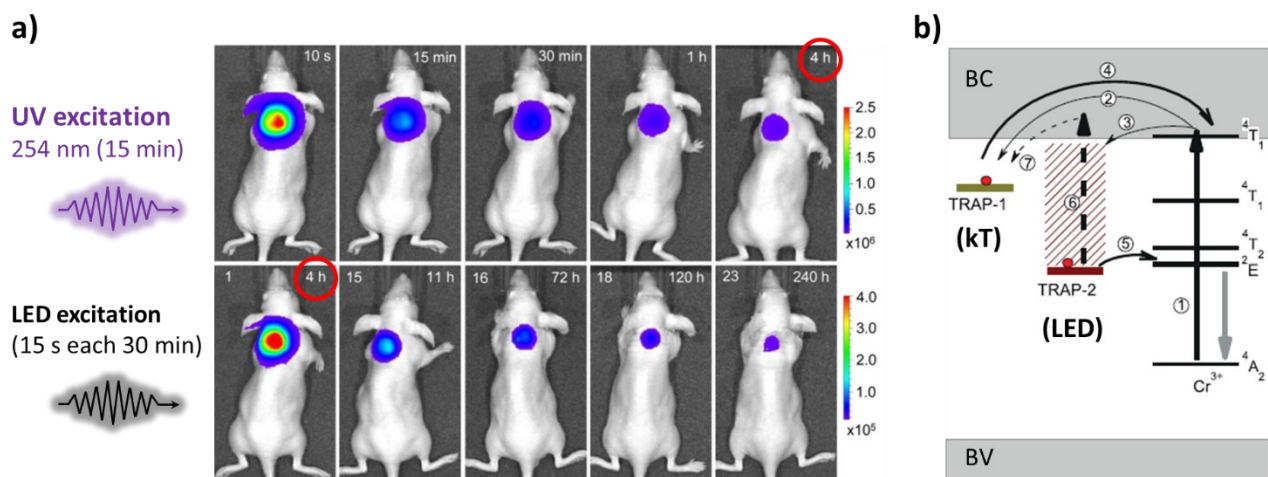


Figure 1.11 a) NIR PersL imaging (10 s – 4 h) from polyethyleneamine–LiGa₅O₈:Cr³⁺ nanoparticles-labeled 4T1 cells, excited with 254 nm by 15 min and then subcutaneously injected onto the back of a nude mouse. Later, the mouse was exposed every 30 min to a white LED flashlight (for 15 s) to refresh NIR PersL signal. **b)** The scheme represents the NIR PersL and LED-stimulated NIR PersL mechanisms, involving detrapping processes from shallow and deep traps, respectively, to the Cr³⁺ ion. Adapted from [79,84].

1.2 Luminescent materials based on rare earth oxysulfides

1.2.1 Structure and optical properties

An oxysulfide is a compound with the general formula $M_xO_yS_z$, where M can be alkaline earth metals, transition metals, lanthanoids, or actinoids. This work focusses on lanthanoid oxysulfides ($\text{Ln}_2\text{O}_2\text{S}$), and by extension, rare earth oxysulfides ($\text{RE}_2\text{O}_2\text{S}$). The discovery of the first $\text{Ln}_2\text{O}_2\text{S}$ materials dates back from the XIX century, for Ln^{3+} : Ce and Er [12]. Nevertheless, the first crystalline oxysulfide structures were elucidated by Pitha *et al.* in 1947 ($\text{La}_2\text{O}_2\text{S}$) [86] and Zachariassen in 1949 ($\text{La}_2\text{O}_2\text{S}$, $\text{Ce}_2\text{O}_2\text{S}$, and $\text{Pu}_2\text{O}_2\text{S}$) [87]. The samples were obtained either by reducing the corresponding sulfate $\text{Ln}_2(\text{SO}_4)_3$ using $\text{H}_2(\text{g})$ or by heating the sesquisulfide compounds (Ln_2S_3) in air atmosphere.

From the contributions of the two authors, it was verified that the $\text{Ln}_2\text{O}_2\text{S}$ crystallizes in the $P\bar{3}m1$ space group, in a structure that can be described as lamellar due to the alternating sheets of $[\text{Ln}_2\text{O}_2]^{2+}$ and S^{2-} (Figure 1.13a and 1.13b). In this crystal structure, the Ln ions are hepta-coordinated to four oxygen and three sulfur atoms in a C_{3v} symmetry site [88]. All three Ln–S bonds are symmetrical, while one of the Ln–O bonds is on the z -axis, having a slightly longer bond length compared to the other three symmetrical Ln–O bonds. (Figure 1.12c).

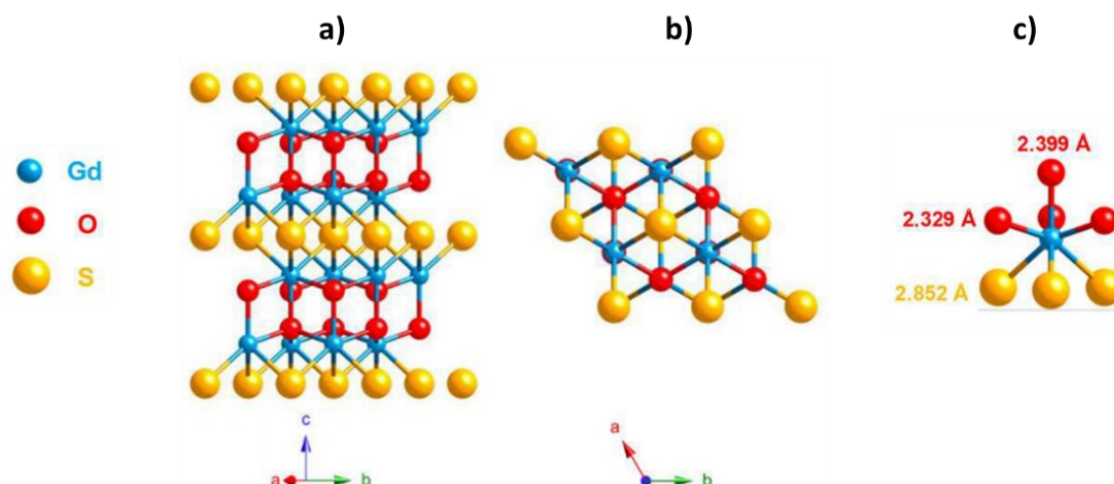


Figure 1.12 $\text{Ln}_2\text{O}_2\text{S}$ (Ln^{3+} : Gd) crystal structure: **a)** lateral and **b)** c -axis view; **c)** Ln^{3+} C_{3v} hepta-coordinated site, showing the bond lengths of Ln–S and the two different Ln–O. Adapted from [12].

Rare earth oxysulfides ($\text{RE}_2\text{O}_2\text{S}$, where RE^{3+} : La, Gd, Y, and Lu) are suitable host lattices for luminescent materials due to their high thermal and chemical stability, low toxicity, and good sensitization of trivalent lanthanoid ions. Thus, such hosts can accommodate different Ln dopants even at high concentrations, since the crystal structure is the same for all $\text{Ln}_2\text{O}_2\text{S}$ [14,89]. Combining these features with the host electronic structure, it is possible to produce Ln-doped $\text{RE}_2\text{O}_2\text{S}$ materials displaying a diversity of photonic phenomena: conventional luminescence, cathodoluminescence, upconversion, downconversion, scintillation, and persistent luminescence.

For example, $\text{Y}_2\text{O}_2\text{S}:\text{Eu}^{3+}$ materials were primary employed as red pixels in cathode ray tubes (CRTs) of television screens in in the 1960s [12]. The $\text{Y}_2\text{O}_2\text{S}:\text{Eu}^{3+}$ is also one of the materials used as red pixels in current computer monitors. The amount of $\text{Y}_2\text{O}_2\text{S}:\text{Eu}^{3+}$ employed (Eu = 0.73%, Y = 13.4% w/w) has become large enough to develop and implement rare-earth recovery technologies [90]. Moreover, down- and upconversion (UC) oxysulfides, *e.g.*, $\text{Gd}_2\text{O}_2\text{S}:\text{Tm}^{3+}$ [91] and $\text{Gd}_2\text{O}_2\text{S}:\text{Er}^{3+},(\text{Yb}^{3+})$ [15,92] have been reported as potential non-linear optical materials to enhance the efficiency of solar cells. Concerning the UC phenomenon, the low phonon energies of Gd- and $\text{Y}_2\text{O}_2\text{S}$ hosts ($\sim 460\text{ cm}^{-1}$) contribute to the generation of UC efficiencies in bulk form that are comparable to the most studied UC system, $\text{Na}(\text{Gd},\text{Y})\text{F}_4$ [55,93,94].

Scintillator materials such as $\text{Gd}_2\text{O}_2\text{S}:\text{Tb}^{3+}$ and $\text{Gd}_2\text{O}_2\text{S}:\text{Pr}^{3+}$ have been deeply investigated since they exhibit the main features necessary to enable good absorption of X-rays beams, such as the presence of heavy atoms (Ln as host and dopants), high material density, and high stability against ionizing radiations. Nowadays, these materials are used as scintillators in X-ray Computed Tomography (CT), Single-Photon Emission Computed Tomography (SPECT), and Positron Emitting Tomography (PET) [12,43,46].

Finally, persistent luminescence for this class of materials was discovered simultaneously and independently in 2003 by Kang *et al.* [13] and Wang *et al.* [95]. Kang reported the PersL for the $\text{Y}_2\text{O}_2\text{S}:\text{Ti}^{4+},\text{Mg}^{2+}$ material, which exhibited a broad emission band centered at 594 nm attributed to

the charge-transfer emission of Ti^{4+} . On the other hand, Wang showed that the PersL emission of $\text{Y}_2\text{O}_2\text{S}:\text{Eu}^{3+},\text{Ti}^{4+},\text{Mg}^{2+}$ material arises from the Eu^{3+} 4f–4f transitions, and that $\text{Y}_2\text{O}_2\text{S}:\text{Eu}^{3+},\text{Ti}^{4+}$ and $\text{Y}_2\text{O}_2\text{S}:\text{Eu}^{3+},\text{Mg}^{2+}$ materials exhibited very short PersL compared to $\text{Y}_2\text{O}_2\text{S}:\text{Ti}^{4+},\text{Mg}^{2+}$ and $\text{Y}_2\text{O}_2\text{S}:\text{Eu}^{3+},\text{Ti}^{4+},\text{Mg}^{2+}$. Various works reported the effects of synthesis methodology [21,96,97], dopant concentration [76,98,99] and alkaline-earth co-dopant [100–102] in the persistent luminescence outcome of $\text{Y}_2\text{O}_2\text{S}:\text{Eu},\text{Ti},\text{Mg}$ material.

Recently, Luo *et al.* [19] reported that both Ti^{4+} and Eu^{3+} act as electron trapping centers while host intrinsic defects act as hole traps. These results imply that the PersL mechanism operating in $\text{Y}_2\text{O}_2\text{S}:\text{Eu},\text{Ti}$ materials is the hole trapping-detrapping (Figure 1.10) instead of more common electron trapping-detrapping (Figure 1.10). On the other hand, Qu *et al.* [103] investigated the PersL mechanism of $\text{Y}_2\text{O}_2\text{S}:\text{Eu},\text{Ti},\text{Mg}$ by first-principles calculations and concluded that electrons are the charge carriers responsible for the Ti^{4+} persistent emission. In addition, the presence of Eu^{3+} 4f–4f transitions in the PersL emission spectra is caused by a $\text{Ti}\rightarrow\text{Eu}$ energy transfer. In this context, research should be conducted on investigating the complex nature of the charge carriers trap/release processes that hinders the actual PersL mechanisms that operate $\text{Y}_2\text{O}_2\text{S}$ -based materials.

1.2.2 Challenging preparation and the microwave-assisted solid-state (MASS) synthesis

Oxysulfides are scarce as natural minerals and are the most often synthetic. One reason for this is the competitive formation of oxides or sulfates, which have higher stability towards oxidation and thus are found in numerous minerals [12]. This oxide/sulfide/sulfate phase competition is also an issue when designing a synthetic route. Within this framework, most scientific publications have reported the preparation of $\text{RE}_2\text{O}_2\text{S}$ materials by the conventional solid-state method [17,19,104,105]. Although it is a well-known synthesis methodology, the employment of high temperatures (~ 1100 °C) during long periods (from 4 to 24 h), occasionally using reducing atmospheres (H_2/N_2 or

CO) makes it quite dispendious. Usually, regrind-reheat steps are also needed to increase the homogeneity of the products, however, it is not unusual to obtain materials without a pure oxysulfide phase [15,106]. The search for environmentally friendly and cost-effective preparation methods for RE₂O₂S materials is then required.

A possible alternative is to use the rapid microwave-assisted solid-state (MASS) synthesis. Although microwave methods are quite common for organic synthesis in solution, it lacks investigation applied to solid-state materials. The advantages of the MASS method include short processing times, low energy consumption, and the use of inexpensive equipment (*e.g.*, domestic microwave ovens). Thus, it is often referred as an environment-friendly synthesis method [107–110]. In the MASS method, likewise conventional solid-state synthesis, the chemicals are ground and homogenized in powder form using a mortar or a ball mill, and then submitted to thermal treatment. The particularity of MASS method is the nature of heating: while conventional ovens heat the sample via resistive heating, microwave ovens induce a punctual dielectric heating on the sample.

Before explaining the microwave heating mechanisms for solid-state materials, a brief description of how microwave ovens operate is necessary. The main component of such ovens is the microwave generator, called magnetron (Figure 1.13a). A high potential difference (2–20 kV) is generated between its cathode and anode, producing a strong electromagnetic field [111]. The heated cylindrical cathode releases electrons radially accelerated towards the anode due to the electric field. The magnets at the top and bottom create a perpendicular magnetic field to the electrode electric field, causing electrons to move in a circular spiral path instead of going straightly to the anode. In this way, when electrons pass through the resonant cavities of the anode, their frequency of oscillation increase proportionally to the size of the cavities, generating microwave radiation. Domestic microwave ovens are designed to generate a microwave output of 2.45 GHz, with operating powers ranging from 750 to 1300 W.

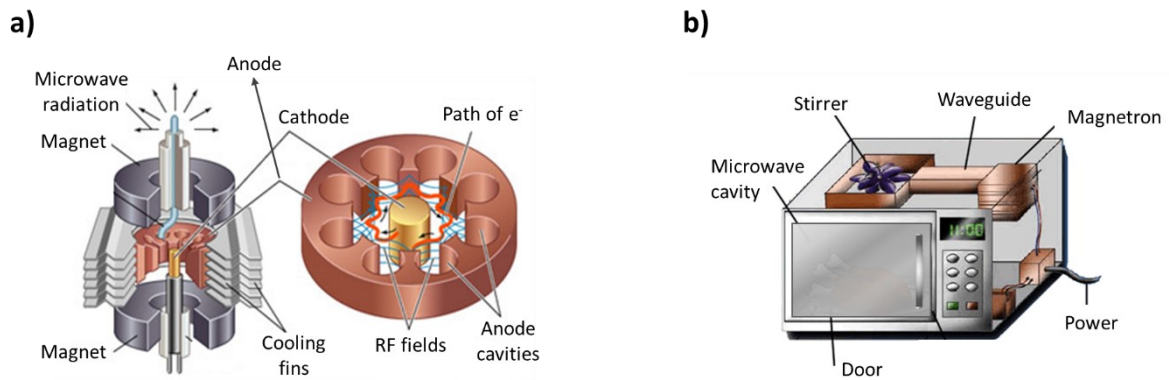


Figure 1.13 a) Structure of a magnetron; b) internal components of a microwave oven. Adapted from [112].

After, the microwaves are directed to the microwave cavity through a waveguide (Figure 1.13b). In most domestic microwave ovens, the magnetron will always operate at full power. That means the output power control is done by the magnetron's operating time. For example, if the microwave oven has a maximum power of 1000 W and the output programmed power was 800 W, then the magnetron will stay on at 80% and off at 20% of the preset time. This feature is done in an alternately way to guarantee a homogeneous heating over time.

When the electromagnetic field of microwave radiation interacts with liquid water, for example, it forces water molecules to align to the applied field. The high frequency of the microwave field (2.45 GHz) induces an extremely fast molecule motion that increases the overall kinetic energy, resulting in a rapid increase in temperature. However, there are no motion-free molecules in the solid-state. The basis of microwave heating in solid state lies in the extent to which a material responds to the microwave alternating electric (also the magnetic field for a magnetic material) [108,109].

According to electromagnetic theory, the two fundamental properties that measure the response of a material to an electric field are the dielectric constant (ϵ') and the dielectric loss (ϵ''). The dielectric constant ϵ' determines the ability of a material to store electric energy, while dielectric loss ϵ'' determines the ability of the material to convert the electric energy to heat [109]. These two components are often expressed in terms of the complex dielectric permittivity ϵ^* (Equation 1.1):

$$\varepsilon^* = \varepsilon' - i\varepsilon'' \quad (1.1)$$

The storage of the electric energy occurs via polarization of the bound charges, while the conversion of the electric energy into heat occurs through the relaxation of the polarized bonds (polarization loss) as well as the conduction of the free electrons (conduction loss). It is worth noting that the polarization response to an external field is not instantaneous. The greater the imaginary fraction of the dielectric permittivity (Equation 1.1), the longer is the response delay, and thus the more efficiently the material will generate heat.

From ε' and ε'' , it is possible to derive the main parameter governing how materials respond to a microwave field, the penetration depth (D_p), which determines the distance at which the intensity of the electromagnetic field decays to $1/e$ of its initial amplitude. Applying some mathematical procedures and approximations which are beyond the scope of this work [109], the penetration depth can be expressed as follows (Equation 1.2):

$$D_p = \frac{v\sqrt{\varepsilon'}}{2\pi\varepsilon''} \quad (1.2)$$

where v is the wavelength of the microwave radiation. By the magnitude of the penetration depth, solid materials can be classified accordingly to Figure 1.14:

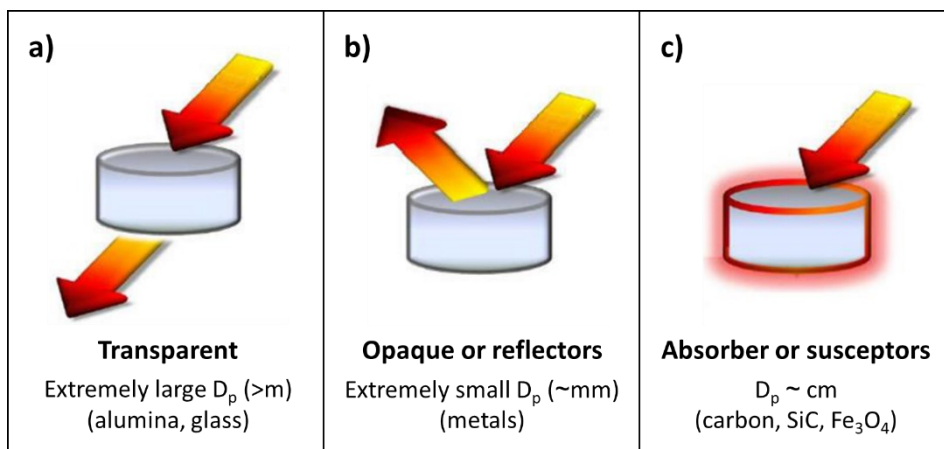


Figure 1.14 Solid-state materials according to their different response to an incident microwave radiation: **a)** transparent, **b)** opaque or reflectors, and **c)** absorber or susceptors.

Susceptor materials (Figure 1.14c) are extremely important for the microwave-assisted solid-state (MASS) method, since these materials can readily absorb microwaves at room temperature and convert the energy into heat (this method is often called susceptor-assisted microwave synthesis) [108,109]. For example, RE oxides and nitrates are often used as precursors in solid-state synthesis, however, they are transparent to microwaves, which in principle makes their transformation using microwaves impossible. Nonetheless, placing a susceptor in close contact with these precursors aids the initial heating of the synthesis. As the dielectric loss ϵ'' is a temperature dependent property, at some high temperature value the RE precursors will also couple with the microwave radiation and heat punctually, increasing the temperature of the reaction medium even faster [107,108].

Recent works employed the MASS method in the preparation of diverse Ln-doped luminescent materials [113,114]. Typical synthesis procedures take less than 30 minutes and yield materials with high crystallinity and phase purity. In this context, it is also worth mentioning is that the MASS method is adequate to obtain kinetically driven products over thermodynamically preferred ones due to the rapid synthesis time. Therefore, the preparation of RE₂O₂S materials can be considered a model of study using this synthesis methodology, since the aim is to achieve the oxysulfide phase instead of the oxide one. Besides, fitting microwave synthesis parameters to obtain RE₂O₂S materials with diverse optical phenomena (scintillation, upconversion, and persistent luminescence) characterizes as an additional challenge of this work.

1.2.3 Going from bulk to nanoscale

The microwave-assisted solid-state (MASS) method presents great synthetic advantages over conventional solid-state synthesis, *e.g.*, short processing time, low energy consumption, and the possibility of obtaining kinetical products over thermodynamical ones. However, it is still essentially a solid-state synthesis, therefore, it suffers from the drawback of inadequate particle size and

morphology control, always leading to the fabrication of bulk ($\geq 1 \mu\text{m}$) materials. In the recent 20 years, diverse synthetic approaches were investigated to prepare Ln-doped luminescent nanocrystals, confining their size to the $< 100 \text{ nm}$ dimension and attempting to preserve their luminescence efficiency. $\text{RE}_2\text{O}_2\text{S}$ nanomaterials were also explored, following the trend of nanomaterials science. For instance, if the main properties of bulk $\text{RE}_2\text{O}_2\text{S}$ (*e.g.*, high thermal and chemical stability, low toxicity, and high versatility for optical phenomena) could be reproduced in the nanoscale, the $\text{RE}_2\text{O}_2\text{S}$ nanomaterials would present many advantages for applications such as optical bioimaging, phototherapy, and theranostics [12,115]. The development of appropriate synthesis methods for nano- $\text{RE}_2\text{O}_2\text{S}$, capable of designing the size and morphology of the crystals, is then of great interest in the fields of luminescence, materials science, biology, and medicine.

The synthesis of $\text{RE}_2\text{O}_2\text{S}$ nanomaterials was first reported by Li *et al.* in 2000 [116], describing a straightforward $\text{RE}_2\text{O}_3 \rightarrow \text{RE}_2\text{O}_2\text{S}$ conversion in organic medium using an autoclave. Using elemental sulfur and ethylenediamine as precursors, the authors obtained pure rare earth oxysulfide phase for RE^{3+} : Pr, Eu, and Gd, mixed oxide/oxysulfide products for La, Nd, Sm, Ho, and Er, and pure oxide phase for Yb, Lu, Y, and Sc. These results corroborate to the Pearson's theory on hard and soft acids and bases [16]. Another benchmark occurred in 2006, when Zhao *et al.* [117] synthesized monodisperse $\text{Eu}_2\text{O}_2\text{S}$ nanoplates through the decomposition of a single-source precursor, the $[\text{Eu}(\text{phen})(\text{ddtc})_3]$ complex (phen: 1,10-phenanthroline, ddtc: diethyldithiocarbamate) in a mixture of oleylamine/oleic acid/octadecene (OM/OA/ODE) under air atmosphere. After these works, several publications described the preparation of $\text{RE}_2\text{O}_2\text{S}$ nanocrystals by diverse methodologies: sol-gel [118], combustion synthesis [119], templated precipitation followed by annealing [96], hydrothermal followed by annealing [21,22,115], electrospinning combined with sulfurization [120], *etc.*

Among all synthetic approaches, colloidal synthesis using the mixture of solvents oleylamine/oleic acid/octadecene (OM/OA/ODE) offers better control of both size and shape of nanocrystals [121–127]. It avoids the hard-to-prepare single-source precursors, and by simply

adjusting the relative concentrations of the solvents, it is possible to tune crystal size from 10 to 50 nm and to adjust their shape into spheres, plates, rods, or flower-like structures. In addition, this method enables the use of elemental sulfur, which is easy to manipulate and less toxic. Recently, Larquet *et al.* developed a series of works [124–127] regarding the preparation and stability of nano-Ln₂O₂S via colloidal synthesis. The very recent work published in 2020 combined the small-angle and wide-angle X-ray scattering techniques (SAXS–WAXS) to investigate the mechanism of RE₂O₂S nanocrystal formation, the role of sodium, and alkali ions in the synthesis [127]. It was concluded that alkali ions form a stabilized oleate mesophase, which acts as a template to nanoparticle growth (Figure 1.15). More importantly, the alkali ions are not incorporated into the RE₂O₂S crystal structure and can therefore be eliminated by washing at the end of the synthesis.

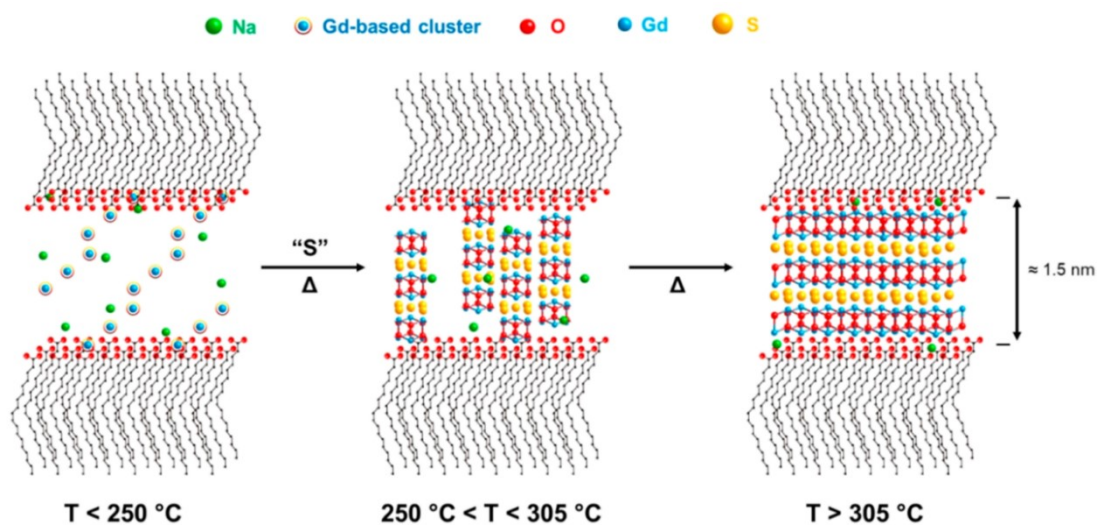


Figure 1.15 Proposed mechanism of Gd₂O₂S nanoparticle formation starting from organized clusters. Reproduced from [127] with permission from the American Chemical Society.

In this work, the synthesis methodology developed by Larquet, *i.e.*, the colloidal synthesis in OM/OA/ODE organic medium, without further annealing processes, was investigated as an alternative to the MASS method, aiming luminescent Ln-doped RE₂O₂S nanocrystals that are promising for biological and medicinal applications.

1.3 Objectives

The main objective of this work was to synthesize rare earth oxysulfide photonic materials at the micro- and nanoscales using the microwave-assisted solid-state (MASS) synthesis and the colloidal synthesis in organic solvents, respectively, aiming at stable and highly luminescent materials exhibiting versatile photonic phenomena.

The specific objectives were:

- Investigate the microwave-assisted solid-state (MASS) synthesis in the preparation of bulk ($\sim 1 \mu\text{m}$) $\text{RE}_2\text{O}_2\text{S}$ materials (RE^{3+} : La, Gd, and Y).
- Optimize MASS synthesis parameters aiming at doped $\text{RE}_2\text{O}_2\text{S}$ materials exhibit different photonic phenomena: *scintillation* – $\text{Gd}_2\text{O}_2\text{S}:\text{Tb}^{3+}$, *upconversion* – $\text{Gd}_2\text{O}_2\text{S}:\text{Er}^{3+}(\text{Yb}^{3+})$, and *persistent luminescence* – $\text{RE}_2\text{O}_2\text{S}:\text{Eu}^{3+},\text{Ti}^{4+},\text{Mg}^{2+}$ and $\text{RE}_2\text{O}_2\text{S}:\text{Yb}^{3+},\text{Ti}^{4+},\text{Mg}^{2+}$.
- Characterize the $\text{RE}_2\text{O}_2\text{S}$ bulk materials using the following techniques: X-ray diffraction (XRD), scanning electron microscopy (SEM), Fourier-transform infrared spectroscopy (FTIR), and X-ray absorption near edge structure (XANES).
- Study the photoluminescent properties of the scintillator, upconversion (UC) and persistent luminescence (PersL) materials using the following optical techniques: photoluminescence excitation and emission spectroscopy, X-ray excited optical luminescence (XEOL for scintillators), laser-excited upconversion emission (for UC materials), and persistent luminescence decay time, persistent luminescence emission spectra and thermoluminescence (TL) for PersL materials.
- Explore the colloidal synthesis in organic solvent in the preparation of nano ($< 50 \text{ nm}$) Ln-doped $\text{RE}_2\text{O}_2\text{S}$ materials (RE^{3+} : La, Gd, and Y).
- Characterize the Ln-doped $\text{RE}_2\text{O}_2\text{S}$ nanocrystal formation using transmission electron microscopy (TEM) and investigate their photoluminescent properties via photoluminescence excitation and emission spectroscopy.

Chapter 2

Experimental part

- 2.1 Preparation of RE₂O₂S-based luminescent materials by the microwave-assisted solid-state (MASS) synthesis
- 2.2 Preparation of RE₂O₂S-based luminescent nanoparticles via colloidal synthesis in organic medium
- 2.3 Structural and morphological characterization techniques
- 2.4 Study of luminescence properties

2. EXPERIMENTAL PART

Firstly, luminescent materials based on rare earth oxysulfides $\text{RE}_2\text{O}_2\text{S}$ (RE^{3+} : La, Gd, and Y) were prepared by the microwave-assisted solid-state (MASS) method (section 2.1). The $\text{RE}_2\text{O}_2\text{S}$ crystalline phase formation over synthesis time was investigated through crystallographic and spectroscopic techniques. Then, $\text{RE}_2\text{O}_2\text{S}$ matrices were doped with distinct ions to obtain materials which exhibit the following luminescent phenomena: scintillation – $\text{Gd}_2\text{O}_2\text{S}:\text{Tb}^{3+}$, upconversion (UC) – $\text{Gd}_2\text{O}_2\text{S}:\text{Er}^{3+}(\text{Yb}^{3+})$, and persistent luminescence (PersL) – $\text{RE}_2\text{O}_2\text{S}:\text{Eu}^{3+}(\text{Yb}^{3+}),\text{Ti}^{4+},\text{Mg}^{2+}$.

Section 2.2 addresses the preparation of $\text{RE}_2\text{O}_2\text{S}$ (RE^{3+} : Gd and Y) luminescent nanocrystals (NCs) by the colloidal synthesis in an organic medium. All synthesis steps, as well as the NCs washing procedures, were explained in detail. In a similar fashion as that used for MASS bulk materials, dopants and their concentrations were varied to achieve diverse optical phenomena – conventional luminescence, UC, and PersL. Furthermore, the influence of the oleic acid addition in the NC formation was also explored.

Finally, the structural and morphological characterization techniques applied to the obtained $\text{RE}_2\text{O}_2\text{S}$ -based bulk and nanomaterials, as well as the optical techniques to investigate the materials' luminescent properties, were covered in sections 2.3 and 2.4, respectively. A description on the technical particularities and measurement parameters were provided for each technique.

2.1 Preparation of $\text{RE}_2\text{O}_2\text{S}$ -based luminescent materials by the microwave-assisted solid-state (MASS) synthesis

2.1.1 Optimization of the MASS method: $\text{RE}_2\text{O}_2\text{S}$ formation *versus* synthesis time

The microwave-assisted solid-state (MASS) synthesis is already being used to synthesize of diverse inorganic materials [107,108]. Nevertheless, the control of synthesis parameters is limited in a domestic microwave oven, since one can only preset the output power and the synthesis duration

time. Therefore, the preparation of undoped Gd₂O₂S and Y₂O₂S matrices were conducted using the MASS method, and the formation of the respective oxysulfide crystal structures was monitored over the synthesis time. Chemicals and instruments used for this task were described in [Table 2.1](#).

Table 2.1 Data on chemicals, company, purity, and microwave oven used in the synthesis of undoped RE₂O₂S (RE³⁺: Gd and Y) on the MASS method optimization.

Chemicals	Company / Purity
Rare earth oxides, RE ₂ O ₃ (RE ³⁺ : Gd and Y)	CSTARM / 99.99%
Elemental sulfur, S	Synth Brazil / 99.5%
Sodium carbonate, Na ₂ CO ₃	Vetec / 99.5%
Activated carbon (1~2 mesh)	Synth Brazil / Analytical Grade
Acetone	Synth Brazil / Analytical Grade
Microwave oven	Max Power / Cavity volume
Electrolux MEF41 (Institute of Chemistry – University of São Paulo)	1000 W / 31 L

The preparation of precursors for the MASS synthesis proceeded as follows: RE₂O₃ (RE³⁺: Gd or Y), S and Na₂CO₃ were ground in an agate mortar with acetone added to aid the homogenization. It is worth noting that, after grinding, the precursor mixture was left to dry under air to evaporate all acetone. For the Gd host, the molar ratio employed between the chemicals was 1 Gd₂O₃ : 1.075 S : 0.25 Na₂CO₃. In other words, the stoichiometry of the RE₂O₃ + S reaction is 1:1, with 7.5 mol-% excess of S added to facilitate the formation of the Gd₂O₂S phase. Differently, for the case of the Y host, the molar ratio was 1 Y₂O₃ : 3 S : 0.25 Na₂CO₃.

The distinct RE₂O₃:S molar ratios for the two different rare earth oxides is justified by the Pearson's theory of hard and soft acids and bases [16]. S²⁻ ions have a significantly larger ionic radius, *i.e.*, 1.84 Å for coordination number (CN) 6 compared to the RE³⁺ ions – Gd³⁺ (1.00 Å for CN 7) and Y³⁺ (0.96 Å for CN 7) [128]. Therefore, the formation of RE³⁺-S²⁻ bonds is not thermodynamically favored due to the poor superposition of valence orbitals. Additionally, this behavior is not homogeneous through the lanthanide series once the ionic radii of Ln³⁺ decrease almost 20% from La

to Lu, and Y^{3+} has radius similar to Er^{3+} [34]. Hence, it can be stated that Y^{3+} ions have a significantly harder acidic character compared to Gd^{3+} . A higher amount of sulfur is therefore necessary to induce the formation of the Y_2O_2S phase.

To the MASS synthesis procedure, 0.5 g of a prepared precursor was added to a 5 cm³ alumina crucible, which was previously surrounded by 11 g of activated carbon (microwave susceptor) placed inside a 50 cm³ alumina crucible (Figure 2.1a). Crucibles were partially covered by an alumina lid and then placed inside aluminosilicate thermal insulating bricks (Figure 2.1b). Finally, the bricks containing the crucibles were introduced in the cavity of a domestic microwave oven to start the syntheses processes (Figure 2.1c). A ceramic wool was placed underneath the bricks for extra thermal protection to the microwave rotating glass plate.



Figure 2.1 a) Arrangement of the crucibles for MASS syntheses, holding the precursor (internal) and the microwave susceptor (external); b) Arrangement of crucibles and the aluminosilicate thermal insulator bricks; c) Accommodation of the system in a domestic microwave oven (Electrolux MEF41).

The standard program for the microwave oven output power (P) and time was set up as follows: P = 90% at 10 minutes + P = 80% at 15 minutes, thus one complete MASS treatment was 25 minutes long. In order to investigate the formation of the RE_2O_2S crystalline phase as a function of synthesis time, several syntheses were performed in a 2 min-step manner, *i.e.*, RE_2O_2S materials (RE^{3+} : Gd or Y) were obtained by the MASS method with synthesis times of 2, 4, 6, ... 20, 22, and

25 minutes. At the end of each 2 min-step, the inner crucible temperature was measured with a laser pyrometer (Homis 467A).

For the case of Y_2O_2S materials, studying the oxysulfide phase formation over time was carried one step further, *i.e.*, a second microwave treatment was employed. Therefore, after a complete 25 min MASS synthesis, the obtained products were ground again with sulfur (40% in mass) and submitted to a second microwave treatment with synthesis times of 2, 4, 6, ... 25 minutes. The scheme in Figure 2.2 simplifies the whole process of MASS synthesis of RE_2O_2S matrices (RE^{3+} : Gd or Y) to investigate the influence of synthesis time in the RE_2O_2S crystalline phase formation.

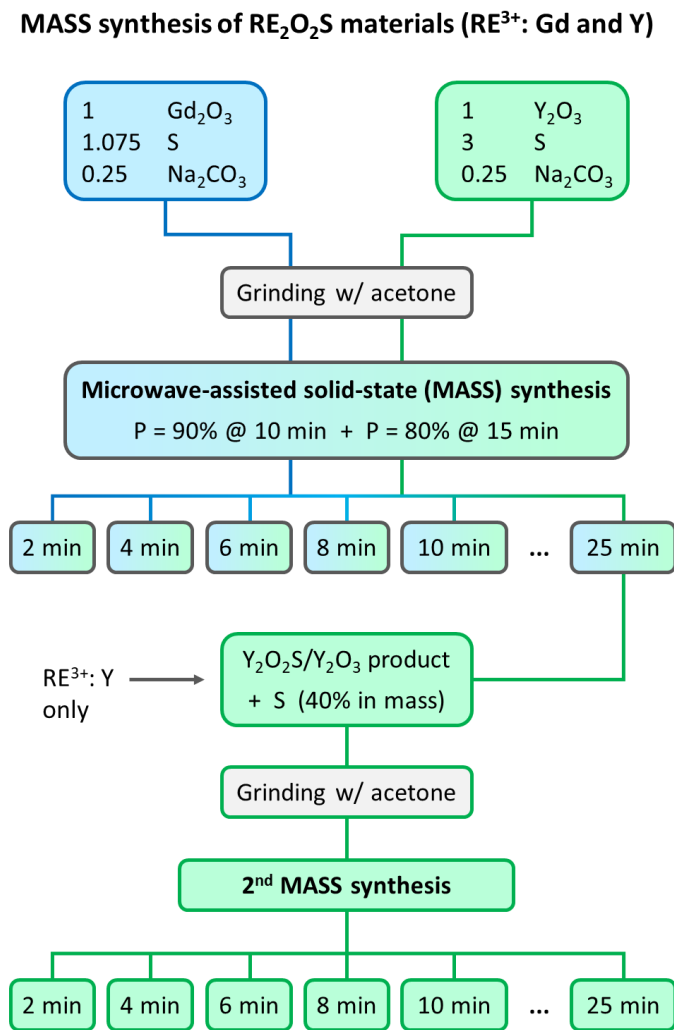


Figure 2.2 Scheme for the microwave-assisted solid-state (MASS) synthesis of undoped RE_2O_2S matrices (RE^{3+} : Gd and Y): investigation of the RE_2O_2S crystal phase formation as a function of synthesis time.

To evaluate the oxysulfide formation over synthesis time, the obtained undoped RE₂O₂S materials (RE³⁺: Gd or Y) were characterized by X-ray powder diffraction (XRD), infrared spectroscopy (FTIR) and soft X-ray absorption spectroscopy (XANES) near the absorption edge of sulfur (~2470 eV), using synchrotron radiation (section 2.3).

2.1.2 Synthesis of Gd₂O₂S:Tb scintillators

After understanding the RE₂O₂S formation as a function of MASS synthesis time, diverse doped oxysulfide materials were also prepared to achieve different photonic phenomena: scintillation – Gd₂O₂S:Tb, upconversion (UC) – Gd₂O₂S:Er(Yb), and persistent luminescence (PersL) – RE₂O₂S:Eu(Yb),Ti,Mg. Firstly, Gd₂O₂S:Tb³⁺ scintillator materials were synthesized in a similar fashion described in section 2.1.1 (chemicals and microwave oven listed in Table 2.2). In summary, the precursors were weighted employing the 0.96 Gd₂O₃ : 0.04 Tb₄O₇ : 1.075 S : 0.25 Na₂CO₃ stoichiometry, then homogenized in an agate mortar with aid of acetone. Therefore, the prepared Gd₂O₂S:Tb³⁺ precursor yielded scintillator materials with Tb³⁺ dopant concentration of 2%.

Table 2.2 Chemicals and microwave oven used in the synthesis of Gd₂O₂S:Tb³⁺ 2% scintillator materials.

Chemicals	Company / Purity
Rare earth oxides, Gd ₂ O ₃ and Tb ₄ O ₇	CSTARM / 99.99%
Elemental sulfur, S	Synth Brazil / 99.5%
Sodium carbonate, Na ₂ CO ₃	Vetec / 99.5%
Activated carbon (1~2 mesh)	Synth Brazil / Analytical Grade
Acetone	Synth Brazil / Analytical Grade
Microwave oven	Max Power / Cavity volume
Electrolux MEF41 (Institute of Chemistry – University of São Paulo)	1000 W / 31 L

To the MASS synthesis, 0.5 g of the precursor was added to the 5 cm³ alumina crucible, which was surrounded by activated carbon, thermally insulated by the aluminosilicate bricks, and introduced

in the cavity of the microwave oven, exactly how it was displayed in [Figure 2.1](#). Two $\text{Gd}_2\text{O}_2\text{S:Tb}^{3+}$ materials were prepared by the MASS method. The first, labeled as “ $\text{Gd}_2\text{O}_2\text{S:Tb}^{3+}$ - 10 min”, was obtained by a single microwave heat treatment of 10 minutes (with microwave power output $P = 90\%$). The second material, labeled “ $\text{Gd}_2\text{O}_2\text{S:Tb}^{3+}$ - 50 min”, was obtained by two MASS treatments of 25 minutes each ($P = 90\%$ at 10 minutes + $P = 80\%$ at 15 minutes), involving a regrind step between the heat treatments ([Figure 2.3](#)). In this regrind step, sulfur (7.5% in mass of the product) was added to aid the formation of the $\text{Gd}_2\text{O}_2\text{S}$ phase during the second MASS treatment.

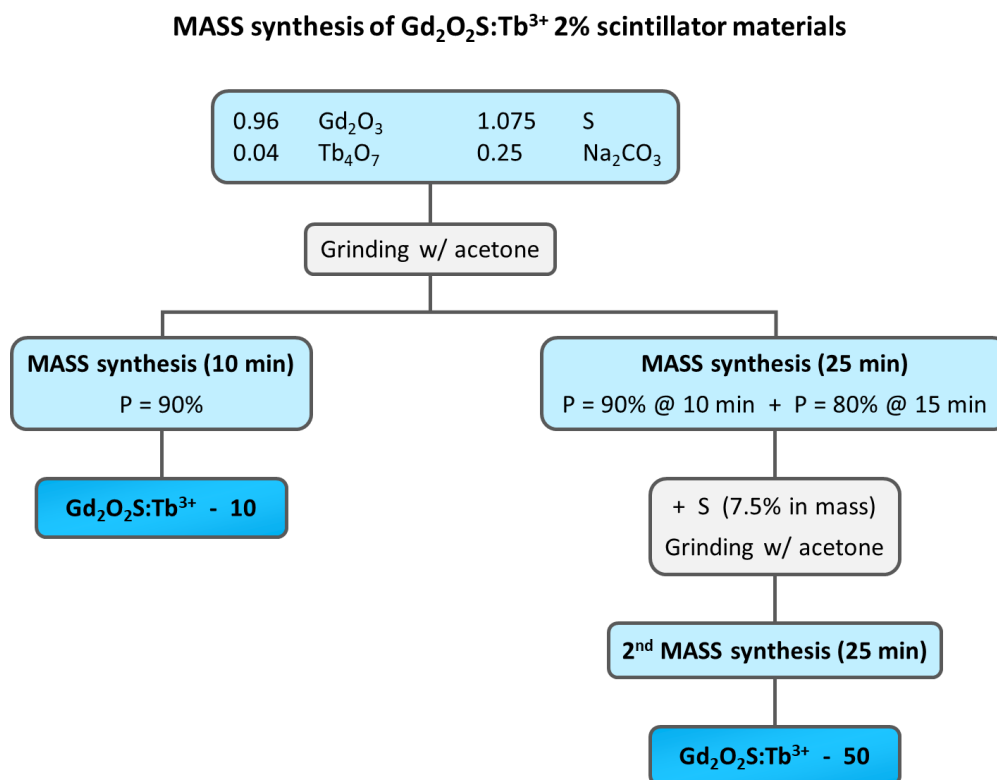


Figure 2.3 Scheme for microwave-assisted solid-state (MASS) synthesis of $\text{Gd}_2\text{O}_2\text{S:Tb}^{3+}$ 2% scintillators.

2.1.3 Synthesis of $\text{Gd}_2\text{O}_2\text{S:Er,Yb}$ upconversion materials

The preparation of $\text{Gd}_2\text{O}_2\text{S:Er}^{3+}$ and $\text{Gd}_2\text{O}_2\text{S:Er}^{3+},\text{Yb}^{3+}$ upconversion (UC) materials was conducted at the Debye Institute for Nanomaterials Science – Utrecht University (The Netherlands). Chemicals and microwave oven utilized were listed in [Table 2.3](#).

Table 2.3 Chemicals and microwave oven used in the synthesis of $\text{Gd}_2\text{O}_2\text{S}:\text{Er}^{3+}$ and $\text{Gd}_2\text{O}_2\text{S}:\text{Er}^{3+},\text{Yb}^{3+}$ upconversion (UC) materials.

Chemicals	Company / Purity
Lanthanide oxides, Ln_2O_3 (Ln^{3+} : Gd, Er, and Yb)	Smart Elements / 99.99%
Nitric acid, HNO_3	Merck / $\geq 65\%$
Urea, $(\text{NH}_2)_2\text{CO}$	Merck / Analytical Grade
Elemental sulfur, S	Alfa Aesar / 99.5%
Sodium carbonate anhydrous, Na_2CO_3	Baker Analyzed / $\geq 99.5\%$
Activated carbon (<2 mm)	Alfa Aesar / Analytical Grade
Acetone	Merck / Analytical Grade
Microwave oven	Max Power / Cavity volume
Daewoo KORIN4A (Debye Institute for Nanomaterials Science – Utrecht University)	1000 W / 31 L

The precursor mixture preparation was slightly different for the case of $\text{Gd}_2\text{O}_2\text{S}$ UC materials. First, the Gd : S molar ratio employed was 1 : 1.1 instead of 1 : 1.075 for the $\text{Gd}_2\text{O}_2\text{S}:\text{Tb}$ scintillators (Figure 2.3), *i.e.*, the molar sulfur excess is now 10% instead of previous 7,5%. In addition, two different lanthanide sources were used to prepare the UC materials: the oxides, Ln_2O_3 , and the hydroxycarbonates, $\text{Ln}(\text{OH})\text{CO}_3$, where Ln^{3+} : Gd, Er, and Yb. These two changes were adopted to improve Er^{3+} and Yb^{3+} insertion in the $\text{Gd}_2\text{O}_2\text{S}$ lattice, since the dopant concentration in UC materials can be relatively high ($\geq 10\%$) and these dopant ions are harder acids compared to Gd^{3+} [16].

Lanthanide hydroxycarbonates are not commercially available, and thus had to be synthesized following a literature procedure [129,130], which was identical for the different Ln^{3+} (Gd, Er, and Yb). Approximately 10 g of Ln_2O_3 was dissolved into 8–10 mL of boiling concentrated HNO_3 . After 30 minutes of stirring, the pH was registered to be 6–7, as a very small amount of suspend powder could be observed. This suspension was filtered, and the resultant $\text{Ln}(\text{NO}_3)_3$ solution was then transferred to a 250 mL round flask, containing ~35 g of urea previously dissolved in 100 mL of deionized water. A condenser was attached to the round flask, which was heated up to boiling under stirring. Instantaneous precipitation was observed once boiling started, indicating the formation of $\text{Ln}(\text{OH})\text{CO}_3$. The suspension remained boiling for 270 minutes, and then left to cool down to room

temperature. The precipitate was washed with 5 L of deionized water to eliminate the NH_4^+ and NO_3^- ions in solution. The obtained $\text{Ln}(\text{OH})\text{CO}_3$ power was then dried at 100 °C for 60 minutes.

The MASS syntheses of UC materials were performed in a similar fashion as described previously, employing the two-step MASS synthesis of 25 minutes each step. Seeking Er^{3+} and Yb^{3+} concentrations that yield an optimal UC efficiency, 8 combinations of $[\text{Er}^{3+}]$, $[\text{Yb}^{3+}]$ were doped into the $\text{Gd}_2\text{O}_2\text{S}$ host. As both Ln_2O_3 and $\text{Ln}(\text{OH})\text{CO}_3$ were employed as precursors, 16 UC materials were therefore obtained, accordingly to the scheme in Figure 2.4.

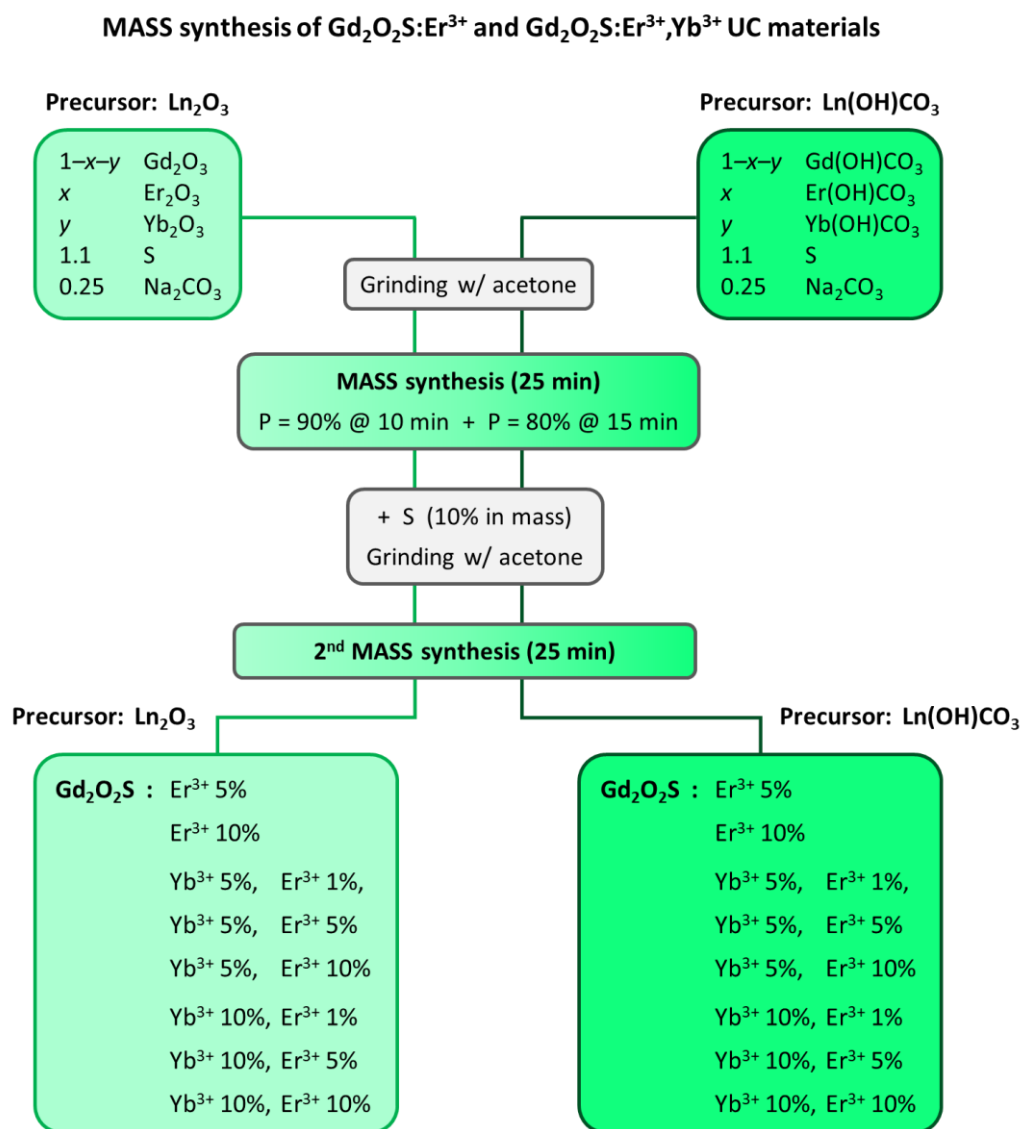


Figure 2.4 Scheme for the microwave-assisted solid-state (MASS) synthesis of $\text{Gd}_2\text{O}_2\text{S}:\text{Er}^{3+}$ and $\text{Gd}_2\text{O}_2\text{S}:\text{Er}^{3+},\text{Yb}^{3+}$ upconversion (UC) materials.

The Gd₂O₂S UC materials were prepared with such nominal Er, Yb dopant concentrations in order to make a direct comparison of UC emission intensities between the commercially available materials (Leuchtstoffwerk® – Germany) and the materials prepared by the MASS methodology. Aiming at an additional luminescence improvement, Ln(OH)CO₃ were employed as Ln source due to their relatively low (<700 °C) decomposition temperature [129,130], making them suitable precursors for high quality Ln ceramic materials.

2.1.4 Synthesis of RE₂O₂S:(Eu, Yb), Ti, Mg persistent luminescence materials

Lastly, RE₂O₂S:Ti, Mg, RE₂O₂S:Yb, Ti, Mg and Y₂O₂S:Eu, Ti, Mg persistent luminescence (PersL) materials (RE³⁺: La, Gd, and Y) were synthesized targeting different potentials for PersL, for example, self-sustained light emitting diodes – RE₂O₂S:Ti, Mg, and near-infrared (NIR) PersL materials – RE₂O₂S:Yb, Ti, Mg. Furthermore, a series of Y₂O₂S:Eu and Y₂O₂S:Eu, Ti, Mg materials with variable Eu³⁺ dopant concentration were prepared for a detailed investigation on the particularities lying behind the PersL mechanism operating for the well-known Y₂O₂S:Eu, Ti, Mg. Table 2.4 shows the chemicals and microwave oven used in the preparation of this class of materials.

Table 2.4 Chemicals and microwave oven used in the synthesis of RE₂O₂S-based PersL materials.

Chemicals	Company / Purity
Rare earth oxides, RE ₂ O ₃ (RE ³⁺ : La, Gd, Y, Eu, and Y)	CSTARM / 99.99%
Titanium oxide, TiO ₂	Merck / 99.5%
Magnesium basic carbonate, (MgCO ₃) ₄ Mg(OH) ₂ ·5H ₂ O	Merck / 99.99%
Elemental sulfur, S	Synth Brazil / 99.5%
Sodium carbonate, Na ₂ CO ₃	Vetec / 99.5%
Activated carbon (1~2 mesh)	Synth Brazil / Analytical Grade
Acetone	Synth Brazil / Analytical Grade
Microwave oven	Max Power / Cavity volume
Electrolux MEF41 (Institute of Chemistry – University of São Paulo)	1000 W / 31 L

The MASS synthesis for the RE₂O₂S-based PersL materials was conducted similarly as described in previous sections, maintaining the 1 RE₂O₃ : 1.075 S stoichiometry for RE³⁺: La and Gd, and 1:3 for RE³⁺: Y. In addition, Ti⁴⁺ and Mg²⁺ were co-doped in the oxysulfide lattice with fixed concentrations of 1.5 and 4.5%, respectively, to improve PersL properties. The MASS synthesis procedures and the obtained PersL materials, classified according to their respective potentials, were displayed in the scheme of [Figure 2.5](#).

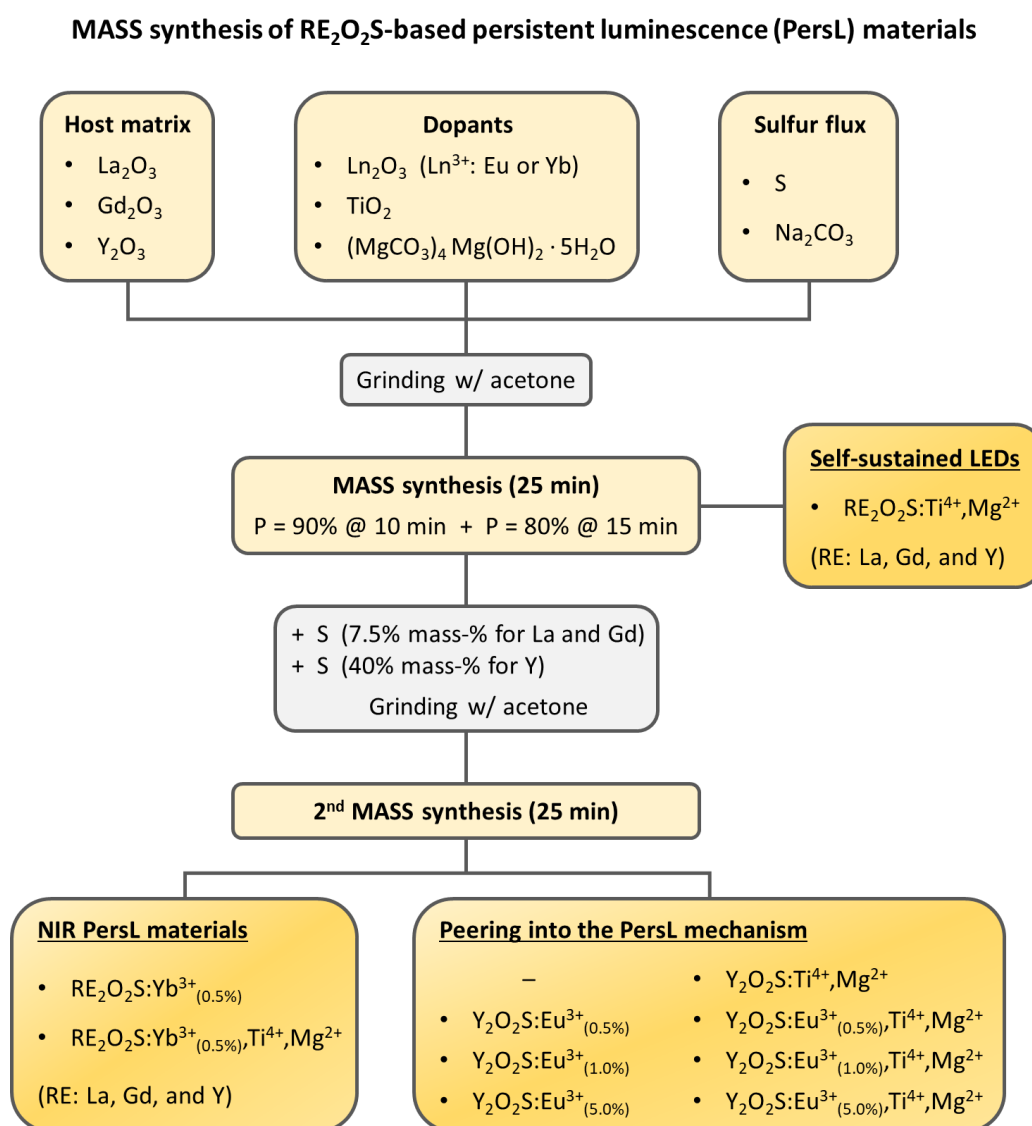


Figure 2.5 Scheme for the microwave-assisted solid-state (MASS) synthesis RE₂O₂S-based persistent luminescence (PersL) materials, aiming at self-sustained LEDs, NIR-emitting PersL materials, and at investigating the PersL mechanism. [Ti⁴⁺] = 1.5% and [Mg²⁺] = 4.5% for all materials co-doped with Ti, Mg.

2.2 Preparation of RE₂O₂S-based luminescent nanoparticles via colloidal synthesis in organic medium

2.2.1 Colloidal synthesis and washing procedures

Completely different from the microwave-assisted solid-state method, the synthesis of RE₂O₂S-based luminescent nanoparticles (NPs) was conducted via a colloidal synthesis methodology in organic medium. The organic solvents commonly employed in the preparation of nano-RE₂O₂S are 1-octadecene (ODE), oleic acid (OA), and oleylamine (OM) (Figure 2.6).

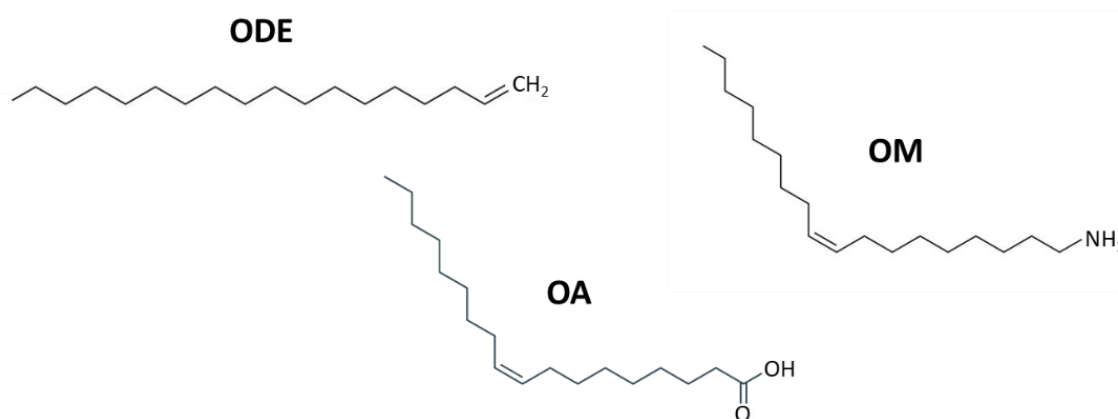


Figure 2.6 Solvent/ligands used in the colloidal synthesis of RE₂O₂S nanocrystals: 1-octadecene (ODE), oleic acid (OA), and oleylamine (OM).

1-octadecene (ODE) is an odorless and colorless alkene of 18 carbons, with molecular formula C₁₈H₃₆. The lack of active groups leads to a high chemical stability at elevated temperatures (boiling point = 315 °C), which allows its use as an inert solvent to the synthesis of inorganic nanocrystals (NCs) via decomposition of organic precursors (250–315 °C) [121,124,127]. Oleic acid (OA – C₁₇H₃₃COOH) is an odorless/colorless carboxylic acid, naturally present in a variety of vegetable and animal oils and fats. Its carboxylic polar head and lipophilic carbon chain make it a suitable ligand, coordinating to the surface of nanocrystals' and preventing them from aggregation. Yellowish OA samples were shown to have oxidized impurity products and should not be used for NP synthesis.

Oleylamine (OM – C₁₈H₃₅NH₂) is a yellowish oil with a smell analogous to ammonia. As its molecular structure is similar to OA (long C₁₈-chain with a polar head, [Figure 2.6](#)), it can also act as a molecular ligand to the surface of NCs [\[131\]](#). However, OM has an essential role for the synthesis of metal sulfide NCs. According to Thomson *et al.* [\[132\]](#), the conversion of elemental sulfur to metal sulfides is mediated by long-chain amine molecules. At room temperature, sulfur–amine solutions exist as alkylammonium polysulfides, which produce H₂S upon heating, available in solution as oleylammonium hydrosulfide (RNH₂ + H₂S → [RNH₃⁺][HS⁻]). This entity is the actual precursor to the formation of a metal sulfides ([Equation 2.1](#), where M²⁺: metal and X⁻: anion). Oxyulfides may be formed if oxygen is available in the reaction medium or in the precursors [\[117,127\]](#).



It is worth mentioning that [Equation 2.1](#) is a simplified chemical process, since the metal precursors usually go under decomposition at the synthesis temperatures [\[131,132\]](#). The precursors and solvents/ligands used in this work to synthesize and wash RE₂O₂S NCs in were listed in [Table 2.5](#). The full scheme for the synthesis and washing procedures was displayed in [Figure 2.7](#).

Table 2.5 Chemicals used in the colloidal synthesis of RE₂O₂S nanocrystals (NCs).

Chemicals	Company / Purity
Lanthanide acetylacetonate, Ln(C ₅ H ₇ O ₂) ₃ · xH ₂ O (Ln ³⁺ : Eu and Gd)	Merck / 99.9%
Lanthanide acetylacetonate, Ln(C ₅ H ₇ O ₂) ₃ · xH ₂ O (Ln ³⁺ : Er and Yb)	Strem / 99.9%
Yttrium acetate, Y(CH ₃ CO ₂) ₃ · xH ₂ O	Merck / 99.9%
Titanium isopropoxide, Ti[OCH(CH ₃) ₂] ₄	Merck / 99.999%
Magnesium acetate tetrahydrate, Mg(CH ₃ CO ₂) ₂ · 4H ₂ O	Merck / ≥ 98%
Elemental sulfur, S	Alfa Aesar / 99.5%
Sodium oleate (NaOA), Na(C ₁₈ H ₃₃ O ₂)	Merck / ≥ 82%
1-Octadecene (ODE), C ₁₈ H ₃₆	Merck / 90%
Oleic acid (OA), C ₁₈ H ₃₄ O ₂	Merck / 90%
Oleylamine (OM), C ₁₈ H ₃₅ NH ₂	Merck / ≥ 98%
Ethanol (EtOH), C ₂ H ₅ OH; and Cyclohexane (CHex), C ₆ H ₁₂	Merck / 99.999%

Colloidal synthesis of RE₂O₂S-based luminescent nanocrystals

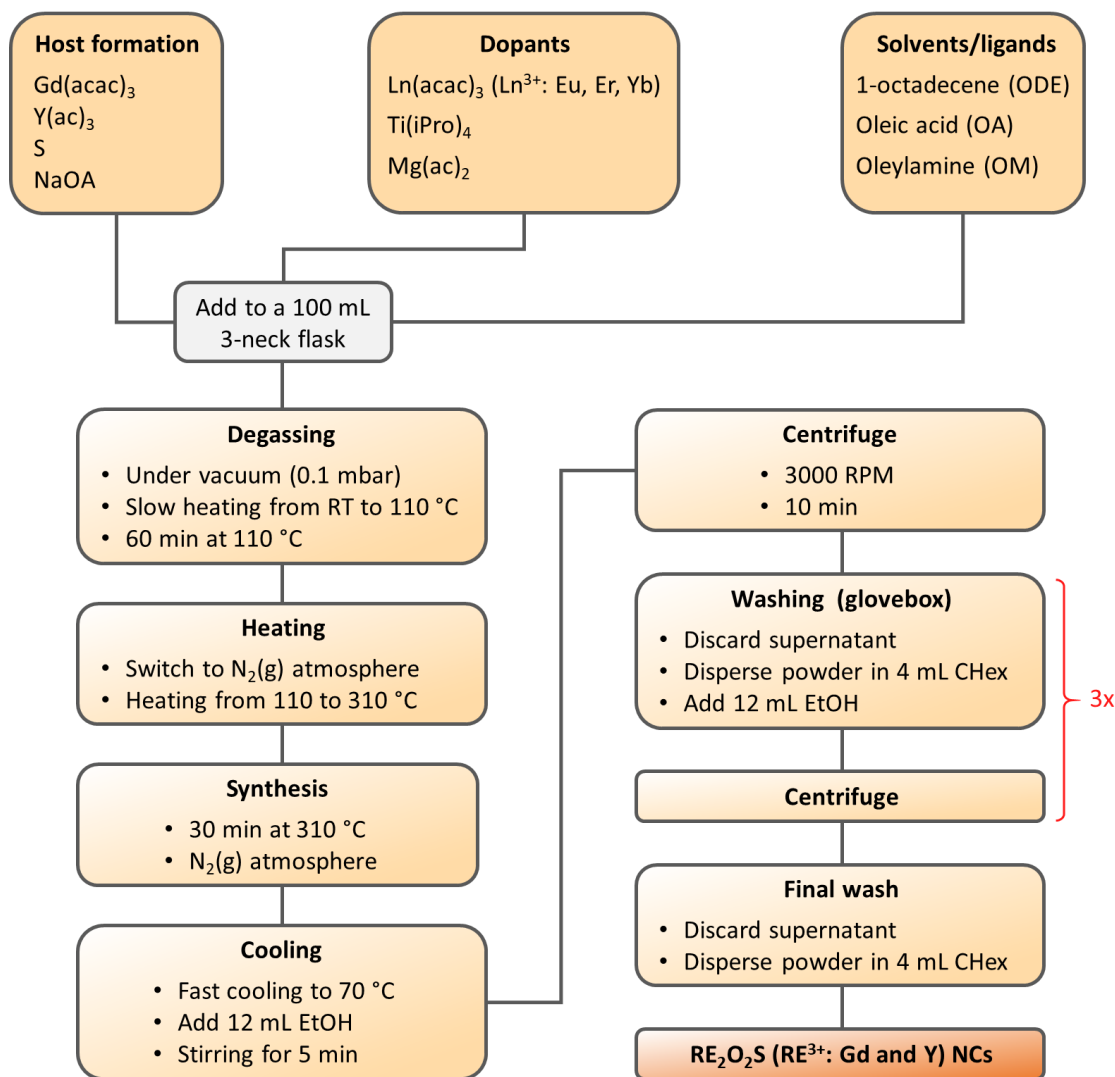


Figure 2.7 Scheme for the colloidal synthesis of luminescent RE₂O₂S nanocrystals (ac: acetate, acac: acetylacetonate, EtOH: ethanol, Chex: cyclohexane).

The synthesis procedures used in this work were adapted from [124]. Chemicals were stoichiometrically weighted in a 3-neck flask, which was then coupled to a schlenkline for atmosphere control via a condenser affixed to the middle neck. A thermometer was attached to the left neck (Figure 2.8a). The degassing step, *i.e.*, the first step of the whole preparation methodology (Figure 2.7), is essential to remove low boiling point impurities from the precursors and solvents, which can strongly affect the formation of the desired RE₂O₂S NCs. This process had to be done carefully and

slowly (heating in a heating plate in steps of 10 °C), since the low pressure could cause the precursor suspension to be sucked out of the flask and thus losing the reaction. Finished degassing, the system was heated up to the synthesis temperature (310 °C) under N₂(g) atmosphere. Once T = 310 °C was achieved, chemicals were left reacting for 30 min. RE₂O₂S NCs nucleate and grow during this period, turning the organic solution into a cloudy suspension (Figure 2.8b).

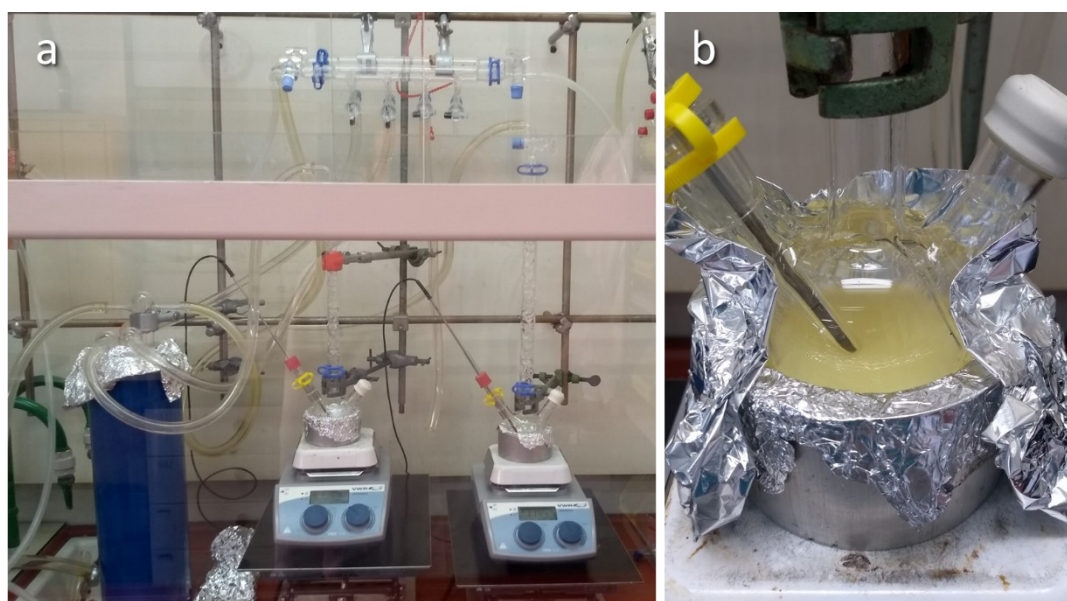


Figure 2.8 a) Synthesis setup for the colloidal preparation of RE₂O₂S nanocrystals (NCs); b) focus on the reaction medium during the synthesis step – the opaque appearance is due to the formation of RE₂O₂S NCs.

After synthesis, the system was quickly cooled down to 70 °C by turning the heating plate off and lowering its height to avoid contact with the flask. At 70°C, absolute ethanol was added to precipitate the NCs, *i.e.*, ethanol was employed as an antisolvent to extract the polar functionalized NCs from the non-polar solvents. After 5 minutes of stirring, the suspension was transferred to a N₂(g) filled glass vial and centrifuged (3000 RPM, 10 min), resulting in a white powder at the bottom. Then, washing steps were employed, which consisted in discarding the supernatant, adding cyclohexane (4 mL) to redisperse the NP powder, then adding ethanol (12 mL) to precipitate and separate the particles again by centrifuging. After three repetitions, the RE₂O₂S NCs were redispersed

in 4 mL of cyclohexane and stored under N₂(g). All washing steps were performed inside a dry N₂(g)-filled glovebox to avoid the decomposition of the RE₂O₂S NCs [124].

Several compositions were tested, aiming at optimizing the synthesis of luminescent RE₂O₂S nanomaterials and obtaining diverse optical phenomena. Initially, NCs were prepared singly doped with the Eu³⁺ ion, which acts as a spectroscopic probe to the formation of the oxysulfide crystalline phase (Table 2.6). Then, other dopants were tested: Er³⁺ and Yb³⁺ to achieve UC (Table 2.7), and Eu³⁺, Ti⁴⁺, Mg²⁺ to obtain PersL nanomaterials (Table 2.8).

Table 2.6 Composition of RE₂O₂S nanomaterials obtained by the colloidal synthesis methodology, singly doped with Eu³⁺ (values in grams when units were not expressed).

Code	Material	Gd(acac) ₃	Y(ac) ₃	Eu(acac) ₃	S	Na**	ODE	OA	OM
Eu 1	Gd ₂ O ₂ S:Eu 4%	0,2476	-	0,0078	0,0160	0,1522	6,4 mL	0,8 mL	5,6 mL
Eu 2	Gd ₂ O ₂ S:Eu 4%	0,2476	-	0,0078	0,0160	0,1522	6,4 mL	0,8 mL*	5,6 mL
Eu 3	Gd ₂ O ₂ S:Eu 4%	0,2476	-	0,0078	0,0160	0,0410	6,4 mL	0 mL**	5,6 mL
Eu 4	Y ₂ O ₂ S:Eu 5%	-	0,1555	0,0131	0,0160	0,1522	6,4 mL	0,8 mL	5,6 mL

* 0,8 mL OA was added after 15 minutes of synthesis

** NaOA for the syntheses of Eu1, Eu2, and Eu4; Na(ac) for Eu3

Table 2.7 Composition of RE₂O₂S nanomaterials obtained by the colloidal synthesis methodology, doped with Er³⁺ and Yb³⁺ to achieve upconversion (UC). The volume of solvents used were identical to all syntheses: ODE: 6.4, OA: 0.8, and OM: 5.6 mL. All values in grams.

Code	Material	Gd(acac) ₃	Er(acac) ₃	Yb(acac) ₃	S	NaOA
UC 1	Gd ₂ O ₂ S : Er 5%	0,2450	0,0103	-	0,0160	0,1522
UC 2	Gd ₂ O ₂ S : Er 1%, Yb 5%	0,2424	0,0021	0,0133	0,0160	0,1522
UC 3	Gd ₂ O ₂ S : Er 2%, Yb 18%	0,2063	0,0042	0,0478	0,0160	0,1522
UC 4	UC 3 @ Gd ₂ O ₂ S	0,2579	-	-	0,0160	0,1522

Table 2.8 Composition of RE₂O₂S nanomaterials obtained by the colloidal synthesis methodology, doped with Eu³⁺, Ti⁴⁺, Mg²⁺ to achieve persistent luminescence (PersL). The volume of solvents used were identical to all syntheses: ODE: 6.4, OA: 0.8, and OM: 5.6 mL. All values in grams.

Code	Material	Gd(acac) ₃	Y(ac) ₃	Eu(acac) ₃	Ti(iPro) ₄	Mg(ac) ₂
PersL 1	Gd ₂ O ₂ S : Eu 5%, Ti 3,4%, Mg 4,5%	0,2450	-	0,0131	50 μL	0,0048
PersL 2	Y ₂ O ₂ S : Eu 5%, Ti 3,4%, Mg 4,5%	-	0,1425	0,0131	50 μL	0,0048

2.2.2 Influence of oleic acid (OA) addition

Oleic acid (OA) is an important ligand to form and stabilize nanoparticles of different natures, preventing them from aggregation [133,134]. It also has a fundamental role on the particle nucleation and growth mechanisms, including for rare earth oxysulfides. As reported by Larquet *et al.* [127], the formation of nano-RE₂O₂S via colloidal synthesis happens through an oleate-mediated mesophase that acts as a template to the growth of nanocrystals. Oleylamine (OM) is not always employed in NC synthesis, but it is essential in the preparation of metal sulfides since it can reduce elemental sulfur to sulfide species available in organic solution [131]. In addition, its structural similarity with OA allows OM to also act as a ligand, functionalizing and spacing the formed NCs.

In this context, the influence of OA addition was investigated in the colloidal synthesis of Gd₂O₂S:Eu³⁺ 4% NCs. More specifically, in the preparation of the materials “Eu2” and “Eu3” (Table 2.6). In the synthesis of Eu2, all steps from Figure 2.7 were followed normally, except for the “synthesis” step itself. In this case, OA was not added in the beginning together with all chemicals, but instead it was added when T = 310 °C for 15 minutes. This means that, when the reaction medium achieved 310 °C, the particles were let to grow for 15 minutes; after this time, 0.8 mL OA was added to the reaction, which lasted for more 30 minutes (total synthesis time: 45 min). For the case of Eu3, no OA was added at all, with the intention to verify if Gd₂O₂S NCs could nucleate and grow in the absence of OA. To guarantee total absence of oleates for this case, the sodium source was substituted: sodium oleate, NaOA, was replaced by sodium acetate, Na(ac).

The synthesized crystals were characterized by transmission electron microscopy (TEM) to examine the differences in the NC size and morphology, and by photoluminescence spectroscopy, using the dopant Eu³⁺ as a local spectroscopical probe. Details about the characterization techniques for all nanocrystal samples were presented in sections 2.3 and 2.4.

2.3 Structural and morphological characterization techniques

2.3.1 X-ray powder diffraction (XRD)

XRD patterns of bulk rare earth oxysulfide materials obtained by the microwave-assisted solid-state (MASS) method were registered to investigate the RE₂O₂S crystal structure formation over MASS synthesis time, as well as to verify the crystal structure and phase purity of doped RE₂O₂S-based luminescent materials. Undoped RE₂O₂S (RE³⁺: Gd and Y), Gd₂O₂S:Tb³⁺ scintillators and all PersL oxysulfides – RE₂O₂S:Ti,Mg and RE₂O₂S:(Eu,Yb),Ti,Mg (RE³⁺: La, Gd and Y) XRD patterns were recorded utilizing a Rigaku Miniflex 2 diffractometer (*Centro de Química e Meio Ambiente, Instituto de Pesquisas Energéticas Nucleares – CQMA-IPEN – Brazil*), employing CuK α ₁ radiation (1.5406 Å), measuring in the 10–80 ° 2 θ range, with a 0.05 ° step and 1 s integration time per step.

The XRD patterns for Gd₂O₂S:Er³⁺ and Gd₂O₂S:Er³⁺,Yb³⁺ UC materials were registered using a Philips PW1700 diffractometer (Condensed Matter and Interfaces, Utrecht University – CMI-UU – The Netherlands), with CuK α radiation (1.5418 Å), measuring in the 10–70 ° 2 θ range and employing a 0.02 ° step with 1 s integration time.

2.3.2 Synchrotron radiation X-ray powder diffraction (SR-XRD)

SR-XRD measurements on the Gd₂O₂S:Tb³⁺ scintillator materials were performed using the XRD1 beamline (Proposal #20160911) [135,136] at the Brazilian Synchrotron Light Laboratory (*Centro Nacional de Pesquisa em Energia e Materiais – LNLS-CNPEM – Brazil*). The Debye-Scherrer setup was employed, scanning in the 3–120 ° 2 θ range. Incident X-ray beam energy was set to 12 keV, and a Mythen 24 k detector was used to collect the signal. A pseudo-Voigt function was employed in the Rietveld refinements using the general structure analysis system (GSAS [137,138]) software suite. The Gd₂O₂S unit cell, as well as the Gd³⁺ coordination polyhedron, were illustrated by the VESTA software [139].

SR-XRD data for the RE₂O₂S:Ti,Mg PersL materials (RE³⁺: La, Gd and Y) were collected at the XPD beamline (Proposals #17180 and #19001, *LNLS-CNPEM* – Brazil), using a θ – 2θ detection system, a linear Dectris Mythen 1K detector, and X-ray beam wavelengths of 1.61332 and 1.90781 Å. The 2θ detection range was 10–120 ° using a step-scanning mode with 0.51 ° of step size. Rietveld refinements were carried out using the general structure analysis system (GSAS [137,138]) software.

2.3.3 Fourier transform infrared spectroscopy (FTIR)

FTIR absorption spectra of undoped Gd₂O₂S matrices obtained with increasing MASS synthesis time were measured using KBr pellets with a Bomem MB102 FTIR spectrometer (*Central Analítica, Instituto de Química, Universidade de São Paulo – CA/IQ-USP* – Brazil), in the 400–4000 cm⁻¹ range with 4.0 cm⁻¹ spectral resolution.

2.3.4 Synchrotron radiation X-ray absorption near edge structure (XANES)

SR-XANES was employed to probe the sulfur oxidation states in undoped RE₂O₂S (RE³⁺: Gd and Y) obtained with increasing MASS synthesis time. XANES data, monitoring at the sulfur K-edge (2470 eV), were collected at the SXS beamline (Proposals #18996 and #20170354, *LNLS-CNPEM* – Brazil) in the soft X-ray energy range (900–5500 eV). Setup consisted in a double Si(111) crystal monochromator, with energy resolution of $\Delta E/E = 10^{-4}$, and two different detector systems, total electron yield (TEY – Keithley electrometer, model 6514) and fluorescence yield (FY – Amptek, model X123). Sulfur standards FeS (S²⁻), S⁰, Na₂SO₃ (S⁴⁺), and CaSO₄ (S⁶⁺) were measured under the same conditions. Hard X-ray XANES was performed at the XAFS2 beamline [140] (Proposal #20170006) to probe the terbium oxidation states in Gd₂O₂S:Tb³⁺ scintillator materials. XANES data were recorded around the terbium L_{III}-edge (7514 eV) in transmission mode, with resolution of $\Delta E/E = 1.7 \times 10^{-4}$. Tb₄O₇ and Tb(acac)₃ standards were measured in the same conditions.

2.3.5 Scanning electron microscopy (SEM)

SEM images for the undoped $\text{Y}_2\text{O}_3\text{S}$ materials were registered to verify to changes in crystal morphology as a function of MASS synthesis time. These samples, together with $\text{RE}_2\text{O}_3\text{S}:\text{Ti,Mg}$ PersL materials (RE^{3+} : La, Gd and Y), were measured with a field emission scanning electron microscope JEOL JSM-7401F (*CA/IQ-USP* – Brazil) in lower secondary electron image (LEI) mode with 20 kV voltage. The samples' pre-treatments were carried out by dispersing 5 mg of each sample in 2.5 mL isopropanol and sonicating these dispersions at 50 Hz in a Quimis Q335D sonicator for 2 minutes. Finally, 30 μL of these dispersions were deposited on a carbon stub.

In addition, SEM images for $\text{Gd}_2\text{O}_3\text{S}:\text{Tb}^{3+}$ scintillators were recorded using a FEI Quanta 650 FEG with High Voltage 20 kV (Proposal #19878, Electron Microscopy Laboratory, Brazilian Nanotechnology National Laboratory – *LME/LNNano-CNPEM* – Brazil), in secondary electrons mode with an Everhart Thornley detector. Sample's pre-treatments were carried in a similar manner described previously.

2.3.6 Transmission electron microscopy (TEM)

TEM images of all $\text{RE}_2\text{O}_3\text{S}$ -based nanomaterials (RE^{3+} : Gd and Y) were obtained using a Tecnai20F microscope (Electron microscopy facility, Veterinary Medicine, Utrecht University – The Netherlands) equipped with a field emission gun (FEI) electron source operating at 120 kV. Sample preparation consisted in diluting 50 μL of the original nanoparticle suspension in 950 μL of pure cyclohexane. Then, a drop of this new suspension was deposited on a copper-grid sample holder, waiting for about two minutes until the solvent completely evaporated. This procedure was performed inside a glovebox.

2.4 Study of luminescence properties

2.4.1 Photoluminescence (PL) spectroscopy

PL spectroscopy of $\text{Gd}_2\text{O}_2\text{S}:\text{Tb}^{3+}$ scintillators and $\text{RE}_2\text{O}_2\text{S}:(\text{Yb}),\text{Ti},\text{Mg}$ PersL materials (RE^{3+} : La, Gd, and Y) were measured on a Horiba Jobin Yvon Fluorolog 3–11 spectrofluorometer (*Laboratório dos Elementos do Bloco f, Instituto de Química, Universidade de São Paulo – LEBf/IQ-USP – Brazil*) equipped with mono- and double grating monochromators (focal lengths of 0.3 and 0.5 m) for excitation and emission, respectively. An OSRAM short-arc xenon lamp (450 W) was used as the excitation source, and a Synapse Horiba Jobin Yvon E2V CCD30 (1024x256 pixels) was used as the detector. Data were collected using the equipment setup at an angle of 22.5° (front face).

$\text{Gd}_2\text{O}_2\text{S}:\text{Er}(\text{Yb})$ UC materials, $\text{Y}_2\text{O}_2\text{S}:\text{Eu},\text{Ti},\text{Mg}$ PersL materials, and all colloidal $\text{RE}_2\text{O}_2\text{S}$ -based NCS (RE^{3+} : Gd and Y) were measured utilizing an Edinburgh Instruments FLS-920 spectrofluorometer (Condensed Matter and Interfaces, Utrecht University – CMI-UU – The Netherlands), equipped with a 450 W Xe lamp as the excitation source, dual excitation and emission monochromators, and a Hamamatsu R928 photomultiplier tube (PMT) as the detector. Data were collected using the equipment setup at an 90° angle, setting the sample holder at 45° . For NCs, the samples were measured in colloidal form, placed inside quartz cuvettes. To record the UC emission spectra, both $\text{Gd}_2\text{O}_2\text{S}:\text{Er}(\text{Yb})$ bulk and nanomaterials were excited with a 500 mW NIR continuous laser ($\lambda = 980$ nm). It is important to mention that, to record the UC emission spectra of the $\text{Gd}_2\text{O}_2\text{S}:\text{Er},\text{Yb}$ bulk materials, all the optical components involved were fixed, as well as the sample volume contained in the sample holder, so that the detected intensities could be directly compared. In this way, the UC emission spectra of commercial $\text{Gd}_2\text{O}_2\text{S}:\text{Er},\text{Yb}$ samples were also recorded (Leuchtstoffwerk Breitung® GmbH – Germany) so that their UC emission intensities could be compared with those of the materials obtained by MASS method.

2.4.2 Synchrotron radiation Vacuum-UV photoluminescence spectroscopy (VUV)

SR-VUV spectroscopy was employed to determine the band gap energy of RE₂O₂S hosts (RE³⁺: La, Gd, and Y), as well as to map the Gd₂O₂S:Tb³⁺ optical band gap and describe its luminescence mechanism. Measurements were performed at the TGM beamline [141] (Proposals #20150060 and #20170007, *LNLS-CNPEM* – Brazil) in the 3D mode, in which the visible luminescence was monitored during an energy scan at the spectral range 4.5–8.0 eV (275–155 nm). Excitation photons were filtered with a special Act Ion Quartz (thickness: 200 mm, cutoff: 8.2 eV) to avoid second order harmonics, and the emitted light was collected through an UV–vis optical fiber from Ocean Optics (optical aperture: 600 mm), which was coupled to a QE65000 spectrometer (Ocean Optics). All measurements were performed in ultra-high vacuum condition ($\leq 10^{-7}$ mbar) at room temperature.

2.4.3 Synchrotron radiation X-ray excited optical luminescence (XEOL)

SR-XEOL emission spectra of Gd₂O₂S:Tb³⁺ scintillators were recorded at the XAFS1 beamline (Proposal #20160900, *LNLS-CNPEM* – Brazil) in a special dark chamber, at room pressure and temperature. Data were collected using an UV–vis optical fiber (aperture: 600 mm) couple to a spectrometer Ocean Optics QE65000. Samples were excited around the Tb L_{III}-edge with fixed energies of 7000, 7500, and 8000 eV.

2.4.4 Persistent luminescence (PersL) decay curves and emission spectra

PersL decay curves for RE₂O₂S:Ti⁴⁺,Mg²⁺ materials (RE³⁺: La, Gd, and Y) were acquired in a SPEX Fluorolog 2 (*LEBf/IQ-USP* – Brazil), equipped with a 450 W Xenon lamp as the excitation source, double excitation and emission monochromators, and a Hamamatsu R928 PMT as the detector system. The materials were excited at 350 nm for 300 s. Then, a delay of 30 s was employed between

the cease of excitation and the detection of PersL, which was monitored at 600 nm for 300 s. PersL emission spectra were registered in a fast scan after ceasing the irradiation source.

For the case of NIR emitting $\text{RE}_2\text{O}_2\text{S}:\text{Yb}^{3+},\text{Ti}^{4+},\text{Mg}^{2+}$ materials (RE^{3+} : La, Gd, and Y), PersL decay curves and emission spectra were recorded using a Horiba Jobin Yvon Fluorolog 3-11 spectrofluorometer (*LEBf/IQ-USP* – Brazil). A Synapse Horiba Jobin Yvon E2V CCD30 (1024x256 pixels) was employed as the detector system, which was able to capture a “picture” of the whole spectral range with 1 s of integration time. The materials were excited at 310 nm for 300 s, and the emission was monitored at 983 nm through 240 s immediately after ceasing excitation source. In addition, PersL decay curves of $\text{Y}_2\text{O}_2\text{S}:\text{Yb}^{3+}$ and $\text{Y}_2\text{O}_2\text{S}:\text{Yb}^{3+},\text{Ti}^{4+},\text{Mg}^{2+}$ materials were also recorded using an Edinburgh FLSP 920 photon counter (*Laboratório Lesões em Biomoléculas – IQ-USP* – Brazil) equipped with a Hamamatsu H10330A-45 PMT apparatus, which was maintained at $-20\text{ }^\circ\text{C}$ by a CO_2 thermoelectric cooler. The NIR light was detected by integrating all signal in the 900–2000 nm range, thus excluding any visible-light influences.

PersL decay curves for the $\text{Y}_2\text{O}_2\text{S}:\text{Eu}^{3+}$ and $\text{Y}_2\text{O}_2\text{S}:\text{Eu}^{3+},\text{Ti}^{4+},\text{Mg}^{2+}$ materials, varying Eu^{3+} concentration, were acquired in an Edinburgh Instruments FLS-920 spectrofluorometer (CMI-UU – The Netherlands). Materials were excited at 360 nm for 120 seconds, and a delay of 60 s was employed between ceasing the excitation and recording the persistent luminescence. The PersL emission was monitored at 626 nm ($\text{Eu}^{3+} \text{ }^5\text{D}_0 \rightarrow \text{ }^7\text{F}_2$). Samples of commercial $\text{Y}_2\text{O}_2\text{S}:\text{Eu}^{3+},\text{Ti}^{4+},\text{Mg}^{2+}$ materials (Glotech International® – New Zealand, and Luming Technology Group Co., Ltd® – China) were also analyzed for comparative purposes. PersL emission spectra of $\text{Y}_2\text{O}_2\text{S}:\text{Eu}^{3+},\text{Ti}^{4+},\text{Mg}^{2+}$ materials were recorded in a similar fashion used for $\text{Y}_2\text{O}_2\text{S}:\text{Yb}^{3+},\text{Ti}^{4+},\text{Mg}^{2+}$ ones, *i.e.*, full emission spectra were recorded using a CCD detector over 240 s after turning the excitation source off.

2.4.5 Thermoluminescence (TL)

TL measurements on the $\text{Y}_2\text{O}_2\text{S}:\text{Eu}^{3+}$ and $\text{Y}_2\text{O}_2\text{S}:\text{Eu}^{3+},\text{Ti}^{4+},\text{Mg}^{2+}$ materials, varying Eu^{3+} concentration, were performed in the temperature range 80–600 K using a Linkam Scientific THMS600 device, connected to a $\text{N}_2(\text{l})$ cooling system, and a set of bifurcated optical fibers from Thorlabs. Initially, the sample of interest was placed inside the Linkam system fixed on an optical table, and the optical fibers were positioned above the sample (Figure 2.9).

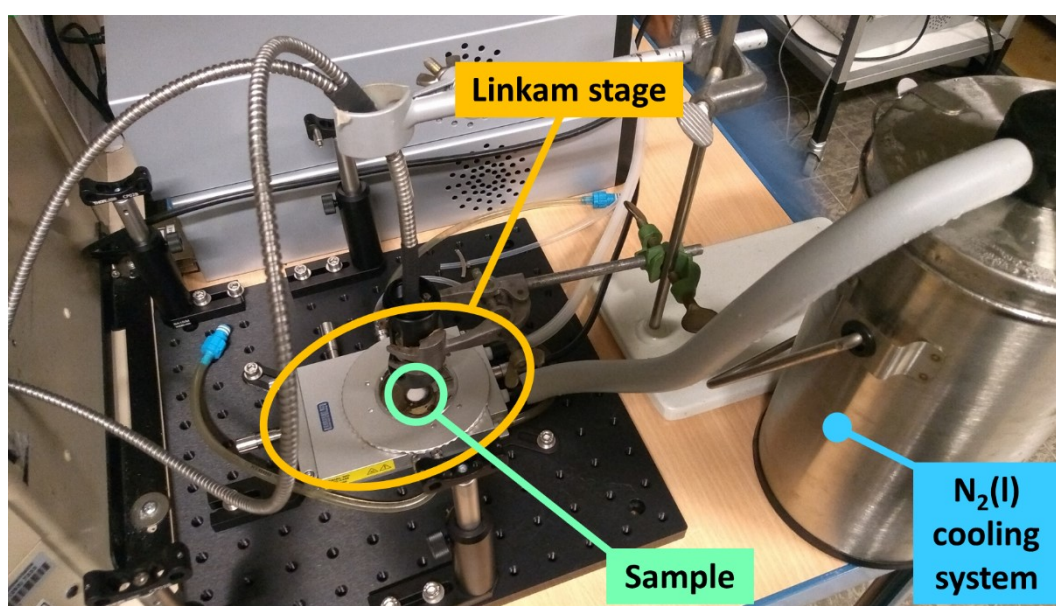


Figure 2.9 Adapted apparatus for thermoluminescence (TL) measurements. The Linkam system is fixed to an optical table, with the $\text{N}_2(\text{l})$ cooling system attached. The optical fibers are affixed above the sample to simultaneously excite it and collect the resulting TL emission.

One of the optical fibers collects the excitation signal from the Xe lamp ($\lambda_{\text{ex}} = 360 \text{ nm}$), illuminating the sample for 120 s. Then, excitation is ceased and the system is quickly cooled down to 80 K. From this point the TL experiment starts: the sample is heated from 80 to 600 K at a 1 K/s rate, and the sample's emission is collected by the second optical fiber, which is directed to the Hamamatsu R928 PMT detector. The emission monochromators were adjusted to collect a monochromatic emission centered on the $\text{Eu}^{3+} \text{ } ^5\text{D}_0 \rightarrow \text{ } ^7\text{F}_2$ transition (626 nm). For samples that did not

contain the Eu^{3+} ion ($\text{Y}_2\text{O}_2\text{S}:\text{Ti}^{4+},\text{Mg}^{2+}$), the TL emission was monitored at 630 nm, which is the maximum intensity for the Ti^{4+} charge transfer emission.

More importantly, several TL runs were performed for each sample, varying the excitation temperature in steps of 20 K, from 100 to 400 K ($T_{\text{ex}} = 100, 120, 140 \dots 280, 300, 320 \dots 400$ K). In this manner, TL curves can be plotted as a function of excitation temperature, aiding the mechanistic study of how traps depopulate upon heating and compare the results between materials with different dopant concentrations.

Chapter 3

Results and discussion

3.1 Microwave-assisted solid-state (MASS) synthesis:
RE₂O₂S formation *versus* synthesis time

3.2 Gd₂O₂S:Tb scintillators

3.3 Gd₂O₂S:Er and Gd₂O₂S:Er,Yb upconversion (UC) materials

3.4 RE₂O₂S:(Eu,Yb),Ti,Mg persistent luminescence (PersL) materials

3.5 RE₂O₂S-based luminescent colloidal nanocrystals (NCs)

3. RESULTS AND DISCUSSION

In this work, different synthetic approaches were explored and applied in the preparation of optically versatile rare earth oxysulfides ($\text{RE}_2\text{O}_2\text{S}$, RE^{3+} : La, Gd, and Y). Sections from 3.1 to 3.4 cover the bulk ($\sim 1 \mu\text{m}$) materials obtained by the rapid microwave-assisted solid-state (MASS) synthesis. At the same time, $\text{RE}_2\text{O}_2\text{S}$ -based nanocrystals ($< 50 \text{ nm}$) obtained by a colloidal synthesis methodology were discussed in section 3.5.

More specifically, section 3.1 deals with the investigation of the rare earth oxysulfide crystal formation as a function of microwave synthesis time. X-ray diffraction, infrared absorption spectroscopy, scanning electron microscopy, and X-ray absorption spectroscopy were employed as tools to construct a particle formation mechanism.

Understood the oxysulfide formation via microwave irradiation, several materials were prepared exhibiting diverse photonic phenomena: scintillation, upconversion (UC), and persistent luminescence (PersL). $\text{Gd}_2\text{O}_2\text{S}:\text{Tb}^{3+}$ scintillator materials were also obtained with different synthesis times to investigate their influence in the output scintillation performance (section 3.2).

Then, section 3.3 comprises $\text{Gd}_2\text{O}_2\text{S}:\text{Er}^{3+}$ and $\text{Gd}_2\text{O}_2\text{S}:\text{Er}^{3+},\text{Yb}^{3+}$ UC materials and how different precursors influence the UC emission efficiency for materials with same dopant concentration. For this purpose, the materials were prepared with different $[\text{Er}^{3+}], [\text{Yb}^{3+}]$ combinations. Comparisons with commercially available materials were also described.

Section 3.4 covers the PersL materials and their different potential for applications, *e.g.*, self-sustained LEDs ($\text{RE}_2\text{O}_2\text{S}:\text{Ti}^{4+},\text{Mg}^{2+}$) and NIR emitting PersL materials ($\text{RE}_2\text{O}_2\text{S}:\text{Yb}^{3+}$ and $\text{RE}_2\text{O}_2\text{S}:\text{Yb}^{3+},\text{Ti}^{4+},\text{Mg}^{2+}$). In addition, a series of $\text{Y}_2\text{O}_2\text{S}:\text{Eu}^{3+}$ and $\text{Y}_2\text{O}_2\text{S}:\text{Eu}^{3+},\text{Ti}^{4+},\text{Mg}^{2+}$ materials were prepared with various dopant concentrations and studied by PersL spectroscopy and thermoluminescence techniques, to peer into the details of persistent luminescence mechanism operating for these materials.

Research developed in this work led to the publication of three papers in peer-reviewed international journals. For instance, the $\text{RE}_2\text{O}_2\text{S}$ (RE^{3+} : La, Gd, and Y) particle formation mechanism using the MASS synthesis, as well as the preparation and characterization of $\text{RE}_2\text{O}_2\text{S}:\text{Ti}^{4+},\text{Mg}^{2+}$ PersL materials, were published in the *Journal of Material Chemistry C* under the title **“Persistent luminescence warm-light LEDs based on Ti-doped $\text{RE}_2\text{O}_2\text{S}$ materials prepared by rapid and energy-saving microwave-assisted synthesis”** (2018, [142] – Appendix A1). The fabrication of self-sustained LED devices was reported in this publication and was also presented in this thesis.

All research regarding $\text{Gd}_2\text{O}_2\text{S}:\text{Tb}^{3+}$ scintillator materials was possible due to a partnership with the Brazilian Synchrotron Light Laboratory (*LNLS-CNPEM* – Brazil). This scientific collaboration resulted in the publication **“X-ray scintillator $\text{Gd}_2\text{O}_2\text{S}:\text{Tb}^{3+}$ materials obtained by a rapid and cost-effective microwave-assisted solid-state synthesis”**, in the *Journal of Alloys and Compounds* (2019, [143] – Appendix A2).

The NIR persistent luminescence features of $\text{RE}_2\text{O}_2\text{S}:\text{Yb}^{3+}$ and $\text{RE}_2\text{O}_2\text{S}:\text{Yb}^{3+},\text{Ti}^{4+},\text{Mg}^{2+}$ materials were reported in **“A new path to design near-infrared persistent luminescence materials using Yb^{3+} -doped rare earth oxysulfides”**, published in *Scripta Materialia* (2019, [144] – Appendix A3). The work developed on $\text{Gd}_2\text{O}_2\text{S}:\text{Er},\text{Yb}$ UC materials, as well as the PersL mechanism studies on the $\text{Y}_2\text{O}_2\text{S}:\text{Eu},\text{Ti},\text{Mg}$, were at the writing stage during the confection of this thesis.

Finally, section 3.5 covers the synthesis and characterization of $\text{RE}_2\text{O}_2\text{S}$ -based luminescent nanocrystals. Firstly, Eu^{3+} was doped into the nanocrystals to act as a spectroscopic probe for the oxysulfide formation at nanoscale. Such NCs were characterized by transmission electron microscopy and photoluminescence spectroscopy. Then, this synthesis methodology was extended to fabricate UC ($\text{Gd}_2\text{O}_2\text{S}:\text{Er},\text{Yb}$) and PersL ($\text{RE}_2\text{O}_2\text{S}:\text{Eu},\text{Ti},\text{Mg}$) nanomaterials. A discussion on non-radiative decay mechanisms for different $\text{RE}_2\text{O}_2\text{S}$ nanocrystals was presented at the end, providing insights on how to avoid luminescence quenching and how to achieve photonic colloidal nanomaterials with high emission efficiency.

3.1 Microwave-assisted solid-state (MASS) synthesis: $\text{RE}_2\text{O}_2\text{S}$ formation *versus* synthesis time

3.1.1 Oxysulfide crystal phase formation and morphology

As stated in the previous chapter (section 2.1), the control of synthesis parameters is limited in a domestic microwave oven since one can only set the time and output power. Thus, for the preparation of rare earth oxysulfides by MASS method, the temperature of the inner alumina crucible was measured after several microwave irradiation times (0.5, 1, 1.5, 2, 3, 4, 5, 6, 8, 10, 12, 14, 16, 18, 20, 22, and 25 minutes) using a Homis 467A hand pyrometer (Figure 3.1). To remind the reader, the inner alumina crucible is the smaller crucible that holds the sample and is surrounded by activated carbon, which was chosen as the microwave susceptor (Figure 2.1a).

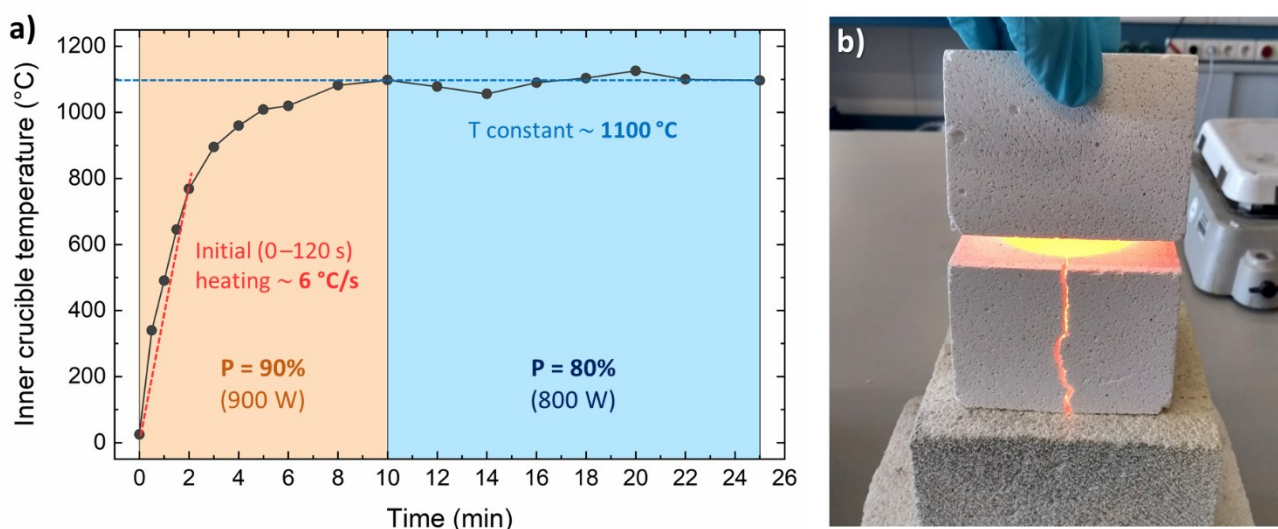


Figure 3.1 a) Correlation between the temperature of the sample crucible (surrounded by activated carbon) and the microwave exposition time; each temperature point was measured with a Homis 467A hand pyrometer; b) Incandescent crucibles ($T \sim 1100\text{ }^\circ\text{C}$) after 25 minutes of microwave irradiation.

From the measured temperature values as a function of microwave irradiation time (Figure 3.1a), it is clear that activated carbon is an excellent susceptor, capable of achieving temperatures

higher than 1000 °C in just 5 minutes of exposition to microwave radiation [107,109]. Considering a linear heating from 0 to 120 s, a rapid heating rate of ~6 °C/s (~360 °C/min) was calculated, making the MASS synthesis methodology 20-fold faster when compared to conventional solid-state methods [17,19]. The microwave oven was programmed to start with a higher output power (P = 90%) to produce this rapid initial heating in the sample. After 10 minutes, the power was decreased (P = 80%) to stabilize the synthesis temperature. The the inner crucible temperature was observed to steady at 1092 ± 19 °C after 10 minutes, which is a suitable temperature for the synthesis of RE₂O₂S materials [17,18]. Furthermore, the incomplete combustion of activated carbon generates a local CO(g) reducing atmosphere, which can reduce elemental sulfur to sulfide ions and aid the formation of the oxysulfide structure. From these results, it can be concluded that activated carbon is an appropriate choice of microwave susceptor to synthesize RE₂O₂S materials.

In this context, undoped Gd₂O₂S and Y₂O₂S matrices were prepared by the MASS method, increasing synthesis times in a two-minute step fashion (0, 2, 4, 6, 8, 10, 12, and 25 min) to evaluate the oxysulfide crystal structure formation as a function of synthesis time. X-ray diffraction (XRD) patterns for the Gd₂O₂S obtained in this manner (Figure 3.2) reveal that the conversion of the solid Gd₂O₃ + S + Na₂CO₃ precursor mixture into the Gd₂O₂S starts at very short synthesis times, e.g., 2 minutes. The oxysulfide is already the major crystal phase at this point. Further increasing in MASS synthesis time leads to a gradual evolution of oxysulfide crystal phase and vanishing of the oxide one. At 10 minutes of MASS synthesis, Gd₂O₃ fraction is barely detected. These results corroborate with the measured temperature values presented in Figure 3.1.

Moreover, the evolution of XRD patterns over time suggests that the Gd₂O₃→Gd₂O₂S conversion occurs with no crystalline intermediates. According to Lo *et al.* [105], sulfuration of rare earth oxides happens with the aid of Na₂S_x flux formed *in situ* by the reaction between S and Na₂CO₃. As the used Na₂CO₃ flux is not detected after the synthesis, it was probably decomposed under heating to form Na₂S_x or other non-crystalline salts.

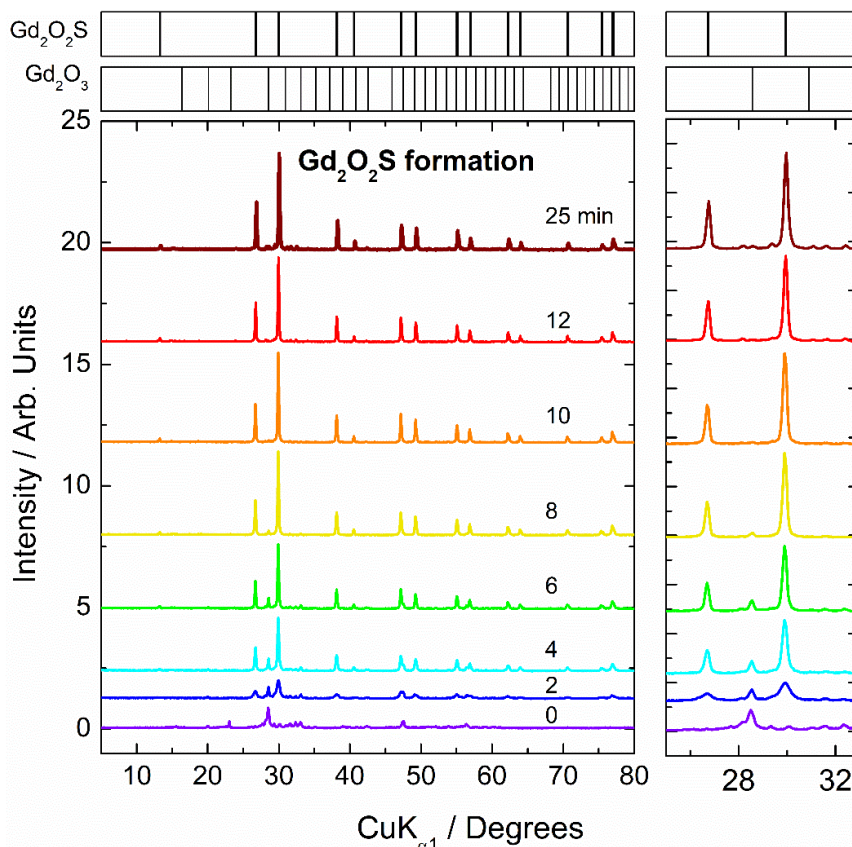


Figure 3.2 XRD patterns of the Gd₂O₂S materials obtained with increasing MASS synthesis time (2, 4, 6, 8, 10, 12, and 25 minutes). $t = 0$ min corresponds to the Gd₂O₃ + S + Na₂CO₃ precursor mixture. Bragg reflections for Gd₂O₂S and Gd₂O₃ were shown at the top. The zoom on the 26–33 ° 2θ range (right) shows the decreasing of the Gd₂O₃ peak (28.5 °) and the rising of the two main Gd₂O₂S peaks (26.7 and 29.9 °) by increasing the synthesis time [142] – A1.

A similar XRD study on the Y₂O₂S crystal formation as a function of MASS synthesis time was conducted (Figure 3.3a). The Y₂O₃→Y₂O₂S conversion was shown to be comparably rapid, *i.e.*, Y₂O₂S is the major crystalline phase after just 2 minutes of synthesis. Up to 8 minutes of synthesis, the prominent Y₂O₃ diffraction peak (29.1 °) decreased while the two main peaks for Y₂O₂S (27.0 and 30.4 °) increased in intensity. However, the reaction stabilized after this synthesis time, yielding a product that is approximately 70% Y₂O₂S / 30% Y₂O₃. This result is expected due to the smaller Y³⁺ ionic radii and thus its harder acidic character compared to Gd³⁺, according to the Pearson’s theory [16,128]. This chemical feature also explains why obtaining Lu₂O₂S materials is an even more challenging task [89]. Up to date, no pure-phase Lu₂O₂S could be prepared by the MASS method.

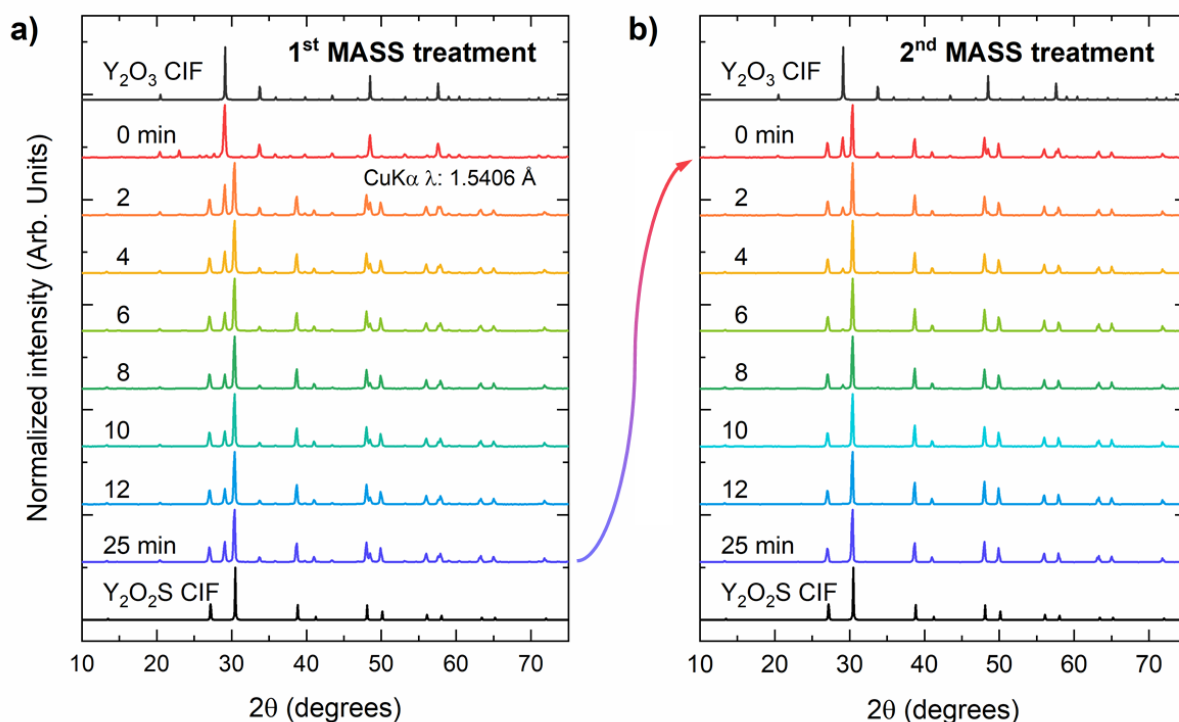


Figure 3.3 XRD patterns of the undoped $\text{Y}_2\text{O}_2\text{S}$ obtained with increasing MASS synthesis time: **a)** first and **b)** second microwave heating treatment (reference patterns for Y_2O_3 41-1105 and $\text{Y}_2\text{O}_2\text{S}$ 24-1424 were exhibited). $t = 0$ min in [Figure 3.3a](#) corresponds to the $\text{Y}_2\text{O}_3 + \text{S} + \text{Na}_2\text{CO}_3$ precursor mixture. The material obtained by a single-25 min step was used as a precursor to the second MASS treatment; therefore, the XRD pattern of “ $\text{Y}_2\text{O}_2\text{S}$ 25 min” in [3.3a](#) is the same for “ $\text{Y}_2\text{O}_2\text{S}$ 0 min” in [3.3b](#).

Although the final product in [Figure 3.3a](#) characterizes a fast $\text{Y}_2\text{O}_3 \rightarrow \text{Y}_2\text{O}_2\text{S}$ crystalline conversion under microwave irradiation, results are still not satisfactory when aiming at high quality luminescent materials. Hence, a second MASS heating treatment was applied, using the obtained “ $\text{Y}_2\text{O}_2\text{S}$ 25 min” material as a precursor and adding 40% of sulfur (in mass) to boost the formation of the desired oxysulfide phase. The XRD patterns for the materials obtained with the second MASS treatment ([Figure 3.3b](#)) show an efficient $\text{Y}_2\text{O}_2\text{S}$ formation within few minutes, *i.e.*, a significant decrease in intensity of the main Y_2O_3 diffraction peak (29.1°) is observed up to 4 minutes of synthesis. Pure $\text{Y}_2\text{O}_2\text{S}$ phase is achieved at the end of the second microwave synthesis (25 min). Therefore, two subsequent MASS heat treatments of 25 minutes each seem to be an optimized synthesis condition to prepare of $\text{Y}_2\text{O}_2\text{S}$ optical materials.

The $\text{Y}_2\text{O}_2\text{S}$ formation over synthesis time was also investigated by scanning electron microscopy (Figure 3.4). A remarkable morphology difference is observed between the SEM images for the precursor mixture (3.4a) and the material obtained with 2 minutes of MASS synthesis (3.4b), supporting the rapidness of the $\text{Y}_2\text{O}_3 \rightarrow \text{Y}_2\text{O}_2\text{S}$ conversion under microwave irradiation. The “ $\text{Y}_2\text{O}_2\text{S}$ 2 min” material, consisting roughly of a 50:50 oxide/oxysulfide mixture, exhibit monodisperse nanocrystals (~ 200 nm) with cubic morphology. Particle size was observed to grow by increasing MASS synthesis time from 2 to 25 minutes (3.4c). “ $\text{Y}_2\text{O}_2\text{S}$ 25 min” crystals display similar morphology but larger size polydispersion (200–600 nm). Moreover, crystals with hexagonal morphology could be spotted in this sample. While cuboid particles are an indicative of RE_2O_3 , hexagonal crystals suggest the formation of the $\text{Y}_2\text{O}_2\text{S}$ crystal phase [18,89]. These results corroborate with the relative $\text{Y}_2\text{O}_3/\text{Y}_2\text{O}_2\text{S}$ proportions found on XRD data (Figure 3.3a).

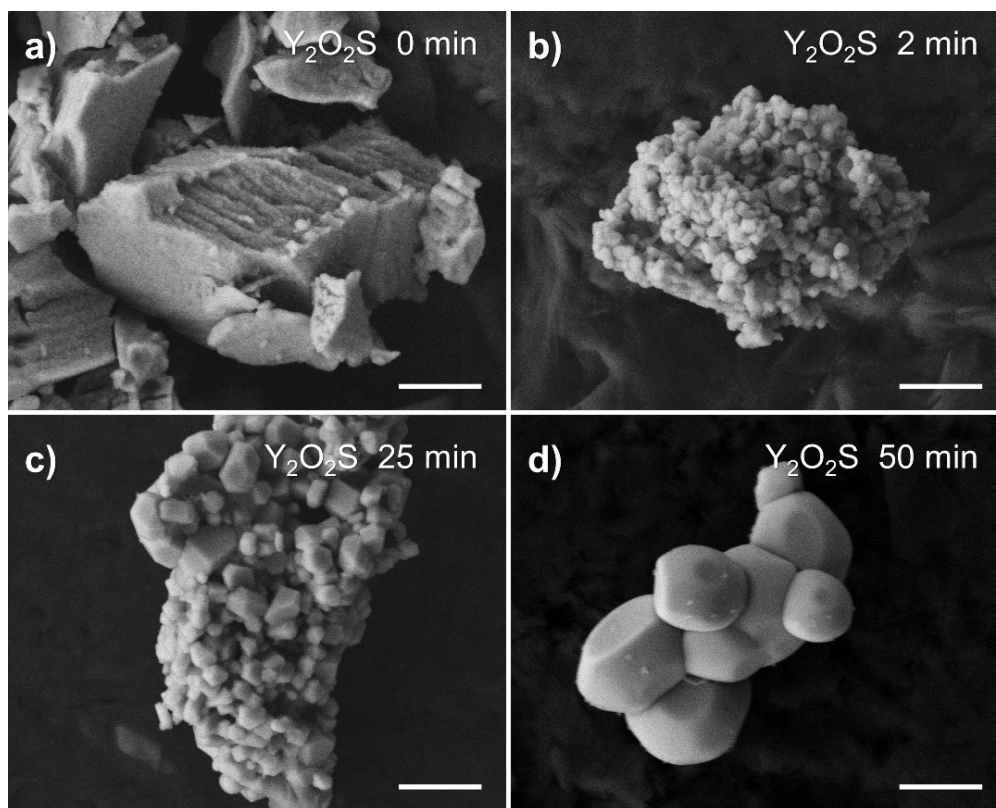


Figure 3.4 SEM images of undoped $\text{Y}_2\text{O}_2\text{S}$ materials obtained with increasing MASS synthesis time: **a)** precursor mixture $\text{Y}_2\text{O}_3 + \text{S} + \text{Na}_2\text{CO}_3$; $\text{Y}_2\text{O}_2\text{S}$ material obtained with **b)** 2 and **c)** 25 minutes of synthesis; **d)** $\text{Y}_2\text{O}_2\text{S}$ material obtained with two MASS heat treatments of 25 min each. Scale bars = 1.0 μm .

By submitting the “Y₂O₂S 25 min” to a second MASS treatment of 25 minutes, a pure oxysulfide phase “Y₂O₂S 50 min” material is obtained. SEM image of this sample (Figure 3.3d) reveals larger crystals, with sizes in the 0.5–1.5 μm range and an average size of 1 μm. Hexagonal-like morphology was also found, but crystal boundaries were observed to smoothen. This result can be attributed to the second MASS heating treatment, which promoted crystal growth by Ostwald ripening processes [145] despite the short synthesis times.

3.1.2 Sulfur K-edge X-ray absorption spectroscopy

Synchrotron radiation X-ray absorption spectroscopy (SR-XAS) is a powerful technique to study the local solid-state structure and oxidation states of elements in materials. In this work, X-ray absorption near edge structure (XANES) spectroscopy was used to investigate the sulfur K-edge energies for the prepared oxysulfide materials and compare it with reference compounds. XANES spectra of undoped Gd₂O₂S obtained with 10 and 25 minutes of MASS synthesis, as well as the spectra of FeS and CaSO₄ references, were presented in Figure 3.5a. The sulfur K-edge absorption edge, which corresponds to the transition of the 1s core electron to the lowest unoccupied antibonding states of sulfur, is located at 2473 ± 0.5 eV for the synthesized Gd₂O₂S matrices.

According to previous works, increasing sulfur oxidation state shifts the sulfur K-edge absorption to higher energies, varying by approximately 12 eV from S²⁻ (2470 eV) to SO₄²⁻ (2482 eV) [146,147]. The K-edge energy for sulfur was found to have a linear correlation with its oxidation state (Figure 3.5b) for the measured FeS, S, Na₂SO₃, and CaSO₄ standards. It is important to mention that the XANES spectra of all standards were recorded and displayed in the Supplementary Information of [142] – A1, showing similar spectral profiles to those reported in the literature [147]. In this context, the edge value observed for the Gd₂O₂S materials is higher than expected for a sulfide edge energy based on the absorption edge of the sulfide standard FeS (2470 eV). Nevertheless, this is in

accordance with how the structural environment affects elemental edge energies [146,148]. The best linear correlation of the sulfur absorption edge as a function of its oxidation state happens between S^0 and S^{6+} , where the nearest neighbors of sulfur are O^{2-} ions, and cations are restricted to the second or more distant coordination spheres. For sulfides and oxysulfides, sulfur is directly bonded to the metal cations, resulting in a different bonding character that strongly influences the position of the sulfur K-absorption edges. Consequently, there is an energy threshold for the absorption edge energies in reduced sulfur species [148,149]. The absorption edge observed at 2473 eV for the Gd_2O_2S materials can therefore be assigned to the K-edge of sulfur in the sulfide state (Figure 3.5b).

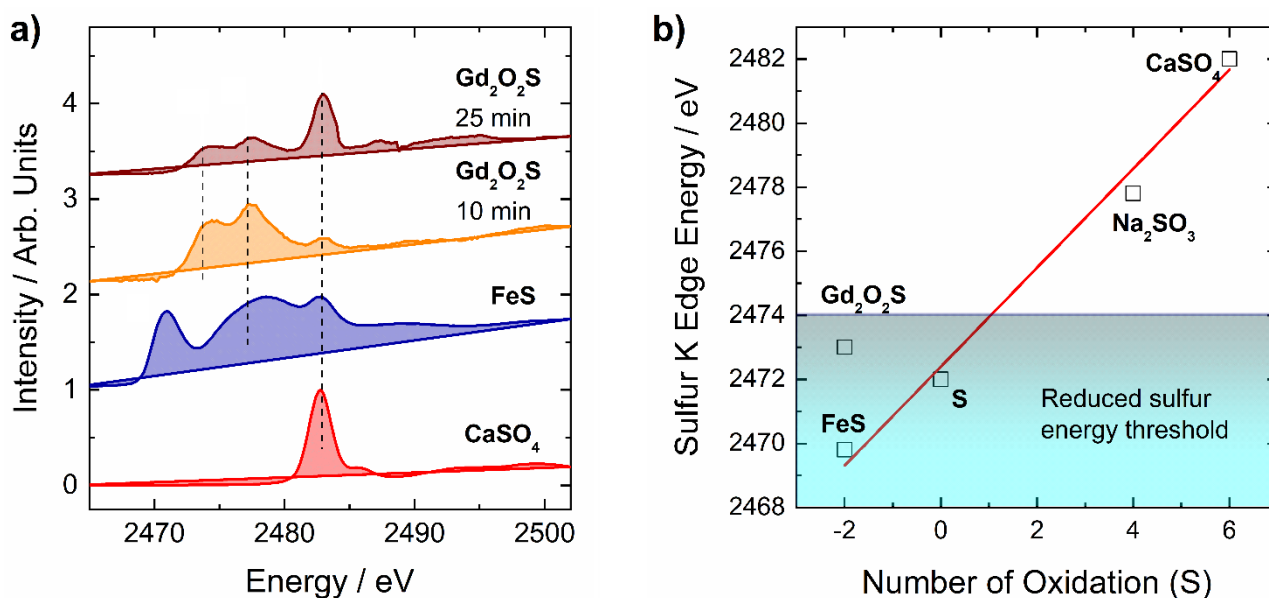


Figure 3.5 a) SR-XANES spectra at the sulfur K-edge of the Gd_2O_2S materials prepared with 10 and 25 min of MASS synthesis time; spectra of FeS and $CaSO_4$ standards were also plotted. **b)** Sulfur K-edge energy as a function of its oxidation state [142] – A1.

After defined the sulfide absorption edge energy, a SR-XANES study was performed on the Gd_2O_2S matrices obtained with different MASS synthesis times to investigate the changes in the sulfur oxidation state as a function of microwave irradiation exposure (Figure 3.6a). XANES spectra of the material obtained with 2 minutes of synthesis show a profile distinct from the precursors

(0 min), supporting the rapid conversion of $\text{Gd}_2\text{O}_3 + \text{S} + \text{Na}_2\text{CO}_3$ into $\text{Gd}_2\text{O}_2\text{S}$ found from the XRD data (Figure 3.2). In addition, the presence of the absorption band at 2482 eV indicates an oxidation process, which is probably associated with the formation of S–O bonds on the surface of the particles. Therefore, these results suggest that elemental sulfur S^0 is concomitantly reduced to S^{2-} and oxidized to $\text{SO}_2/\text{SO}_4^{2-}$ species by oxygen in the local atmosphere. The processes involving sulfur reduction were further discussed in section 3.1.3.

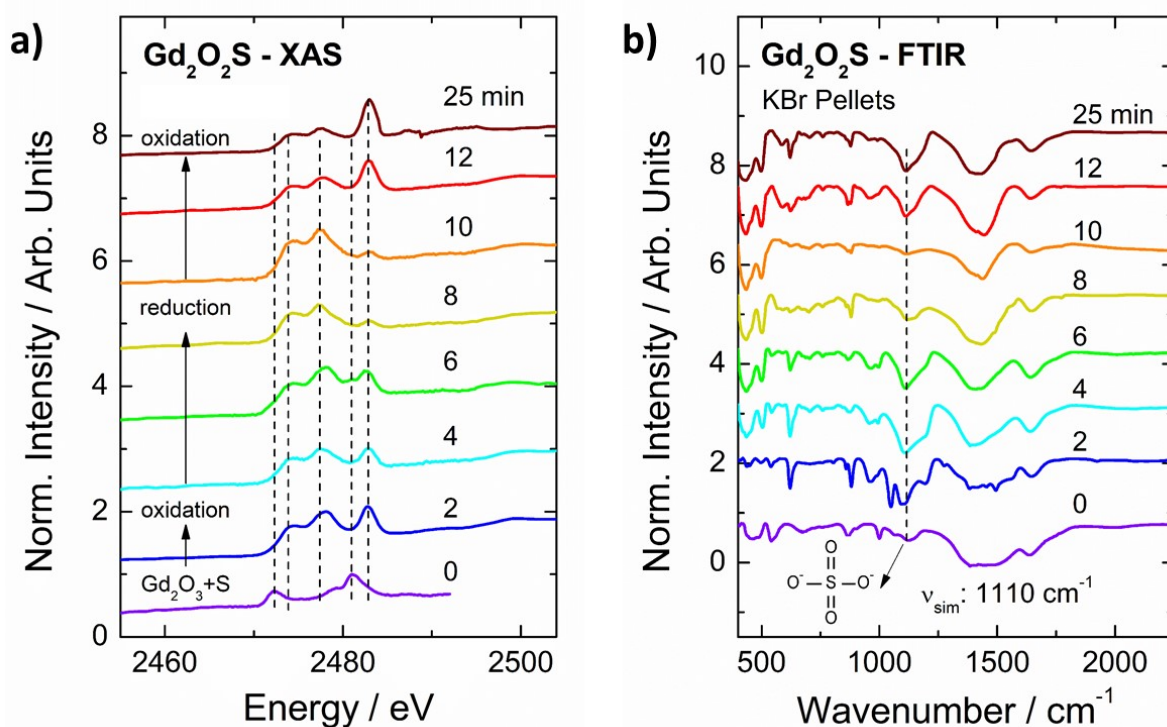


Figure 3.6 Undoped $\text{Gd}_2\text{O}_2\text{S}$ matrix obtained with increasing MASS synthesis time: **a)** Sulfur K-edge XANES spectra and **b)** FTIR spectra [142] – A1.

The absorption peak at 2482 eV decreases in intensity by rising reaction time from 2 to 10 minutes, with a minimum at 10 minutes (Figure 3.6a). On the other hand, at longer reaction times (12 and 25 minutes) this peak rises again, with maximum at 25 minutes. This increase in the oxidation character corroborates the hypothesis of SO_4^{2-} attached to the surface of the particles, as the $\text{Gd}_2\text{O}_2\text{S}$ oxysulfide crystal structure is not destroyed with longer MASS synthesis times according to DRX

data (Figure 3.2). FTIR analyses as a function of synthesis time (Figure 3.6b) confirms the XANES results, *i.e.*, the absorption band centered at 1100 cm^{-1} is assigned to the stretching of SO_4^{2-} groups [150]. From the FTIR spectra, one can notice that the SO_4^{2-} absorption band decreases in intensity up to 10 minutes, but increases again for longer reaction times.

The same XANES study as a function of MASS synthesis time was performed on the undoped $\text{Y}_2\text{O}_2\text{S}$ (Figure 3.7). For the first MASS heating treatment, XANES spectra (Figure 3.7a) reveal a sulfur reduction process from 0 up to 10 minutes of microwave irradiation. After this time, XANES profile steadies until the finishing time of 25 minutes. The same behavior was observed for the $\text{Y}_2\text{O}_2\text{S}$ XRD patterns (Figure 3.3a), demonstrating that the $\text{Y}_2\text{O}_3 \rightarrow \text{Y}_2\text{O}_2\text{S}$ conversion reaction stabilizes at 10–12 minutes during the first MASS synthesis. Moreover, the presence of the absorption band at 2482 eV indicates that the sulfur redox reactions also occurs for $\text{Y}_2\text{O}_2\text{S}$ matrices.

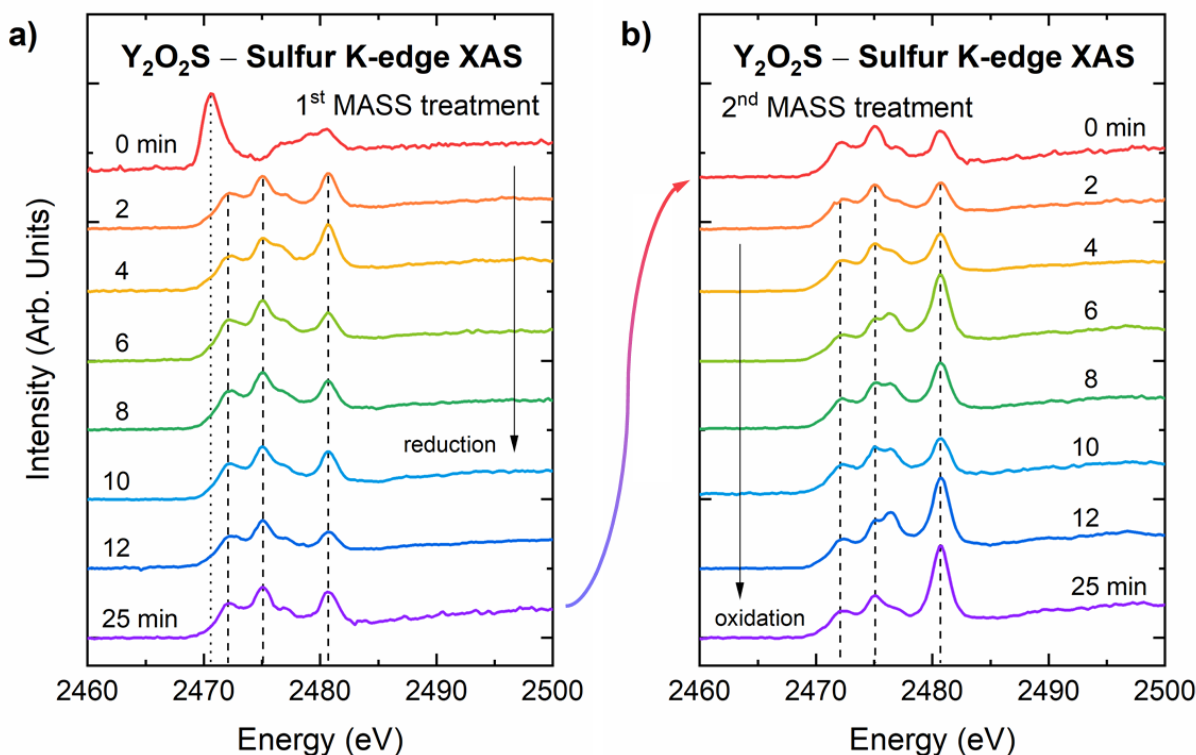


Figure 3.7 SR-XANES at the sulfur K-edge of undoped $\text{Y}_2\text{O}_2\text{S}$ matrix obtained with increasing MASS synthesis time: **a)** first, and **b)** second MASS treatment.

As described previously, the “Y₂O₂S 25 min” material obtained in the first MASS synthesis was used as a precursor in a second MASS heating treatment to pursuit a pure oxysulfide crystal phase. SR-XANES spectra as a function of microwave irradiation time for the second synthesis (Figure 3.7b) indicates a gradual sulfur change towards higher oxidation states by increasing synthesis time, similar behavior observed for the undoped Gd₂O₂S matrix (Figure 3.6a). Nevertheless, the Y₂O₂S crystal structure was also shown not to suffer any sign of deterioration (Figure 3.3b), confirming that the oxidized SO₄²⁻ species must be bond to the surface of the particles rather than incorporated into the materials’ crystal structure.

3.1.3 RE₂O₂S particle formation mechanism

Based on the XRD, SEM, FTIR, and SR-XANES results presented and discussed above, a particle formation mechanism was proposed for RE₂O₂S matrix obtained by the rapid microwave-assisted solid-state (MASS) method (Figure 3.8).

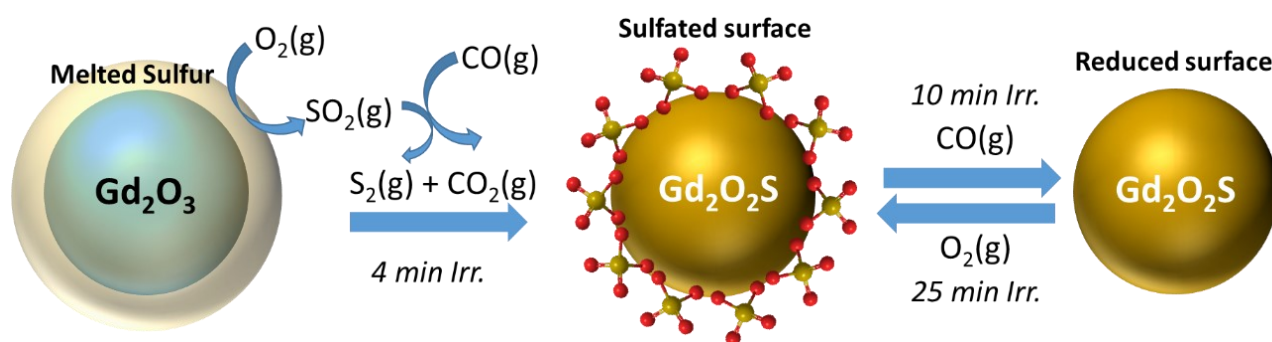


Figure 3.8 Schematic representation of rare earth oxysulfide (RE₂O₂S, RE³⁺: La, Gd, and Y) formation mechanism with the participation of gases assisting the redox process of sulfur. Reproduced from [142] – A1.

First, sulfur is molten within less than 30 seconds due to the quick rising in temperature under microwave irradiation, forming a liquid–solid interface over the RE₂O₃ + Na₂CO₃ mixture where

RE₂O₂S precipitation–dissolution processes will occur. Then, sulfur goes through redox reactions. The S(l)→SO₂(g) oxidation process can happen with the aid of oxygen in the local atmosphere, producing SO₂ molecules that might chemically bond to the oxide surface. On the other hand, sulfur reduction takes place with the aid of CO(g) generated by the activated carbon, reducing S–O species to S²⁻ and forming CO₂(g). Furthermore, the S + Na₂CO₃ reaction yields Na₂S_x, which acts as the flux responsible for the RE₂O₃→RE₂O₂S conversion [18]. All these reactions can occur at T < 500 °C, *i.e.*, less than 2 minutes of microwave heating (Figure 3.1). This explains the rapid RE₂O₂S formation within only 2 minutes, with the oxysulfide crystal phase being clearly major over the oxide at 4 minutes of synthesis (Figure 3.2 and 3.3a).

Finally, a continuous increase in microwave irradiation time (12–25 min) promotes oxidation of the particle surface, regenerating the sulfate–functionalized surfaces. This redox process is supported by the reversible RE₂O₂S↔RE₂O₂SO₄ conversion reaction described previously by Machida *et al.* [151], where oxysulfates were formed by heating the oxysulfides in the presence of oxygen. This particle formation mechanism corroborates the findings reported by Ding *et al.* [18], emphasizing the importance of the local atmosphere and the sodium fluxes. Besides, on Ding’s work, the oxysulfides were obtained by a conventional solid-state synthesis employing a 1 Gd₂O₃ : 1.5 Na-flux ratio, a considerably larger amount of flux compared to the oxysulfides synthesized in this work (1 RE₂O₃ : 0.25 Na₂CO₃).

Hence, the MASS method was proven to efficiently fabricate RE₂O₂S bulk matrices with high crystal purity within short processing times. Considering the two-step synthesis of 50 minutes, the MASS method offers a reduction of ≥ 85% in processing time and ≥ 95% in energy consumption when compared to conventional solid-state methods [17,19]. In this way, the optimized MASS synthesis parameters were employed to prepare rare earth oxysulfide materials with distinct optical phenomena – scintillation Gd₂O₂S:Tb, upconversion Gd₂O₂S:Er(Yb), and persistent luminescence RE₂O₂S:(Eu,Yb)Ti,Mg, which will be covered in the following sections.

3.2 Gd₂O₂S:Tb³⁺ scintillators

3.2.1 Materials' structure and morphology

One of the stages of the scintillation mechanism is the charge carrier migration, in which electrons and holes migrate through the crystal lattice before finding a recombination center to yield luminescence [40]. However, trapping levels can be induced in the forbidden energy gap due to point defects and flaws in the crystal structure, which can considerably delay the migration process and decrease scintillation performance. The presence of defects in a solid-state material is strongly dependent on the manufacturing process [6,40]. As discussed in section 3.1, the MASS method offers rapid heating rates, and thus the formed Gd₂O₂S crystal structure (Figure 3.2), as well as the luminescence properties of Gd₂O₂S-based materials, are intricately dependent on the synthesis time.

In this context, Gd₂O₂S:Tb³⁺ 2% scintillator materials were prepared by the microwave-assisted solid-state (MASS) synthesis employing two different synthesis times. First, the material labeled “Gd₂O₂S:Tb³⁺ - 10” was prepared by a single-step synthesis of 10 minutes, with microwave power output $P = 90\%$. Then, the “Gd₂O₂S:Tb³⁺ - 50” material was obtained by a two-step synthesis of 25 minutes each step ($P = 90\%$ at 10 min + $P = 80\%$ at 15 min), resulting in a total synthesis time of 50 minutes.

Figure 3.9a shows the synchrotron radiation X-ray diffraction (SR-XRD) patterns and Rietveld refinement results for the Gd₂O₂S:Tb³⁺ - 10 and Gd₂O₂S:Tb³⁺ - 50 materials. Gd₂O₂S trigonal crystal structure (PDF 26-1422, space group $P\bar{3}m1$) was successfully obtained for both materials. One can observe the heptacoordinated Gd³⁺ site in this crystal structure (Figure 3.9b), where the metal cation is bonded to four oxygen and three sulfur atoms in a C_{3v} symmetry site. Rietveld refinement results pointed a small amount of cubic-Gd₂O₃ impurity (PDF 43-1014, space group $Ia\bar{3}$) in the material prepared by a single-step synthesis [143] – A2. This impurity phase consists in only 4% in crystalline fraction of the sample, which is a promising result considering the

very short synthesis time (10 min). This result also agrees with the XRD data in Figure 3.2. On the other hand, the $\text{Gd}_2\text{O}_2\text{S:Tb}^{3+}$ - 50 material has a pure $\text{Gd}_2\text{O}_2\text{S}$ phase, demonstrating that the two-step synthesis procedure (25 min each step) is indeed optimal to yield pure materials.

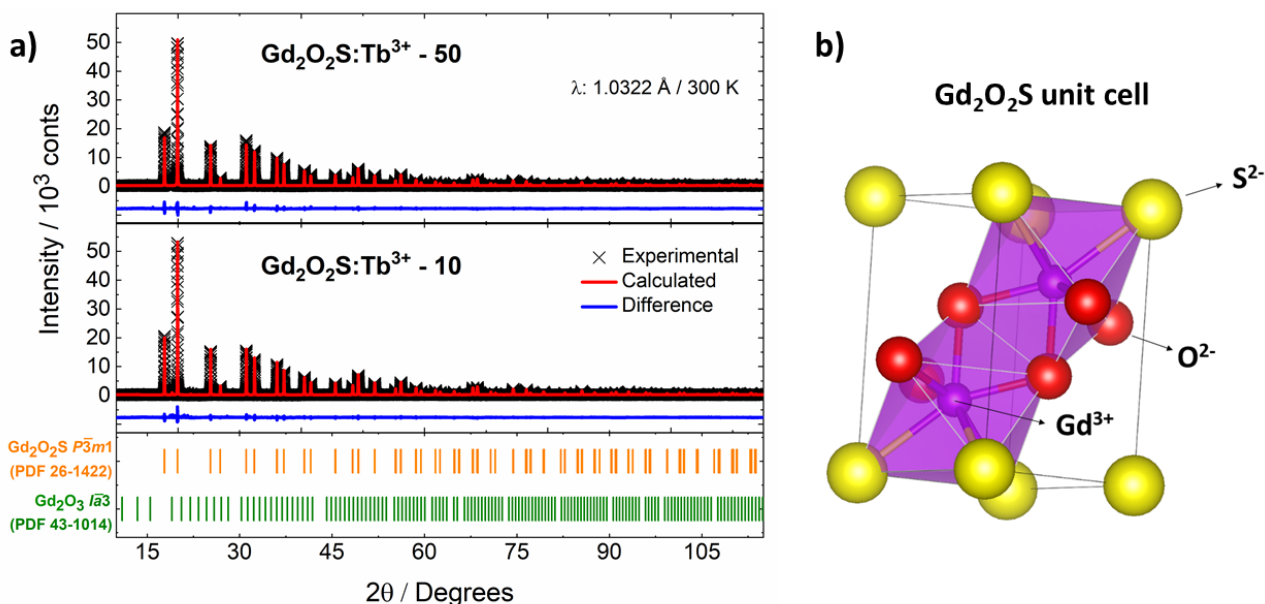


Figure 3.9 a) Synchrotron radiation X-ray diffraction (SR-XRD) patterns of the $\text{Gd}_2\text{O}_2\text{S:Tb}^{3+}$ - 10 and $\text{Gd}_2\text{O}_2\text{S:Tb}^{3+}$ - 50 materials, including Rietveld refinement for the $\text{Gd}_2\text{O}_2\text{S}$ and Gd_2O_3 structures. b) VESTA representation of $\text{Gd}_2\text{O}_2\text{S}$ unit cell, showing the metal site with C_{3v} symmetry [143] – A2.

SEM images of $\text{Gd}_2\text{O}_2\text{S:Tb}^{3+}$ - 10 and $\text{Gd}_2\text{O}_2\text{S:Tb}^{3+}$ - 50 materials show similar morphologies, both exhibiting spherical particles with high sintering degrees and uniform surface (Figure 3.10). However, particle size clearly augments by increasing synthesis time from 10 to 50 minutes. The $\text{Gd}_2\text{O}_2\text{S:Tb}^{3+}$ - 10 has particles in the nanoscale with a small size distribution, while the material prepared by the two-step synthesis shows a particle size ranging from 0.5 to 3 μm . These results are in accordance with SEM images for undoped $\text{Y}_2\text{O}_2\text{S}$ (Figure 3.4), which indicate that the particle formation and growth are ruled by an Ostwald ripening process [145]. Morphological differences between $\text{Y}_2\text{O}_2\text{S}$ and $\text{Gd}_2\text{O}_2\text{S:Tb}^{3+}$ might be related to thermodynamic and kinetic parameters on the $\text{RE}_2\text{O}_2\text{S}$ formation for the distinct RE [152] via microwave irradiation.

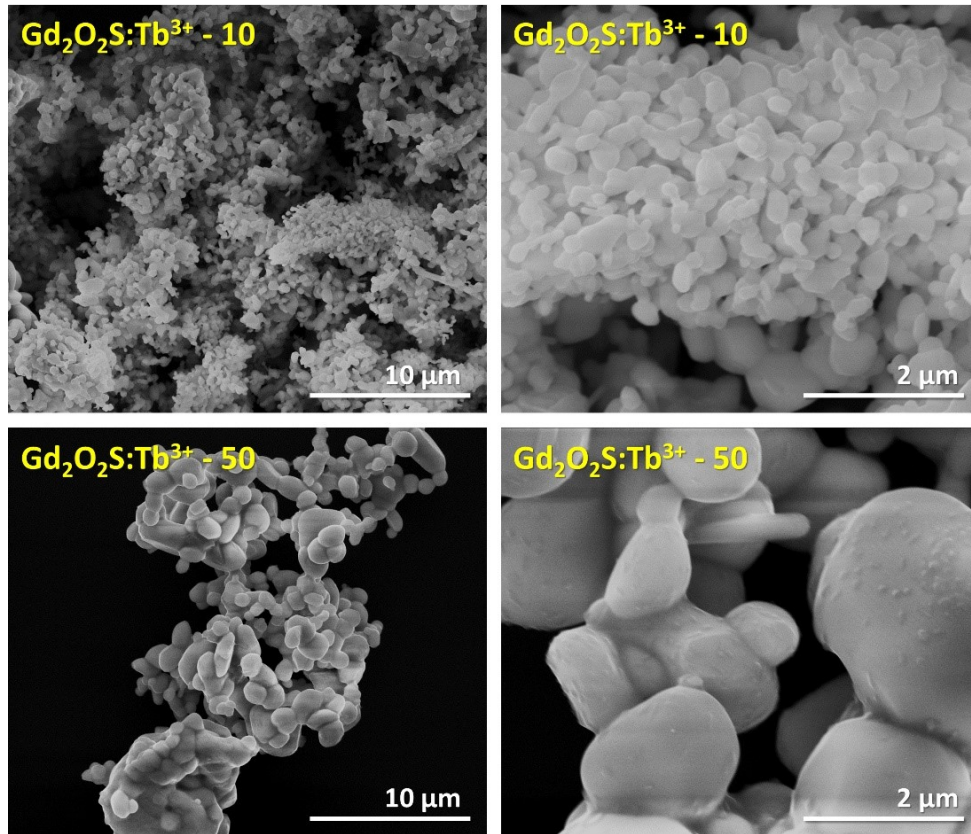


Figure 3.10 SEM images of $\text{Gd}_2\text{O}_2\text{S:Tb}^{3+} - 10$ (above) and $\text{Gd}_2\text{O}_2\text{S:Tb}^{3+} - 50$ (below) materials under magnifications of 10000x (left) and 50000x (right) [143] – A2.

3.2.2 Valence of terbium dopant

Terbium was added as Tb_4O_7 to act as a recombination center in the gadolinium oxysulfides. However, Tb_4O_7 is an oxide with mixed Tb valences, $(\text{Tb}^{3+})_2(\text{Tb}^{4+})_2\text{O}_7$, but only Tb^{3+} is of interest as a luminescent ion due to its characteristic electronic structure and emission in the visible range, with maximum intensity at around 540 nm. Therefore, to probe terbium valence in Tb-doped $\text{Gd}_2\text{O}_2\text{S}$ materials prepared by the MASS method, X-ray Absorption Near Edge Structure (XANES) analyses were performed in the Tb-L_{III} edge energy (Figure 3.11a). Tb_4O_7 and $\text{Tb}(\text{acac})_3$ (Tb^{3+} complex) were also measured as Tb-XANES references. First analyzing the reference compounds, $\text{Tb}(\text{acac})_3$ exhibits a single absorption edge located at 7524 eV, while Tb_4O_7 exhibits two absorption bands at 7524 and 7533 eV. It is safe to affirm that these two absorption edges at 7524 and 7533 eV are respectively assigned to the 3+ and 4+ valence states of terbium [114].

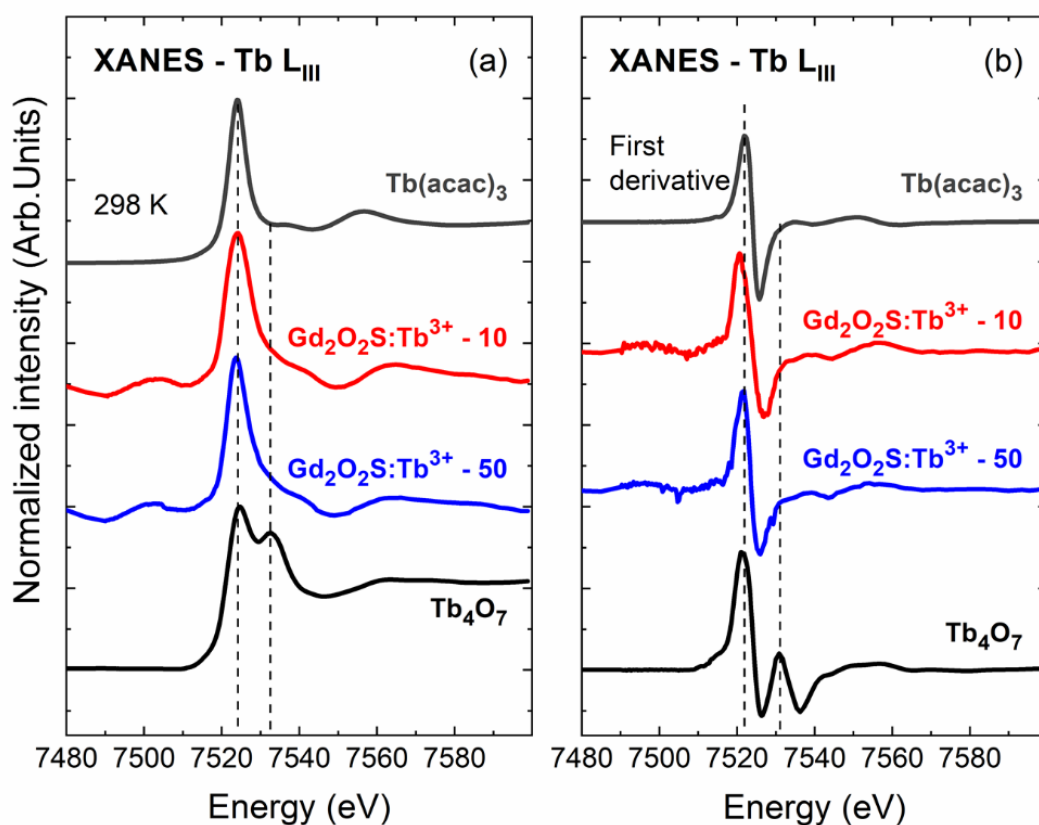


Figure 3.11 a) Tb L_{III} edge XANES spectra of Gd₂O₂S:Tb³⁺ - 10 and Gd₂O₂S:Tb³⁺ - 50 materials, as well as reference compounds Tb₄O₇ and Tb(acac)₃; **b)** The first derivative of Tb L_{III} XANES spectra [143] – A2.

Tb-L_{III} XANES spectra of both Gd₂O₂S:Tb³⁺ materials exhibited an intense absorption peak at 7524 eV with a weak shoulder at 7533 eV (Figure 3.11a). The first derivative of Tb-L_{III} XANES spectra was plotted (Figure 3.11b) and one can conclude that the shoulder observed at 7533 eV is actually attributed to Tb³⁺ post-edge features instead of a Tb⁴⁺ absorption edge. This confirms the quick generation of the reducing CO(g) atmosphere by the activated carbon under microwave heating, which leads to an efficient reduction of Tb₄O₇ precursor to Tb³⁺. The Tb⁴⁺ smaller ionic radius (0.76 Å), together with the charge mismatch and the reducing CO(g) atmosphere, make Tb⁴⁺ unstable in the RE³⁺ C_{3v} sites of rare earth oxysulfides. Tb-L_{III} XANES results are also in accordance with the particle formation mechanism proposed in section 3.1.3 ([142] – A1).

3.2.3 Photoluminescence spectroscopy: excitation using UV, VUV, and X-rays

Various photoluminescence spectroscopy (PL) techniques were employed in the characterization of $\text{Gd}_2\text{O}_2\text{S}:\text{Tb}^{3+}$ materials to investigate the Tb^{3+} emission under a broad range of excitation wavelengths, *e.g.*, UV-vis PL, synchrotron radiation vacuum ultraviolet (SR-VUV) PL, and SR X-ray excited optical luminescence (SR-XEOL). UV-vis excitation and emission spectra of $\text{Gd}_2\text{O}_2\text{S}:\text{Tb}^{3+} - 10$ and $\text{Gd}_2\text{O}_2\text{S}:\text{Tb}^{3+} - 50$ materials were presented in Figure 3.12. The excitation spectra (blue line) exhibit a broad absorption band ranging from 250 to 330 nm, which is an overlap of the interconfigurational $\text{Tb}^{3+} 4f^8 \rightarrow 4f^7 5d^1$ transitions with the host lattice absorption, around 4.6 eV (~ 270 nm) for $\text{Gd}_2\text{O}_2\text{S}$ [14]. In addition, 4f-4f narrow bands can also be observed, assigned to the $\text{Gd}^{3+} {}^8\text{S}_{7/2} \rightarrow {}^6\text{P}_{7/2}$ (~ 313 nm) and $\text{Tb}^{3+} {}^7\text{F}_6 \rightarrow {}^5(\text{L},\text{G})_J$ (350–380 nm) transitions. The emission spectra (green line) show narrow emission bands in the 410–630 nm range, attributed to the transitions from ${}^5\text{D}_{4,3}$ excited states to the ${}^7\text{F}_{6-3}$ ground levels of Tb^{3+} . The most intense band is assigned to the $\text{Tb}^{3+} {}^5\text{D}_4 \rightarrow {}^7\text{F}_5$ transition, which is responsible for the characteristic green emission color (~ 546 nm).

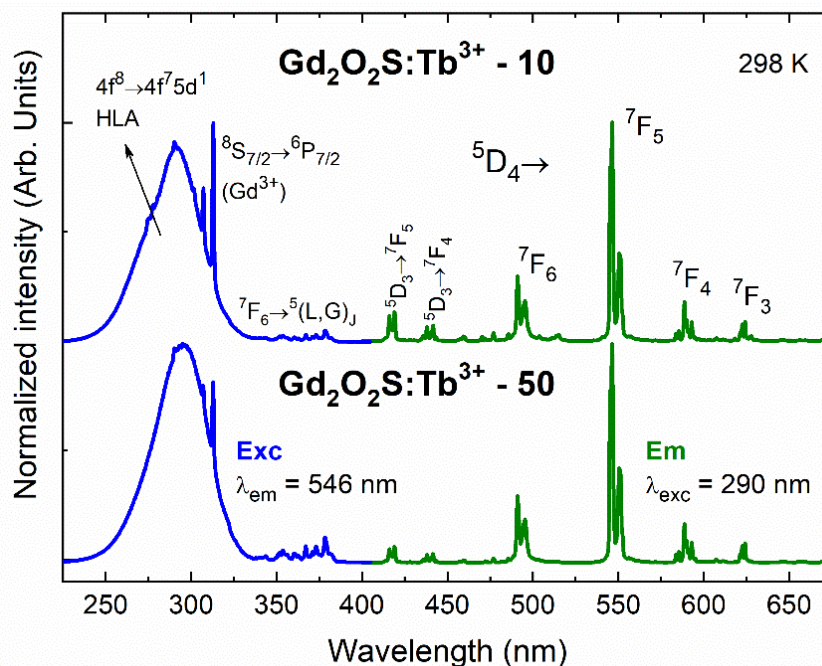


Figure 3.12 Photoluminescence excitation (blue line) and emission (green line) spectra of $\text{Gd}_2\text{O}_2\text{S}:\text{Tb}^{3+} - 10$ and $\text{Gd}_2\text{O}_2\text{S}:\text{Tb}^{3+} - 50$ materials (HLA: host lattice absorption) [143] – A2.

VUV 3D spectra of $\text{Gd}_2\text{O}_2\text{S:Tb}^{3+}$ - 10 and $\text{Gd}_2\text{O}_2\text{S:Tb}^{3+}$ - 50 materials were recorded under excitation in the 4.5–8.0 eV range and registering the emission from 300 to 800 nm (Figure 3.13). The band gap absorption energy is observed at 4.6 eV for both materials, in agreement with the band gap values found for this material prepared by conventional solid-state methods [14]. Distinct spectral features can be noticed when comparing the VUV excitation spectra between the two synthesized oxysulfides. For the $\text{Gd}_2\text{O}_2\text{S:Tb}^{3+}$ - 50 (Figure 3.13b), Tb^{3+} emission intensity is higher when exciting at the band gap absorption energy, diminishing by gradually increasing the excitation energy. This behavior is expected since Tb^{3+} ion is better sensitized in $\text{Gd}_2\text{O}_2\text{S}$ host when excited at the energies close to $\text{Tb}^{3+} 4f^8 \rightarrow 4f^7 5d^1$ transitions (4.3) and the host absorption (4.6 eV). However, $\text{Gd}_2\text{O}_2\text{S:Tb}^{3+}$ - 10 (Figure 3.13a) exhibits higher emission intensity when excited at 5.3 eV. This luminescence feature might be related to the structural differences between the materials, *i.e.*, the c- Gd_2O_3 impurity, as revealed by SR-XRD data (Figure 3.9a) and Rietveld refinement results [143] – A2.

It is also observed that the material prepared with 10 min of MASS synthesis exhibits Eu^{3+} 4f emission bands, *e.g.*, $^5\text{D}_0 \rightarrow ^7\text{F}_{2,4}$ at 620 and 705 nm, under VUV excitation (3.13a). It is likely to find Eu^{3+} impurity in Gd_2O_3 precursors since Gd^{3+} and Eu^{3+} ions are difficult to separate [2,153]. The occurrence of Eu^{3+} emission only in the $\text{Gd}_2\text{O}_2\text{S:Tb}^{3+}$ - 10 might be attributed to either the presence of the Gd_2O_3 impurity phase or to the presence of structural defects caused by the shorter microwave synthesis time. $\text{Gd}_2\text{O}_3:\text{Eu}^{3+}$ is a well-known red emitter [154]. Therefore, Eu^{3+} emission can be effectively triggered in the $\text{Gd}_2\text{O}_2\text{S:Tb}^{3+}$ - 10 material even at minimal Eu^{3+} concentrations (nmol/L). Besides, small Gd_2O_3 impurity particles on this material can affect the local structure surrounding the emitting ions, leading to higher Eu^{3+} emission intensity even on the $\text{Gd}_2\text{O}_2\text{S}$ phase [155]. In addition, Pires *et al.* [156] reported the luminescent properties of Eu^{3+} -doped $\text{Gd}_2\text{O}_2\text{S}$ materials, demonstrating the formation of oxide and oxysulfate impurities in oxysulfide materials employing Eu^{3+} as a spectroscopic probe. On the other hand, the $\text{Gd}_2\text{O}_2\text{S:Tb}^{3+}$ - 50 material exhibits no Eu^{3+} emission (3.13b) due to its higher phase purity, which leads to a better sensitization of Tb^{3+} ions.

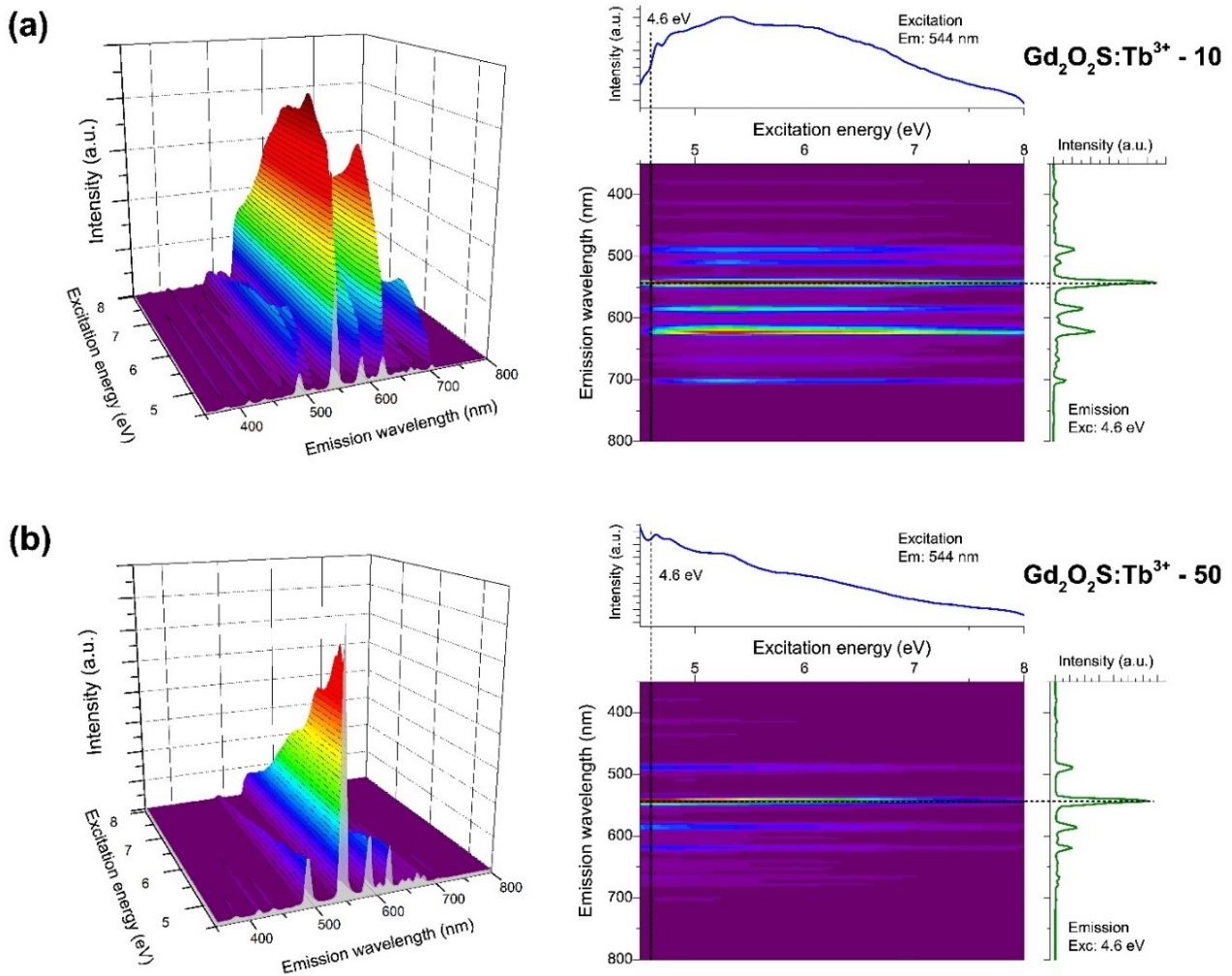


Figure 3.13 VUV 3D maps, followed by the excitation (monitored at 544 nm) and emission (monitored under excitation of 4.6 eV or 270 nm) profiles: **a)** $\text{Gd}_2\text{O}_2\text{S}:\text{Tb}^{3+} - 10$ and **b)** $\text{Gd}_2\text{O}_2\text{S}:\text{Tb}^{3+} - 50$ materials [143] – A2.

Finally, high luminescence intensities were also observed when irradiating the $\text{Gd}_2\text{O}_2\text{S}:\text{Tb}^{3+}$ materials with SR X-rays (7000, 7500, and 8000 keV). The X-ray excited optical luminescence (XEOL) spectra (Figure 3.14) show similar profile as the photoluminescence emission spectra (Figure 3.10) but with lower spectral resolution due to the available experimental setup, causing the broadening of narrow $\text{Tb}^{3+} \ ^5\text{D}_4 \rightarrow \ ^7\text{F}_{6-0}$ emission bands. No spectral changes can be observed when varying the SR excitation energy from 7.0 to 8.0 keV. However, when comparing the two distinct materials, the $\text{Gd}_2\text{O}_2\text{S}:\text{Tb}^{3+} - 10$ exhibits the Eu^{3+} emission from the $\ ^5\text{D}_0 \rightarrow \ ^7\text{F}_2$ hypersensitive transition overlapped with the $\text{Tb}^{3+} \ ^5\text{D}_4 \rightarrow \ ^7\text{F}_3$ transition at ~ 620 nm (Figure 3.14a). The $\text{Eu}^{3+} \ ^5\text{D}_0 \rightarrow \ ^7\text{F}_4$

transition can also be observed at ~ 708 nm. The presence of Eu^{3+} emission bands is attributed to the structural defects of the $\text{Gd}_2\text{O}_2\text{S:Tb}^{3+} - 10$, *i.e.*, c- Gd_2O_3 impurity phase selectively sensitizing Eu^{3+} ions, in the same way it was observed for the SR-VUV spectroscopy results. On the other hand, the $\text{Gd}_2\text{O}_2\text{S:Tb}^{3+} - 50$ material does not exhibit any Eu^{3+} -related emission bands, similarly as observed on the SR-VUV (Figure 3.13b) spectra.

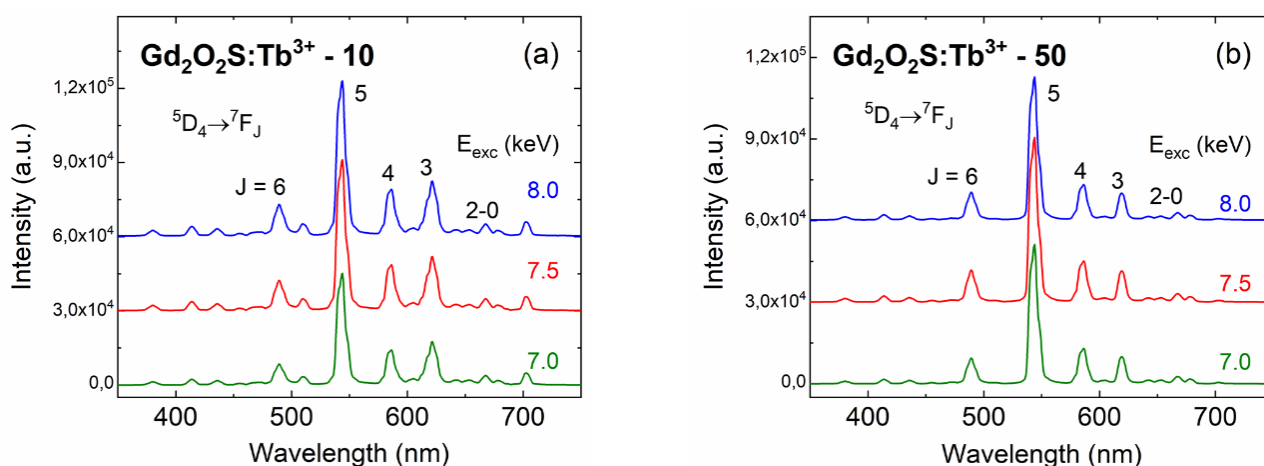


Figure 3.14 X-ray excited optical luminescence (XEOL) spectra of **a)** $\text{Gd}_2\text{O}_2\text{S:Tb}^{3+} - 10$ and **b)** $\text{Gd}_2\text{O}_2\text{S:Tb}^{3+} - 50$ materials. Excitation energies = 7000, 7500, and 8000 eV [143] – A2.

$\text{Gd}_2\text{O}_2\text{S:Tb}^{3+}$ x,y coordinates in the CIE (Commission Internationale l'Éclairage) chromaticity diagram (Figure 3.15) exhibit the overall emission colors as a function of the excitation energy. Points A and B represent the similar emission colors of $\text{Gd}_2\text{O}_2\text{S:Tb}^{3+} - 50$ and $\text{Gd}_2\text{O}_2\text{S:Tb}^{3+} - 10$ materials, respectively, under UV excitation (290 nm). On the other hand, major color changes are observed in x,y coordinates when the materials are excited with X-rays (7000 eV). These photonic features can be attributed to the variation in the relative intensities of $\text{Tb}^{3+} \ ^5\text{D}_4 \rightarrow \ ^7\text{F}_J$ emission bands ($J = 6-0$) and the band broadening when exciting with X-rays (Figure 3.14). Moreover, for the $\text{Gd}_2\text{O}_2\text{S:Tb}^{3+} - 10$ material, Eu^{3+} emission bands led to the higher contribution of red color (Figure 3.15, point D).

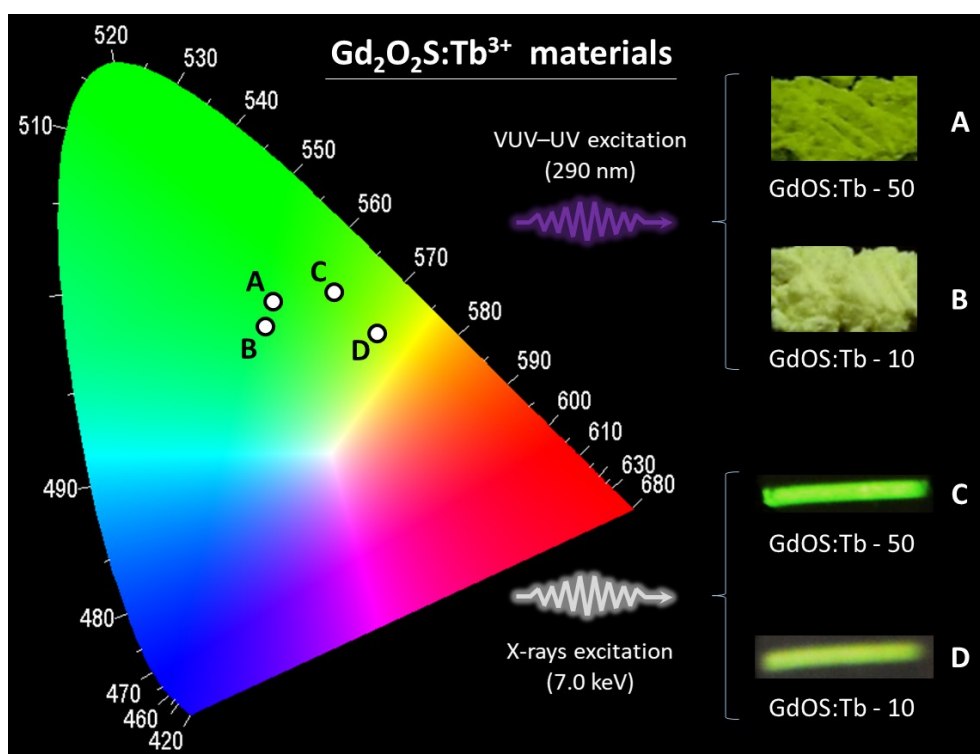


Figure 3.15 CIE x,y diagram showing the $\text{Gd}_2\text{O}_2\text{S:Tb}^{3+} - 10$ and $\text{Gd}_2\text{O}_2\text{S:Tb}^{3+} - 50$ materials when excited by UV light (290 nm) and by X-rays (7000 eV) [143] – A2.

In general, both the $\text{Gd}_2\text{O}_2\text{S:Tb}^{3+} - 10$ and the $\text{Gd}_2\text{O}_2\text{S:Tb}^{3+} - 50$ materials exhibited high luminescence intensities over a large excitation spectral range, varying from UV (~ 4.0 eV) to SR X-rays (8000 eV). Nevertheless, the $\text{Gd}_2\text{O}_2\text{S:Tb}^{3+} - 50$ displays the best scintillation performance owing to its higher crystal purity and luminescence intensity. In this sense, high quality $\text{Gd}_2\text{O}_2\text{S:Tb}^{3+}$ scintillator materials were rapidly obtained by MASS method, opening paths to versatile technological applications such as X-ray bioimaging, which requires low X-ray exposure doses.

3.3 Gd₂O₂S:Er³⁺ and Gd₂O₂S:Er³⁺,Yb³⁺ upconversion (UC) materials

3.3.1 Crystal structure of Gd₂O₂S-based UC materials: the influence of the precursor

Similarly to scintillators, the quantum efficiency of upconversion (UC) materials can drop radically due to the presence of defects in the crystal lattice and/or on the particles surface [7,58]. In the previous section (3.2), the MASS method was proven to be a suitable synthesis methodology to fabricate Gd₂O₂S:Tb³⁺ bulk scintillator materials. Furthermore, luminescence intensity substantially increased when the material was prepared by a two-step microwave-assisted synthesis, 25 minutes each step (P = 90% at 10 min + P = 80% at 15 min). In this section, the same microwave program was employed to synthesize Gd₂O₂S:Er³⁺ and Gd₂O₂S:Er³⁺,Yb³⁺ UC materials. Seeking highly luminescent UC systems, several Er³⁺ and Yb³⁺ dopant concentrations were tested to find which [Er³⁺],[Yb³⁺] combinations yield the highest UC emission intensity.

XRD patterns for Gd₂O₂S:Er³⁺ and Gd₂O₂S:Er³⁺,Yb³⁺ materials synthesized by the MASS method employing Ln₂O₃ (Ln³⁺: Gd, Er, and Yb) as precursors (Figure 3.16a) show the Gd₂O₂S crystalline structure (PDF 26-1422) formation for all materials. No impurity phases could be detected for materials singly doped with Er³⁺ regardless of its concentration (5 and 10%). However, all Gd₂O₂S materials co-doped with Yb³⁺ (5 and 10%) exhibited a small intensity peak at 29.1 °, which is related to the cubic Yb₂O₃ phase (PDF 41-1106). The poor incorporation of Yb³⁺ co-dopant in the Gd₂O₂S lattice is because Yb³⁺ is a harder acid ion compared to Gd³⁺ according to Pearson's theory [16], which was discussed previously. In summary, decomposing the Yb₂O₃ (and Er₂O₃) oxides and incorporating Yb³⁺ (and Er³⁺) cations into the oxysulfide lattice are thermodynamically non-favorable [152]. The 29.1 ° diffraction peak slightly shifts to higher 2θ angles by increasing Er³⁺ and Yb³⁺ concentrations. This might be due to alterations in the Gd₂O₂S lattice parameters by a further inclusion of the dopants. X-ray diffraction (XRD) and X-ray absorption (XANES/EXAFS) experiments using synchrotron radiation are needed to confirm these results.

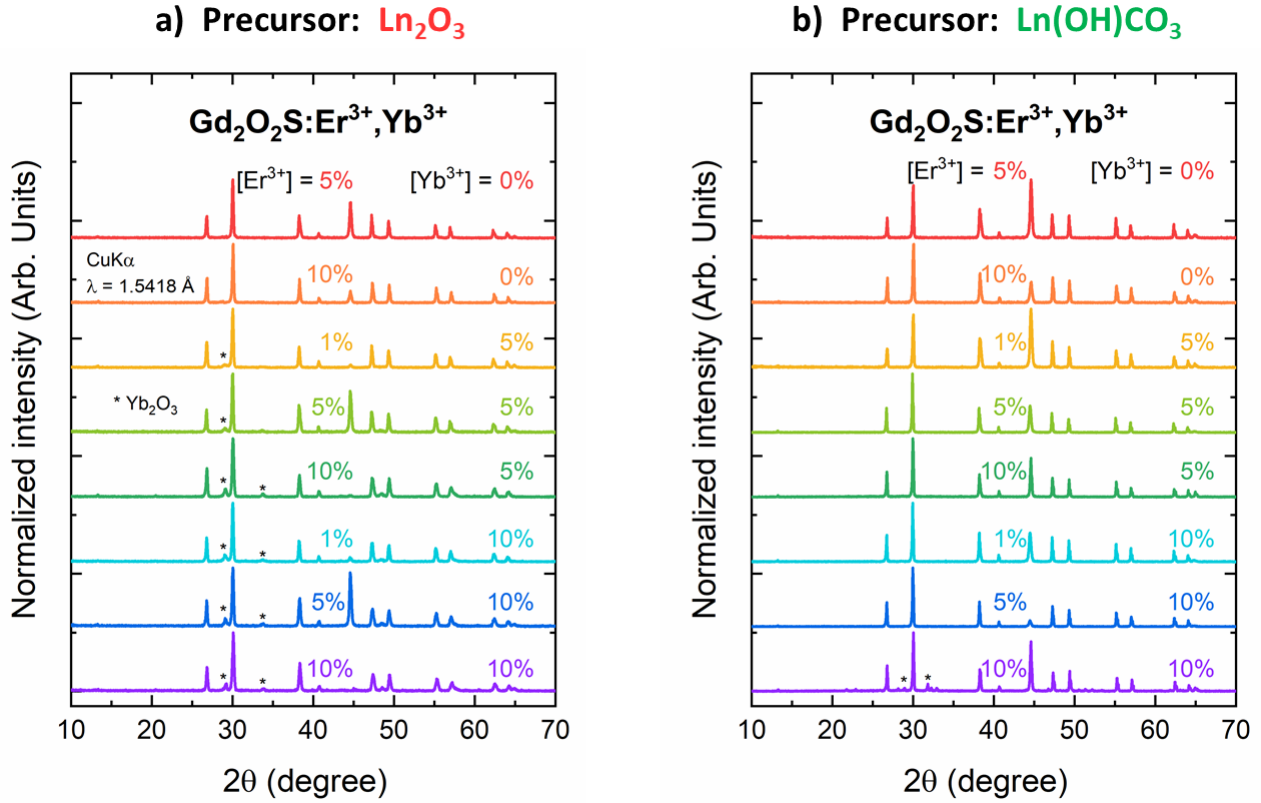


Figure 3.16 XRD patterns of the $\text{Gd}_2\text{O}_2\text{S}:\text{Er}^{3+}$ and $\text{Gd}_2\text{O}_2\text{S}:\text{Er}^{3+},\text{Yb}^{3+}$ upconversion (UC) materials obtained by the MASS method, employing **a)** lanthanide oxides Ln_2O_3 and **b)** hydroxycarbonates $\text{Ln}(\text{OH})\text{CO}_3$ as precursors (Ln^{3+} : Gd, Er, and Yb). Er^{3+} and Yb^{3+} doping percentages were displayed.

Although the obtained $\text{Gd}_2\text{O}_2\text{S}:\text{Er}^{3+}$ and $\text{Gd}_2\text{O}_2\text{S}:\text{Er}^{3+},\text{Yb}^{3+}$ materials show high crystal purity concerning the oxysulfide crystal phase (Figure 3.16a), the detected impurities can significantly quench the UC emission. Therefore, instead of using oxides, the lanthanide hydroxycarbonates $\text{Ln}(\text{OH})\text{CO}_3$ (Ln^{3+} : Gd, Er, and Yb) were used as precursors to the MASS synthesis of $\text{Gd}_2\text{O}_2\text{S}:\text{Er}^{3+}$ and $\text{Gd}_2\text{O}_2\text{S}:\text{Er}^{3+},\text{Yb}^{3+}$, employing the same previous $\text{Er}^{3+},\text{Yb}^{3+}$ concentrations. XRD patterns (Figure 3.16b) now reveal pure $\text{Gd}_2\text{O}_2\text{S}$ crystal phase for all materials regardless of the Er^{3+} and Yb^{3+} dopant concentration. The only exception was the $\text{Gd}_2\text{O}_2\text{S}:\text{Er}^{3+}_{(10\%)},\text{Yb}^{3+}_{(10\%)}$ material, however, one should note that the low intensity diffraction peaks at $31.8\text{--}32.8^\circ$ do not correspond to Er or Yb impurities. This impurity fraction may be related to Al-based compounds, *e.g.*, Al_2O_3 (PDF 35-121) and $\text{GdAl}_{11}\text{O}_{18}$ (PDF 38-1059), originated from the alumina crucible during the synthesis. Nevertheless,

given the ease and reproducibility of the MASS method, it is possible to repeat and improve the synthesis of this material in order to eliminate the observed impurities.

3.3.2 Photoluminescence spectroscopy: UC emission

Under a 980 nm continuous-wave laser excitation (500 mW), all $\text{Gd}_2\text{O}_2\text{S:Er}^{3+}$ and $\text{Gd}_2\text{O}_2\text{S:Er}^{3+},\text{Yb}^{3+}$ materials exhibited strong UC luminescence. A similar emission spectral profile can be observed between the materials prepared using the different precursors – Ln_2O_3 (Figure 3.17a) and $\text{Ln}(\text{OH})\text{CO}_3$ (Figure 3.17b). The overall greenish emission color is attributed to the ${}^2\text{H}_{11/2} \rightarrow {}^4\text{I}_{15/2}$ (523, 528, and 533 nm) and ${}^4\text{S}_{3/2} \rightarrow {}^4\text{I}_{15/2}$ (548 and 554 nm) transitions in the green region, together with the ${}^4\text{F}_{9/2} \rightarrow {}^4\text{I}_{15/2}$ (max. 670 nm) transition in the red region of the visible spectrum (Figure 3.17c).

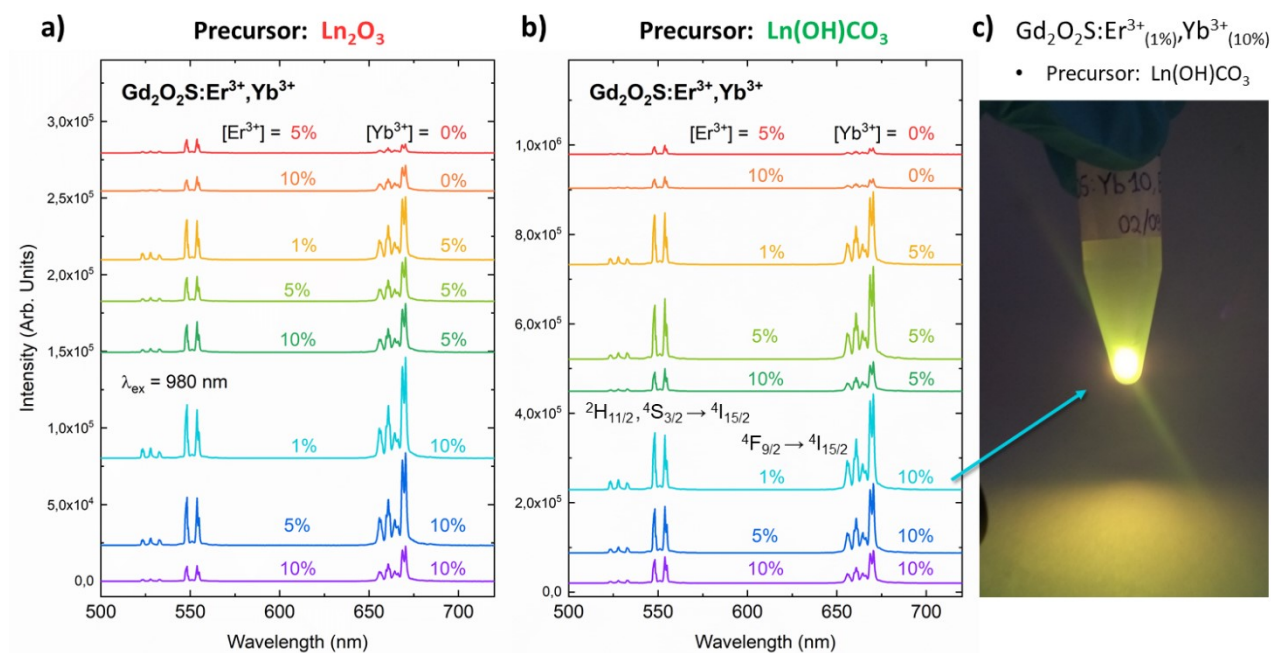


Figure 3.17 Upconversion (UC) emission spectra of $\text{Gd}_2\text{O}_2\text{S:Er}^{3+}$ and $\text{Gd}_2\text{O}_2\text{S:Er}^{3+},\text{Yb}^{3+}$ prepared by the MASS method, using **a)** Ln_2O_3 and **b)** $\text{Ln}(\text{OH})\text{CO}_3$ as precursors (Ln^{3+} : Gd, Er, and Yb); **c)** UC emission of $\text{Gd}_2\text{O}_2\text{S:Er}^{3+}_{(1\%)},\text{Yb}^{3+}_{(10\%)}$ – precursor $\text{Ln}(\text{OH})\text{CO}_3$ – under 980 nm laser excitation.

The experimental setup was fixed onto an optical table to measure accurate UC emission intensities, allowing a direct intensity comparison between different samples (Figure 3.17). Among singly doped oxysulfides, the higher Er^{3+} concentration (10%) yields higher emission intensity than the lower concentration (5%). Moreover, co-doping $\text{Gd}_2\text{O}_2\text{S}:\text{Er}^{3+}$ materials with Yb^{3+} significantly increase the UC intensity, indicating an efficient energy transfer from Yb^{3+} sensitizing Er^{3+} ions. By increasing Er^{3+} concentration from 1 to 5 and 10% in co-doped $\text{Gd}_2\text{O}_2\text{S}:\text{Er}^{3+},\text{Yb}^{3+}$ materials, one could expect an increase in luminescent intensity since UC phenomenon requires high dopant concentrations to guarantee an efficient energy transfer from sensitizer to acceptor ions [157]. However, the opposite optical behavior was observed in Figure 3.17a and 3.17b. This can be explained due to the complex energy level structure of Er^{3+} ions (Figure 1.2), which favors cross-relaxation processes in these conditions, leading to non-radiative losses of the excitation energy. Er^{3+} green emitting $^2\text{H}_{11/2}$ and $^4\text{S}_{3/2}$ levels are the most affected by concentration quenching, transferring energy to the red emitting $^4\text{F}_{9/2}$ level. In this way, the UC emission color can be modulated in $\text{Gd}_2\text{O}_2\text{S}:\text{Er}^{3+},\text{Yb}^{3+}$ materials by adjusting the concentration of Er^{3+} and Yb^{3+} ions.

UC luminescence quenching is also a function of the sample crystallinity and the number of defects (quenching centers) present. Different UC efficiencies are therefore expected in materials with the same $\text{Er}^{3+},\text{Yb}^{3+}$ dopant concentration, but obtained by distinct routes. Figure 3.18a show the UC emission spectra of the $\text{Gd}_2\text{O}_2\text{S}:\text{Er}^{3+}_{(5\%)},\text{Yb}^{3+}_{(5\%)}$ materials synthesized using Ln_2O_3 and $\text{Ln}(\text{OH})\text{CO}_3$ as precursors. The UC emission spectrum of a commercial sample was recorded under the same conditions and displayed for comparison. A substantial increase in UC intensity was confirmed when using $\text{Ln}(\text{OH})\text{CO}_3$ as precursors, *i.e.*, 8-fold for the $^4\text{S}_{3/2}\rightarrow^4\text{I}_{15/2}$ transition compared to the material obtained using Ln_2O_3 as precursors. The same result was observed for all materials, *i.e.*, UC emission intensity increased when using $\text{Ln}(\text{OH})\text{CO}_3$ as precursors in the MASS synthesis instead of Ln_2O_3 , for a given $\text{Er}^{3+},\text{Yb}^{3+}$ concentration. For example, a 4-fold intensity increase ($^4\text{S}_{3/2}\rightarrow^4\text{I}_{15/2}$) was found the $\text{Gd}_2\text{O}_2\text{S}:\text{Er}^{3+}_{(1\%)},\text{Yb}^{3+}_{(10\%)}$ (Figure 3.18b), which exhibited the highest

UC intensity among MASS materials This spectroscopical feature is attributed to the higher crystal purity of the Gd_2O_2S host achieved when employing easier decomposable $Ln(OH)CO_3$ precursors.

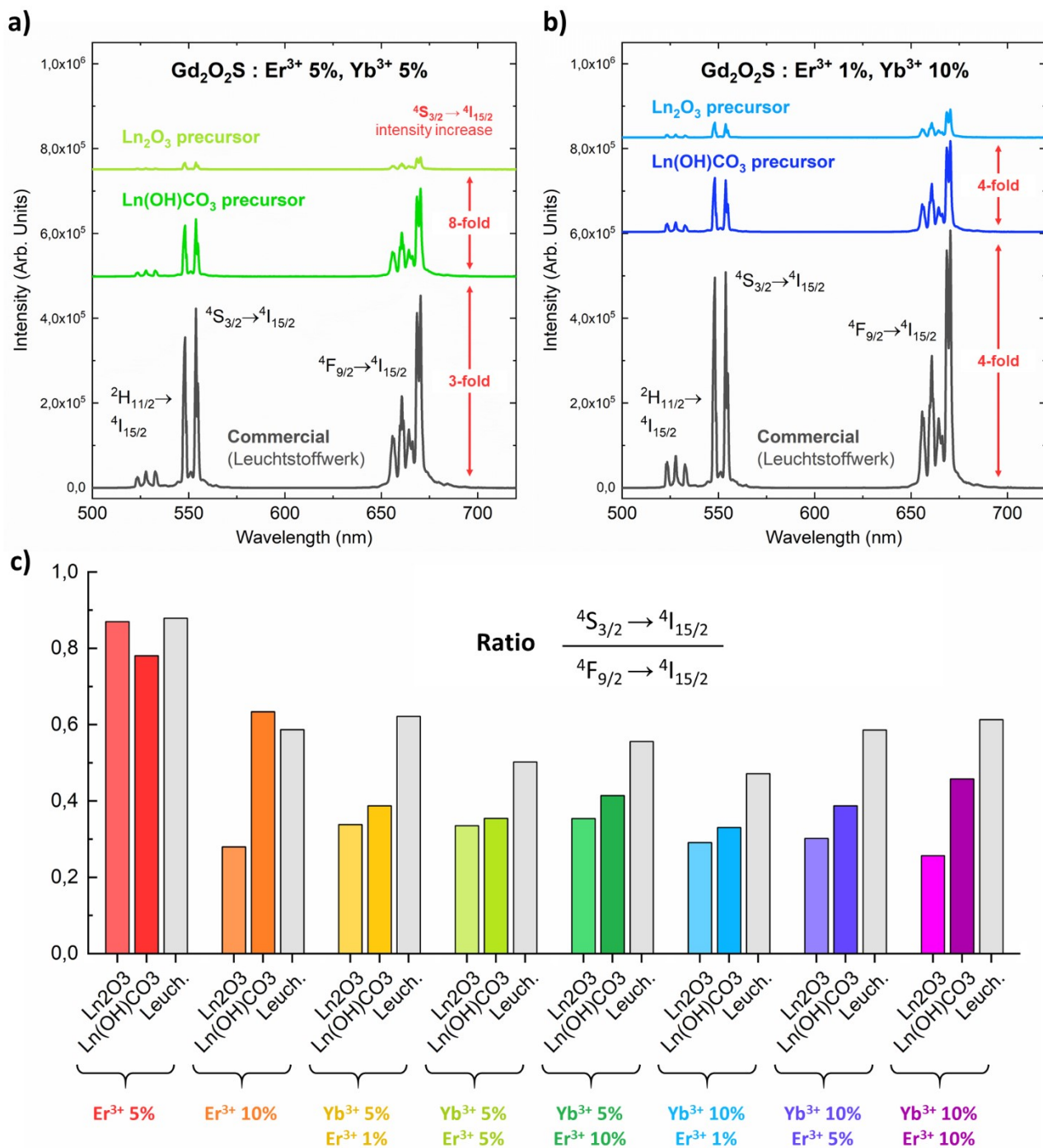


Figure 3.18 Comparison of upconversion (UC) intensities among the most efficient MASS-obtained materials and commercial samples: **a)** $Gd_2O_2S:Er^{3+}(5\%),Yb^{3+}(5\%)$, and **b)** $Gd_2O_2S:Er^{3+}(1\%),Yb^{3+}(10\%)$. **c)** Electronic transition ratio $(^4S_{3/2} \rightarrow ^4I_{15/2}) / (^4F_{9/2} \rightarrow ^4I_{15/2})$ calculated for all $Gd_2O_2S:Er^{3+}(Yb^{3+})$ UC materials as a function of Er^{3+}, Yb^{3+} concentration (including commercial samples from Leuchtstoffwerk).

Figure 3.18c displays the $(^4S_{3/2} \rightarrow ^4I_{15/2}) / (^4F_{9/2} \rightarrow ^4I_{15/2})$ transition ratio (here simply called $^4S_{3/2}/^4F_{9/2}$ ratio) as a quenching parameter for the main green-emitting $^4S_{3/2}$ level as a function of the MASS synthesis precursor and the Er^{3+}, Yb^{3+} concentrations (ratio calculated from the integrated areas of the respective emission bands). First observation one could derive from this data is that $^4S_{3/2}/^4F_{9/2} < 1$ for all materials, meaning the $Er^{3+} \ ^4F_{9/2} \rightarrow ^4I_{15/2}$ red UC emission band has always a higher intensity compared to the $^4S_{3/2} \rightarrow ^4I_{15/2}$ green emission for $Gd_2O_2S:Er^{3+}(,Yb^{3+})$ materials.

The $^4S_{3/2}/^4F_{9/2}$ ratio gets closer to 1 for singly doped $Gd_2O_2S:Er^{3+}$ materials, especially for the $Gd_2O_2S:Er^{3+}(5\%)$, in which Er^{3+} concentration is not too high to trigger longer-extent cross-relaxation processes. On the other hand, co-doped $Gd_2O_2S:Er^{3+}, Yb^{3+}$ materials exhibit superior UC emission intensities but lower $^4S_{3/2}/^4F_{9/2}$ ratios. This might suggest different sensitizing processes between Er^{3+} singly doped and Er^{3+}, Yb^{3+} co-doped materials, even though both ESA and ETU mechanisms were shown to operate for singly doped [92] and co-doped [15,158] materials. Time-resolved UC spectroscopic techniques will be utilized in the future to answer such issues.

From the presented results, it can be concluded that the microwave-assisted solid-state (MASS) method is an efficient alternative to synthesize $Gd_2O_2S:Er^{3+}$ and $Gd_2O_2S:Er^{3+}, Yb^{3+}$ materials with high upconversion (UC) emission intensity. UC efficiencies were remarkably increased by changing a single synthesis parameter, *i.e.*, substituting lanthanide precursor from Ln_2O_3 to $Ln(OH)CO_3$ (Ln^{3+} : Gd, Er, and Yb). Superior UC emission efficiency observed for commercial samples (Leuchtstoffwerk) must be due to the synthesis methodology employed, which was probably the conventional solid-state method using heating procedures of several hours at high (>1000 °C) temperatures. In this context, the MASS method produces materials with slightly lower UC efficiency, but with an enormous reduction of processing time and energy consumption.

3.4 RE₂O₂S:(Eu,Yb),Ti,Mg persistent luminescence (PersL) materials

3.4.1 RE₂O₂S:Ti,Mg self-sustained LEDs

This section covers the characterization and optical properties of a variety of persistent luminescence (PersL) materials based on rare earth oxysulfides prepared by the microwave-assisted solid-state (MASS) synthesis. First, RE₂O₂S:Ti,Mg²⁺ PersL materials (RE³⁺: La, Gd, and Y) were synthesized by the MASS method using a single heat treatment of 25 minutes (P = 90% at 10 min + P = 80% at 15 min). A detailed discussion on the preparation, and structural and optical characterization of these materials were already reported elsewhere by our group ([142] – A1 and [159]). Replicating those results is therefore out of the scope of this thesis. Nevertheless, a brief summary on the main photoluminescence and PersL features of RE₂O₂S:Ti,Mg²⁺ materials suits well to our final goal of fabricating self-sustained light emitting diode (LED) devices.

The excitation spectra of the RE₂O₂S:Ti,Mg²⁺ (RE³⁺: La, Gd, and Y) show two overlapped broad absorption bands for each material, centered at around 265 and 350 nm (Figure 6-left in [142] – A1). The higher energy band is attributed to the RE₂O₂S host absorption, while the band at lower energy is assigned to the ligand-to-metal charge transfer (LMCT) transitions, *i.e.*, O²⁻(2p) and S²⁻(3p) to Ti⁴⁺(3d⁰) [160]. The LMCT absorption bands are very intense for Gd- and Y₂O₂S:Ti,Mg²⁺ compared with the La oxysulfide since the Ti⁴⁺ CT transition has a low quenching temperature (~165 K) in La₂O₂S:Ti [19].

The emission spectra of RE₂O₂S:Ti,Mg²⁺ (Figure 6-middle in [142] – A1) show a broad emission band centered at 590, 615 and 625 nm for La, Gd and Y oxysulfides, respectively. Two origins for this emission band can be assigned. The first is a Ti⁴⁺ d⁰ charge transfer (CT) emission, generated by exciting Ti⁴⁺ ions into a Ti^{3+*} excited state and subsequent radiative decay. The large Stokes shift between CT excitation and emission energies, together with the redshift of CT bands by reducing the host cation radius (La > Gd > Y) supports this hypothesis [19]. However, the presence

of Ti^{3+} ions cannot be ruled out due to the better charge/radius match between Ti^{3+} and RE^{3+} , which avoids charge compensation processes, as well as the reducing $\text{CO}(\text{g})$ atmosphere formed during the MASS synthesis. Thus, the second possibility for the origin of such band are Ti^{3+} d-d emissions. The nature of Ti emission band will be further discussed for the next classes of PersL materials.

The PersL decay curves of $\text{RE}_2\text{O}_2\text{S}:\text{Ti},\text{Mg}^{2+}$ materials (Figure 7-left in [142] – A1) show a very fast decay for the La- material, but a substantially longer decay time for Gd- and $\text{Y}_2\text{O}_2\text{S}:\text{Ti},\text{Mg}^{2+}$ materials, indicating a better energy storage capacity for these two systems. The PersL emission spectra (Figure 7-middle in [142] – A1) confirmed that the PersL is generated by the Ti ions.

White-LED devices can be fabricated by combining a single light emitting semiconductor chip with a proper conversion phosphor, as in the case of modern white-LEDs composed of a blue-emitting InGaN LED (450 nm) sensitizing the yellow-emitting YAG: Ce^{3+} phosphor (550 nm) [4,5]. Within this framework, one possible application for $\text{RE}_2\text{O}_2\text{S}:\text{Ti},\text{Mg}^{2+}$ materials are as solid-state lighting devices, with the additional persistent luminescence feature when turning the LED off. The LED device was mounted (Figure 3.19) by coating a AlGaN UV LED chip (λ_{em} : 280 nm) with a silicon polymer matrix doped with 10% in mass of a $\text{RE}_2\text{O}_2\text{S}:\text{Ti},\text{Mg}$ PersL material. Only RE^{3+} : Gd and Y materials were used to the LED fabrication due to their higher PersL efficiency.

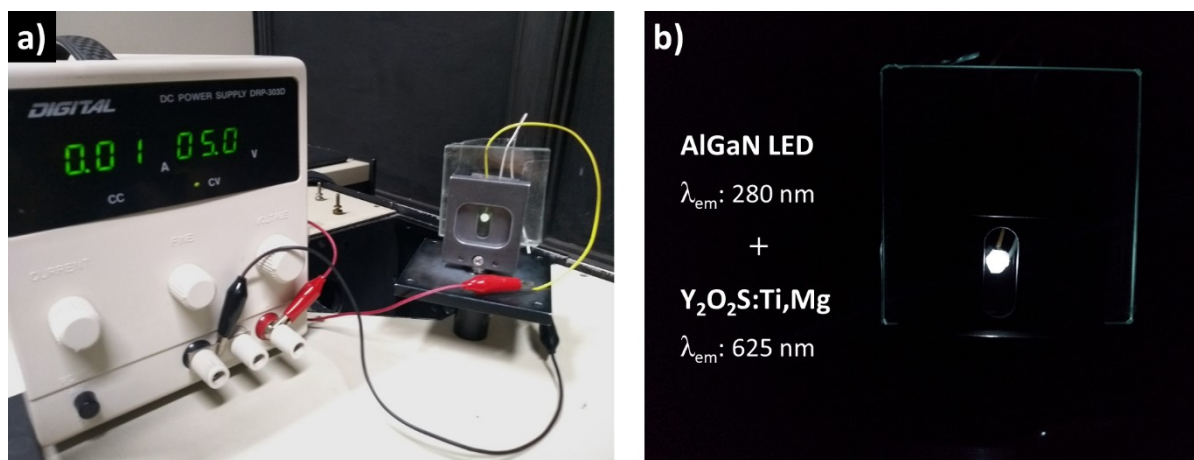


Figure 3.19 a) LED device assembly: an UV LED (AlGaN, $\lambda_{\text{em}}^{\text{max}} = 280 \text{ nm}$) covered with a silicon polymer matrix doped with 10 w-% of $\text{RE}_2\text{O}_2\text{S}:\text{Ti},\text{Mg}$ PersL material (RE^{3+} : Gd and Y). **b)** LED emission in the dark.

The fabricated LED device emits warm-white light due to the contributions of Ti broad emission band together with rare earth impurities (*e.g.*, Er^{3+} ions) present in the $\text{Y}_2\text{O}_2\text{S}$ matrix (Supporting material of [142] – A1). The emission of Ln^{3+} ions can be now observed once the LED emission wavelength is close to the host absorption energy (4.4 eV), causing a selective sensitization of Ln^{3+} impurities. As stated previously (section 3.2.3), $\text{RE}_2\text{O}_2\text{S}$ hosts are efficient sensitizers of trivalent lanthanide dopants even at small concentrations. In addition to the warm-white light emission, the LED self-sustained light emission could be detected for several minutes after turning the continuous current source off (Figure 3.20). The orange persistent luminescence, originated from the Ti broad persistent emission, can be useful for applications in solid-state lighting devices with a built-in emergency light feature.

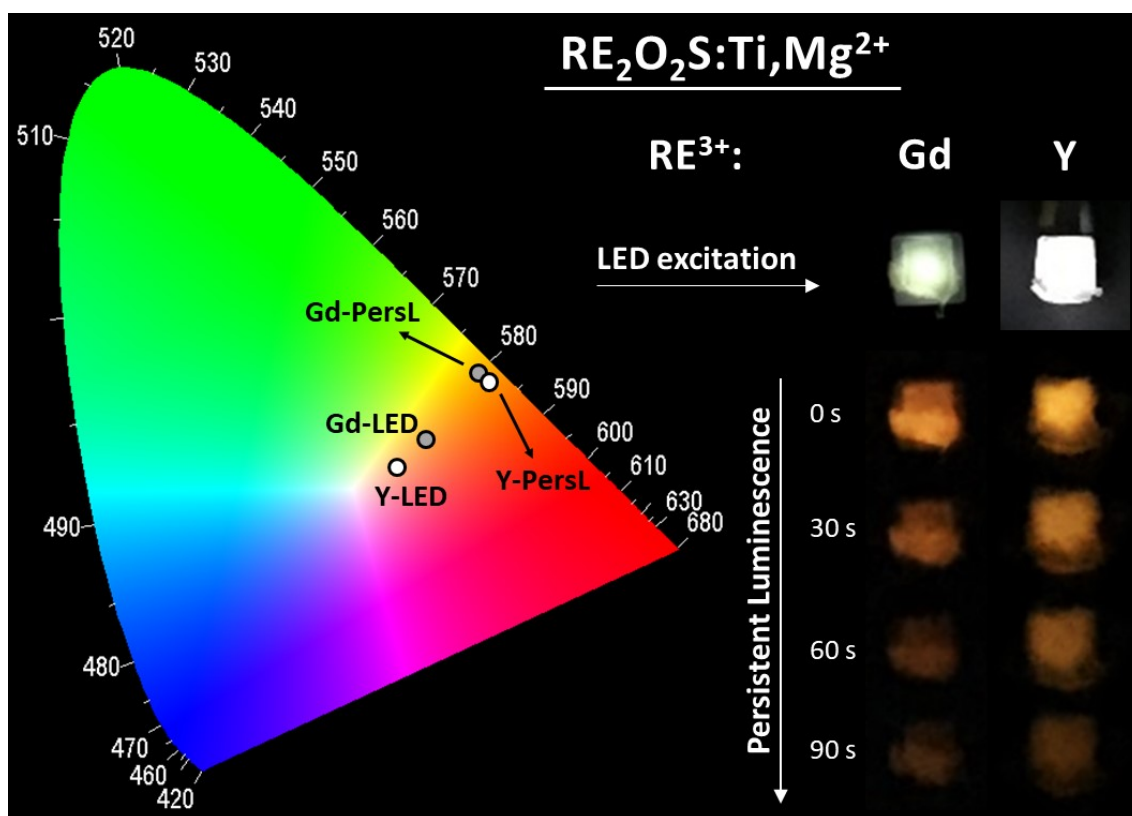


Figure 3.20 CIE x,y color position of LED emission (on) and PersL emission (off); inserted pictures show the LED warm-white light emission when on and the fading orange PersL when turned off. [142] – A1.

3.4.2 RE₂O₂S:Yb and RE₂O₂S:Yb,Ti,Mg near-infrared PersL

Near infrared (NIR) PersL materials are of great interest for biological applications such as *in vivo* optical imaging since the NIR wavelengths are less absorbed/scattered by tissues. Additionally, the materials can be charged before being injected in the biological system, reducing the autofluorescence of tissues to zero during the probing/imaging process. The design of new NIR PersL materials is a challenging task, and multiple strategies are being approached in recent literature. The strategy adopted in this work can be defined as a VRBE- or HRBE-guided photonic design [75].

According to general Host Referred Binding Energy (HRBE) diagrams [33,39,161], the Eu³⁺ (4f⁶) and Yb³⁺ (4f¹³) ions exhibit similar electronic properties, *e.g.*, their ground states (⁷F₀ and ²F_{7/2}) differ in energy by only 0.24 eV, and their LMCT energies are comparable for a given host since both ions achieve stable electronic configurations (4f⁷ and 4f¹⁴). Aiming for alternative NIR PersL materials, this work proposed a HRBE-guided substitution of Eu³⁺ by Yb³⁺ dopant to generate PersL arising from the Yb³⁺ ²F_{5/2}→²F_{7/2} emission (~980 nm). The Y₂O₂S:Eu,Ti,Mg is undoubtedly one of the most well-known red-emitting (626 nm) PersL materials, therefore being a good candidate as a starting point to achieve efficient Yb³⁺ NIR persistent luminescence.

In this way, RE₂O₂S:Yb³⁺ and RE₂O₂S:Yb³⁺,Ti,Mg²⁺ materials (RE³⁺: La, Gd, and Y) were successfully prepared by the MASS synthesis employing the two-step synthesis methodology (25 min each step). The reader is redirected to [Appendix A3 \[144\]](#) for detailed information on the synthesis and photoluminescence characterization of these materials. In summary, all materials exhibited Yb³⁺ ²F_{5/2}→²F_{7/2} narrow emission bands in the 900–1050 nm range (Figure 1 in [\[144\] – A3](#)). Crystal field splitting of Yb³⁺ Stark levels in RE₂O₂S hosts resulted in three main emission bands centered at 953, 983 (highest intensity), and 1010 nm. Furthermore, a broad emission band centered at 610 nm was observed in the Y₂O₂S:Yb,Ti,Mg material and is assigned to the emission from Ti ions [\[13,142\] – A1](#). In the excitation spectra, the oxysulfides exhibit broad absorption bands in the 280–350 nm range assigned to the O²⁻(2p)→Yb³⁺(4f) and S²⁻(3p)→Yb³⁺(4f) LMCT transitions, together with the host

lattice absorption at 260–280 nm. A broad absorption band (~370 nm) arising from Ti ions is observed for the Y₂O₂S:Yb,Ti,Mg material, showing that Ti species can sensitize Yb³⁺ ions in the Y₂O₂S host. This optical feature is less pronounced for Gd₂O₂S:Yb,Ti,Mg and absent for La₂O₂S:Yb,Ti,Mg, indicating a dependence with the electronic structure of each RE₂O₂S host.

To investigate the persistent luminescence properties of Yb³⁺-doped oxysulfides, the PersL emission spectra of RE₂O₂S:Yb,Ti,Mg materials (RE³⁺: La, Gd, and Y) were registered by exciting the samples at 310 nm for 5 minutes and then recording several quick emission spectra over time, covering the whole 400–1100 nm spectral range using a CCD detector (Figure 3.21). It was confirmed that NIR persistent luminescence arises from Yb³⁺ ²F_{5/2}→²F_{7/2} transitions when ceasing the irradiation source. Narrow emission bands in the 500–720 nm range were observed for the La- and Gd₂O₂S:Yb,Ti,Mg materials (3.21a and 3.21b, respectively), especially strong for the latter one, which are related to the ⁵D₁→⁷F₀₋₃ and ⁵D₀→⁷F₀₋₄ transitions of Eu³⁺ impurities. In addition, a broadband persistent emission is observed in the 500–800 nm spectral range, originated from the Ti co-dopant. This Ti broad PersL band is particularly intense for the Y₂O₂S:Yb,Ti,Mg (Figure 3.21c), showing that Ti PersL efficiency drastically increases moving through La → Gd → Y oxysulfides.

According to the NIR persistent luminescence decay curves (Figure 3.22a), singly doped RE₂O₂S:Yb³⁺ materials (RE³⁺: La, Gd, and Y) exhibit short PersL decay times (~30 s). Moreover, Ti,Mg addition had no influence on the decay time and profile for La and Gd hosts. Serendipitously, the decay time was significantly improved by Ti,Mg co-doping in Y₂O₂S:Yb. For a more accurate verification of the decay time enhancement, longer NIR PersL decay curves were acquired for the Y₂O₂S:Yb and Y₂O₂S:Yb,Ti,Mg materials using a CO₂ – cooled Hamamatsu H10330A-45 PMT, which is a suitable detector to work in the NIR spectral region (Figure 3.22b). An enhancement of at least one order of magnitude was detected by Ti,Mg co-doping, leading to an efficient NIR persistent luminescence (983 nm) for the Y₂O₂S:Yb,Ti, Mg material, which could be detected for almost 1 hour.

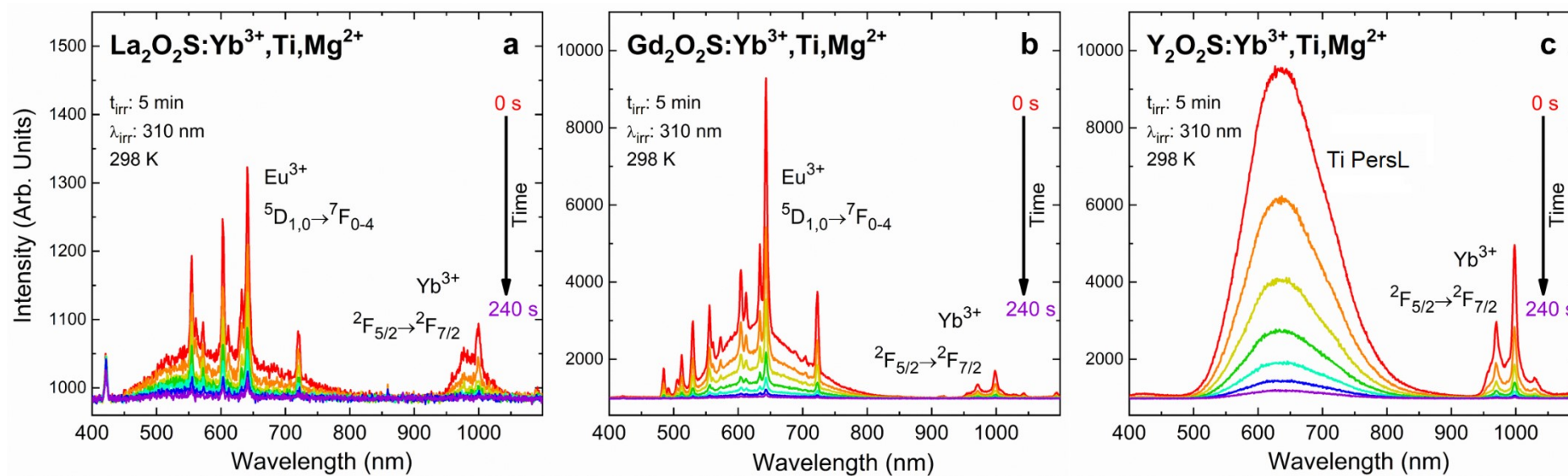


Figure 3.21 Persistent luminescence (PersL) emission spectra of $\text{RE}_2\text{O}_2\text{S}:\text{Yb}^{3+},\text{Ti},\text{Mg}^{2+}$ materials – RE^{3+} : **a)** La, **b)** Gd, and **c)** Y. PersL emission spectra of singly doped $\text{RE}_2\text{O}_2\text{S}:\text{Yb}^{3+}$ materials were displayed in the Supplementary material of [144] – A3.

It is worth noting that a similar PersL behavior concerning $\text{Y}_2\text{O}_2\text{S}:\text{Eu}^{3+},\text{Ti}^{4+},\text{Mg}^{2+}$ materials was reported in literature. For example, Wang *et al.* [95] showed that $\text{Y}_2\text{O}_2\text{S}:\text{Eu}^{3+},\text{Ti}^{4+}$ and $\text{Y}_2\text{O}_2\text{S}:\text{Eu}^{3+},\text{Mg}^{2+}$ materials exhibited very short PersL when compared to $\text{Y}_2\text{O}_2\text{S}:\text{Ti}^{4+},\text{Mg}^{2+}$ and $\text{Y}_2\text{O}_2\text{S}:\text{Eu}^{3+},\text{Ti}^{4+},\text{Mg}^{2+}$.

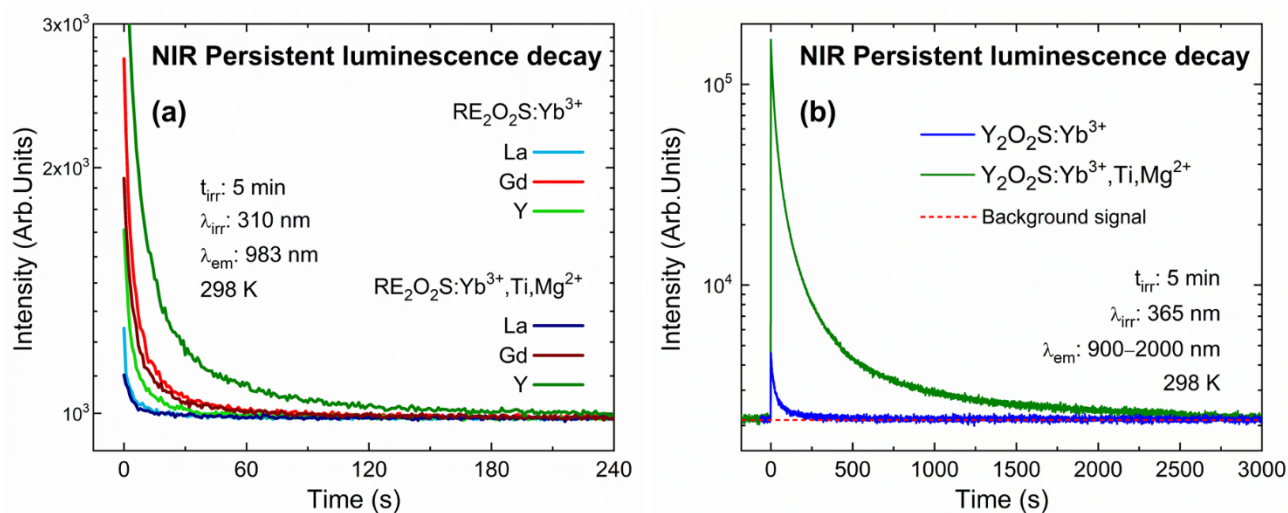


Figure 3.22 a) Persistent luminescence (PersL) decay curves of $\text{RE}_2\text{O}_2\text{S}:\text{Yb}^{3+}$ and $\text{RE}_2\text{O}_2\text{S}:\text{Yb}^{3+},\text{Ti},\text{Mg}^{2+}$ materials (RE^{3+} : La, Gd, and Y). b) Long-time PersL decay curves of $\text{Y}_2\text{O}_2\text{S}:\text{Yb}^{3+}$ and $\text{Y}_2\text{O}_2\text{S}:\text{Yb}^{3+},\text{Ti},\text{Mg}^{2+}$ detected using a CO_2 – cooled NIR PMT detector (Hamamatsu H10330A-45) [144] – A3.

The experimental data reported above show that the persistent luminescence and photoluminescence properties arising from Yb and Ti ions are host dependent, *i.e.*, on the $\text{RE}_2\text{O}_2\text{S}$ crystalline and/or electronic structures. According to literature [19,162], PersL mechanism operating for $\text{RE}_2\text{O}_2\text{S}:\text{Eu}^{3+}$ materials is a hole-trapping process (Figure 1.11), where holes (h^+), generated after excitation at band gap or LMCT $\text{O}^{2-}(\text{S}^{2-}) \rightarrow \text{Eu}^{3+}$ energies, are the charge carriers responsible for PersL. Therefore, due to the similar energy positions of ground levels and CT states of Eu^{3+} and Yb^{3+} , persistent luminescence of Yb^{3+} in rare earth oxysulfides works in a similar fashion to those for $\text{RE}_2\text{O}_2\text{S}:\text{Eu}^{3+}$, as illustrated in the HRBE diagram of Figure 3.23.

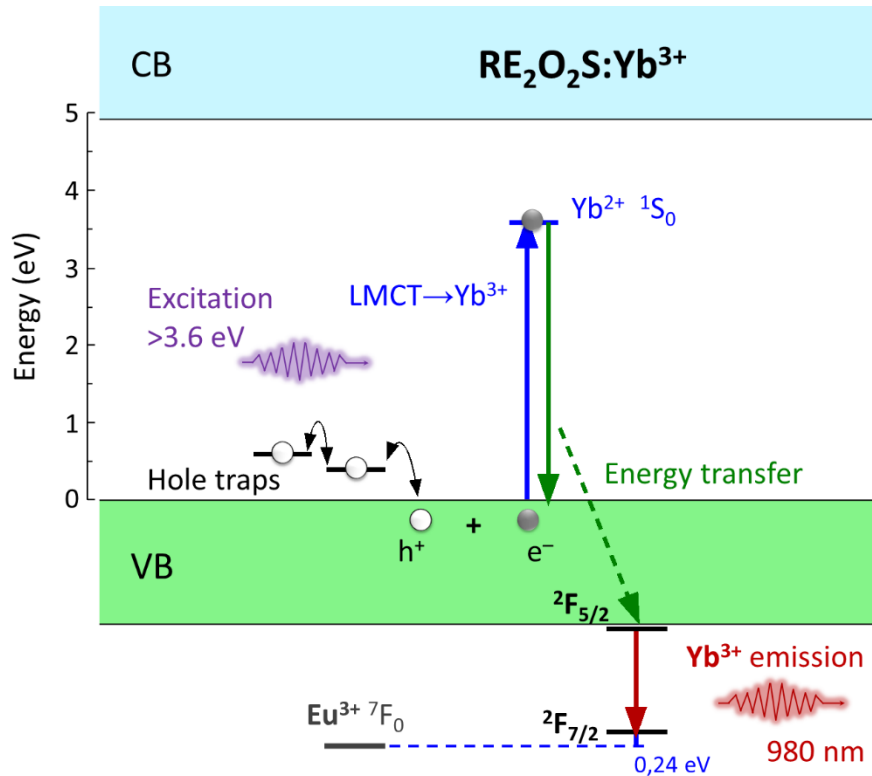


Figure 3.23 HRBE diagram and persistent luminescence (PersL) mechanism for the $\text{RE}_2\text{O}_2\text{S}:\text{Yb}^{3+}$ (RE^{3+} : La, Gd, and Y) [144] – A3. CT energies were obtained from the excitation spectra. Band gap values are consistent with [14] and [142] – A1. $\text{Eu}^{3+} {}^7\text{F}_0$ and $\text{Yb}^{3+} {}^2\text{F}_{7/2}$ ground states were placed accordingly to the references [36,161,163].

First, Yb^{3+} excitation at CT energy (or at band gap energy) promotes an electron (e^-) from the top of valence band (VB) to CT state $\text{Yb}^{2+} {}^1\text{S}_0$ (or to conduction band CB). This excitation process creates a hole (h^+) in VB, which can be captured by nearby hole traps, *e.g.*, cation vacancies or interstitial $\text{O}^{2-}, \text{S}^{2-}$ in the lattice. Then, the return of h^+ to VB and subsequent $e^- - h^+$ recombination transfers energy to the Yb^{3+} excited ${}^2\text{F}_{5/2}$ level, yielding ${}^2\text{F}_{5/2} \rightarrow {}^2\text{F}_{7/2}$ NIR persistent luminescence.

This mechanism (Figure 3.23) illustrates how NIR PersL works for the singly doped $\text{RE}_2\text{O}_2\text{S}:\text{Yb}^{3+}$ materials. Furthermore, Ti, Mg co-doping was showed to strongly enhance Yb^{3+} NIR PersL for the $\text{Y}_2\text{O}_2\text{S}$ host, even though this effect is very small on La and Gd oxysulfides. In this way, two additional and distinct processes, considering both Ti^{3+} or Ti^{4+} valences, could explain the longer persistent luminescence of the $\text{Y}_2\text{O}_2\text{S}:\text{Yb}, \text{Ti}, \text{Mg}$ material:

- I. Hole-trapping process:** The Ti^{4+} LMCT excitation is more efficient to trap h^+ than the Yb^{3+} LMCT, and thus more energy can be stored. Since Ti can sensitize Yb^{3+} ions, this would increase the Yb^{3+} NIR PersL decay time. A similar sensitization process was described by Sontakke *et al.* for the $\text{Ce}^{3+}/\text{Yb}^{3+}$ pair [164,165]. Yb^{3+} sensitization by Ti increases moving through the $\text{La} \rightarrow \text{Gd} \rightarrow \text{Y}$ oxysulfides (Figures 3.21 and 3.22). Therefore, the increase in crystal field strength leads to a decrease of $\text{O}^{2-} \rightarrow \text{Ti}^{4+}$ and $\text{S}^{2-} \rightarrow \text{Ti}^{4+}$ CT energies values [19], which might find an optimal position to transfer the energy to Yb^{3+} in the $\text{Y}_2\text{O}_2\text{S}$ host. Besides, Ti^{4+} increases the concentration of hole traps through charge compensation, contributing to a higher energy storage.
- II. Electron trapping process:** Ti^{3+} d-d excitation leads to e^- capture by traps with energy close to the CB, *e.g.*, O^{2-} and S^{2-} vacancies. After the kT bleaching of traps, the e^- returns to Ti^{3+} levels and then $\text{Ti}^{3+} \rightarrow \text{Yb}^{3+}$ energy transfer occurs, increasing the NIR PersL efficiency. In this hypothesis, energy transfer is dependent on Ti^{3+} 3d levels, therefore the increasing crystal fields strengths through the $\text{La} \rightarrow \text{Gd} \rightarrow \text{Y}$ oxysulfides could be a reason for the higher efficiency observed for the $\text{Y}_2\text{O}_2\text{S}:\text{Yb}^{3+},\text{Ti},\text{Mg}^{2+}$. The e^- trapping via CB process is directly related to the concentration of positive defects, which can be generated by Mg^{2+} co-doping via charge compensation. This is supported Wang *et al.* [95], which showed that the persistent luminescence of $\text{Y}_2\text{O}_2\text{S}:\text{Eu},\text{Ti},\text{Mg}$ is much longer than for $\text{Y}_2\text{O}_2\text{S}:\text{Eu},\text{Ti}$.

The first mechanistic hypothesis (I) seems more plausible since it is more likely that Ti ions are majorly in the 4+ state in oxysulfides. However, since divalent dopants create positive defects (*e.g.*, anion vacancies and interstitial cations) in a trivalent lanthanide lattice, the energy storage enhancement caused by Mg^{2+} co-dopant could be explained if the PersL mechanism operates via

conduction band (II). In this context, it is worth remarking that both e^- -trapping and h^+ -trapping mechanisms might simultaneously occur in PersL materials [69,162].

In summary, the MASS synthesis was proven to be an effective synthesis method also to prepare persistent luminescence materials, in this case, NIR PersL materials – $RE_2O_2S:Yb^{3+}$ and $RE_2O_2S:Yb^{3+},Ti,Mg^{2+}$ (RE^{3+} : La, Gd, Y). Based on the energy level positions of Eu^{3+} and Yb^{3+} ions in the HRBE diagrams, the hypothesis of a Yb^{3+} -activated PersL in RE_2O_2S systems was validated. Therefore, a new NIR-emitting persistent luminescence material $RE_2O_2S:Yb,Ti,Mg$ was designed. Yb^{3+} PersL ($\lambda_{em} = 983$ nm) was observed for all materials, exhibiting the highest efficiency for the $Y_2O_2S:Yb,Ti,Mg$, in which the NIR emission could be detected for almost 1 hour after ceasing the excitation (Figure 3.22b).

Furthermore, PersL enhancement by Ti,Mg co-doping was shown to be an exclusive effect on the Y_2O_2S host, suggesting that the energy storage and transfer processes in $Y_2O_2S:Yb,Ti,Mg$ are associated with intrinsic properties of the host matrix. Therefore, a synergic effect between the three dopants and the host must be responsible for enhancing the PersL decay time in rare earth oxysulfide materials. In the next section, thermoluminescence experiments were performed in several $Y_2O_2S:Eu$ and in $Y_2O_2S:Eu,Ti,Mg$ materials in order to go deeper into the persistent luminescence mechanism for these systems.

3.4.3 Y₂O₂S:Eu and Y₂O₂S:Eu,Ti,Mg: Peering into the PersL mechanism

Previously, a HRBE-guided substitution was performed in the Y₂O₂S:Eu,Ti,Mg to achieve efficient NIR (980 nm) persistent luminescence with the Y₂O₂S:Yb,Ti,Mg material. In addition, Ti,Mg co-doping was demonstrated to enhance the Yb³⁺ NIR PersL in the same fashion as the Eu³⁺ red PersL. However, there are still unanswered questions on how exactly the charge carriers are excited, stored, released, and recombined to generate PersL for these systems. In this context, a quick literature review is necessary to contextualize the reader about the research on the Y₂O₂S:Eu,Ti,Mg persistent luminescence mechanism.

Let us start with a well-defined statement: Eu³⁺ PersL in singly doped Y₂O₂S:Eu³⁺ is a hole-trapping mechanism via valence band (VB). This was described by Clabau *et al.* [162] and Luo *et al.* [19], and was confirmed in this work [144] – A3 for the next of kin Y₂O₂S:Yb³⁺ (Figure 3.23). However, the building of this knowledge dates to the early 1970s, when the nature of the Eu³⁺ charge transfer (CT) and energy storage in Eu³⁺-doped oxysulfides were studied Forest *et al.* [166] and Struck *et al.* [167,168]. These authors demonstrated that excitation at the Eu³⁺ ⁵D₂ level or at higher energies induce an energy storage effect, which was attributed to the Eu³⁺ acting as an electron trapping center. In this sense, the Eu³⁺ ion capture an e⁻ under UV excitation to form a Eu²⁺ CT state, and the h⁺ left behind should be trapped elsewhere in the host lattice. Similar conclusions were drawn by Hoshina *et al.* [169], which proposed a CT model where a h⁺ is transferred from Eu³⁺ to the ligands.

After the discovery of the triply doped Y₂O₂S:Eu,Ti,Mg PersL materials in 2003 [13,95], several works attempted to describe how the PersL mechanism operates for such systems [13,17,19,22,76,95–103,162,170–173]. After a thorough review on these works, this thesis must highlight some of the main results and conclusions:

- Nakazawa and Yamamoto [170] deeply investigated the trapping mechanism in singly doped $\text{Y}_2\text{O}_2\text{S}:\text{Ln}^{3+}$ and concluded that, after excitation, the e^- and the h^+ are trapped outside the Ln^{3+} 4f subshell, but they recombine in the Ln^{3+} 4f states to yield 4f–4f persistent emission.
- Zhang *et al.* contribution was reported in a series of papers [98,100,101]. In the latter one, the authors stressed that the PersL decay time of $\text{Y}_2\text{O}_2\text{S}:\text{Ti}$ and $\text{Y}_2\text{O}_2\text{S}:\text{Eu},\text{Ti}$ are similar, but exceedingly longer compared to $\text{Y}_2\text{O}_2\text{S}:\text{Eu}$. Additionally, PersL emission spectra of $\text{Y}_2\text{O}_2\text{S}:\text{Eu},\text{Ti}$ shows both $\text{Eu}^{3+} \ ^5\text{D}_0 \rightarrow \ ^7\text{F}_2$ and Ti^{4+} CT emission bands with similar intensities. Therefore, this work was the first to propose a cooperative effect between these two ions. More specifically, a $\text{Ti} \rightarrow \text{Eu}$ energy transfer probability was calculated to be $\sim 59\%$.
- Hölsä *et al.* [17,171] postulated that Ti^{3+} ions might be the actual responsible for PersL in $\text{Y}_2\text{O}_2\text{S}:\text{Eu},\text{Ti},\text{Mg}$. In addition, when co-doping with Zr^{4+} (an exclusive tetravalent ion) instead of Ti, the resultant PersL decay time of $\text{Y}_2\text{O}_2\text{S}:\text{Eu},\text{Zr}$ was 10 times shorter than for $\text{Y}_2\text{O}_2\text{S}:\text{Eu},\text{Ti}$, indicating different PersL mechanisms.
- Focusing on the triply doped $\text{Y}_2\text{O}_2\text{S}:\text{Eu},\text{Ti},\text{Mg}$ materials, Cai'e Cui *et al.* published a series of papers investigating distinct parameters, *e.g.*, divalent co-dopant employed ($\text{Y}_2\text{O}_2\text{S}:\text{Eu},\text{Ti},\text{M}$, where M^{2+} : Mg, Ca, Sr, and Ba) [102], Ti and Mg co-dopant concentrations [99], and Eu^{3+} concentration [22]. In summary, Mg^{2+} is the best co-dopant to enhance PersL decay time, and $[\text{Eu}^{3+}] = 5.0\%$ seems to be optimal to enhance both photoluminescence and PersL.
- An interesting work of Zhou *et al.* [97] reported a detailed description on the PersL and thermoluminescence (TL) of $\text{Y}_2\text{O}_2\text{S}:\text{Eu},\text{Ti},\text{Mg}$. The key concluding remarks were: *i)* Ti is the main activator ion for PersL, *ii)* $\text{Ti} \rightarrow \text{Eu}$ energy transfer was showed to enhance Eu^{3+} persistent emission, and *iii)* Mg^{2+} aids in incorporating of Ti^{4+} ions in the $\text{Y}_2\text{O}_2\text{S}$ structure and increases trap concentration. In this way, the e^- was considered the main charge carrier responsible for the PersL mechanism.

- Luo *et al.* [19] demonstrated from a series of TL experiments that the main charge carrier responsible for $\text{Y}_2\text{O}_2\text{S}:\text{Eu}^{3+}$ and $\text{Y}_2\text{O}_2\text{S}:\text{Ti}^{4+}$ PersL are the h^+ , which are captured by hole traps close to the valence band. This work, however, does not consider co-dopant ions in the $\text{Y}_2\text{O}_2\text{S}:\text{Eu}$ (or $\text{Y}_2\text{O}_2\text{S}:\text{Ti}$) material.
- Qu *et al.* recently investigated the PersL mechanism of $\text{Y}_2\text{O}_2\text{S}:\text{Eu},\text{Ti},\text{Mg}$ by first-principles calculations [103] and stated that the e^- are the charge carriers responsible for the Ti^{4+} persistent emission. Moreover, the presence of Eu^{3+} 4f–4f transitions in the PersL emission spectra is caused by a $\text{Ti} \rightarrow \text{Eu}$ energy transfer. Nevertheless, the authors only consider a band gap excitation in their PersL mechanism, excluding the excitation at the Eu^{3+} and Ti^{4+} CT energies, which also generates PersL.

One shall not think that these different results are conflicting or that the proposed mechanism models are incorrect. Instead, the complex nature of the processes involving the trap and release of charge carriers hinders the actual PersL mechanism of $\text{Y}_2\text{O}_2\text{S}$ -based materials. Among the unsolved issues, the main questions could be summarized as: *i)* What charge carriers are truly responsible for the PersL of Eu and Ti ions? *ii)* Is there only one type of PersL mechanism operating? With these in perspective, this section describes the optical characterization of $\text{Y}_2\text{O}_2\text{S}:\text{Eu}$ and $\text{Y}_2\text{O}_2\text{S}:\text{Eu},\text{Ti},\text{Mg}$ PersL materials by PL and PersL spectroscopies, PersL decay curves, and TL glow curves to investigate more of the hidden features of PersL mechanisms operating for these systems.

Firstly, $\text{Y}_2\text{O}_2\text{S}:\text{Eu}$ and $\text{Y}_2\text{O}_2\text{S}:\text{Eu},\text{Ti},\text{Mg}$ materials were synthesized by the MASS method, employing the two-step synthesis methodology (25 min each step). XRD patterns for the singly doped $\text{Y}_2\text{O}_2\text{S}:\text{Eu}$ (Figure 3.24a) show the successful formation of the $\text{Y}_2\text{O}_2\text{S}$ crystal phase (PDF 24-1424 displayed as reference), with minimal contributions of the Y_2O_3 impurity phase. The same results were observed for co-doped $\text{Y}_2\text{O}_2\text{S}:\text{Eu},\text{Ti},\text{Mg}$ materials (Figure 3.24b), demonstrating an efficient inclusion of Ti^{4+} and Mg^{2+} co-dopants in the $\text{Y}_2\text{O}_2\text{S}$ crystal lattice despite their charge/radius

mismatch respective to Y^{3+} . Increasing Eu^{3+} concentration from 0 to 0.5, 1.0 and 5.0% were shown not to disturb the Y_2O_2S formation due to the easy substitution of Y^{3+} by Eu^{3+} ions into the Y_2O_2S lattice. In fact, the $Y_2O_2S:Ti,Mg$ material ($[Eu^{3+}] = 0$) exhibited a higher Y_2O_3 impurity fraction. Rietveld refinement studies will be further carried to investigate the lattice parameters of Y_2O_2S -based PersL materials prepared with different dopant concentrations.

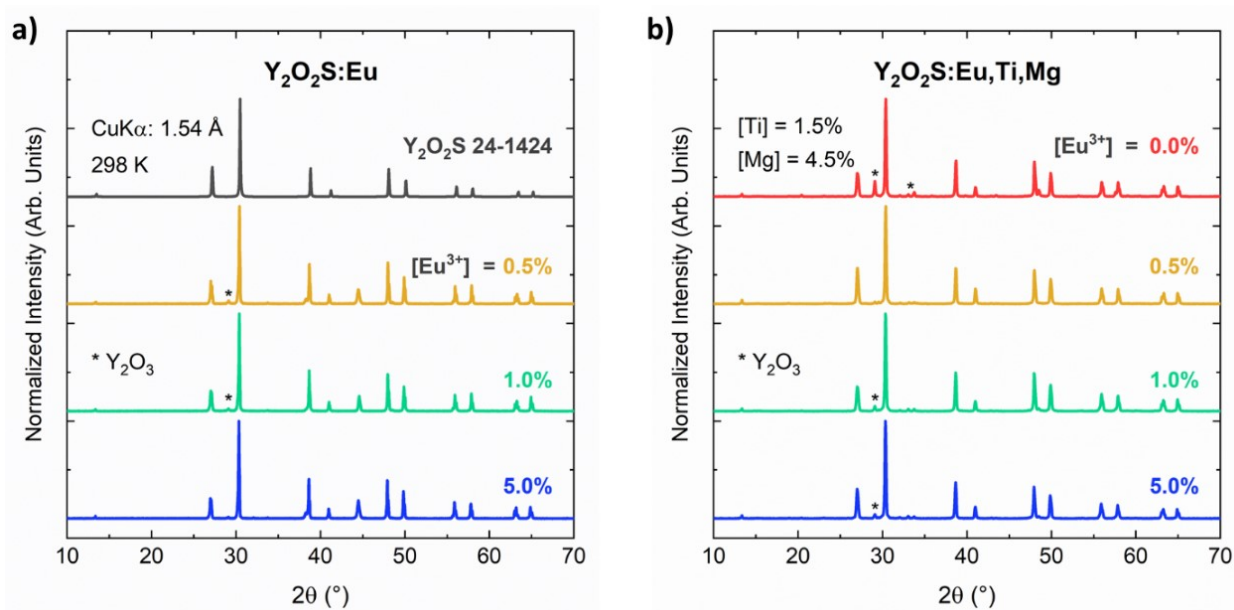


Figure 3.24 X-ray diffraction (XRD) patterns for **a)** $Y_2O_2S:Eu$ and **b)** $Y_2O_2S:Eu,Ti,Mg$ materials prepared by the MASS method (reference Y_2O_2S pattern PDF 24-1424 also displayed).

The excitation spectra of $Y_2O_2S:Eu,Ti,Mg$ materials (Figure 3.25a) were registered by monitoring near the maximum intensities of the $Eu^{3+} \ ^5D_0 \rightarrow \ ^7F_2$ and Ti emissions. For the $Y_2O_2S:Ti,Mg$ material, a significantly broad absorption band was observed in the 270–470 nm range, which is assigned to the Ti^{4+} CT excitation, *i.e.*, $O(S)^{2-} \rightarrow Ti^{4+}$ leading to the $Ti^{4+} + e^- \rightarrow Ti^{3+*}$ excitation process. For the Eu^{3+} -doped materials, $O(S)^{2-} \rightarrow Eu^{3+}$ LMCT absorption band is observed in the 270–400 nm range. The ${}^7F_{0,1} \rightarrow {}^5L_6$ (396) and ${}^7F_{0,1} \rightarrow {}^5D_2$ (467 nm) absorption bands of Eu^{3+} ions are also present. In addition, small intensity absorption bands can be spotted at around 265 nm for all materials, which are related to the band gap absorption of the Y_2O_2S host matrix (>4.7 eV).

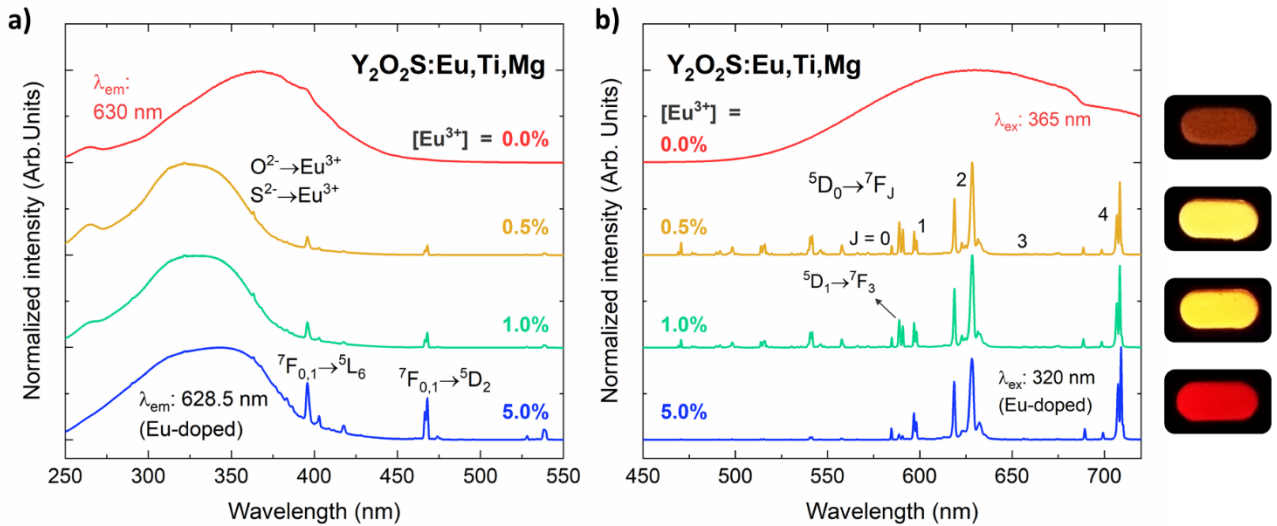


Figure 3.25 Photoluminescence a) excitation and b) emission spectra of $\text{Y}_2\text{O}_2\text{S}:\text{Eu},\text{Ti},\text{Mg}$ materials prepared by the MASS method. Inserted pictures show the materials emission color under 365 nm excitation.

The emission spectra of $\text{Y}_2\text{O}_2\text{S}:\text{Eu},\text{Ti},\text{Mg}$ materials doped with 0.5 and 1.0% of Eu^{3+} exhibit a similar emission profile, *i.e.*, high-intensity $^5\text{D}_0 \rightarrow ^7\text{F}_{0-4}$ emission bands, with the lower intensity transitions from the higher energy levels $^5\text{D}_2 \rightarrow ^7\text{F}_0$ and $^5\text{D}_1 \rightarrow ^7\text{F}_3$ unambiguously assigned (Figure 3.25b). Further increasing Eu^{3+} concentration to 5.0% triggers cross-relaxation processes that almost extinguishes the transitions from the $^5\text{D}_{2,1}$ levels, leading to a non-radiative decay from $^5\text{D}_{2,1}$ to the $^5\text{D}_0$ emitting level. Hence, the luminescence of the $\text{Y}_2\text{O}_2\text{S}:\text{Eu}_{(5.0\%)},\text{Ti},\text{Mg}$ material was significantly redshifted compared to $\text{Y}_2\text{O}_2\text{S}:\text{Eu}_{(0.5\%)},\text{Ti},\text{Mg}$ and $\text{Y}_2\text{O}_2\text{S}:\text{Eu}_{(1.0\%)},\text{Ti},\text{Mg}$, indicating the possibility of emission color modulation by adjusting Eu^{3+} concentration.

On the other hand, the emission spectra of the $\text{Y}_2\text{O}_2\text{S}:\text{Eu}_{(0\%)},\text{Ti},\text{Mg}$ has a completely different spectral profile (Figure 3.25b). The absence of Eu^{3+} ions led to a pure broadband emission (500–750 nm) originated from the Ti ions. The photoluminescence emission intensity of Ti is noticeably lower than the Eu^{3+} one. This result is interesting but not unexpected, since Ti doping in $\text{RE}_2\text{O}_2\text{S}$ causes significant disturbances in the first coordination sphere. As formerly stated, the Y^{3+} occupy heptacoordinated C_{3v} sites in $\text{Y}_2\text{O}_2\text{S}$, bonded to 4 oxygens and 3 sulfur atoms. Since there are no reports on stable heptacoordinated Ti ions, a defect must be generated to accommodate Ti^{4+} in a

hexacoordinated site after substituting a Y^{3+} site in the Y_2O_2S lattice (Figure 3.26). Since the Y–O bond in the c -axis has a slightly longer bond length (2.31) compared to the other three symmetrical Y–O bonds (2.23 Å) [88], the formation of the C_{3v} site (Figure 3.26a) is favored over the C_s (Figure 3.26b). Nevertheless, sulfur-vacant C_s sites (Figure 3.26c) are the most likely to occur due to the lower energy of Y–S bonds compared to Y–O [174]. These findings are corroborated by Zhang *et al.* [98], which reported a decreasing in Ti photoluminescence intensity allied with a enhancing in Ti PersL by increasing Mg^{2+} concentration. The reader is asked to keep this discussion in mind once we will return to that later, on exploring the role of each dopant ion in the PersL mechanism.

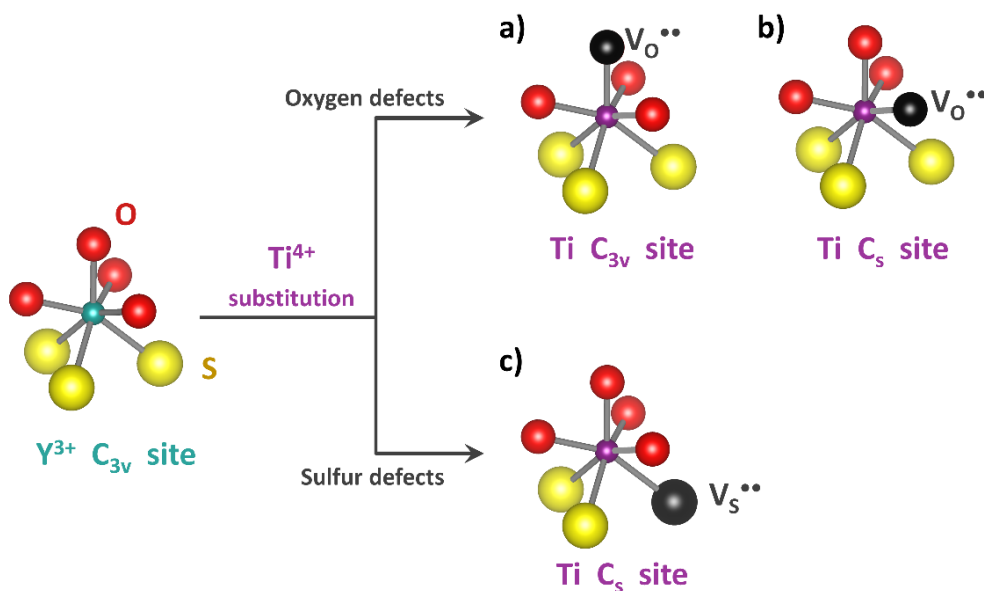


Figure 3.26 Ti^{4+} substitutional doping in the Y_2O_2S lattice, forming hexacoordinated metal sites by generating different defects: **a)** oxygen vacancy in the c -axis, maintaining the former C_{3v} symmetry, **b)** oxygen vacancy in one of the three symmetrical (and shorter) Y–O bonds, creating a C_s symmetry site, and **c)** sulfur vacancy (the three Y–S are symmetrical), also creating a C_s symmetry site.

The absence of Ti broad emission band in the materials containing Eu^{3+} (Figure 3.25b) is due to two reasons. First, RE_2O_2S hosts can efficiently accommodate Ln^{3+} ion due to the charge/radius similarity, as well as symmetry compatibility, yielding highly luminescent $RE_2O_2S:Ln^{3+}$ materials [14,143] – A2. Ti ions are also sensitized in RE_2O_2S but less efficiently due to the symmetry-related

defect formation (Figure 3.26). The second reason is the excitation wavelength employed. As europium ions are better sensitized than Ti ones, excitation wavelengths up to 400 nm yield only Eu^{3+} narrow emission bands once the Eu^{3+} CT absorption band is predominant on the 270–400 nm range. In this way, since the Ti^{4+} CT absorption ranges up to 470 nm (Figure 3.25a), exciting beyond 400 nm causes the Ti broad emission band to appear together with the $\text{Eu}^{3+} \ ^5\text{D}_{1,0} \rightarrow \ ^7\text{F}_J$ transitions.

Persistent luminescence emission spectra of the $\text{Y}_2\text{O}_2\text{S}:\text{Eu},\text{Ti},\text{Mg}$ materials (Figure 3.27) were registered by exciting the samples for 5 min at 320 nm, then recording quick emission spectra over the 0–240 s time range. Analyzing the $\text{Y}_2\text{O}_2\text{S}:\text{Eu},\text{Ti},\text{Mg}$ material doped with 0.5% of Eu^{3+} , its PersL emission spectra (Figure 3.27a) have a completely different spectral profile compared to its photoluminescence spectra (Figure 3.25b). One can observe that both the narrow $\text{Eu}^{3+} \ ^5\text{D}_0 \rightarrow \ ^7\text{F}_{0-4}$ transitions overlapped with the Ti broad emission band compose the PersL emission profile. In addition, emission bands from the higher excited $\ ^5\text{D}_1$ and $\ ^5\text{D}_2$ levels of Eu^{3+} are not present.

Increasing the Eu^{3+} concentration from 0.5 to 1.0% leads to a higher relative contribution of the $\text{Eu}^{3+} \ ^5\text{D}_0 \rightarrow \ ^7\text{F}_{0-4}$ emissions to the outcome PersL emission profile (Figure 3.27b). Further increasing the Eu^{3+} concentration 5.0% significantly diminishes the contribution from the Ti emission band to the PersL emission, *i.e.*, PersL spectra of the $\text{Y}_2\text{O}_2\text{S}:\text{Eu}(5.0\%),\text{Ti},\text{Mg}$ material are composed only by the $\text{Eu}^{3+} \ ^5\text{D}_0 \rightarrow \ ^7\text{F}_{0-4}$ narrow emission bands (Figure 3.27c). These results suggest an efficient persistent Ti→Eu energy transfer process, as described in [17,101,103]. The PersL emission spectra of the $\text{Y}_2\text{O}_2\text{S}:\text{Ti},\text{Mg}$ material ($[\text{Eu}^{3+}] = 0$) were not shown here, but it has a similar behavior compared to the visible portion of the $\text{Y}_2\text{O}_2\text{S}:\text{Yb},\text{Ti},\text{Mg}$ PersL emission spectra (Figure 3.21c), exhibiting only the Ti broad emission band (500–800 nm) decreasing over time.

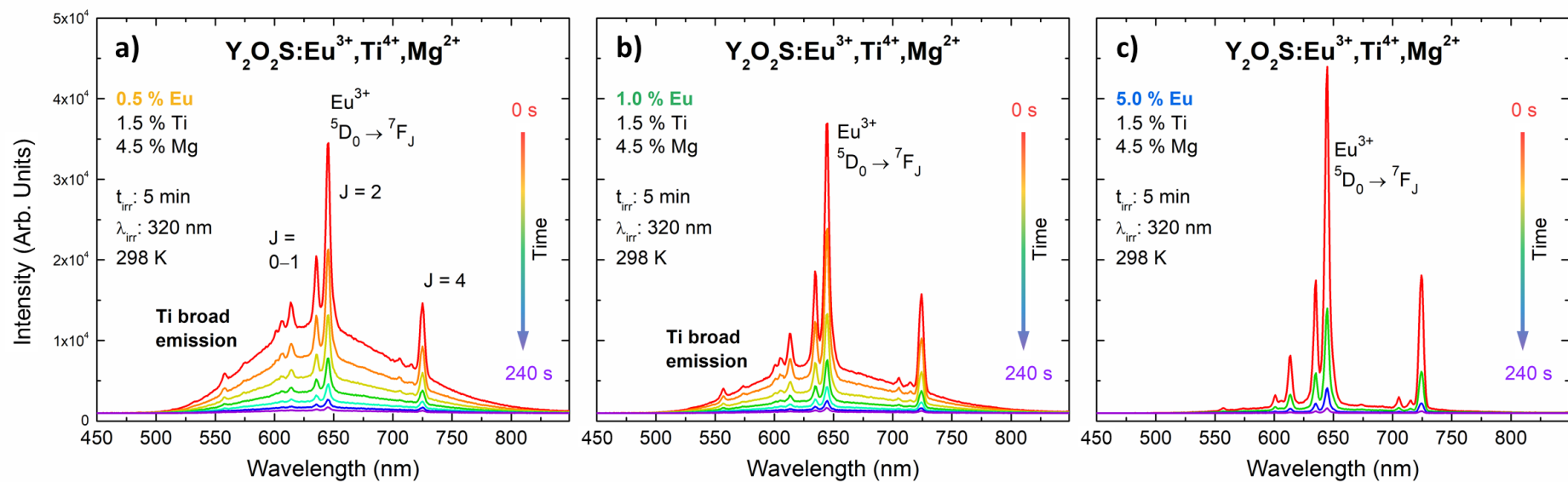


Figure 3.27 Persistent luminescence (PersL) emission spectra of $\text{Y}_2\text{O}_2\text{S}:\text{Eu}, \text{Ti}, \text{Mg}$ materials prepared by the MASS method – Eu^{3+} ion concentration: **a)** 0.5, **b)** 1.0, and **c)** 5.0%.

Regardless of the distinct PersL spectra observed, the PersL decay curves of the $\text{Y}_2\text{O}_2\text{S}:\text{Eu},\text{Ti},\text{Mg}$ materials show similar profile and decay time for the different Eu^{3+} concentrations (Figure 3.28). Measured PersL decay times for the materials obtained by the MASS method follow the order: $\text{Y}_2\text{O}_2\text{S}:\text{Ti},\text{Mg} \approx \text{Y}_2\text{O}_2\text{S}:\text{Eu}_{(0.5\%)},\text{Ti},\text{Mg} < \text{Y}_2\text{O}_2\text{S}:\text{Eu}_{(5.0\%)},\text{Ti},\text{Mg} < \text{Y}_2\text{O}_2\text{S}:\text{Eu}_{(1.0\%)},\text{Ti},\text{Mg}$. The distinct PersL efficiencies and decay profiles observed between the commercial samples and the ones synthesized in this work (Figure 3.28) are related to the preparation methodology rather than the dopant concentrations. Conventional solid-state methods, which were probably used in the preparation of Glotech and Luming samples, is the most suitable to obtain efficient PersL materials, since the high temperatures and long synthesis times favor ion migration and stabilize the traps responsible for energy storage. However, when performing a MASS synthesis, the electromagnetic field of microwaves tends to concentrate in the lattice defects/boundaries and enhance ion mobility at the interfaces, increasing the mass transport rate at a given temperature [175]. Therefore, the MASS method can still be further optimized to produce PersL materials with equivalent or even higher efficiencies compared to the best commercial samples up to date.

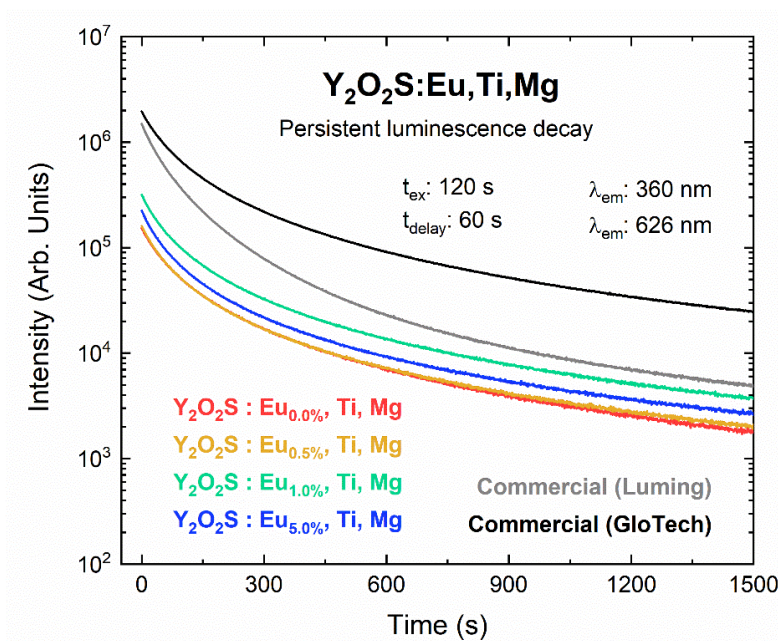


Figure 3.28 Persistent luminescence (PersL) decay curves of $\text{Y}_2\text{O}_2\text{S}:\text{Eu},\text{Ti},\text{Mg}$ materials prepared by the MASS method. Commercial samples (Glotech and Luming) were measured under the same conditions.

Despite the synthesis methodology being essential to the PersL outcome, dopants, and their concentrations also play an important role in creating new traps and the stabilization of their energies to enhance PersL decay time. Thermoluminescence (TL) technique allows a visualization of the traps responsible for energy storage in a material, and how these traps communicate in the charge carrier trapping/releasing processes. In this way, TL glow curves for the $Y_2O_2S:Eu$ and $Y_2O_2S:Eu,Ti,Mg$ materials, prepared by the MASS method with different Eu^{3+} concentrations, were registered in the 100–600 K temperature range (Figure 3.29). Samples were excited for 120 s at 360 nm in different temperatures (T_{ex}), then emission was recorded at 626 nm employing a 1 K s^{-1} heating rate.

The TL glow curve of the $Y_2O_2S:Ti,Mg$ (without Eu^{3+} dopant) shows three main TL peak structures, centered at 125, 202, and 295 K (Figure 3.29a). The highest intensity TL peak (295 K) is assigned to the defects primarily responsible for the long decay time in $Y_2O_2S:Ti,Mg$ and $Y_2O_2S:Eu,Ti,Mg$ PersL materials [95,171,172]. This broad TL peak is then assigned to the traps relative to the Ti and Mg PersL mechanism. Most works report the position of this TL peak slightly shifted to higher temperatures, *e.g.*, ~350 K. This result is attributed to the temperature in which the material is excited, which normally is at room temperature (RT). By exciting at RT, most of the lower energy traps cannot be filled, and thus the full profile of the TL peak is lost. For example, the light-blue TL curve of $Y_2O_2S:Ti,Mg$, registered after exciting the sample at RT, is centered at 320 K.

In this context, registering TL curves after exciting a PersL material with a fixed wavelength but at different temperatures (T_{ex}) allows the study of how traps communicate during the charge carrier capture/release processes. By increasing T_{ex} , one can observe a gradual decrease in the lower temperature TL peak, as these traps were not filled by e^- or h^+ . In addition, a new TL peak centered at 475 K was observed to rise when $T_{ex} > 320\text{ K}$ (Figure 3.29a). This result indicates the existence of deeper traps in the $Y_2O_2S:Ti,Mg$ material, which might contribute to prolongate the PersL decay time even at room temperature.

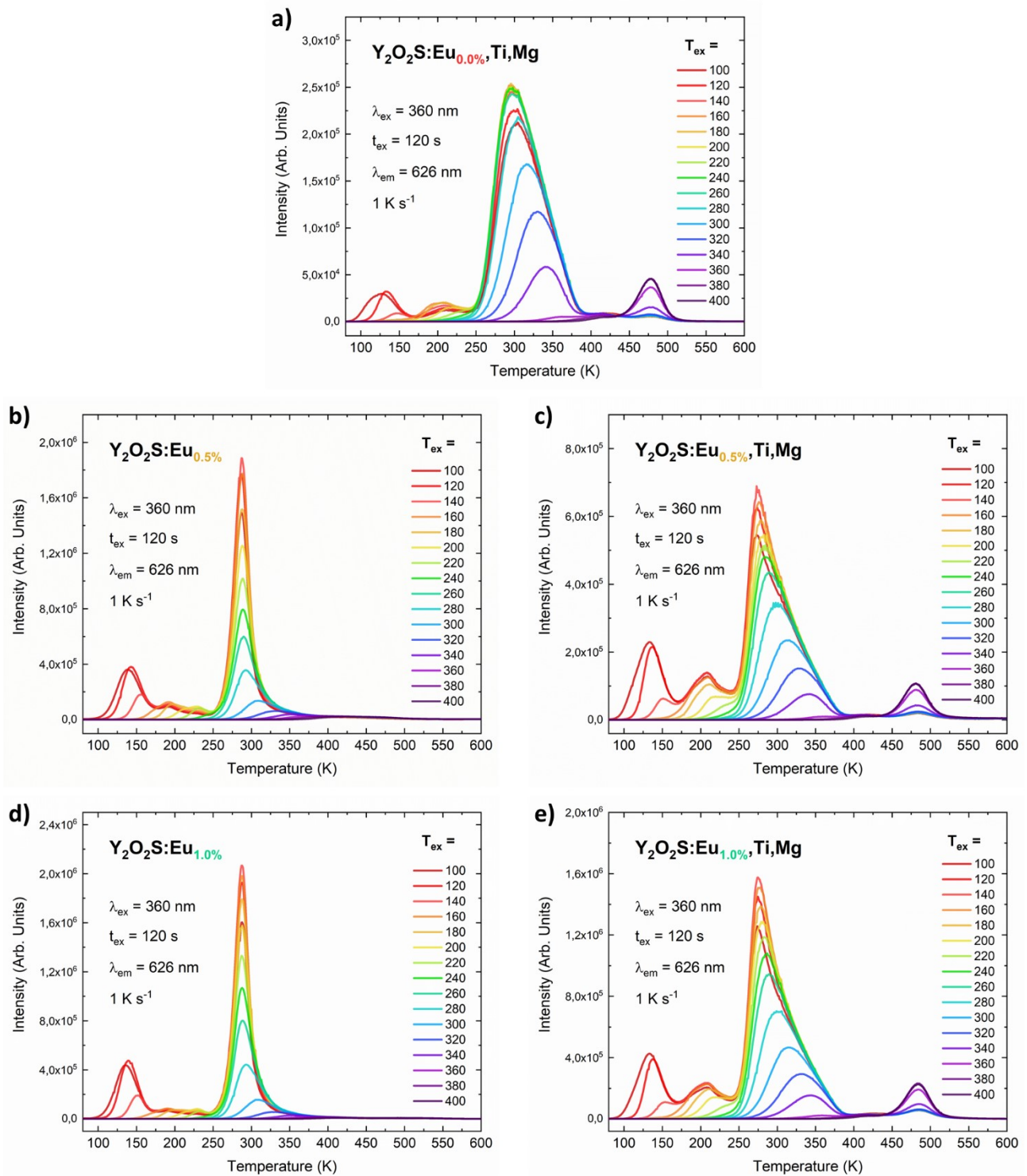


Figure 3.29 Thermoluminescence (TL) glow curves of singly doped $\text{Y}_2\text{O}_2\text{S}:\text{Eu}$ and co-doped $\text{Y}_2\text{O}_2\text{S}:\text{Eu},\text{Ti},\text{Mg}$ materials prepared by the MASS method with different Eu^{3+} concentrations: **a)** $\text{Y}_2\text{O}_2\text{S}:\text{Eu}(0\%),\text{Ti},\text{Mg}$, **b)** $\text{Y}_2\text{O}_2\text{S}:\text{Eu}(0.5\%)$, **c)** $\text{Y}_2\text{O}_2\text{S}:\text{Eu}(0.5\%),\text{Ti},\text{Mg}$, **d)** $\text{Y}_2\text{O}_2\text{S}:\text{Eu}(1.0\%)$, and **e)** $\text{Y}_2\text{O}_2\text{S}:\text{Eu}(1.0\%),\text{Ti},\text{Mg}$. Distinct color curves show the temperature T_{ex} in which the sample was excited before being cooled down to 80 K to start the TL measurement. $[\text{Ti}] = 1.5$ and $[\text{Mg}] = 4.5\%$ for all co-doped materials.

Interesting results arise when comparing the TL glow curves of the singly doped $\text{Y}_2\text{O}_2\text{S}:\text{Eu}_{(0.5\%)}$ (Figure 3.29b) and the co-doped $\text{Y}_2\text{O}_2\text{S}:\text{Eu}_{(0.5\%)},\text{Ti},\text{Mg}$ (Figure 3.29c) materials. For the singly doped $\text{Y}_2\text{O}_2\text{S}:\text{Eu}_{(0.5\%)}$, a narrow TL peak centered at 288 K was detected, in contrast to the broad TL peak in the 250–380 K range observed for $\text{Y}_2\text{O}_2\text{S}:\text{Eu}_{(0.5\%)},\text{Ti},\text{Mg}$. Furthermore, this broad TL peak in $\text{Y}_2\text{O}_2\text{S}:\text{Eu}_{(0.5\%)},\text{Ti},\text{Mg}$ (Figure 3.29c) is similar to one registered for $\text{Y}_2\text{O}_2\text{S}:\text{Ti},\text{Mg}$ (Figure 3.29a). Therefore, one can assign the narrow TL peak to the Eu^{3+} -related PersL traps and the broad TL peak to the Ti,Mg -related PersL traps. An equal behavior was observed for the TL glow curves of $\text{Y}_2\text{O}_2\text{S}:\text{Eu}_{(1.0\%)}$ (Figure 3.29d) and $\text{Y}_2\text{O}_2\text{S}:\text{Eu}_{(1.0\%)},\text{Ti},\text{Mg}$ (Figure 3.29e). In addition, the broad TL peak centered in 202 K was shown to be a particular feature of the co-doped materials (Figure 3.29a,c,e), since the singly doped $\text{Y}_2\text{O}_2\text{S}:\text{Eu}$ (Figure 3.29b,d) exhibit two low intensity TL peaks centered at 190 and 225 K.

As stated previously, dopants and their concentrations play an important role in energy storage and therefore influence the TL glow curve profile. The Glotech sample, for instance, exhibited a high red luminescence, which is similar to the emission profile of the MASS material prepared with higher Eu^{3+} concentration, *i.e.*, $\text{Y}_2\text{O}_2\text{S}:\text{Eu}_{(5.0\%)},\text{Ti},\text{Mg}$. Therefore, the TL curves of the $\text{Y}_2\text{O}_2\text{S}:\text{Eu}_{(5.0\%)},\text{Ti},\text{Mg}$ (Figure 3.30a) and the Glotech (Figure 3.30b) materials were plotted side by side for comparison. Both samples exhibit similar TL profile, indicating a similar trap structure, however, some differences are worth mentioning. First, the broad TL peak at 250–380 K is significantly more intense in the Glotech material. As this peak is assigned to the traps relative to the Ti,Mg PersL mechanism, it corroborates the best PersL performance of the Glotech material at RT. On the other hand, the TL peak at 202 K is exclusive for the MASS-obtained materials, indicating a type of defect that must be favored by the microwave synthesis methodology. Furthermore, the TL peak at higher temperatures (475 K) is less pronounced for these two materials, probably due to the higher relative intensity of the TL peaks in the 280–400 K range.

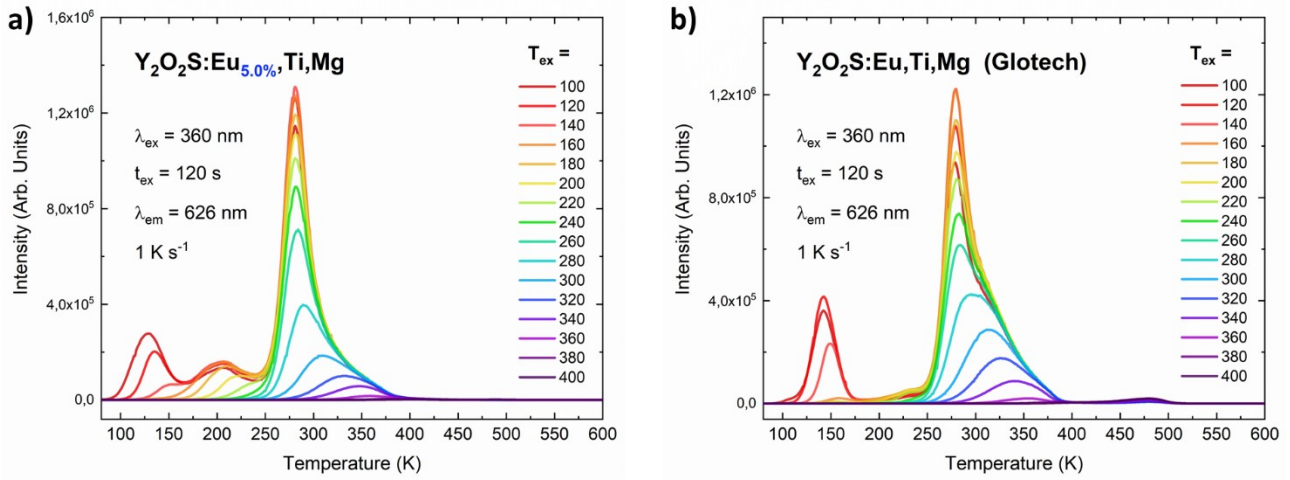
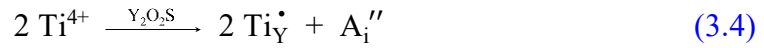
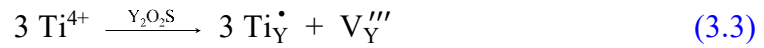
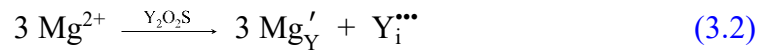


Figure 3.30 Thermoluminescence (TL) glow curves of **a)** $\text{Y}_2\text{O}_2\text{S}:\text{Eu}_{(5.0\%)},\text{Ti}_{(1.5\%)},\text{Mg}_{(4.5\%)}$ PersL material obtained by the MASS method, and **b)** Commercial $\text{Y}_2\text{O}_2\text{S}:\text{Eu},\text{Ti},\text{Mg}$ sample (Glotech).

Based on the presented results, one can conclude that singly doped $\text{Y}_2\text{O}_2\text{S}:\text{Eu}$ and triply doped $\text{Y}_2\text{O}_2\text{S}:\text{Eu},\text{Ti},\text{Mg}$ materials have a different trap structure that originates PersL. The aliovalent substitution of Ti^{4+} and Mg^{2+} ions into the $\text{Y}_2\text{O}_2\text{S}$ matrix generate a series of possible charge compensation processes to neutralize lattice charge [97]. The processes that have a higher probability of occurring are expressed in Equations 3.1–3.4, using Kröger-Vink notation [176] (A = O or S):



Among the referred processes, the one represented by equation 3.1 is the most likely to occur since the formation energies for anion vacancies are smaller compared to interstitial anions (3.4) in these lattices [174]. More specifically, sulfide vacancies are easier formed since the RE–O bonds stronger than the RE–S. Nevertheless, it was previously discussed that if Ti^{4+} substitutes the Y^{3+} heptacoordinated sites, an anion vacancy tends to be formed to accommodate Ti^{4+} in a

hexacoordinated site (Figure 3.26). The same proposition goes to Mg^{2+} ions substituting in Y^{3+} sites. Therefore, while Mg^{2+} co-doping is mostly responsible for creating anion vacancies (3.1), Ti^{4+} co-doping can generate both anion vacancies and yttrium vacancies (3.3). There is a possibility of both Ti^{4+} and Mg^{2+} entering interstitial sites in the $\text{Y}_2\text{O}_2\text{S}$ lattice due to their smaller ionic radii (0.72 and 0.61 Å for coordination number 6) compared to Y^{3+} (0.96 Å). However, charge compensation processes will still occur since the net charge will be also disbalanced in this way. From this defect formation model, one can conclude that clusters of defects must be common in $\text{Y}_2\text{O}_2\text{S}:\text{Eu},\text{Ti},\text{Mg}$ materials, which may also contribute in the charge migration processes and thus enhancing PersL performance [162].

Hence, uniting the knowledge of Eu^{3+} and Ti^{4+} hole-trapping mechanism with the PersL features found in the co-doped $\text{Y}_2\text{O}_2\text{S}:\text{Eu},\text{Ti},\text{Mg}$ materials (Figures 3.25–3.30), the synergic effect among the three Eu, Ti, and Mg dopant ions, and the $\text{Y}_2\text{O}_2\text{S}$ matrix, can be summarized as:

- I. **Ti⁴⁺ doping**: Through $\text{O}(\text{S})^{2-} \rightarrow \text{Ti}^{4+}$ LMCT excitation (Figure 3.25a), PersL is induced via VB by trapping e^- in the Ti^{4+} (forming Ti^{3+*}) and generating a free h^+ in VB. The free h^+ can then be captured by hole traps with energy close to the top of the VB, e.g., Y^{3+} vacancies and interstitial anions. According to charge compensation processes of equations 3.3 and 3.4, Ti^{4+} doping also increases the concentration of such defects, thus intrinsically enhancing the PersL decay time.
- II. **Mg²⁺ doping**: First, Mg^{2+} acts as stabilizer of the defects induced by Ti^{4+} doping due to its higher ionization potential and thus higher stabilization of traps in the $\text{Y}_2\text{O}_2\text{S}$ crystal lattice, according to the defect conglomeration model proposed by Clabau *et al.* [162]. In this model, Mg^{2+} ions tend to migrate to the vicinity of Ti^{4+} and induce a local charge and orbital stabilization, forming defect clusters. Moreover, Mg^{2+} doping increases the concentration of anion vacancy defects (equation 3.1), which decreases Ti^{4+}

photoluminescence due to defect suppression (Figure 3.26) but enhances Ti^{4+} PersL by increasing the concentration of trapped charge carriers. These postulates are corroborated by the findings of Zhang *et al.* [98] and Cai'e Cui *et al.* [102].

III. Eu³⁺ doping: Eu^{3+} -activated $\text{Y}_2\text{O}_2\text{S}$ exhibits intense red photoluminescence but an inefficient hole-trapping PersL via VB. Ti^{4+} doping can enhance Eu^{3+} PersL in two ways. First, by increasing the concentration of hole traps (Equations 3.3 and 3.4). However, the PersL emission spectra is composed of both $\text{Eu}^{3+} \ ^5\text{D}_0 \rightarrow \ ^7\text{F}_2$ and Ti^{4+} CT emission bands with comparable intensities and decay profile. In addition, increasing Eu^{3+} concentration decreases the Ti^{4+} broadband contribution to the PersL spectra. Serendipitously, the PersL decay curves show a similar profile and decay time despite Eu^{3+} concentration. These results suggest a $\text{Ti}^{4+} \rightarrow \text{Eu}^{3+}$ PersL energy transfer process, as reported in [17,101,103]. For unambiguous confirmation of the $\text{Ti}^{4+} \rightarrow \text{Eu}^{3+}$ energy transfer, time-resolved spectroscopy studies will be performed soon in the $\text{Y}_2\text{O}_2\text{S}:\text{Eu}$ and $\text{Y}_2\text{O}_2\text{S}:\text{Eu},\text{Ti},\text{Mg}$ PersL materials.

In this sense, the nature of the Ti emission was assigned to a $\text{Ti}^{4+} \text{ d}^0$ charge transfer (CT) emission. This is corroborated by *i)* the large Stokes shift between Ti^{4+} CT absorption and emission energies, *ii)* the redshift of CT bands by reducing the RE^{3+} host cation radius [19], and *iii)* the PersL energy transfer process $\text{Ti}^{4+} \rightarrow \text{Eu}^{3+}$ PersL, mediated via a hole-trapping mechanism. One must recall that PersL in $\text{Y}_2\text{O}_2\text{S}:\text{Eu},\text{Ti},\text{Mg}$ can also be produced by exciting these materials with energies higher than the Eu^{3+} and Ti^{4+} LMCT (3.6 and 3.3 eV, respectively), *e.g.*, a band gap excitation (4.8 eV). Such irradiation energy promotes the excitation of e^- from the VB to the CB, which activates Ti^{4+} h^+ -trapping PersL via VB, but it might also trigger e^- -trapping PersL mechanisms via CB. In this context, the Mg^{2+} co-dopant could have an additional role, which is to increase the concentration of

e^- traps close to the bottom of CB (Equation 3.1) and further enhancing PersL decay time. Although an e^- -trapping PersL mechanism via CB using Ti^{3+} ions offers an elegant explanation for boosting the PersL by Ti,Mg co-doping, the presence of Ti^{3+} ions could still not be proven in rare earth oxysulfides. Therefore, the hypothesis of e^- -trapping PersL mechanism described in section 3.4.2 still needs further experimental data to be verified or discarded

Finally, we should now return to the two questions asked in the beginning of this section.

i) What charge carriers are truly responsible for the PersL of Eu and Ti ions? The h^+ was shown to be the main charge carrier instead of the e^- for the PersL of both singly doped $Y_2O_2S:Eu$ and co-doped $Y_2O_2S:Eu,Ti,Mg$ materials, in a PersL mechanism operating via the VB. *ii) Is there only one type of PersL mechanism operating?* So far, only the h^+ -trapping mechanism could be verified, where an e^- -trapping PersL mechanism still needs further investigation. However, $Ti^{4+} \rightarrow Eu^{3+}$ PersL energy transfer seems to have an important role on enhancing the Eu^{3+} PersL decay time. Further experiments should also be carried to verify the influence of tunneling processes in the overall PersL outcome. Therefore, even though some questions are still seeking for an answer, the synergic effect among the Eu^{3+},Ti^{4+},Mg^{2+} ions was revealed to be the responsible for the exceptional long red persistent luminescence in $Y_2O_2S:Eu,Ti,Mg$ materials.

3.5 RE₂O₂S-based luminescent colloidal nanocrystals (NCs)

3.5.1 Eu³⁺ as a spectroscopic probe for nano-RE₂O₂S

Previous sections dealt with the bulk (~1 μm) RE₂O₂S-based luminescent materials prepared by the microwave-assisted solid-state (MASS) synthesis. Now, aiming at luminescent nanomaterials (<50 nm), an organic-medium synthesis methodology was approached to synthesize colloidal RE₂O₂S-based (RE³⁺: Gd and Y) luminescent nanocrystals (NCs). It is worth noting that different methodologies reported in the literature [122,123] were reproduced in laboratory, but some flaws were faced, especially in handling the sulfur precursor, which prevented synthesis reproducibility. Lin *et al.* [122] employed CS₂ as the sulfur source, a highly volatile and toxic liquid. Lei *et al.* [123] uses elemental sulfur, but in huge molar excess (1 RE : 20 S) to guarantee the formation of the RE₂O₂S phase. Both cases were observed to cause explosions in the reaction medium during the synthesis.

Seeking for a straightforward and reproducible method, the synthesis methodology used in this work was adapted from Larquet *et al.* [124–127], which presented an one-step synthesis to achieve monodisperse RE₂O₂S NCs with fairly easy-to-control parameters (section 2.2). In a typical synthesis, RE(acac)₃, S, and Na(oleate) were stoichiometrically weighted and added to a 3-neck round flask containing the mixture of solvents 1-octadecene (ODE), oleylamine (OM), and oleic acid (OA). The system was degassed under vacuum (0.1 mbar) at T = 110 °C for 60 min. Then, the atmosphere was switched to N₂(g) and the reaction medium was directly heated up to 310 °C. After 30 min reacting at 310 °C, the system was cooled down to 70 °C to start the washing procedures.

Washing was shown to be crucial to isolate the obtained NCs from the excess of organic byproducts. In summary, a standard washing step consisted in precipitating the nanoparticles by adding ethanol and separating them from the organic fraction by centrifuging (3000 rpm). After the first centrifuging process, a grayish nanoparticle precipitate was observed to segregate from the yellow organic waste (Figure 3.31a). The supernatant was thus discarded, and the NCs were

redispersed in cyclohexane to produce a stable colloidal suspension. This washing procedure must be repeated until a clear supernatant plus a white nanoparticle precipitate is obtained. In the case of this work's syntheses, three times were shown to be enough (Figure 3.31b). All washing steps were performed in a dry N₂(g)-filled glovebox to avoid the decomposition of the RE₂O₂S NCs [124].

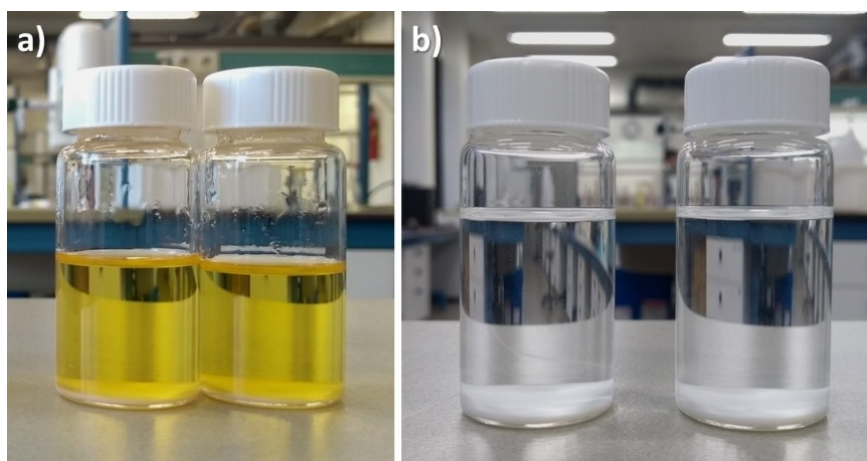


Figure 3.31 Product of colloidal synthesis after washing procedures, where one can notice the NCs deposited on the bottom of the vials: **a)** after first centrifuging and **b)** after third centrifuging procedure.

After several attempts, the synthesis of RE₂O₂S NCs could be carried out reproducibly. In this way, three groups of doped RE₂O₂S NCs were prepared: *i)* the “EuGroup”, in which the NCs were singly doped with the Eu³⁺ ion, *i.e.*, RE₂O₂S:Eu³⁺ (RE³⁺: Gd and Y); *ii)* the “UC-Group”, doping Gd₂O₂S NCs with Er³⁺ and Yb³⁺ aiming at upconversion nanoparticles; and *iii)* the “PersL-Group”, seeking persistent luminescence in colloidal RE₂O₂S:Eu,Ti,Mg nanomaterials (RE³⁺: Gd and Y).

The first group, *i.e.*, RE₂O₂S:Eu³⁺ NCs, was prioritized since the Eu³⁺ ion can be used as local spectroscopic probe to investigate the formation of the oxysulfide crystal phase. The Eu³⁺ ⁵D₀→⁷F₂ emission is an electronic transition allowed by the forced electric dipole mechanism, being hypersensitive to changes in the chemical environment. This emission band is located at ~626 nm if the Eu³⁺ is allocated in the C_{3v} site of the RE₂O₂S structure (Figure 3.25b) [117,174], and at ~613 nm

for the C₂ (and S₆) sites of c-RE₂O₃ [154]. In this way, by synthesizing Eu³⁺-doped RE₂O₂S NCs it is possible to assign if the desired oxysulfide crystal phase was obtained instead of the oxide.

The formation of rare earth oxysulfide nanomaterials was investigated by transmission electron microscopy (TEM). TEM image of the Eu1 sample – Gd₂O₂S:Eu³⁺ 4% (Figure 3.32a) reveals nanocrystals with irregular morphologies but exhibiting a homogeneous size distribution of ~20 nm. These NCs undergo agglomeration processes, probably due to the exclusion of a portion of ligand molecules from their surfaces after consecutive washing steps. The size and morphology of the obtained nanocrystals are similar to those RE₂O₂S reported by Larquet *et al.* [124,126,127].

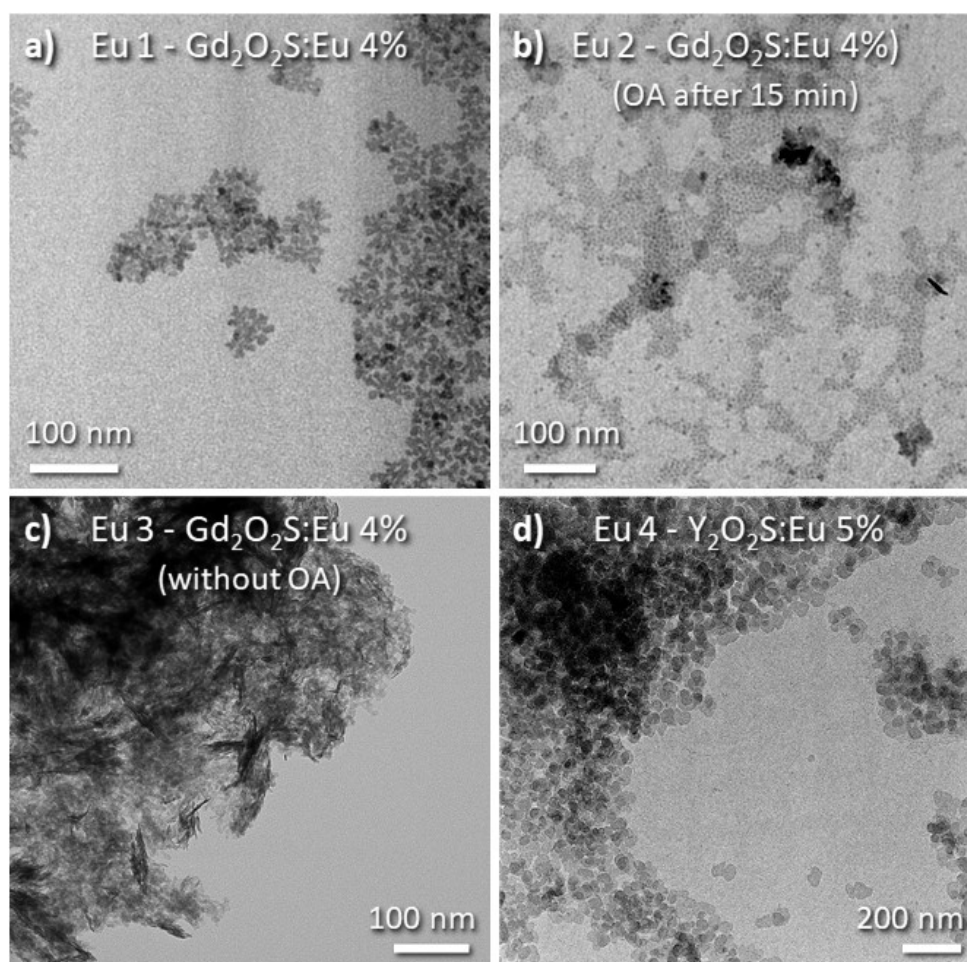


Figure 3.32 Transmission electron microscopy (TEM) images of RE₂O₂S:Eu³⁺ nanocrystals (RE³⁺: Gd and Y, OA: oleic acid): **a)** Eu1 – Gd₂O₂S:Eu³⁺_(4%) synthesized by the colloidal synthesis using standard procedures, **b)** Eu2 – Gd₂O₂S:Eu³⁺_(4%) adding OA after 15 min of synthesis, **c)** Eu3 – Gd₂O₂S:Eu³⁺_(4%) synthesis without OA, and **d)** Eu4 – Y₂O₂S:Eu³⁺_(5%) conventional synthesis.

OA is known as one of the main ligands/surfactants to aid the synthesis of metal nanoparticles and prevent aggregation. Nevertheless, the OM employed as a reducing agent and sulfur precursor in the preparation of nano-RE₂O₂S can also act as a ligand. Therefore, the influence of OA addition on the formation of Gd₂O₂S:Eu³⁺ NCs was investigated in this work. [Figure 3.32b](#) displays the TEM image of Gd₂O₂S:Eu³⁺ 4% NCs (sample Eu2) obtained when OA was added 15 minutes after the reaction medium reached T = 310 °C instead of being added in the beginning together with ODE and OM as for sample Eu1. The particle size was drastically reduced to <10 nm in comparison with Eu1 – Gd₂O₂S:Eu³⁺ 4% NCs ([Figure 3.32a](#)) but maintaining the small size polydispersity. This result is promising when considering biological and medicinal fields, where sub-nanometric (<10 nm) NCs are desired for different applications, such as in bioimaging, optical thermometry, and theranostics.

TEM image of Eu3 – Gd₂O₂S:Eu³⁺ 4% NCs obtained with no OA at all ([Figure 3.32c](#)) reveal even further changes in the NCs formation. Particles now showed to strongly agglomerate, creating bundle arrays of NCs. It is worth noting that, to exclude all oleate influence in the synthesis of this nanomaterial, the sodium oleate was substituted by sodium acetate. One possibility is that the desired Gd₂O₂S phase was successfully formed by OM being the only ligand present, but the absence of oleates led to a more pronounced nanoparticle packing, which impossibilities the extraction of parameters such as the nanocrystal size. In the case of Eu4 sample – Y₂O₂S:Eu³⁺ 5% ([Figure 3.32d](#)), the synthesis conditions were the same as for Eu1, *i.e.*, OA added together with ODE and OM. TEM image indicates rather cubic NCs with homogeneous sizes, with average particle size (~50 nm) much larger than the 20 nm obtained for sample Eu1 – Gd₂O₂S:Eu³⁺. This increase in particle diameter is probably linked to the chemical differences between the Gd³⁺ and Y³⁺ ions, which also influences the formation of bulk RE₂O₂S.

[Figure 3.33](#) exhibits the photoluminescence characterization of the RE₂O₂S:Eu³⁺ nanocrystals (RE³⁺: Gd and Y). Samples were measured in colloidal form using quartz cuvettes. First analyzing the emission spectra ([Figure 3.33b](#)), one can observe that the emission band relative to the Eu³⁺

$^5D_0 \rightarrow ^7F_2$ transition is centered at 626 nm for RE^{3+} : Gd, proving that the Gd nanomaterials (Eu1, Eu2 and Eu3) correspond to the Gd_2O_2S crystal phase. Indeed, the $Gd_2O_2S:Eu^{3+}$ NCs exhibited high luminescence efficiency in cyclohexane suspension under UV (365 nm) excitation (Figure 3.33c).

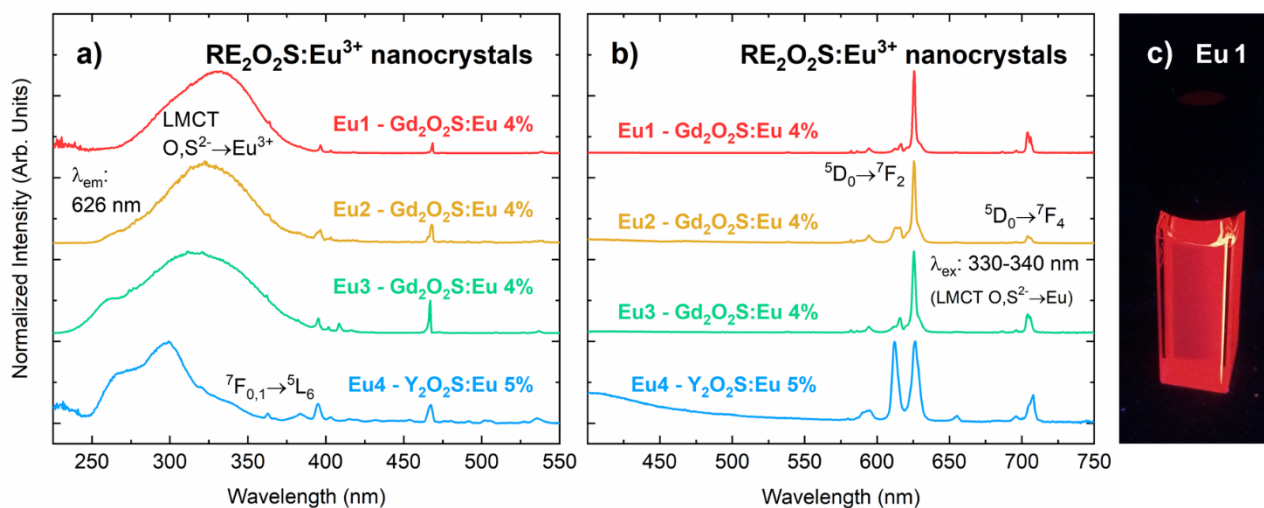


Figure 3.33 Photoluminescence **a)** excitation and **b)** emission spectra of $RE_2O_2S:Eu^{3+}$ nanocrystals (RE^{3+} : Gd and Y). Inset picture: emission of the Eu1 colloidal nanocrystals material under UV excitation (365 nm).

Furthermore, samples Eu2 and Eu3 exhibit a similar emission spectrum profile, demonstrating that the oxysulfide structure could be formed with a delayed OA addition or even in the total absence of oleates in the reaction medium. Larquet *et al.* [127] studied the RE_2O_2S nanoparticle formation mechanism via SAXS measurements and proposed an alkali-stabilized oleate mesophase acting as a template for NC nucleation and growth. In this way, OM appears to work similarly as oleates forming this template mesophase if alkali ions are present as charge stabilizers [121]. However, TEM images (Figure 3.32) suggest distinct nucleation/growth mechanisms for OM-only syntheses.

In contrast, the emission spectra of Eu4 nanomaterial – $Y_2O_2S:Eu^{3+}$ 5% exhibits two narrow emission bands with equal intensities, centered at 612 and 626 nm. This indicates that the Eu4 nanomaterial is a mixed $Y_2O_2S:Eu/Y_2O_3:Eu$ product, which may also explain the larger particle size

observed in TEM (Figure 3.32d) compared to the Gd nanocrystals. The excitation spectra (Figure 3.33a) corroborate these results, once the spectral profile of the $O^{2-} \rightarrow Eu^{3+}$ and $S^{2-} \rightarrow Eu^{3+}$ LMCT bands for the Eu1, Eu2, and Eu3 samples match the CT absorption band in $Gd_2O_2S:Eu^{3+}$ bulk materials. For the Eu4 sample, however, the higher contribution of the absorption band at around 265 nm, *i.e.*, $O^{2-} \rightarrow Eu^{3+}$ LMCT in Y_2O_3 , demonstrates the presence of the Y_2O_3 oxide phase in these NCs, directly impacting the $Y_2O_2S:Eu^{3+}$ photoluminescence behavior. Furthermore, these NCs exhibited high colloidal stability, as their emission profile remained unchanged for months after synthesis.

3.5.2 Attempting UC and PersL RE_2O_2S NCs by the colloidal synthesis method

$Gd_2O_2S:Eu^{3+}$ NCs were successfully obtained, exhibiting high luminescence efficiency under UV excitation. In this context, $Gd_2O_2S:Er^{3+}$ and $Gd_2O_2S:Er^{3+},Yb^{3+}$ nanomaterials were also synthesized by the colloidal synthesis method (adding OA together with all chemicals), aiming at the upconversion (UC) phenomenon at the nanoscale. TEM image of UC1 sample – $Gd_2O_2S:Er^{3+}_{(5\%)}$ (Figure 3.34a) exposes similar NCs to those of Eu1 – $Gd_2O_2S:Eu^{3+}_{(4\%)}$ nanomaterial (Figure 3.32a), *i.e.*, monodisperse particle size with an average diameter of 15–20 nm. This result indicates that the formed NCs also correspond to the Gd_2O_2S phase as the synthesis procedures were identical.

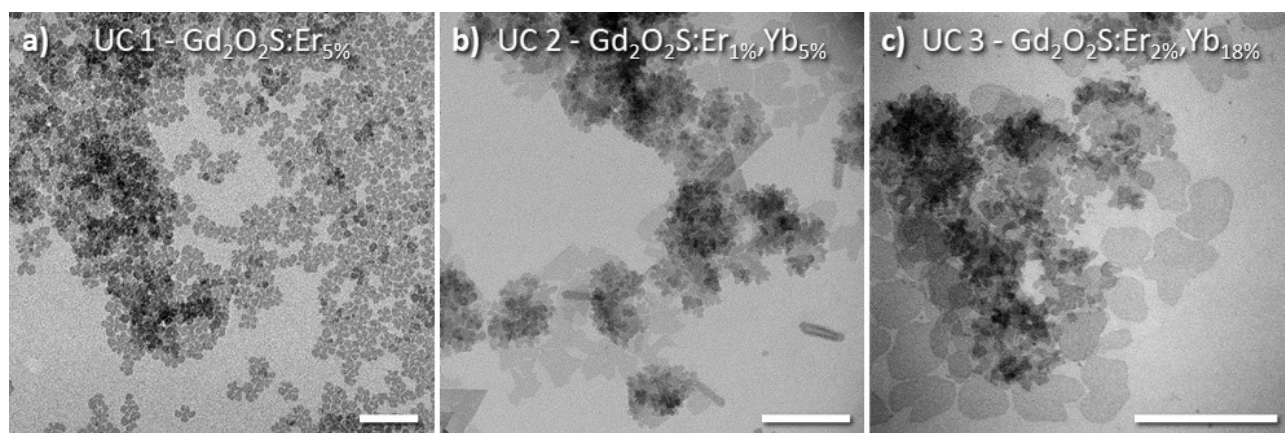


Figure 3.34 TEM images of $Gd_2O_2S:Er^{3+}$ and $Gd_2O_2S:Er^{3+},Yb^{3+}$ nanocrystals: **a)** UC1 – $Gd_2O_2S:Er^{3+}_{(5\%)}$, **b)** UC2 – $Gd_2O_2S:Er^{3+}_{(1\%)},Yb^{3+}_{(5\%)}$, and **c)** UC3 – $Gd_2O_2S:Er^{3+}_{(2\%)},Yb^{3+}_{(18\%)}$. Scale bars = 100 nm.

On the other hand, for the nanomaterials co-doped with the Yb^{3+} ion, *i.e.*, UC2 – $\text{Gd}_2\text{O}_2\text{S}:\text{Er}^{3+}_{(1\%)},\text{Yb}^{3+}_{(5\%)}$ (Figure 3.34b) and UC3 – $\text{Gd}_2\text{O}_2\text{S}:\text{Er}^{3+}_{(2\%)},\text{Yb}^{3+}_{(18\%)}$ (Figure 3.34c), the nanocrystals were formed in a considerably different way. Two different particle populations were spotted, one similar to those observed for UC1 (monodisperse 15–20 nm NCs), and thin plates in the 30–80 nm size range, exhibiting variable shapes. These observations suggest a phase segregation process for these samples, generating different products additionally to the desired $\text{Gd}_2\text{O}_2\text{S}$ phase. A probable explanation for the two crystalline populations would be the presence of the Yb^{3+} ion, which has a higher Pearson's acidic character compared to the Gd^{3+} host [16]. This issue is the same for the bulk materials as discussed in previous sections. The higher the energy to form RE–S bonds, the harder will be the incorporation of Ln^{3+} dopants in the $\text{Gd}_2\text{O}_2\text{S}$ crystalline structure [152].

Upconversion (UC) emission spectra of the $\text{Gd}_2\text{O}_2\text{S}:\text{Er}^{3+}$ and $\text{Gd}_2\text{O}_2\text{S}:\text{Er}^{3+},\text{Yb}^{3+}$ NCs were registered by exciting their colloidal suspensions (in cyclohexane) with a 980 nm continuous wave laser (Figure 3.35a). Unfortunately, a very weak UC emission was measured for all three samples. The $\text{Er}^{3+} \ ^4\text{S}_{3/2} \rightarrow \ ^4\text{I}_{15/2}$ transition could be detected with a signal slightly above the background noise level by increasing the integration time to 2 s under large emission slits (bandpass: 5 nm). The same laser power (500 mW) was used in all measurements.

Given that the $\text{Gd}_2\text{O}_2\text{S}:\text{Eu}^{3+}$ NCs exhibited intense luminescence under UV excitation (Figure 3.33), the luminescence quenching observed for $\text{Gd}_2\text{O}_2\text{S}:\text{Er}^{3+}$ and $\text{Gd}_2\text{O}_2\text{S}:\text{Er}^{3+},\text{Yb}^{3+}$ NCs can be explained by the non-radiative decay of Er^{3+} ions assisted by vibrational levels of ligand molecules (Figure 3.35b). It was demonstrated for $\text{NaYF}_4:\text{Er}^{3+},\text{Yb}^{3+}$ NCs that solvent vibrations comprise an important quenching pathway for excited Er^{3+} ions as the C–H stretching energies (2800–3000 cm^{-1}) matches the energy difference between the $\ ^4\text{S}_{3/2} / \ ^4\text{F}_{9/2}$ and $\ ^4\text{F}_{9/2} / \ ^4\text{I}_{9/2}$ levels in Er^{3+} ions [58]. Additionally, OA/OM ligands attached to the NCs surface exert an extra quenching route due to the high-energy O–H and N–H vibrations. These quenching mechanisms have less influence in the luminescence of Eu^{3+} -doped oxysulfides since the energy difference between the excited $\ ^5\text{D}_0$ and

fundamental 7F_J levels is greater than the solvent vibrational levels. Hence, the $\text{Eu}^{3+} {}^5D_{3-1}$ levels, once populated by UV excitation, decay non-radiatively to the 5D_0 level, which radiatively decays the ${}^7F_{0-6}$ ground states (Figure 3.35b).

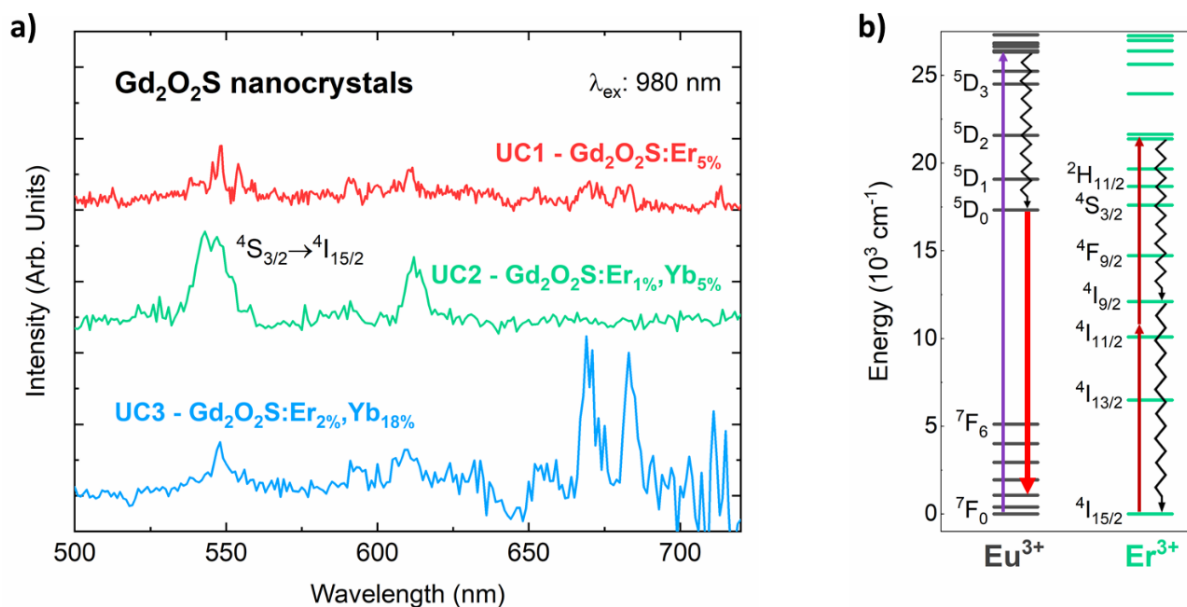


Figure 3.35 a) Upconversion (UC) emission spectra (λ_{ex} : 980 nm) of $\text{Gd}_2\text{O}_2\text{S}:\text{Er}^{3+}$ and $\text{Gd}_2\text{O}_2\text{S}:\text{Er}^{3+},\text{Yb}^{3+}$ nanocrystals prepared with different Er^{3+} and Yb^{3+} concentrations. **b)** Energy level diagram demonstrating the radiative decay of Eu^{3+} and the luminescence quenching of Er^{3+} in colloidal nanocrystals.

As reported by Rabouw *et al.* [58], one possibility to reduce solvent/ligand quenching is by synthesizing core-shell NPs, *i.e.*, growing an optically inert NaYF_4 shell over the $\text{NaYF}_4:\text{Er}^{3+},\text{Yb}^{3+}$ UCNPs. For the case of sodium yttrium fluorides, experimental protocols are already available to prepare such core-shell structures [59]. This is not the case for rare earth oxysulfides, especially concerning the synthesis of colloidal NCs. Therefore, a new core-shell nanomaterial was synthesized, *i.e.*, UC4 – $\text{Gd}_2\text{O}_2\text{S}:\text{Er}^{3+}_{(2\%)},\text{Yb}^{3+}_{(18\%)}@\text{Gd}_2\text{O}_2\text{S}$. Preparation procedure consisted of performing the synthesis of undoped $\text{Gd}_2\text{O}_2\text{S}$ matrix, but adding $\text{Gd}_2\text{O}_2\text{S}:\text{Er}^{3+}_{(2\%)},\text{Yb}^{3+}_{(18\%)}$ NCs (UC3) together with all chemicals to act as seeds for the nucleation of the core-shell nanostructures. The amount of precursor material was calculated to cover NCs of 20 nm in diameter, generating a 10 nm thick shell.

TEM image of the UC4 sample – $\text{Gd}_2\text{O}_2\text{S}:\text{Er}^{3+}_{(2\%)}, \text{Yb}^{3+}_{(18\%)}@\text{Gd}_2\text{O}_2\text{S}$ (Figure 3.36) reveals particles with monodisperse size (20–30 nm) and very similar morphology to the NCs observed for samples Eu1 (Figure 3.32a) and UC1 (Figure 3.34a). This suggests that undoped $\text{Gd}_2\text{O}_2\text{S}$ NCs must have crystallized independently rather than forming core-shell nanostructures, which corroborates to the low UC intensity of this nanomaterial (figure not shown, but similar as for the previous UC1, UC2, and UC3 samples). The possibility of achieving upconversion from colloidal $\text{Gd}_2\text{O}_2\text{S}:\text{Er}^{3+}, \text{Yb}^{3+}$ nanomaterials is not ruled out from these results. However, improvements in the synthesis methodology are necessary, especially concerning the inclusion of Yb^{3+} dopant in the oxysulfide structure and the methodological optimization to prepare core-shell nanostructures.

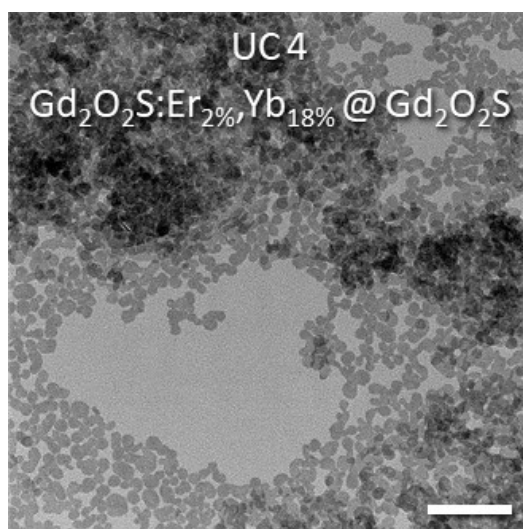


Figure 3.36 TEM image of UC4 – $\text{Gd}_2\text{O}_2\text{S}:\text{Er}^{3+}_{(2\%)}, \text{Yb}^{3+}_{(18\%)}@\text{Gd}_2\text{O}_2\text{S}$ nanocrystals. Scale bar = 100 nm.

Finally, $\text{RE}_2\text{O}_2\text{S}$ colloidal NCs were synthesized doped with Eu^{3+} , Ti^{4+} and Mg^{2+} ions, seeking the phenomenon of persistent luminescence (PersL). Figure 3.37 shows the photoluminescence spectra of the $\text{Gd}_2\text{O}_2\text{S}:\text{Eu}, \text{Ti}, \text{Mg}$ (PersL1) and $\text{Y}_2\text{O}_2\text{S}:\text{Eu}, \text{Ti}, \text{Mg}$ (PersL2) nanomaterials. Both excitation and emission spectral profiles are similar for the two samples. Excitation spectra show the $\text{O}^{2-} \rightarrow \text{Eu}^{3+}$ and $\text{S}^{2-} \rightarrow \text{Eu}^{3+}$ LMCT broad absorption bands (270–400 nm), together with the narrow ${}^7\text{F}_{0,1} \rightarrow {}^5\text{L}_6$ and ${}^7\text{F}_{0,1} \rightarrow {}^5\text{L}_6$ absorption bands of the Eu^{3+} ion. The emission spectra show the ${}^5\text{D}_0 \rightarrow {}^7\text{F}_2$

emission band centered at 626 nm for both nanomaterials, corresponding to the Eu^{3+} ion introduced in the C_{3v} site of the oxysulfide crystal structure. It is important to mention that, unlike the Eu^{3+} -doped $\text{Y}_2\text{O}_2\text{S}:\text{Eu}$ nanomaterial, PersL2 – $\text{Y}_2\text{O}_2\text{S}:\text{Eu},\text{Ti},\text{Mg}$ NCs exhibited an emission profile which corresponds to the pure $\text{Y}_2\text{O}_2\text{S}$ crystal phase. Thus, it was found that the fine adjustment of the synthesis parameters can lead to pure phase $\text{Y}_2\text{O}_2\text{S}$ nanomaterials, despite the harder acidic character of Y^{3+} compared to Gd^{3+} . This promising result also shows the possibility of including the Yb^{3+} ion in the structure of UC nanomaterials, as well as the colloidal preparation of even more challenging oxysulfides, *e.g.*, nano- $\text{Lu}_2\text{O}_2\text{S}$ materials.

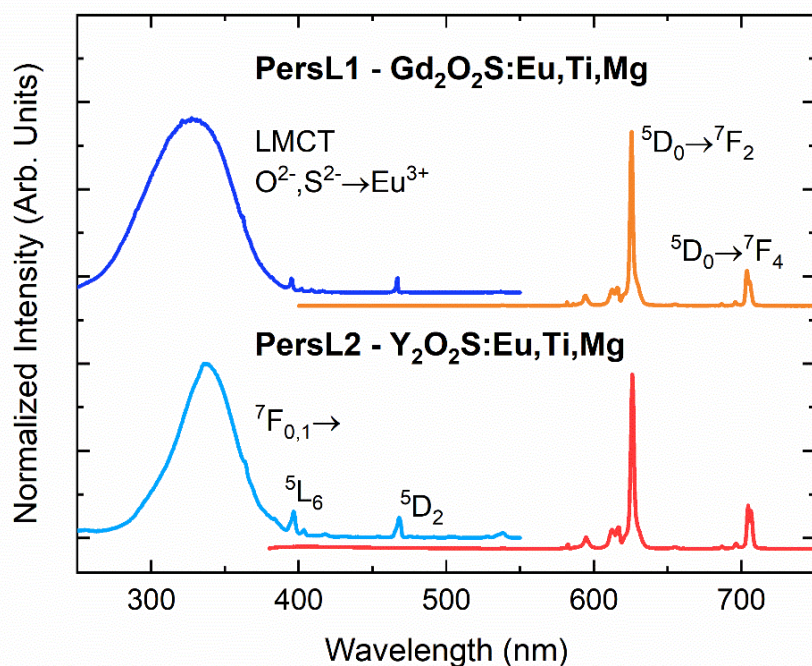


Figure 3.37 Photoluminescence **a**) excitation and **b**) emission spectra of $\text{RE}_2\text{O}_2\text{S}:\text{Eu}^{3+}_{(5\%)},\text{Ti}^{4+}_{(3.4\%)},\text{Mg}^{2+}_{(4.5\%)}$ nanocrystals (RE^{3+} : Gd and Y).

Both $\text{Gd}_2\text{O}_2\text{S}:\text{Eu},\text{Ti},\text{Mg}$ and $\text{Y}_2\text{O}_2\text{S}:\text{Eu},\text{Ti},\text{Mg}$ nanomaterials showed intense red luminescence in colloidal form under UV excitation, similarly to the Eu^{3+} singly doped NCs (Figure 3.33). However, when removing the excitation source, none of them exhibited any detectable persistent luminescence. Comparable to UC phenomenon, PersL also suffers from various quenching

mechanisms when the materials are synthesized in the nanoscale. As formerly emphasized, the main quenching pathway is the non-radiative relaxation from the vibrational modes of solvent molecules and ligands attached to the surface of NCs. One strategy adopted in literature is to heat up the NCs at high temperatures (>600 °C), eliminating organic ligands and stabilizing the defects responsible for energy storage in the PersL material [102].

Despite the hard-to-avoid quenching mechanism operating in the nanoscale, the intense red emission achieved for $\text{RE}_2\text{O}_2\text{S}:\text{Eu}^{3+}$ nanocrystals already characterize a significant starting point to achieve chemically stable and highly luminescent colloidal nanomaterials with potential for applications in monitoring biological processes *in vitro* and *in vivo*. In this context, a new synthetic approach is necessary to be develop core-shell $\text{RE}_2\text{O}_2\text{S}$ nanostructures to efficiently remove the organic ligands from the nanocrystals surface, without losing the intrinsic and desired properties of the photonic nanomaterials.

Chapter 4

Conclusion and perspectives

4.1 Conclusion

4.2 Perspectives

4. CONCLUSION AND PERSPECTIVES

4.1 Conclusion

Optical materials based on rare earth oxysulfide systems have been known for decades, being applied as *e.g.*, red pigments in LED screens and photodetectors for computerized X-ray tomography. However, synthesizing high quality RE₂O₂S materials (RE³⁺: La, Gd, and Y) is challenging, both at the microscale and at the nanoscale, the latter being attractive for applications in imaging and monitoring biological processes. In this doctorate work, such obstacles were overcome by successfully preparing highly luminescent RE₂O₂S-based materials by two different synthetic approaches: *i*) the microwave-assisted solid-state (MASS) synthesis, which produced bulk (~1 μm) materials displaying a variety of optical phenomena, and *ii*) the colloidal synthesis in organic medium, yielding RE₂O₂S:Eu³⁺ nanomaterials (<50 nm) exhibiting intense red emission in colloidal form.

The MASS synthesis parameters were deeply investigated through an extensive *ex-situ* characterization of the RE₂O₂S matrices formed as a function of microwave irradiation time. Results pointed that the conversion of the RE₂O₃ + S precursors into RE₂O₂S starts with the redox reactions between S and the Na₂CO₃ flux at T < 500 °C. By using activated carbon as the microwave susceptor, such temperatures were achieved in ~1 minute of microwave irradiation. This rapid rising in temperature led to the production RE₂O₂S materials with high crystal purity within just 10 minutes of synthesis. The optimized MASS synthesis condition was evaluated as the two-step synthesis of 25 minutes each step, in which pure Y₂O₂S crystal phase was obtained. Furthermore, this 50-min synthesis consisted in a reduction of ≥ 85% in processing time and of ≥ 95% in energy consumption when comparing the MASS method to conventional solid-state synthesis methods. In this way, the optimized MASS parameters were applied to synthesize several RE₂O₂S-based luminescent materials, designed to display diverse photonic phenomena: ***scintillation*** – Gd₂O₂S:Tb, ***upconversion*** – Gd₂O₂S:Er(Yb), and ***persistent luminescence*** – RE₂O₂S:Eu(Yb),Ti,Mg.

The influence of the MASS synthesis time in the luminescence outcome was confirmed for $\text{Gd}_2\text{O}_2\text{S:Tb}^{3+}$ scintillators as two different materials were prepared, *i.e.*, one-step synthesis of 10 minutes ($\text{Gd}_2\text{O}_2\text{S:Tb}^{3+}$ - 10) and two-step synthesis of 25 minutes each step ($\text{Gd}_2\text{O}_2\text{S:Tb}^{3+}$ - 50). SR-XRD data showed that the $\text{Gd}_2\text{O}_2\text{S:Tb}^{3+}$ - 10 material was composed of 96% $\text{Gd}_2\text{O}_2\text{S}$ / 4% Gd_2O_3 , while the $\text{Gd}_2\text{O}_2\text{S:Tb}^{3+}$ - 50 exhibited pure oxysulfide phase. Due to its absence of point defects and impurity phases confirmed by SR-XRD and SR-VUV spectroscopy, the $\text{Gd}_2\text{O}_2\text{S:Tb}^{3+}$ - 50 exhibited superior photoluminescence and scintillation performances, opening paths to applications such as low-cost and highly-photostable X-ray imaging materials. Moreover, $\text{Gd}_2\text{O}_2\text{S:Er}^{3+}$ and $\text{Gd}_2\text{O}_2\text{S:Er}^{3+},\text{Yb}^{3+}$ upconversion (UC) materials were synthesized by the MASS method, employing the optimized two-step synthesis of 25 min each step. By substituting the oxide precursors by hydroxycarbonates $\text{Ln}(\text{OH})\text{CO}_3$ (Ln^{3+} : Gd, Er, and Yb), UC materials could be obtained with pure oxysulfide phase even at higher $\text{Er}^{3+},\text{Yb}^{3+}$ concentrations, yielding higher UC efficiencies. The $\text{Ln}(\text{OH})\text{CO}_3$ was then attested as good alternative precursors for MASS syntheses. In addition, different ($^4\text{S}_{3/2} \rightarrow ^4\text{I}_{15/2}$) / ($^4\text{F}_{9/2} \rightarrow ^4\text{I}_{15/2}$) emission ratios were calculated for singly doped and co-doped materials, suggesting distinct UC sensitizing/quenching mechanisms of the excited Er^{3+} levels. These results contribute to the development of optimized UC materials, reducing luminescence quenching and determining the fundamental limits of UC efficiency.

Versatile doped $\text{RE}_2\text{O}_2\text{S}$ -based materials were prepared exhibiting persistent luminescence (PersL). Initially, PersL originated from Ti ions in $\text{RE}_2\text{O}_2\text{S:Ti,Mg}$ inspired the fabrication of an innovative self-sustained LED device. The $\text{Y}_2\text{O}_2\text{S:Ti}^{4+},\text{Mg}^{2+}$ was shown to yield efficient warm-white light emission when sensitized by an UV LED chip. When turning the LED off, the device exhibited the additional self-sustained orange-color emission, which could be detected for several minutes. Such devices can be useful for applications in solid-state lighting with a built-in emergency light feature. Then, focus relied on researching near-infrared (NIR) PersL materials. A HRBE-guided substitution of Yb^{3+} into the $\text{Y}_2\text{O}_2\text{S:Eu,Ti,Mg}$ was performed, and a new NIR PersL was therefore

designed – $\text{Y}_2\text{O}_2\text{S}:\text{Yb},\text{Ti},\text{Mg}$. The PersL decay time in $\text{Y}_2\text{O}_2\text{S}:\text{Yb}$ was significantly enhanced by Ti,Mg co-doping. Furthermore, PersL emission spectra of the $\text{Y}_2\text{O}_2\text{S}:\text{Yb},\text{Ti},\text{Mg}$ material was composed by the Ti^{4+} CT emission (500–800 nm) together with $\text{Yb}^{3+} \ ^2\text{F}_{5/2} \rightarrow \ ^2\text{F}_{7/2}$ transitions (950–1050 nm), both being detected for almost one hour after ceasing the excitation.

The PersL mechanism operating for $\text{Y}_2\text{O}_2\text{S}:\text{Eu},\text{Ti},\text{Mg}$ materials is still an issue in the spectroscopy community due to the difficulty on assigning the diverse processes involving the charge carrier storage and release. In this work, a comprehensive explanation for the main doubts was constructed based on a series of PersL spectroscopy and thermoluminescence (TL) experiments performed on $\text{Y}_2\text{O}_2\text{S}:\text{Eu}$ and $\text{Y}_2\text{O}_2\text{S}:\text{Eu},\text{Ti},\text{Mg}$ materials. The nature of the Ti emission band was defined as a Ti^{4+} CT emission. Moreover, both $\text{Eu}^{3+} \ ^5\text{D}_0 \rightarrow \ ^7\text{F}_J$ and Ti^{4+} CT emission bands compose the PersL emission spectra, similarly as for the Yb^{3+} -doped materials. Surprisingly Increasing Eu^{3+} concentration reduces the Ti^{4+} contribution to the PersL spectra, without significant disturbances in the PersL decay curves. TL glow curves showed that the trap structures for $\text{Y}_2\text{O}_2\text{S}:\text{Eu}$ and $\text{Y}_2\text{O}_2\text{S}:\text{Ti},\text{Mg}$ are combined in the $\text{Y}_2\text{O}_2\text{S}:\text{Eu},\text{Ti},\text{Mg}$ materials. From these results, the supremacy of this red-emitting PersL material is explained by a synergic effect among the Eu^{3+} , Ti^{4+} , and Mg^{2+} dopants, involving a $\text{Ti}^{4+} \rightarrow \text{Eu}^{3+}$ persistent energy transfer process mediated by a h^+ -trapping mechanism via the valence band of the $\text{Y}_2\text{O}_2\text{S}$ host.

Additionally to those contributions, the MASS method can be even further improved by investigating other synthesis parameters: *i)* vary the Ln : S : Na_2CO_3 stoichiometry, *ii)* pellet the precursor mixture to increase surface contact, *iii)* perform a higher number of heat treatments under microwave irradiation, and *iv)* employ different precursors such as $\text{RE}(\text{OH})\text{CO}_3$ to prepare optically versatile materials. Besides, laboratory microwave ovens are available for solid-state synthesis, permitting better control of the synthesis parameters. Such upgrade allows a deep investigation on the influence of ion/defect migration through a crystal lattice as a function of microwave irradiation time, extending the study of particle formation to a wide range of advanced photonic materials.

Lastly, moving from the bulk materials obtained by the MASS method, colloidal luminescent nanomaterials (<50 nm) based ($\text{RE}_2\text{O}_2\text{S}$, RE^{3+} : Gd and Y) were also a target of study in this thesis. A one-step synthesis method was successfully adapted to the preparation of $\text{RE}_2\text{O}_2\text{S}$ nanocrystals (NCs), employing $\text{RE}(\text{acac})_3$, S, and Na(oleate) as precursors, dissolved in the well-known ODE/OA/OM solvent mixture. Monodisperse (~20 nm) $\text{Gd}_2\text{O}_2\text{S}$ NCs were obtained by this methodology in a reproducible manner. The influence of OA in the synthesis was investigated, providing novel results on the particle formation and size control. $\text{Gd}_2\text{O}_2\text{S}:\text{Er}^{3+}$ NCs suffered from solvent quenching, resulting in a weak UC emission. On the other hand, $\text{Gd}_2\text{O}_2\text{S}:\text{Eu}^{3+}$ NCs exhibited strong red luminescence, originated from the $\text{Eu}^{3+} \ ^5\text{D}_0 \rightarrow \ ^7\text{F}_2$ transition 626 nm. Furthermore, these NCs showed long colloidal stability as their emission profile remained unchanged in months. Therefore, the synthesized colloidal $\text{Gd}_2\text{O}_2\text{S}:\text{Eu}^{3+}$ is a promising nanomaterial for applications as optical probes for bioimaging *in vitro*, where the intense red emission could easily overcome thin tissue barriers.

4.2 Perspectives

- Further improve the MASS synthesis parameters to obtain $\text{RE}_2\text{O}_2\text{S}$ -based photonic materials with higher quantum efficiencies to match commercially available samples.
- Perform a time-resolved spectroscopy study for the series of bulk $\text{Gd}_2\text{O}_2\text{S}:\text{Er}^{3+}(\text{Yb}^{3+})$ UC materials to investigate the energy transfer and quenching processes.
- Explore the persistent luminescence mechanism of $\text{Y}_2\text{O}_2\text{S}:\text{Eu}^{3+}, \text{Ti}^{4+}, \text{Mg}^{2+}$ materials using new optical techniques such as luminance measurements and time-resolved spectroscopy.
- Improve the colloidal synthesis method to develop core-shell nanostructures, aiming at $\text{RE}_2\text{O}_2\text{S}$ -based optical nanoprobe with even higher potential for biological applications.
- Extend both the MASS method and the colloidal synthesis to prepare new host matrices, targeting at novel and highly efficient advanced photonic materials.

References

- [1] KLINGER, J.M. “A historical geography of rare earth elements: From discovery to the atomic age.,” *The Extractive Industries and Society*. v. 2, p. 572–580, 2015.
- [2] LUCAS, J.; LUCAS, P.; LE MERCIER, T.; ROLLAT, A.; DAVENPORT, W. *Rare Earths: Science, Technology, Production and Use*. Amsterdam: Elsevier, 2015.
- [3] BLASSE, G.; BRIL, A. A new phosphor for flying-spot cathode-ray tubes for color television: yellow-emitting $\text{Y}_3\text{Al}_5\text{O}_{12}:\text{Ce}^{3+}$, *Applied Physics Letters*. v. 1, p. 53–55, 1967.
- [4] ADVANCED INFORMATION. NOBELPRIZE.ORG. NOBEL MEDIA AB 2021. MON. 15 FEB 2021. <[HTTPS://WWW.NOBELPRIZE.ORG/PRIZES/PHYSICS/2014/ADVANCED-INFORMATION/](https://www.nobelprize.org/prizes/physics/2014/advanced-information/)>
- [5] PUST, P.; SCHMIDT, P.J.; SCHNICK, W. A revolution in lighting, *Nature Materials*. v. 14, p. 454–458, 2015.
- [6] DUJARDIN, C.; AUFRAY, E.; BOURRET-COURCHESNE, E.; ET AL. Needs, trends, and advances in inorganic scintillators, *IEEE Transactions on Nuclear Science*. v. 65, p. 1977–1997, 2018.
- [7] ZHOU, J.; LIU, Q.; FENG, W.; SUN, Y.; LI, F. Upconversion luminescent materials: Advances and applications, *Chemical Reviews*. v. 115, p. 395–465, 2015.
- [8] LIU, X.; YAN, C.H.; CAPOBIANCO, J.A. Photon upconversion nanomaterials, *Chemical Society Reviews*. v. 44, p. 1299–1301, 2015.
- [9] BRITO, H.F.; HÖLSÄ, J.; LAAMANEN, T.; LASTUSAARI, M.; MALKAMÄKI, M.; RODRIGUES, L.C.V. Persistent luminescence mechanisms: human imagination at work, *Optical Materials Express*. v. 2, p. 371, 2012.
- [10] VAN DEN EECKHOUT, K.; SMET, P.F.; POELMAN, D. Persistent luminescence in Eu^{2+} -doped compounds: A review, *Materials*. v. 3, p. 2536–2566, 2010.
- [11] EECKHOUT, K. VAN DEN; POELMAN, D.; SMET, P.F. Persistent Luminescence in Non- Eu^{2+} -Doped Compounds: A Review, *Materials*. v. 6, p. 2789–2818, 2013.
- [12] LARQUET, C.; CARENCO, S. Metal Oxysulfides: From Bulk Compounds to Nanomaterials, *Frontiers in Chemistry*. v. 8, p. 179, 2020.
- [13] KANG, C.C.; LIU, R.S.; CHANG, J.C.; LEE, B.J. Synthesis and Luminescent Properties of a New Yellowish-Orange Afterglow Phosphor $\text{Y}_2\text{O}_2\text{S}:\text{Ti},\text{Mg}$, *Chemistry of Materials*. v. 15, p. 3966–3968, 2003.
- [14] WANG, F.; CHEN, X.; LIU, D.; YANG, B.; DAI, Y. Experimental and theoretical study of pure and doped crystals: $\text{Gd}_2\text{O}_2\text{S}$, $\text{Gd}_2\text{O}_2\text{S}:\text{Eu}^{3+}$ and $\text{Gd}_2\text{O}_2\text{S}:\text{Tb}^{3+}$, *Journal of Molecular Structure*. v. 1020, p. 153–159, 2012.
- [15] KATARIA, V.; MEHTA, D.S. Impact of firing temperature on multi-wavelength selective Stokes and anti-Stokes luminescent behavior by $\text{Gd}_2\text{O}_2\text{S}:\text{Er},\text{Yb}$ phosphor and its application in solar energy harvesting, *Journal of Physics D: Applied Physics*. v. 51, p. 145501, 2018.

- [16] PEARSON, R.G. Hard and soft acids and bases, *Journal of the American Chemical Society*. v. 85, p. 3533–3539, 1963.
- [17] HÖLSÄ, J.; LAAMANEN, T.; LASTUSAARI, M.; MALKAMÄKI, M.; NIITTYKOSKI, J.; ZYCH, E. Effect of Mg^{2+} and Ti^{IV} doping on the luminescence of $\text{Y}_2\text{O}_2\text{S}:\text{Eu}^{3+}$, *Optical Materials*. v. 31, p. 1791–1793, 2009.
- [18] DING, Y.; ZHANG, Z.; WANG, L.; ZHANG, Q.; PAN, S. The role of sodium compound fluxes used to synthesize $\text{Gd}_2\text{O}_2\text{S}:\text{Tb}^{3+}$ by sulfide fusion method, *Journal of Materials Science: Materials in Electronics*. v. 28, p. 2723–2730, 2017.
- [19] LUO, H.; BOS, A.J.J.; DORENBOS, P. Charge Carrier Trapping Processes in $\text{RE}_2\text{O}_2\text{S}$ (RE = La, Gd, Y, and Lu), *Journal of Physical Chemistry C*. v. 121, p. 8760–8769, 2017.
- [20] THIRUMALAI, J.; CHANDRAMOHAN, R.; DIVAKAR, R.; MOHANDAS, E.; SEKAR, M.; PARAMESWARAN, P. Eu^{3+} doped gadolinium oxysulfide ($\text{Gd}_2\text{O}_2\text{S}$) nanostructures - Synthesis and optical and electronic properties, *Nanotechnology*. v. 19, p. 1–7, 2008.
- [21] LI, W.; LIU, Y.; AI, P. “Synthesis and luminescence properties of red long-lasting phosphor $\text{Y}_2\text{O}_2\text{S}:\text{Eu}^{3+},\text{Mg}^{2+},\text{Ti}^{4+}$ nanoparticles, *Materials Chemistry and Physics*. v. 119, p. 52–56, 2010.
- [22] CUI, C.; JIANG, G.; HUANG, P.; WANG, L.; LIU, D. Effect of Eu^{3+} concentration on the luminescence properties of $\text{Y}_2\text{O}_2\text{S}:\text{Eu}^{3+},\text{Mg}^{2+},\text{Ti}^{4+}$ nanotubes, *Ceramics International*. v. 40, p. 4725–4730, 2014.
- [23] BLASSE, G.; GRABMAIER, B.C. *Luminescent Materials*. Springer Netherlands, 1994.
- [24] LAPORTE, O.; MEGGERS, W.F. Some rules of spectral structure, *Journal of the Optical Society of America*. v. 11, p. 459–463, 1925.
- [25] BINNEMANS, K. Interpretation of europium(III) spectra, *Coordination Chemistry Reviews*. v. 295, p. 1–45, 2015.
- [26] DIEKE, G.H.; CROSSWHITE, H.M.; DUNN, B. Emission Spectra of the Doubly and Triply Ionized Rare Earths, *Journal of the Optical Society of America*. v. 51, p. 820–827, 1961.
- [27] DIEKE, G.H.; CROSSWHITE, H.M. The Spectra of the Doubly and Triply Ionized Rare Earths, *Applied Optics*. v. 2, p. 675–686, 1963.
- [28] JUDD, B.R. “Optical Absorption Intensities of Rare-Earth Ions, *Physical Review*. v. 127, p. 750–761, 1962.
- [29] OFELT, G.S. Intensities of Crystal Spectra of RareEarth Ions, *The Journal of Chemical Physics*. v. 37, p. 511–520, 1962.
- [30] WALSH, B.M. Judd-Ofelt theory: principles and practices, *Advances in Spectroscopy for Lasers and Sensing*. p. 403–433, 2006.
- [31] TANNER, P.A. Some misconceptions concerning the electronic spectra of tri-positive europium and cerium, *Chemical Society Reviews*. v. 42, p. 5090–5101, 2013.
- [32] HÖLSÄ, J.; LAMMINMÄKI, R.J. Analysis of the $4f^{\text{N}}$ energy-level structure of the RE^{3+} ions in REOCl ,” *Journal of Luminescence*. v. 69, p. 311–317, 1996.

- [33] DORENBOS, P. Systematic behaviour in trivalent lanthanide charge transfer energies, *Journal of Physics Condensed Matter*. v. 15, p. 8417–8434, 2003.
- [34] COTTON, S. *Lanthanide and Actinide Chemistry*, John Wiley & Sons Ltd, 2006.
- [35] DORENBOS, P. Lanthanide 4f-electron binding energies and the nephelauxetic effect in wide band gap compounds, *Journal of Luminescence*. v. 136, p. 122–129, 2013.
- [36] DORENBOS, P. Ce^{3+} 5d-centroid shift and vacuum referred 4f-electron binding energies of all lanthanide impurities in 150 different compounds, *Journal of Luminescence*. v. 135, p. 93–104, 2013.
- [37] DORENBOS, P. Locating lanthanide impurity levels in the forbidden band of host crystals, *Journal of Luminescence*. v. 108, p. 301–305, 2004.
- [38] DORENBOS, P. Electron binding energies and how it relates to activator luminescence and bonding in compounds, *Journal of Luminescence*. v. 169, p. 381–386, 2016.
- [39] DORENBOS, P. Modeling the chemical shift of lanthanide 4f electron binding energies, *Physical Review B - Condensed Matter and Materials Physics*. v. 85, p. 1–10, 2012.
- [40] NIKL, M. Scintillation detectors for x-rays, *Measurement Science and Technology*. v. 17, R37–R54, 2006.
- [41] ROGULIS, U.; ELSTS, E.; JANSONS, J.; ET AL. Rare earth activated oxyfluoride glasses and glass-ceramics for scintillation applications, *IEEE Transactions on Nuclear Science*. v. 59, p. 2201–2206, 2012.
- [42] TEIXEIRA, V.C.; MONTES, P.J.R.; VALERIO, M.E.G. Structural and optical characterizations of $Ca_2Al_2SiO_7:Ce^{3+},Mn^{2+}$ nanoparticles produced via a hybrid route, *Optical Materials*. v. 36, p. 1580–1590, 2014.
- [43] DAVID, S.; MICHAÏL, C.; SEFERIS, I.; ET AL. Evaluation of $Gd_2O_2S:Pr$ granular phosphor properties for X-ray mammography imaging, *Journal of Luminescence*. v. 169, p. 706–710, 2016.
- [44] BIZARRI, G. Scintillation mechanisms of inorganic materials: From crystal characteristics to scintillation properties, *Journal of Crystal Growth*. v. 312, p. 1213–1215, 2010.
- [45] BLASSE, G. Classical phosphors: A Pandora's box. *Journal of Luminescence*. v. 72–74, p. 129–134, 1997.
- [46] JUNG, I.D.; CHO, M.K.; LEE, S.M.; ET AL. Flexible $Gd_2O_2S:Tb$ scintillators pixelated with polyethylene microstructures for digital x-ray image sensors, *Journal of Micromechanics and Microengineering*. v. 19, p. 015014, 2009.
- [47] MADDALENA, F.; TIAHJANA, L.; XIE, A.; ET AL. Inorganic, organic, and perovskite halides with nanotechnology for high-light yield x- and γ -ray scintillators, *Crystals*. v. 9, p. 88, 2019.
- [48] AUZEL, F. History of upconversion discovery and its evolution, *Journal of Luminescence*. v. 223, p. 116900, 2020.
- [49] AUZEL, F. Upconversion processes in coupled ion systems, *Journal of Luminescence*. v. 45, p. 341–345, 1990.

- [50] LI, Z.; ZHANG, Y. An efficient and user-friendly method for the synthesis of hexagonal-phase NaYF₄:Yb,Er/Tm nanocrystals with controllable shape and upconversion fluorescence, *Nanotechnology*. v. 19, p. 345606, 2008.
- [51] AUZEL, F. Upconversion and Anti-Stokes Processes with f and d Ions in Solids, *Chemical Reviews*. v. 104, p. 139–173, 2004.
- [52] SHALAV, A.; RICHARDS, B.S.; TRUPKE, T.; KRÄMER, K.W.; GÜDEL, H.U. Application of NaYF₄:Er³⁺ up-converting phosphors for enhanced near-infrared silicon solar cell response, *Applied Physics Letters*. v. 86, p. 1–4, 2005.
- [53] LAVÍN, V.; LAHOZ, F.; MARTÍN, I.R.; RODRÍGUEZ-MENDOZA, U.R.; CÁCERES, J.M. Infrared-to-visible photon avalanche upconversion dynamics in Ho³⁺-doped fluorozirconate glasses at room temperature, *Optical Materials*. v. 27, p. 1754–1761, 2005.
- [54] LEE, C.; XU, E.Z.; LIU, Y.; ET AL. Giant nonlinear optical responses from photon-avalanching nanoparticles, *Nature*. v. 589, p. 230–235, 2021.
- [55] FISCHER, S.; MARTÍN-RODRÍGUEZ, R.; FRÖHLICH, B.; KRÄMER, K.W.; MEIJERINK, A.; GOLDSCHMIDT, J.C. Upconversion quantum yield of Er³⁺-doped β-NaYF₄ and Gd₂O₂S: The effects of host lattice, Er³⁺ doping, and excitation spectrum bandwidth, *Journal of Luminescence*. v. 153, p. 281–287, 2014.
- [56] FISCHER, S.; IVATURI, A.; JAKOB, P.; ET AL. Upconversion solar cell measurements under real sunlight, *Optical Materials*. v. 84, n. May, p. 389–395, 2018.
- [57] ZHU, X.; ZHANG, J.; LIU, J.; ZHANG, Y. Recent Progress of Rare-Earth Doped Upconversion Nanoparticles: Synthesis, Optimization, and Applications, *Advanced Science*. v. 6, p. 1901358, 2019.
- [58] RABOUW, F.T.; PRINS, P.T.; VILLANUEVA-DELGADO, P.; CASTELIJNS, M.; GEITENBEEK, R.G.; MEIJERINK, A. Quenching Pathways in NaYF₄:Er³⁺,Yb³⁺ Upconversion Nanocrystals, *ACS Nano*. v. 12, p. 4812–4823, 2018.
- [59] WANG, F.; DENG, R.; LIU, X. Preparation of core-shell NaGdF₄ nanoparticles doped with luminescent lanthanide ions to be used as upconversion-based probes, *Nature Protocols*. v. 9, p. 1634–1644, 2014.
- [60] CHATTERJEE, D.K.; RUFAlHAH, A.J.; ZHANG, Y. Upconversion fluorescence imaging of cells and small animals using lanthanide doped nanocrystals, *Biomaterials*. v. 29, p. 937–943, 2008.
- [61] AITASALO, T.; DEREN, P.; HÖLSÄ, J.; ET AL. Persistent luminescence phenomena in materials doped with rare earth ions, *Journal of Solid State Chemistry*. v. 171, p. 114–122, 2003.
- [62] XU, J.; TANABE, S. Persistent luminescence instead of phosphorescence: History, mechanism, and perspective, *Journal of Luminescence*. v. 205, p. 581–620, 2019.
- [63] SMET, P.F.; POELMAN, D.; HEHLEN, M.P. Focus issue introduction: persistent phosphors, *Optical Materials Express*. v. 2, p. 452, 2012.
- [64] HÖLSÄ, J. Persistent luminescence beats the afterglow: 400 Years of persistent luminescence, *Electrochemical Society Interface*. v. 18, p. 42–45, 2009.
- [65] VIRK, H.S. History of Luminescence from Ancient to Modern Times, *Defect and Diffusion Forum*. v. 361, p. 1–13, 2015.

- [66] LASTUSAARI, M.; LAAMANEN, T.; MALKAMÄKI, M.; ET AL. The Bologna Stone: History's first persistent luminescent material. *European Journal of Mineralogy*. v. 24, p. 885–890, 2012.
- [67] JOHNSON, R.P. Luminescence of Sulphide and Silicate Phosphors, *Journal of the Optical Society of America*. v. 29, p. 387, 1939.
- [68] MATSUZAWA, T.; AOKI, Y.; TAKEUCHI, N.; MURAYAMA, Y. A new long phosphorescent phosphor with high brightness, $\text{SrAl}_2\text{O}_4:\text{Eu}^{2+}, \text{Dy}^{3+}$, *Journal of Electrochemical Society*. v. 143, p. 2670–2673, 1996.
- [69] AITASALO, T.; HÖLSÄ, J.; JUNGNER, H.; LASTUSAARI, M.; NIITTYKOSKI, J. Thermoluminescence study of persistent luminescence materials: Eu^{2+} - and R^{3+} -doped calcium aluminates, $\text{CaAl}_2\text{O}_4:\text{Eu}^{2+}, \text{R}^{3+}$, *Journal of Physical Chemistry B*. v. 110, p. 4589–4598, 2006.
- [70] MCKEEVER, S.W.S. *Thermoluminescence of solids.*, Cambridge University Press, 1983.
- [71] BOS, A.J.J. Thermoluminescence as a research tool to investigate luminescence mechanisms, *Materials*. v. 10, p. 1357, 2017.
- [72] DORENBOS, P. The hole picture as alternative for the common electron picture to describe hole trapping and luminescence quenching, *Journal of Luminescence*. v. 197, p. 62–65, 2018.
- [73] DOBROWOLSKA, A.; BOS, A.J.J.; DORENBOS, P. Electron tunnelling phenomena in $\text{YPO}_4:\text{Ce}, \text{Ln}$ (Ln = Er, Ho, Nd, Dy), *Journal of Physics D: Applied Physics*. v. 47, p. 335301, 2014.
- [74] BOTTERMAN, J.; JOOS, J.J.; SMET, P.F. Trapping and detrapping in $\text{SrAl}_2\text{O}_4:\text{Eu}, \text{Dy}$ persistent phosphors: Influence of excitation wavelength and temperature, *Physical Review B - Condensed Matter and Materials Physics*. v. 90, p. 1–15, 2014.
- [75] UEDA, J.; MAKI, R.; TANABE, S. Vacuum Referred Binding Energy (VRBE)-Guided Design of Orange Persistent $\text{Ca}_3\text{Si}_2\text{O}_7:\text{Eu}^{2+}$ Phosphors, *Inorganic Chemistry*. v. 56, p. 10353–10360, 2017.
- [76] WANG, Y.; WANG, Z. “Characterization of $\text{Y}_2\text{O}_2\text{S}:\text{Eu}^{3+}, \text{Mg}^{2+}, \text{Ti}^{4+}$ long-lasting phosphor synthesized by flux method, *Journal of Rare Earths*. v. 24, p. 25–28, 2006.
- [77] PAN, Z.; LU, Y.Y.; LIU, F. Sunlight-activated long-persistent luminescence in the near-infrared from Cr^{3+} -doped zinc gallogermanates, *Nature Materials*. v. 11, p. 58–63, 2012.
- [78] BASAVARAJU, N.; SHARMA, S.; BESSIÈRE, A.; VIANA, B.; GOURIER, D.; PRIOLKAR, K.R. Red persistent luminescence in $\text{MgGa}_2\text{O}_4:\text{Cr}^{3+}$; A new phosphor for in vivo imaging, *Journal of Physics D: Applied Physics*. v. 46, p. 2–7, 2013.
- [79] LIU, F.; YAN, W.; CHUANG, Y.J.; ZHEN, Z.; XIE, J.; PAN, Z. Photostimulated near-infrared persistent luminescence as a new optical read-out from Cr^{3+} -doped LiGa_5O_8 , *Scientific Reports*. v. 3, p. 1–9, 2013.
- [80] LIANG, Y.-J.; LIU, F.; CHEN, Y.-F.; WANG, X.-J.; SUN, K.-N.; PAN, Z. New function of the Yb^{3+} ion as an efficient emitter of persistent luminescence in the short-wave infrared, *Light: Science & Applications*. v. 5, p. e16124–e16124, 2016.
- [81] SINGH, S.K. Red and near infrared persistent luminescence nano-probes for bioimaging and targeting applications, *RSC Advances*. v. 4, p. 58674–58698, 2014.
- [82] WU, S.; LI, Y.; DING, W.; XU, L.; MA, Y.; ZHANG, L. Recent Advances of Persistent Luminescence Nanoparticles in Bioapplications, *Nano-Micro Letters*, v. 12, p. 70, 2020.

- [83] FRITZEN, D.L.; GIORDANO, L.; RODRIGUES, L.C.V.; MONTEIRO, J.H.S.K. Opportunities for persistent luminescent nanoparticles in luminescence imaging of biological systems and photodynamic therapy, *Nanomaterials*. v. 10, p. 1–38, 2020.
- [84] CHUANG, Y.J.; ZHEN, Z.; ZHANG, F.; ET AL. Photostimulable near-infrared persistent luminescent nanoprobes for ultrasensitive and longitudinal deep-tissue bio-imaging, *Theranostics*. v. 4, p. 1112–1122, 2014.
- [85] LIU, J.; LÉCUYER, T.; SEGUIN, J.; ET AL. Imaging and therapeutic applications of persistent luminescence nanomaterials, *Advanced Drug Delivery Reviews*. v. 138, p. 193–210, 2019.
- [86] PITHA, J.J.; SMITH, A.L.; WARD, R. The Preparation of Lanthanum Oxysulfide and its Properties as a Base Material for Phosphors Stimulated by Infrared, *Journal of American Chemical Society*. v. 69, p. 1870–1871, 1947.
- [87] ZACHARIASEN, W.H. Crystal Chemical Studies of the 5f-Series of Elements. VII. The Crystal Structure of $\text{Ce}_2\text{O}_2\text{S}$, $\text{La}_2\text{O}_2\text{S}$ and $\text{Pu}_2\text{O}_2\text{S}$, *Acta Crystallographica*. v. 2, p. 60–62, 1949.
- [88] SOVERS, O.J.; YOSHIOKA, T. Fluorescence of Trivalent-Europium-Doped Yttrium Oxysulfide, *The Journal of Chemical Physics*. v. 49, p. 4945–4954, 1968.
- [89] PASBERG, N.; DEN ENGELSEN, D.; FERN, G.R.; HARRIS, P.G.; IRELAND, T.G.; SILVER, J. Structure and luminescence analyses of simultaneously synthesised $(\text{Lu}_{1-x}\text{Gd}_x)_2\text{O}_2\text{S}:\text{Tb}^{3+}$ and $(\text{Lu}_{1-x}\text{Gd}_x)_2\text{O}_3:\text{Tb}^{3+}$, *Dalton Transactions*. v. 46, p. 7693–7707, 2017.
- [90] RESENDE, L. V; MORAIS, C.A. Process development for the recovery of europium and yttrium from computer monitor screens, *Minerals Engineering*. v. 70, p. 217–221, 2015.
- [91] YU, D.C.; MARTÍN-RODRÍGUEZ, R.; ZHANG, Q.Y.; MEIJERINK, A.; RABOUW, F.T. Multi-photon quantum cutting in $\text{Gd}_2\text{O}_2\text{S}:\text{Tm}^{3+}$ to enhance the photo-response of solar cells, *Light: Science and Applications*. v 4, p. 1–8, 2015.
- [92] MARTÍN-RODRÍGUEZ, R.; FISCHER, S.; IVATURI, A.; ET AL. Highly efficient IR to NIR upconversion in $\text{Gd}_2\text{O}_2\text{S}:\text{Er}^{3+}$ for photovoltaic applications, *Chemistry of Materials*. v. 25, p. 1912–1921, 2013.
- [93] LUO, X.; CAO, W. Blue, green, red upconversion luminescence and optical characteristics of rare earth doped rare earth oxide and oxysulfide, *Science in China, Series B: Chemistry*. v. 50, p. 505–513, 2007.
- [94] DELGADO DA VILA, L.; STUCCHI, E.B.; DAVOLOS, M.R. Preparation and characterization of uniform, spherical particles of $\text{Y}_2\text{O}_2\text{S}$ and $\text{Y}_2\text{O}_2\text{S}:\text{Eu}$, *Journal of Materials Chemistry*. v. 7, p. 2113–2116, 1997.
- [95] WANG, X.; ZHANG, Z.; TANG, Z.; LIN, Y. Characterization and properties of a red and orange $\text{Y}_2\text{O}_2\text{S}$ -based long afterglow phosphor, *Materials Chemistry and Physics*. v. 80, p. 1–5, 2003.
- [96] AI, P.F.; LIU, Y.L.; XIAO, L.Y.; WANG, H.J.; MENG, J.X. Synthesis of $\text{Y}_2\text{O}_2\text{S}:\text{Eu}^{3+},\text{Mg}^{2+},\text{Ti}^{4+}$ hollow microspheres via homogeneous precipitation route, *Science and Technology of Advanced Materials*. v. 11, p. 035002, 2010.
- [97] ZHOU, X.; XING, M.; JIANG, T.; ET AL. Afterglow performance enhancement and mechanism studies on $\text{Y}_2\text{O}_2\text{S}:\text{Eu},\text{Mg},\text{Ti}$ prepared via cold isostatic pressing, *Journal of Alloys and Compounds*. v. 585, p. 376–383, 2014.

- [98] PENGYUE, Z.; ZHANGLIAN, H.; HUAXIANG, S.; ZHENXIU, X.; XIANPING, F. Luminescence Characterization of Mg Doped Y₂O₂S:Ti Long Afterglow Phosphor, *Journal of Rare Earths*. v. 24, p. 115–118, 2006.
- [99] CUI, C.E.; LIU, H.; HUANG, P.; WANG, L. Influence of Mg²⁺,Ti⁴⁺ co-doping concentration on the luminescence properties of Y₂O₂S:Eu³⁺,Mg²⁺,Ti⁴⁺ nanotube arrays, *Journal of Luminescence journal*. v. 149, p. 196–199, 2014.
- [100] ZHANG, P.; HONG, Z.; WANG, M.; FANG, X.; QIAN, G.; WANG, Z. Luminescence characterization of a new long afterglow phosphor of single Ti-doped Y₂O₂S, *Journal of Luminescence*. v. 113, p. 89–93, 2005.
- [101] HONG, Z.; ZHANG, P.; FAN, X.; WANG, M. Eu³⁺ red long afterglow in Y₂O₂S:Ti, Eu phosphor through afterglow energy transfer, *Journal of Luminescence*. v. 124, p. 127–132, 2007.
- [102] LIU, D.; CUI, C.; HUANG, P.; WANG, L.; JIANG, G. Luminescent properties of red long-lasting phosphor Y₂O₂S:Eu³⁺, M²⁺ (M = Mg, Ca, Sr, Ba), Ti⁴⁺ nanotubes via hydrothermal method, *Journal of Alloys and Compounds*. v. 583, p. 530–534, 2014.
- [103] QU, B.; WANG, J.; LIU, K.; ZHOU, R.; WANG, L. Comprehensive Study of the Red Persistent Luminescence Mechanism of Y₂O₂S:Eu, Ti, Mg, *Physical Chemistry Chemical Physics*. v. 21, p. 25118–25125, 2019.
- [104] ABDEL-KADER, A.; ELKHOLY, M.M. Cathodoluminescence emission spectra of trivalent europium-doped yttrium oxysulphide, *Journal of Materials Science*. v. 27, p. 2887–2895, 1992.
- [105] LO, C.L.; DUH, J.G.; CHIOU, B.S.; PENG, C.C.; OZAWA, L. Synthesis of Eu³⁺-activated yttrium oxysulfide red phosphor by flux fusion method, *Materials Chemistry and Physics*. v. 71, p. 179–189, 2001.
- [106] GUO, C.; LUAN, L.; CHEN, C.; HUANG, D.; SU, Q. Preparation of Y₂O₂S:Eu³⁺ phosphors by a novel decomposition method, *Materials Letters*. v. 62, p. 600–602, 2008.
- [107] RAO, K.J.; VAIDHYANATHAN, B.; GANGULI, M.; RAMAKRISHNAN, P.A. Synthesis of inorganic solids using microwaves, *Chemistry of Materials*. v. 11, p. 882–895, 1999.
- [108] KITCHEN, H.J.; VALLANCE, S.R.; KENNEDY, J.L.; ET AL. Modern microwave methods in solid-state inorganic materials chemistry: From fundamentals to manufacturing, *Chemical Reviews*. v. 114, p. 1170–1206, 2014.
- [109] BHATTACHARYA, M.; BASAK, T. A review on the susceptor assisted microwave processing of materials, *Energy*. v. 97, p. 306–338, 2016.
- [110] LEVIN, E.E.; GREBENKEMPER, J.H.; POLLOCK, T.M.; SESHADRI, R. Protocols for High Temperature Assisted-Microwave Preparation of Inorganic Compounds, *Chemistry of Materials*. v. 31, p. 7151–7159, 2019.
- [111] MEREDITH, R. Engineers' Handbook of Industrial Microwave Heating. *Engineers' Handbook of Industrial Microwave Heating*, p. 2–4, 1998.

- [112] PEDROSO, C.C.S. *Investigação da luminescência persistente dos materiais $\text{Lu}_2\text{O}_3:\text{TR}^{3+},\text{M}$ ($\text{TR},\text{M}:\text{Pr},\text{Hf}^{IV}; \text{Eu},\text{Ca}^{2+}$ ou Tb,Ca^{2+}) preparados pelo método de estado-sólido assistido por micro-ondas*. Ph.D. thesis, Institute of Chemistry, University of São Paulo, 2016.
- [113] BIRKEL, A.; DENAULT, K.A.; GEORGE, N.C.; ET AL. Rapid microwave preparation of highly efficient Ce^{3+} -substituted garnet phosphors for solid state white lighting, *Chemistry of Materials*. v 24, p. 1198–1204, 2012.
- [114] PEDROSO, C.C.S.; CARVALHO, J.M.; RODRIGUES, L.C.V.; HÖLSÄ, J.; BRITO, H.F. Rapid and Energy-Saving Microwave-Assisted Solid-State Synthesis of Pr^{3+} -, Eu^{3+} -, or Tb^{3+} -Doped Lu_2O_3 Persistent Luminescence Materials, *ACS Applied Materials and Interfaces*. v. 8, p. 19593–19604, 2016.
- [115] ROSTICHER, C.; CHANÉAC, C.; VIANA, B.; FORTIN, M.A.; LAGUEUX, J.; FAUCHER, L. Red persistent luminescence and magnetic properties of nanomaterials for multimodal imaging, *Oxide-based Materials and Devices VI*. v. 9364, p. 936419, 2015.
- [116] LI, Y.; HUANG, Y.; BAI, T.; LI, L. Straightforward conversion route to nanocrystalline monothiooxides of rare earths through a high-temperature colloid technique, *Inorganic Chemistry*. v. 39, p. 3418–3420, 2000.
- [117] ZHAO, F.; YUAN, M.; ZHANG, W.; GAO, S. Monodisperse lanthanide oxysulfide nanocrystals, *Journal of the American Chemical Society*. v. 128, p. 11758–11759, 2006.
- [118] THIRUMALAI, J.; JAGANNATHAN, R.; TRIVEDI, D.C. $\text{Y}_2\text{O}_2\text{S}:\text{Eu}^{3+}$ nanocrystals, a strong quantum-confined luminescent system, *Journal of Luminescence*. v. 126, p. 353–358, 2007.
- [119] HYPÄNEN, I.; HÖLSÄ, J.; KANKARE, J.; LASTUSAARI, M.; PIHLGREN, L. Up-conversion luminescence properties of $\text{Y}_2\text{O}_2\text{S}:\text{Yb}^{3+},\text{Er}^{3+}$ nanophosphors, *Optical Materials*. v. 31, p. 1787–1790, 2009.
- [120] LU, X.; YANG, M.; YANG, L.; MA, Q.; DONG, X.; TIAN, J. $\text{Y}_2\text{O}_2\text{S}:\text{Yb}^{3+},\text{Er}^{3+}$ nanofibers: novel fabrication technique, structure and up-conversion luminescent characteristics, *Journal of Materials Science: Materials in Electronics*. v. 26, p. 4078–4084, 2015.
- [121] DING, Y.; GU, J.; KE, J.; ZHANG, Y.W.; YAN, C.H. Sodium doping controlled synthesis of monodisperse lanthanide oxysulfide ultrathin nanoplates guided by density functional calculations, *Angewandte Chemie - International Edition*. v. 50, p. 12330–12334, 2011.
- [122] LIN, H.; LUO, Q.; TONG, W.Y.; ET AL. Facile preparation of rare-earth semiconductor nanocrystals and tuning of their dimensionalities, *RSC Advances*. v 5, p. 86885–86890, 2015.
- [123] LEI, L.; ZHANG, S.; XIA, H.; TIAN, Y.; ZHANG, J.; XU, S. Controlled synthesis of lanthanide-doped $\text{Gd}_2\text{O}_2\text{S}$ nanocrystals with novel excitation-dependent multicolor emissions, *Nanoscale*. v. 9, p. 5718–5724, 2017.
- [124] LARQUET, C.; NGUYEN, A.-M.; ÁVILA-GUTIÉRREZ, M.; ET AL. Synthesis of $\text{Ce}_2\text{O}_2\text{S}$ and $\text{Gd}_{2(1-y)}\text{Ce}_{2y}\text{O}_2\text{S}$ nanoparticles and reactivity from in situ XAS and XPS, *Inorganic Chemistry*. v. 56, p. 14227–14236, 2017.
- [125] LARQUET, C.; HOURLIER, D.; NGUYEN, A.M.; ET AL. Thermal Stability of Oleate-Stabilized $\text{Gd}_2\text{O}_2\text{S}$ Nanoplates in Inert and Oxidizing Atmospheres, *ChemNanoMat*. v. 5, p. 539–546, 2019.

- [126] LARQUET, C.; NGUYEN, A.-M.; GLAIS, E.; ET AL. Band Gap Engineering from Cation Balance: The Case of Lanthanide Oxysulfide Nanoparticles, *Chemistry of Materials*. v. 31, p. 5014–5023, 2019.
- [127] LARQUET, C.; CARRIERE, D.; NGUYEN, A.-M.; ET AL. Unraveling the Role of Alkali Cations in the Growth Mechanism of Gd₂O₂S Nanoparticles, *Chemistry of Materials*. v. 32, p. 1131–1139, 2020.
- [128] SHANNON, R.D. Revised Effective Ionic Radii and Systematic Studies of Interatomic Distances in Halides and Chalcogenides, *Acta Crystallographica*. v. A32, p. 751–766, 1976.
- [129] D'ASSUNÇÃO, L.M.; IONASHIRO, M.; GIOLITO, I. Thermal decomposition of the hydrated basic carbonates of lanthanides and yttrium in CO₂ atmosphere, *Thermochimica Acta*. v. 219, p. 225–233, 1993.
- [130] LUIZ, J.M.; MATOS, J.R.; GIOLITO, I.; IONASHIRO, M. Thermal behaviour of the basic carbonates of lanthanum-europium, *Thermochimica Acta*. v. 254, p. 209–218, 1995.
- [131] MOURDIKOU DIS, S.; LIZ-MARZÁN, L.M. Oleylamine in nanoparticle synthesis, *Chemistry of Materials*. v. 25, p. 1465–1476, 2013.
- [132] THOMSON, J.W.; NAGASHIMA, K.; MACDONALD, P.M.; OZIN, G.A. From sulfur-amine solutions to metal sulfide nanocrystals: Peering into the oleylamine-sulfur black box, *Journal of the American Chemical Society*. v. 133, p. 5036–5041, 2011.
- [133] SOARES, P.I.P.; LAIA, C.A.T.; CARVALHO, A.; ET AL. Iron oxide nanoparticles stabilized with a bilayer of oleic acid for magnetic hyperthermia and MRI applications, *Applied Surface Science*. v. 383, p. 240–247, 2016.
- [134] KANNINEN, P.; JOHANS, C.; MERTA, J.; KONTTURI, K. Influence of ligand structure on the stability and oxidation of copper nanoparticles, *Journal of Colloid and Interface Science*. v. 318, p. 88–95, 2008.
- [135] CARVALHO, A.M.G.; ARAÚJO, D.H.C.; CANOVA, H.F.; ET AL. X-ray powder diffraction at the XRD1 beamline at LNLS, *Journal of Synchrotron Radiation*. v. 23, p. 1501–1506, 2016.
- [136] CARVALHO, A.M.G.; NUNES, R.S.; COELHO, A.A. X-ray powder diffraction of high-Absorption materials at the XRD1 beamline off the best conditions: Application to (Gd,Nd)₅Si₄ compounds, *Powder Diffraction*. v. 32, p. 10–14, 2017.
- [137] LARSON, A.C.; DREELE, R.B. VON General Structure Analysis System (GSAS), 2004.
- [138] TOBY, B.H. General Structure Analysis System - GSAS/EXPGUI, A Graphical user interface for GSAS, *J. Appl. Crystallogr.* v. 34, p. 210–213, 2001.
- [139] MOMMA, K.; IZUMI, F. VESTA: A three-dimensional visualization system for electronic and structural analysis, *Journal of Applied Crystallography*. v. 41, p. 653–658, 2008.
- [140] FIGUEROA, S.J.A.; MAURICIO, J.C.; MURARI, J.; ET AL. Upgrades to the XAFS2 beamline control system and to the endstation at the LNLS, *Journal of Physics: Conference Series*. v. 712, p. 012022, 2016.
- [141] CAVASSO FILHO, R.L.; LAGO, A.F.; HOMEM, M.G.P.; PILLING, S.; NAVES DE BRITO, A. Delivering high-purity vacuum ultraviolet photons at the Brazilian toroidal grating monochromator (TGM) beamline, *Journal of Electron Spectroscopy and Related Phenomena*. v. 156–158, p. 168–171, 2007.

- [142] MIRANDA DE CARVALHO, J.; PEDROSO, C.C.S.; MACHADO, I.P.; ET AL. Persistent luminescence warm-light LEDs based on Ti-doped RE₂O₂S materials prepared by rapid and energy-saving microwave-assisted synthesis, *Journal of Materials Chemistry C*. v. 6, p. 8897–8905, 2018.
- [143] MACHADO, I.P.; TEIXEIRA, V.C.; PEDROSO, C.C.S.; BRITO, H.F.; RODRIGUES, L.C.V. X-ray scintillator Gd₂O₂S:Tb³⁺ materials obtained by a rapid and cost-effective microwave-assisted solid-state synthesis, *Journal of Alloys and Compounds*. v. 777, p. 638–645, 2019.
- [144] MACHADO, I.P.; PEDROSO, C.C.S.; CARVALHO, J.M. DE; TEIXEIRA, V. DE C.; RODRIGUES, L.C.V.; BRITO, H.F. A new path to design near-infrared persistent luminescence materials using Yb³⁺-doped rare earth oxysulfides, *Scripta Materialia*. v. 164, p. 57–61, 2019.
- [145] KAHLWEIT, M. Ostwald ripening of precipitates, *Advances in Colloid and Interface Science*. v. 5, p. 1–35, 1975.
- [146] FLEET, M.E. XANES spectroscopy of sulfur in Earth materials, *Canadian Mineralogist*. v. 43, p. 1811–1838, 2005.
- [147] PARIS, E.; GIULI, G.; CARROLL, M.R.; CAMERINO, U.; FISICA, D.; TOR, R. The valence and speciation of sulfur in glasses by X-ray absorption spectroscopy, *The Canadian Mineralogist*. v. 39, p. 331–339, 2001.
- [148] FLEET, M.E.; LIU, X.; HARMER, S.L.; KING, P.L. Sulfur K-edge XANES spectroscopy: Chemical state and content of sulfur in silicate glasses, *Canadian Mineralogist*. v. 43, p. 1605–1618, 2005.
- [149] HENDERSON, G.S.; DE GROOT, F.M.F.; MOULTON, B.J.A. X-ray absorption near-edge structure (XANES) spectroscopy, *Reviews in Mineralogy and Geochemistry*. v. 78, p. 75–138, 2014.
- [150] PEAK, D.; FORD, R.G.; SPARKS, D.L. An in Situ ATR-FTIR Investigation of Sulfate Bonding Mechanisms on Goethite, *Journal of Colloid and Interface Science*. v. 218, p. 289–299, 1999.
- [151] MACHIDA, M.; KAWAMURA, K.; ITO, K.; IKEUE, K. Large-capacity oxygen storage by lanthanide oxysulfate/oxysulfide systems, *Chemistry of Materials*. v. 17, p. 1487–1492, 2005.
- [152] ADACHI, G.Y.; IMANAKA, N. The binary rare earth oxides, *Chemical Reviews*. v. 98, p. 1479–1514, 1998.
- [153] CHATTERJEE, S.; SHANKER, V.; CHANDER, H. Thermoluminescence of Tb doped Gd₂O₂S phosphor, *Materials Chemistry and Physics*. v. 80, p. 719–724, 2003.
- [154] SILVA, I.G.N.; RODRIGUES, L.C.V.; SOUZA, E.R.; ET AL. Low temperature synthesis and optical properties of the R₂O₃:Eu³⁺ nanophosphors (R³⁺: Y, Gd and Lu) using TMA complexes as precursors, *Optical Materials*. v. 40, p. 41–48, 2015.
- [155] CHEN, H.; MOORE, T.; QI, B.; ET AL. Monitoring pH-triggered drug release from radioluminescent nanocapsules with X-ray excited optical luminescence, *ACS Nano*. v. 7, p. 1178–1187, 2013.
- [156] PIRES, A.M.; DAVOLOS, M.R.; STUCCHI, E.B. Eu³⁺ as a spectroscopic probe in phosphors based on spherical fine particle gadolinium compounds, *International Journal of Inorganic Materials*. v. 3, p. 785–790, 2001.

- [157] WANG, Z.; MEIJERINK, A. Concentration Quenching in Upconversion Nanocrystals, *Journal of Physical Chemistry C*. v. 122, p. 26298–26306, 2018.
- [158] AVRAM, D.; TISEANU, C. Thermometry properties of Er,Yb-Gd₂O₂S microparticles: Dependence on the excitation mode (cw versus pulsed excitation) and excitation wavelength (980 nm versus 1500 nm), *Methods and Applications in Fluorescence*. v. 6, p. 025004, 2018.
- [159] CARVALHO, J.M. *Síntese e investigação espectroscópica de novos fósforos dopados com Ti e Ce³⁺ para aplicação em luminescência persistente e iluminação de estado sólido*. Ph.D. thesis, Institute of Chemistry, University of São Paulo, 2015.
- [160] CARVALHO, J.M.; RODRIGUES, L.C.V.; FELINTO, M.C.F.C.; NUNES, L.A.O.; HÖLSÄ, J.; BRITO, H.F. Structure–property relationship of luminescent zirconia nanomaterials obtained by sol–gel method, *Journal of Materials Science*. v. 50, p. 873–881, 2015.
- [161] DORENBOS, P. The Eu³⁺ charge transfer energy and the relation with the band gap of compounds, *Journal of Luminescence*. v. 111, p. 89–104, 2005.
- [162] CLABAU, F.; ROCQUEFELTE, X.; LE MERCIER, T.; DENIARD, P.; JOBIC, S.; WHANGBO, M.H. Formulation of phosphorescence mechanisms in inorganic solids based on a new model of defect conglomeration, *Chemistry of Materials*. v. 18, p. 3212–3220, 2006.
- [163] DORENBOS, P. A Review on How Lanthanide Impurity Levels Change with Chemistry and Structure of Inorganic Compounds, *ECS Journal of Solid State Science and Technology*. v. 2, p. R3001–R3011, 2013.
- [164] SONTAKKE, A.D.; UEDA, J.; KATAYAMA, Y.; DORENBOS, P.; TANABE, S. Experimental insights on the electron transfer and energy transfer processes between Ce³⁺-Yb³⁺ and Ce³⁺-Tb³⁺ in borate glass, *Applied Physics Letters*. v. 106, p. 131906, 2015.
- [165] SONTAKKE, A.D.; UEDA, J.; KATAYAMA, Y.; ZHUANG, Y.; DORENBOS, P.; TANABE, S. “Role of electron transfer in Ce³⁺ sensitized Yb³⁺ luminescence in borate glass, *Journal of Applied Physics*. v. 117, p. 013105, 2015.
- [166] FOREST, H.; COCCO, A.; HERSH, H. Energy storage in La₂O₂S:Eu⁺³ with direct 4f⁶ Eu⁺³ excitation, *Journal of Luminescence*. v. 3, p. 25–36, 1970.
- [167] STRUCK, C.W.; FONGER, W.H. Role of the charge-transfer states in feeding and thermally emptying the 5D states of Eu⁺³ in yttrium and lanthanum oxysulfides, *Journal of Luminescence*. v. 1–2, p. 456–469, 1970.
- [168] FONGER, W.H.; STRUCK, C.W. Energy Loss and Energy Storage from the Eu⁺³ Charge-Transfer States in Y and La Oxysulfides, *Journal of Electrochemical Society*. v. 118, p. 273–280, 1971.
- [169] HOSHINA, T.; IMANAGA, S.; YOKONO, S. Charge transfer effects on the luminescent properties of Eu³⁺ in oxysulfides, *Journal of Luminescence*. v. 15, n. 4, p. 455–471, 1977.
- [170] NAKAZAWA, E.; YAMAMOTO, H. Trapping mechanism in the afterglow process of the rare-earth activated Y₂O₂S phosphors, *Journal of Luminescence*. v. 128, p. 494–498, 2008.

- [171] BETTENTRUP, H.; ESKOLA, K.O.; HÖLSÄ, J.; KOTLOV, A.; LASTUSAARI, M.; MALKAMÄKI, M. Luminescence properties of Eu^{3+} and $\text{Ti}^{\text{IV}}/\text{Zr}^{\text{IV}}$ doped yttrium oxysulfides ($\text{Y}_2\text{O}_2\text{S}:\text{Eu}^{3+},\text{Ti}^{\text{IV}}/\text{Zr}^{\text{IV}}$), *IOP Conference Series: Materials Science and Engineering*. v. 15, p. 012085, 2010.
- [172] LEI, B.; LIU, Y.; ZHANG, J.; MENG, J.; MAN, S.; TAN, S. Persistent luminescence in rare earth ion-doped gadolinium oxysulfide phosphors, *Journal of Alloys and Compounds*. v. 495, p. 247–253, 2010.
- [173] HUANG, P.; YANG, F.; CUI, C.; WANG, L.; LEI, X. Luminescence improvement of $\text{Y}_2\text{O}_2\text{S}:\text{Tb}^{3+},\text{Sr}^{2+},\text{Zr}^{4+}$ white-light long-lasting phosphor via Eu^{3+} addition, *Ceramics International*. v. 39, p. 5615–5621, 2013.
- [174] MIKAMI, M.; OSHIYAMA, A. First-principles study of intrinsic defects in yttrium oxysulfide, *Physical Review B*. v. 60, p. 1707–1715, 1999.
- [175] WHITTAKER, A.G. Diffusion in microwave-heated ceramics, *Chemistry of Materials*. v. 17, p. 3426–3432, 2005.
- [176] KRÖGER, F.A.; VINK, H.J. Relations between the Concentrations of Imperfections in Crystalline Solids, *Solid State Physics - Advances in Research and Applications*. v. 3, p. 307–435, 1956.

Appendix I

Publications

A1) Carvalho, J.M., Pedroso, C.C.S., Machado, I.P., Hölsä, J., Rodrigues, L.C.V., Gluchowski, P., Lastusaari, M., Brito, H.F. **Persistent luminescence warm-light LEDs based on Ti-doped RE₂O₂S materials prepared by rapid and energy-saving microwave-assisted synthesis.** *Journal of Materials Chemistry C*, 6 (2018) 8897–8905.*

<https://doi.org/10.1039/C8TC01826J>

A2) Machado, I.P., Teixeira, V.C., Pedroso, C.C.S., Brito, H.F., Rodrigues, L.C.V. **X-ray scintillator Gd₂O₂S:Tb³⁺ materials obtained by a rapid and cost-effective microwave-assisted solid-state synthesis.** *Journal of Alloys and Compounds*, 777 (2018) 638–645.*

<https://doi.org/10.1016/j.jallcom.2018.10.348>

A3) Machado, I.P., Pedroso, C.C.S., Carvalho, J.M., Teixeira, V.C., Rodrigues, L.C.V., Brito, H.F. **A new path to design near-infrared persistent luminescence materials using Yb³⁺-doped rare earth oxysulfides,** *Scripta Materialia*, 164 (2019) 57–61.*

<https://doi.org/10.1016/j.scriptamat.2019.01.023>

* All published figures were reproduced in this Thesis with proper permission (author permission) from The Royal Society of Chemistry and Elsevier.

Appendix II

Curriculum Vitae

CURRICULUM VITAE

1) Personal data

Name: Ian Pompermayer Machado

Date of birth: 20/07/1992

Local of birth: Vila Velha, ES – Brazil

2) Education

Year	Activity	Institution
2010 – 2014	Bachelor's in Chemistry	Federal University of Espírito Santo, Department of Chemistry – Brazil
2014 – 2016	Master's in Chemistry	University of São Paulo, Institute of Chemistry – Brazil
2016 – 2021	PhD in Chemistry	University of São Paulo, Institute of Chemistry – Brazil
2019 – 2020	PhD visitor (CNPq SWE)	Utrecht University, Condensed Matter and Interfaces (CMI), Debye Institute for Nanomaterials Science – The Netherlands

3) Occupation

Institution	<i>Núcleo de Competências em Química do Petróleo, Federal University of Espírito Santo – Brazil</i>
Occupation	Technician Trainee – Instrumentation Laboratory
Period	2012 – 2013
Activity	Characterization of crude oil, oil fractions, tubular incrustation products, and inorganic materials using thermogravimetric analyses (TGA), differential scanning calorimetry (DSC), absorption spectroscopy (UV-Vis), and Fourier-transform infrared spectroscopy (FTIR).

Institution	Institute of Chemistry, University of São Paulo – Brazil
Occupation	<i>Estágio em Docência do Programa de Aperfeiçoamento de Ensino (PAE)</i>
Period	2016
Activity	<ul style="list-style-type: none">• QFL1103 – <i>Química Geral II</i> – 2016/1• QFL1101 – <i>Química Geral I</i> – 2016/2

4) Scientific publications

1. Franco, M.K.K.D., Sepulveda, A.F., Vigato, A.A., Oshiro, A., Machado, I.P., Kent, B., Clemens, D., Yokaichiya, F., Araujo, D.R. Supramolecular Structure of Temperature-Dependent Polymeric Hydrogels Modulated by Drug Incorporation. *ChemistrySelect*, 5 (2020) 12853–12861.
2. Machado, I.P., Pedroso, C.C.S., Carvalho, J.M., Teixeira, V.C., Rodrigues, L.C.V., Brito, H.F. A new path to design near-infrared persistent luminescence materials using Yb³⁺-doped rare earth oxysulfides, *Scripta Materialia*, 164 (2019) 57–61.
3. Machado, I.P., Teixeira, V.C., Pedroso, C.C.S., Brito, H.F., Rodrigues, L.C.V. X-ray scintillator Gd₂O₂S:Tb³⁺ materials obtained by a rapid and cost-effective microwave-assisted solid-state synthesis. *Journal of Alloys and Compounds*, 777 (2018) 638–645.
4. Carvalho, J.M., Pedroso, C.C.S., Machado, I.P., Hölsä, J., Rodrigues, L.C.V., Gluchowski, P., Lastusaari, M., Brito, H.F. Persistent luminescence warm-light LEDs based on Ti-doped RE₂O₂S materials prepared by rapid and energy-saving microwave-assisted synthesis. *Journal of Materials Chemistry C*, 6 (2018) 8897–8905.
5. Querobino, S.M., Faria, N.C., Vigato, A.A., Silva, B.G.M., Machado, I.P., Costa, M.S., Costa, F.N., Araujo, D.R., Alberto-Silva, C. Sodium alginate in oil-ploxamer organogels for intravaginal drug delivery: Influence on structural parameters, drug release mechanisms, cytotoxicity and *in vitro* antifungal activity. *Materials Science & Engineering C – Materials for Biological Applications*, 99 (2019) 1350–1361.
6. Vigato, A.A., Querobino, S.M., Faria, N.C., Candido, A.C.B.B., Magalhães, L.G., Cereda, C.M.S., Tófoli, G.R., Campos, E.V.R., Machado, I.P., Fraceto, L.F., Sairre, M.Inês., Araujo, D.R. Physico-Chemical Characterization and Biopharmaceutical Evaluation of Lipid-Poloxamer-Based Organogels for Curcumin Skin Delivery. *Frontiers in Pharmacology*, 10 (2019) 1006.
7. Querobino, S.M., Faria, N.C., Vigato, A.A., Silva, B.G.M., Machado, I.P., Costa, M.S., Costa, F.N., Araujo, D.R., Alberto-Silva, C. Physicochemical data of oleic acid-ploxamer organogel for intravaginal voriconazole delivery. *Data in Brief*, 25 (2019) 104180.
8. Passos, C.A.C., Rodrigues Junior, V.A., Abilio, V.T., Silva, G.M., Machado, L.C., Machado, I.P., Marins, A.A.L., Muri, E.J.B., Cruz, P.C.M., Merizio, L.G. Development and test of a small resistive fault current limiting device based on Hg, Re-1223 and Sm-123 ceramics. *Materials Research*, 17 (2014) 28–32.

5) Academic prizes

Featured Article – Best publications at the Institute of Chemistry, University of São Paulo (period 2017/2018):

Carvalho, J.M., Pedroso, C.C.S., Machado, I.P., Hölsä, J., Rodrigues, L.C.V.; Gluchowski, P., Lastusaari, M., Brito, H.F. Persistent luminescence warm-light LEDs based on Ti-doped RE₂O₂S materials prepared by rapid and energy-saving microwave-assisted synthesis. *Journal of Materials Chemistry C*, 6 (2018) 8897–8905.

6) Student supervisions

Bo Van Schie. *Designing Gd₂O₂S-based luminescent nanoparticles towards upconversion*. Bachelor's thesis, Condensed Matter and Interfaces (CMI), Debye Institute for Nanomaterials Science, Utrecht University. Supervisors: M.Sc Ian Pompermayer Machado and Prof. Andries Meijerink.

7) Other scientific contributions: organization of conferences

Name of event	1 st Chemistry Week of the Federal University of ABC
Date / Place	18 to 22 of September 2017 / Federal University of ABC, Santo André, Brazil
Activities	<ul style="list-style-type: none">• Participation in the organizing committee• As a lecturer in the course “<i>How the periodic table emerged?</i>” (3 hours)• Poster evaluator

Name of event	2 nd Germany-Brazil Bilateral Workshop: New light on mechanisms of chemical reactions
Date / Place	4 to 6 of December 2018 / University of São Paulo, São Paulo, Brazil
Activities	<ul style="list-style-type: none">• Participation in the organizing committee

8) External links and contact

Curriculum Lattes: <http://lattes.cnpq.br/0138746289165765>

ResearchGate profile: <https://www.researchgate.net/profile/Ian-Pompermayer-Machado>

E-mail: imachado@iq.usp.br and i.pompermayermachado@uu.nl

Phone: +55 11 98491-6579